CLEAVAGE FRACTURE ASSESSMENT INCORPORATING STRAIN GRADIENT PLASTICITY

ZHANG SUFEN

NATIONAL UNIVERSITY OF SINGAPORE

2011

CLEAVAGE FRACTURE ASSESSMENT INCORPORATING STRAIN GRADIENT PLASTICITY

ZHANG SUFEN
(*B. Eng., M. Eng.*)

A THESIS SUBMITTED
FOR THE DEGREE OF DOCTOR OF PHILOSOPHY

DEPARTMENT OF CIVIL AND ENVIRONMENTAL ENGINEERING
NATIONAL UNIVERSITY OF SINGAPORE

2011

ACKNOWLEDGEMENTS

The author wishes to express her sincere gratitude to her supervisors, Professor Somsak Swaddiwudhipong and Assistant Professor Qian Xudong for their help, guidance, and encouragement throughout the Ph.D study. Their mentally responsive, perceptive and meticulous attitude in the research left deep impression to her and will influence her for her whole life.

The author is extremely grateful for the Research Scholarship provided by the National University of Singapore.

In addition, the author would like to thank all the colleagues in the same research group, specially, Mr Petchdemaneengam Yuthdanai, Mr Ou Zhiyong who gave a lot of advice and meaningful discussions. The author would also like to thank the technicians, Mr Koh, Mr Wong, Mr Kamsan, and Mr Ang, in NUS structure lab and Ms Shen Lu in IMRE for their kind help in fracture tests and nanoindentation experiments. The Engineering IT Unit is also acknowledged for the technical assistances on computing facilities.

Last but not least, the author wishes to take this opportunity to thank her beloved parents and brothers for their love, support and encouragement.

SUMMARY

Brittle (cleavage) fracture of the steel material often causes catastrophic failures in the structures operating under low temperatures. In contrast to the ductile fracture, the assessment of brittle fracture generally unitizes a probability-based approach, represented by the widely recognized Weibull stress model, which depends significantly on the accurate computation of near-tip singular stress field. The existing research work shows that the conventional mechanism-based strain gradient (CMSG) plasticity theory, which defines the material hardening not only on the strain but also on the gradient of strain, is able to capture the asymptotic stress fields near the crack tip when the non-uniform plastic deformation is at the intrinsic material length scale whereas the classical theory of plasticity is unable to. However, the CMSG plasticity theory has not been applied to the cleavage fracture study, thus, the purpose of this work is to study the cleavage fracture incorporating the strain gradient plasticity.

For this purpose, the work adopts the CMSG plasticity theory to study the stress field near the crack tip and recalibrates the Weibull stress parameters for structural steels tested at low temperatures of $-20\,^{\circ}\mathrm{C}, -40\,^{\circ}\mathrm{C}$, and $-110\,^{\circ}\mathrm{C}$. As the material length scale is an essential parameter in the CMSG plasticity theory, we also carry out the indentation tests on two types of structural steels (S355 and S690) under different temperatures and various load levels from 30 to 500 mN. The corresponding finite element simulations incorporating the CMSG plasticity are performed to quantify the material length scale of the two types of steels. Based on the value of material length scale, this thesis continues to study the plastic strain gradient effect on the near-tip crack opening displacement by a compact tension finite element model and a plane strain small scale yielding model. A fracture test is also tried to experimentally quantify the plastic strain gradient effect on the near-tip crack opening displacement.

In the recalibration procedure of Weibull parameters (Weibull modulus m and the threshold fracture toughness K_{min}), the strain-gradient dependent material hardening described by the CMSG plasticity theory leads to significant increases in the Weibull stress magnitudes compared to those derived from the classical plasticity for fracture specimens under the same crack-opening load. The CMSG plasticity analysis generates slightly larger values of the Weibull modulus than those from the classical theory of plasticity analysis. The threshold fracture toughness values exhibit mild dependence on the material strain hardening properties. The magnitudes of the Weibull stress and the calibrated m and K_{min} values indicate negligible dependence on the material length scales of 5 and 10 μm. The calibrated Weibull stress model predicts a higher probability of fracture from the CMSG plasticity analysis than that from the classical plasticity analysis for a macro-crack under the same opening load for the same or calibrated Weibull modulus values.

This study also shows that the crack front constraints, characterized by the linear-elastic T-stress, impose a strong effect on the magnitude of the Weibull stresses, especially for crack fronts experiencing low plasticity constraints. Both proportional and non-proportional loadings cause significant differences in the Weibull stress values and the constraint-correction function.

The simulations of the indentation test at two different temperatures, $20\ ^{o}\mathrm{C}$ and $300\ ^{o}\mathrm{C}$, for structural steels S355 and S690 using the CMSG plasticity theory show that the material length scale of the structural steel is around 7 μm at the two different temperatures. Finite element analyses also show that the strain gradient effect on the crack tip opening displacement (CTOD) is negligible based on the traditional definition of the CTOD as the location to determine the CTOD moves further away from the crack tip with the increasing loads. However, the CTOD values near the true crack tip depend strongly on the plastic strain gradient. These displacements computed using the CMSG plasticity theory are lower than those from the classical plasticity theory, indicating that the strain gradient stiffens the material deformation near the crack tip, thus, reduces the crack opening displacement.

In conclusion, the current study of cleavage fracture based on the CMSG plasticity theory shows that the CMSG plasticity could strongly raise the magnitudes of Weibull stresses compared with those computed from the classical plasticity, while both constitutive models provide the similar Weibull stress parameters (Weibull modulus m and the threshold fracture toughness K_{min}). The CMSG plasticity theory provides drastically different estimation of the near-tip crack opening displacement, implying the plastic strain gradient hardens the material and limits the plastic deformation near the crack tip. In a practical sense, the CMSG plasticity theory provides a new insight to the study of cleavage fracture and helps understand the micro scale deformation mechanism of cleavage fracture.

TABLE OF CONTENTS

LIST OF FIGURES

LIST OF TABLES

NOMENCLATURE

a	crack depth
$\bar{b}$	Burgers vector
b	remaining ligament in a specimen
B	thickness of a specimen
E	elastic modulus
g	constraint function
G	energy release rate for linear elastic material
J	energy release rate for nonlinear elastic material
K	bulk modulus
K_I	mode I stress intensity factor
K_{Ic}	mode I fracture toughness
K_{Jc}	critical stress-intensity factor
K_{min}	threshold fracture toughness
l	material length scale
l_s	size of micro cracks
m	Weibull modulus
M	nondimensional loading parameter
n	rate sensitivity exponent
N	strain-hardening exponent
n_{xC}	number of high constraint specimens (n_{HC}) or number of low constraint specimens (n_{LC})
p_f	probability of fracture within a single volume of material
P_f	cumulative probability of fracture

r	distance measured from the crack tip
r^*	number of valid specimens
R	radius of the modified boundary layer model
R_0	initial root radius at the crack tip
T_0	reference temperature
T	linear-elastic T-stress
u_i	displacement in i-th direction ($i = x$ or y)
V	volume of the fracture process zone
V_0	reference volume
W	width of a specimen
α	empirical constant to determine the material length scale
β	biaxiality ratio
χ	material parameter characterizing the distribution of micro cracks in the material
ε_{ij}	strain tensor
ε'_{ij}	deviatoric strain tensor
η^p	effective plastic strain gradient
κ	material parameter characterizing the distribution of micro cracks in material
λ	stress cutting parameter in the Weibull stress model
μ	shear modulus
θ	angle
Θ	temperature
σ_c	critical stress
σ_e	effective stress

σ_f	flow stress
σ_{eff}	a stress component effectively driving the opening of micro cracks in the material
σ_{ij}	stress tensor
σ'_{ij}	deviatoric stress tensor
σ_u	Weibull scaling parameter
σ_w	Weibull stress
σ_y	yield stress
σ_{y-ref}	reference yield stress
υ	Poisson’s ratio

LIST OF ABBREVIATIONS

CMOD	crack mouth opening displacement
CMSG	conventional mechanism-based strain gradient
C(T)	compact tension
CTOD	crack tip opening displacement
DBT	ductile-to-brittle transition
FPZ	fracture process zone
MBL	modified boundary layer
SE(B)	single-edge-notched bend
SSY	small scale yielding

CHAPTER 1 INTRODUCTION

1.1 Background

The fracture of engineering structures turns into a heated research topic since the World War II as fracture failures result in great economic losses and even human’s lives. Though safety measures have been taken during the design stage, fracture failure may still occur due to various reasons such as the temperature variations and the unavoidable micro cracks existing in welded components. From the investigation of Chang and Lin [1], around 30% of the 242 storage tank accidents in the past 40 years are due to tank crack and rupture.

There are two types of fracture often observed in structural steels. One type is ductile fracture (see Figure 1.1(a)) [2]. The ductile fracture normally starts from the nucleation of the micro voids and the growth of micro voids between inclusions and the matrix. When the load increases, these micro voids coalesce to form a macroscopic crack. The sufficiently high load level causes the severe plastic deformation around the large crack before the final rupture.

Cleavage fracture is another type of fracture (see Figure 1.1(b)) [2]. It occurs with rapid crack propagation with less plastic deformation at the crack tip. The existing sharp micro crack and the second-phase particles in the matrix can provide sufficient local stress to initiate the cleavage fracture to break the bonds of grains and lead to final fracture failure.

The ductile fracture can transform into cleavage fracture for body-centred-cubic (bcc) metals with the decreasing of temperature. At high temperatures (normally greater than 100 ^{o}C), the steel often fails by micro void coalescence (i.e., ductile fracture mode) while at low temperatures (normally below 0 ^{o}C), the ferritic steel exhibits cleavage fracture mode. At the transition temperatures (-150 ^{o}C-100 ^{o}C), both types of fractures can occur. The ferritic steel may initially undergo ductile fracture and finally fail by cleavage fracture. Therefore, at the transition temperatures, the fracture toughness data for cleavage fracture are normally scattering. The assessment of brittle fracture generally unitizes a probability-based approach, e.g., the Weibull stress model, instead of a deterministic method which is often used to access the ductile fracture. The widely recognized Weibull stress model depends significantly on the accurate computation of near-tip singular stress field. The existing research work [3-5] shows that the conventional mechanism-based strain gradient (CMSG) plasticity theory, which defines the material hardening not only on the strain but also on the gradient of strain, is able to capture the asymptotic stress fields near the crack tip when the non-uniform plastic deformation is at the intrinsic material length scale whereas the classical theory of plasticity is unable to. Most research work [6-10] studies the Weibull model based on the classical plasticity theory. As the CMSG plasticity theory has not been applied to the cleavage fracture study, this work is to study the cleavage fracture incorporating the CMSG plasticity.

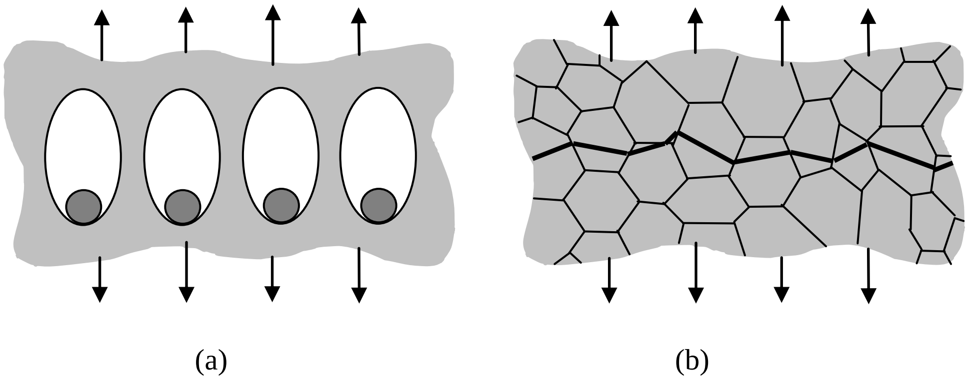

(a) (b)

Figure 1.1 Two fracture micro mechanisms in metals (a) Ductile fracture; (b) Cleavage fracture

1.2 Literature Review

Cleavage fracture of steel often causes sudden catastrophic structural failures without extensive plastic deformations. Some examples of failures due to cleavage fracture can be seen in pressure vessels after many years of exposure to radiation and in offshore platforms in the arctic zone under very low temperatures. In the ductile-to-brittle transition (DBT) region, the fracture toughness of laboratory specimens show scattered results. This drives a probability-based approach to assess the cleavage fracture failure.

A three-parameter statistical model adopted in ASTM E 1921 [11] is developed from extensive experimental database of laboratory fracture specimens fabricated from a wide range of ferritic steels. The fracture toughness, K_J, is directly converted from the fracture toughness and the energy release rate, J, in the small scale yielding plane strain conditions. Thus, this Weibull statistical model applies only to the configuration with small scale yielding and high constraint conditions, that is, the plastic zone resides in a localized material around the crack tip. However, the specimens always gradually lose constraint with increased plastic deformation ahead of the crack tip. In order to include both high and low constraint conditions that may exist at the crack tip, Beremin's group [12] propose the "Weibull stress" model to characterize the cumulative probability of cleavage fracture. This model uses the average stress concept to describe the fracture driving force instead of using the micro scale toughness concept, thus, eliminates the limitation from the constraints ahead of the crack tip.

From the observation of fracture tests, the fracture failure actually does not occur if the stress intensity factor is below a certain value. Therefore, Bakker and Koers [13] extend Beremin model by introducing the threshold stress, σ_{th}. Zero failure probability happens when the stress acting on the micro crack is less than the threshold value.

Following Bakker and Koers [13], the parameters m and σ_{th} in the Weibull stress model are studied [10, 14-24]. Moorman [25] also derives the probability accounting for the critically sized carbide in the fracture zone to provide the theoretical basis for the cleavage fracture in three-dimensional cracked structures. However, the value of σ_{th} is difficult to determine. Gao *et al*. [19] propose that the threshold stress σ_{th} can be the minimum Weibull stress σ_{w-min} corresponding to the minimum toughness $K_{\min}$. The proposed micro scale Weibull stress model has a similar form as the macro three-parameter statistical model employed in ASTM E 1921 [11]. The research group in the University of Illinois [10, 20, 23] further modify the Weibull stress model by combining the effects of the constraint loss, the length of the crack front and the minimum value of the Weibull stress. Gao *et al.* [19] and Petti and Dodds [10] present procedures to calibrate the parameters, m and σ_{w-min}. In the later work of Wasiluk *et al*. [20], the parameter σ_u is shown to increase as the temperature increases, while m is independent of the temperature. The method of treating scattered fracture toughness also gradually reaches maturity and more researchers [26-31] put effort to improve the Weibull stress model. Bostjan and Anuradha [32] develop the Weibull model for cleavage fracture and crack extension direction for graded structural steels in which the yield stress and fracture toughness vary spatially. Jorg *et al*. [33] concern the micro defect nucleation role in the probabilistic modeling of cleavage failure in ferritic steels and then propose [34] the Weibull model for the probabilistic cleavage fracture assessment of ferritic materials by including the nucleation and propagation of micro defects.

On the other hand, a series of micro scale experiments show that a significant plastic flow exists when the cleavage cracks in the bimaterial interface of niobium and sapphire [35, 36]. The macroscopic work for the interface fracture is 1000 times more than the atomic work for the separation of the two materials. Similar phenomena are also found in other materials' system [37-39].

Various micromechanical experiments are adopted to study the material properties and the micro scale plastic deformation mechanism of materials since the 1990s. The experimental observations by Fleck and Hutchinson [40], Ma and Clark [41] and Nix [42] show that the indentation hardness of metals and ceramic increases when the indentation depth decreases to the micron or nanometer level. These size dependent phenomena are found to be caused by the dislocation of crystal planes which cannot be explained by the classical theory of plasticity. Ashby [43] discovers that the size effect is related to the presence of a large spatial gradient of strain which requires the storage of geometrically necessary dislocations. Fleck and Hutchinson [40] give the physical arguments for the size effect in the framework of continuum plasticity, and the material flow strength is controlled by the total density of stored dislocations, which can be described by the Taylor dislocation model that incorporates both the statistically stored dislocation density and the geometrically necessary dislocation density. The plastic strain is associated with the statistically stored dislocation while the strain gradient plasticity is related to the geometrical dislocation. Therefore, the state of the stress is observed to be a function of both the strain and the strain gradient only if the non-uniform plastic deformation and the material length scales are of the same order [44-46].

Gao *et al.* [46] and Huang *et al*. [47] propose a multi-scale framework based on the mechanism-based strain gradient (MSG) plasticity, to provide a systematic approach for constructing the meso-scale constitutive laws, incorporating the micro scale plasticity based on the Taylor’s dislocation model.

Huang *et al*. [3] find that in the mixed-mode (mode I and II), the stresses near the crack tip with the strain gradient is 2.5 times higher than the HRR solutions. Chen *et al*. [48] also apply the MSG theory to the near-tip stress field analysis in both mode I and II. In the two modes, the maximum shear stresses are 2 and 3 times higher than the corresponding HRR solutions, respectively. Jiang *et al*. [49] implement the mechanism-based strain gradient (MSG) plasticity in mode I fracture model. The numerical results demonstrate that the stress level near the crack tip from the MSG plasticity is higher than that from the classical plasticity, explaining the observed cleavage fracture phenomenon in ductile materials. Wei *et al*. [50] study the steady-state crack growth based on the MSG theory. The results show that the steady-state fracture toughness depends on the material length scale.

Even though the mechanism-based strain gradient (MSG) plasticity has been applied to study the fracture, it involves the higher order stress in the governing equation [4]. Thus, much computational effort is necessary to solve the additional governing equations as well as the boundary conditions. Huang *et al*. [4] propose a conventional mechanism-based strain gradient (CMSG) plasticity theory. The theory is based on the Taylor dislocation model and preserves the classical continuum plasticity requirements. The higher order stress appears only in the constitutive model, and no additional higher order stress related boundary conditions need to be satisfied. Therefore, the CMSG plasticity theory can be conveniently implemented in strain hardening material. Results from the MSG plasticity theory and the CMSG plasticity theory are consistent for most cases except in the region near the boundary [4].This is expected as the MSG plasticity theory introduces additional higher order stress in the boundary conditions while CMSG plasticity theory does not. As the deviation from the two approaches are due to the presence of higher order stress at the boundary for MSG theory and based on Saint-Venant’s principle, this deviation is normally confined in the region near the boundary.

Qu *et al.* [51] apply the CMSG plasticity theory to investigate the stress field of interface crack between niobium and sapphire by simulating the test done by Elssner *et al.* [35] and Korn *et al.* [36]. The opening stress is 4 times higher than that from the classical plasticity analysis and is enough to initiate the cleavage fracture at the interface of the bimaterials.

Swaddiwudhipong *et al.* [5] apply the CMSG plasticity theory to C^0 element and study the stress distribution ahead of the crack tip and the obtained results coincide with Jiang *et al.* [49] and Qiu *et al.* [52]. The stress ahead of the crack tip obtained from CMSG plasticity theory is higher than that computed from the classical plasticity theory. Swaddiwudhipong *et al.* [53, 54] implement the CMSG plasticity theory in the C^0 type solid, axisymmetric and plane elements to simulate the micro scale material plastic deformation using the classical finite element (FE) formulation. The CMSG plasticity theory predicts closely the material plastic deformation and the size effects observed in micron and submicron scale indentation experiments for a wide range of engineering materials [55, 56].

As described by the Weibull stress model, the cumulative probability of cleavage fracture depends on the scalar Weibull stress, σ_w, which is defined in this study as the integration of the maximum principal stress over the fracture process zone around the crack tip. Therefore, it is necessary to accurately predict the values of Weibull stress or the maximum principal stress ahead of the crack tip. Existing researches [5, 49, 51] find that the plastic strain gradient can significantly raise the stress field near the crack tip when the plastic deformation becomes comparable with the material length scale at micron or submicron level. However, the plastic strain gradient theory has not yet been applied to compute the Weibull stress and assess the cleavage fracture toughness data measured in laboratories. The calibration of the Weibull parameters for Euro steels (22-Ni-MoCr37 steels) is still based on the classical plasticity, which fails to explain the high stress at the crack tip as the constitutive model of classical plasticity does not contain the material intrinsic length. All these issues inspire the current work to explore the plastic strain gradient effect on the cleavage crack driving force, and recalibrate the Weibull stress parameter for the experimental data provided by the European Union project entitled "Fracture toughness of steel in the ductile to brittle transition regime".

1.3 Objective and Scope of Research

The main objective of current work is to study the cleavage fracture by the conventional mechanism-based strain gradient (CMSG) plasticity theory.

To this purpose, the current work adopts the small scale yielding (SSY) modified boundary layer (MBL) model to study the plastic strain gradient effect on the stress field near the crack tip.

To verify the plastic strain gradient effect on the Weibull parameters, this work recalibrates the Weibull parameters by both the CMSG plasticity theory and the classical plasticity theory for 22-Ni-MoCr37 steel at various temperatures (–20 ^{o}C, –40 ^{o}C, and –110 ^{o}C), at which experimental fracture toughness data were provided by the European Union project.

As the magnitude of burgers vector of 22-Ni-MoCr37 steels in the European Union project are currently not available, it is impossible to estimate the material length scales for the 22-Ni-MoCr37 steels. As the offshore-structure steels, such as S355 and S690, are readily available, the indentation tests are carried out to investigate the material length scales on these two types of steels instead of 22-Ni-MoCr37 steels. Also as it has difficulty in the experimental set up for the indentation tests at low temperatures (–20 ^{o}C,

–40 °C, and –110 °C), the current tests are performed at other two temperatures (20 °C and 300 °C) to verify the temperature effect on the material length scale of the steels (S355 and S690). Thus, the load-displacement curves from indentation tests at temperatures 20 °C and 300 °C are simulated to quantify the values of material length scale for these types of steels by varying the material length scale values in the CMSG plasticity constitutive model. The simulations of the indentation tests on the two types of steels at –40 °C are also performed though currently the indentation tests have not been done.

Finally, the finite element CMSG plasticity analyses are performed using the material length scale that predicted by the indentation tests analyses for S355 to study the plastic strain gradient effect on the near-tip crack opening displacement.

1.4 Organization of Thesis

The research background and literature review are presented in Chapter 1.

Chapter 2 introduces the fundamental knowledge of the cleavage fracture model and the conventional mechanism-based strain gradient (CMSG) plasticity. It also presents the method of treating the scattered fracture toughness data at low temperatures spanning over the ductile to brittle transition region.

Chapter 3 describes the stress field near the crack tip by the finite element analyses of a small scale yielding model. Two types of meshes (model with sharp crack and model with initial root at the crack tip) are used in modeling the crack tip. The stress distributions along the crack surface are studied and compared by the classical plasticity theory and the CMSG plasticity theory.

In Chapter 4, both the classical plasticity and the CMSG plasticity analyses are performed to assess the fracture toughness of European material at low temperatures (–20 ^{o}C, –40 ^{o}C, –110 ^{o}C). The two parameters in Weibull stress model, Weibull modulus m and the threshold fracture toughness K_{min} are calibrated through the classical plasticity and the CMSG plasticity analyses.

Chapter 5 presents both the uni-axial tensile tests at different temperatures (20 ^{o}C, 300 ^{o}C and -40 ^{o}C), and the indentation tests for two grades of steels (S355 and S690) at 20 ^{o}C and 300 ^{o}C as currently it has difficulties in instrumental setting up for indentation tests at -40 ^{o}C. The basic material parameters (E, σ_{y}, and N) are obtained through fitting the uni-axial stress strain curves by the plastic hardening law. The three material parameters and assumed material length scales are introduced to the CMSG plasticity constitutive model to simulate the indentation tests. The value of material length scale is estimated through fitting the load-displacement curves of the indentation tests at temperatures 20 ^{o}C and 300 ^{o}C. The simulations for indentation test on the two types of steel at –40 ^{o}C are also performed for the reference of future indentation tests at this temperature.

Chapter 6 involves the plastic strain gradient effect on the near-tip crack opening displacement by a compact tension model with the thickness of half an inch and a plane strain small scale yielding model with/without T-stress.

Lastly, the conclusions and recommendation for future work are presented in chapter 7.

CHAPTER 2 THEORETICAL BACKGROUND

2.1 Weibull Stress Framework

2.1.1 Weakest-Link Based Model

The cleavage fracture is a highly localized phenomenon [57]. It is very sensitive to the material characteristics, the structural geometry, the loading history and the temperature variation that spans over the ductile-to-brittle (DBT) region. The inhomogeneity in the local material causes the scatter in the measured fracture toughness data from the laboratory tests. Thus, a probability-based approach is needed to assess the cleavage fracture toughness data rather than a deterministic approach for the ductile fracture.

In ASTM E 1921 [11], the weakest link concept is applied to the DBT region of ferritic steels. This concept simplifies the crack front loading condition to a uniform distribution of the *J*-integral along the crack front and a small scale yielding condition prevailing at the fracture failures. Based on these, a three-parameter statistical model as shown in Equation (2.1) is used to predict the cumulative fracture probability at each DBT temperature [6].

$$P_f\left(K_{JC}\right) = 1 - \exp\left[-\left(\frac{K_{JC} - K_{min}}{K_0 - K_{min}}\right)^4\right] \tag{2.1}$$

where K_{JC} is the fracture toughness, which can be derived from $K_{JC} = \sqrt{EJ/(1-\upsilon^2)}$ under the conditions of plane strain and small scale yielding. K_{min} is the threshold fracture toughness, which denotes the vanishing of the fracture cumulative probability when the stress intensity factor K_{JC} is less than or equal the threshold toughness K_{min}. In ASTM E 1921 [11], K_{min} is 20 $\text{MPa}\sqrt{\text{m}}$. K_0 is the temperature dependent toughness and its corresponding cumulative fracture probability, P_f is 63.2%. K_0 is determined through the maximum likelihood method as shown in Equation (2.2) [11].

$$K_0 = \left[\sum_{i=1}^{N_t} \frac{\left(K_{JC(i)} - K_{min}\right)^4}{r^* - 0.3068} \right]^{1/4} + K_{min} \tag{2.2}$$

where N_t is the total number of the specimens in a dataset, r^* is the number of validate specimens.

Since the statistical fracture model is applicable only to the small scale yielding high constraint specimens, Beremin's group [12] propose a mechanical Weibull stresss model to predict the fracture probability of both high plastic constraint and low plastic constraint fracture specimens.

2.1.2 Weibull Stress Model

The Weibull stress model assumes that the fracture process zone consists of a number of non-overlapping and uniformly stressed small volumes of material. Each volume of material contains a series of randomly distributed micro cracks. The distribution of the size (l_s) of micro cracks follows from the probability density function [12]

$$q\left(l_s\right) = \left(\frac{\kappa}{l_s}\right)^{\chi} \tag{2.3}$$

where κ and χ characterize the distribution of micro cracks ahead of the crack tip. By the Griffith-type fracture criterion, the fracture probability, p_f within a single volume of material is a function that relies on the stress field near the micro cracks [12].

$$p_f\left(\sigma_{eff} > \sigma_c\right) = \left(\frac{\sigma_{eff}}{\sigma_u}\right)^m \tag{2.4}$$

where σ_{eff} is the effective stress component such as the maximum principal stress. σ_c is the critical stress for occurrence of cleavage fracture. m is the material parameter, which derives from κ and χ, and depends on the size distribution of micro cracks; and σ_u is scale parameter and represents the aggregate fracture toughness of micro cracks. For a large number of volumes of material in the fracture process zone, the Weibull stress model adopts the weakest link hypothesis to compute the cumulative fracture probability (see Equation (2.5)). The weakest link hypothesis assumes that failure happens once the cleavage fracture occurs in any volumes of the material [12].

$$P_f\left(\sigma_w\right) = 1 - \exp\left[-\left(\frac{\sigma_w}{\sigma_u}\right)^m\right] \tag{2.5}$$

where the Weibull stress σ_w is equal the normalized integral of the effective stress, σ_{eff} over the volume of the fracture process zone [12]:

$$\sigma_w = \left[\frac{1}{V_0}\int_V \sigma_{eff}^m \, dV\right]^{1/m} \tag{2.6}$$

The parameter V_0 is a reference volume and is arbitrarily chosen to equal 1 mm^3 in the current study. The effective stress is taken as the maximum principal stress, σ_1. The fracture process zone is defined by the region $\sigma_1 > \lambda\sigma_y$. The stress cutting parameter, λ , is taken as 2.0 in this study following Wasiluk *et al.* [24], who have calibrated the Euro steel fracture toughness data using the classical plasticity theory. This typical value of λ has been generally accepted to include the highly stressed material surrounding the crack tip in computing the Weibull stress values.

In plane strain and small scale yielding conditions, the macroscopic and microscopic fracture models are connected by [19],

$$\sigma_w^m = CBJ^2 \text{ or } \sigma_w^m = \bar{C}BK_J^4 \tag{2.7}$$

where $\bar{C}$ equals $C\left[\left(1-\upsilon^2\right)/E\right]^2$ and B is the thickness of the fracture specimen.

Since the small scale yielding condition can be violated by the increased plastic deformation ahead of the crack tip, Gao *et al.* [58] propose a non-dimensional $g(M)$ function to characterize the constraint differences between the plane strain small scale yielding conditions and the actual fracture specimens as follows,

$$\sigma_w^m = CBJ_{avg}^2 g(M) \text{ or } \sigma_w^m = \bar{C}BK_{J(avg)}^4 g(M) \tag{2.8}$$

where M is the non-dimensional loading parameter and $M = b\sigma_y / J$; b is the remaining ligament length of the fracture specimen; the constraint function, $g(M)$ equals 1 in small scale yielding condition; and the constant C is derived from relations between the Weibull stress σ_w and the J values from a MBL model under remote K_I loading and zero T-stress.

Petti and Dodds [23] argue that the microscopic Weibull stress model shall reflect the cumulative probability of cleavage fracture observed on the macroscopic level computed from Equation (2.1). Therefore, Equation (2.8) is substituted into Equation (2.1) to cancel the effect of the reference volume V_0 on the estimated probability of fracture, and the following is obtained by Petti and Dodds [23]:

$$P_f\left(\sigma_w\right) = 1 - \exp\left[-\left(\frac{\sigma_w^{m/4} - \sigma_{w-min}^{m/4}}{\sigma_u^{m/4} - \sigma_{w-min}^{m/4}}\right)^4\right] \qquad \text{for } \sigma_w > \sigma_{w-min} \tag{2.9}$$

$$P_f\left(\sigma_w\right) = 0 \qquad \text{for } \sigma_w \le \sigma_{w-min} \tag{2.10}$$

where the threshold Weibull stress σ_{w-min} and the Weibull scaling parameter σ_u equals the Weibull stress value corresponding to K_{min} and K_0, respectively. Petti and Dodds [1] prove that the Weibull scaling parameter σ_u depends on the fracture toughness K_0, which is described by the Master Curve [11] at temperature Θ and corresponds to the fracture failure probability of 63.2%:

$$K_0 = 31 + 77\exp\left[0.019(\Theta - T_0)\right] \tag{2.11}$$

where T_0 refers to the reference temperature at which the median fracture toughness measured from 1T (1 inch thick) fracture specimens equals $100\,\mathrm{MPa}\sqrt{\mathrm{m}}$. ASTM E 1921 [11] provides the standard experimental procedure to determine the T_0 value.

2.1.3 Calibration of Weibull Parameters

As the value of σ_u follows the temperature dependence described by the Master Curve, the cumulative fracture probability in Equation (2.9) relies on two parameters, the Weibull modulus m and the threshold Weibull stress σ_{w-min}. Wasiluk *et al.* [24] outline the detailed procedures for calibrating the two Weibull parameters based on the fracture toughness data measured from two sets of specimens with different crack front constraint conditions at the same transition temperature.

The calibration procedure first sets the high constraint (HC) data obtained from the fracture specimens with high crack front constraint condition and low constraint (LC) data obtained from specimens with low crack front constraint conditions. The fracture probability is calculated as follows [59],

$$P_f = \frac{i - 0.3}{n_{xC} + 0.4} \tag{2.12}$$

where i is the rank number, and n_{xC} is the total number of the specimens in the high constraint data set (n_{HC}) or the total number of the specimens in the low constraint dataset (n_{LC}). With the material stress-strain data measured at the same temperature, the relations between the Weibull stress σ_w and the macroscopic crack driven force J of the modified boundary layer (MBL) model can be obtained from the finite element analysis. The $g(M)$ function equals 1 for the MBL model when the plane strain, K_I displacement field is imposed on its outer radius. The constant C in Equation (2.8) then can be determined by the relations of J and σ_w in the MBL model. The J and σ_w relations obtained from the finite element (FE) analysis for fracture specimens can determine the constraint correction function, $g(M)$ in Equation (2.8) with the constant C obtained from MBL model. With the trial pairs of Weibull parameters (m and K_{min}), the constraint correction function $g(M)$ scales the original toughness data of the fracture specimens which are either high constraint or low constraint specimens to the 1T small scale yielding condition [24].

$$K_{JC}^{SSY(1T)} = K_{min} + \left[g\left(M^{(xT)}\right)^{1/4} K_{JC}^{(xT)} - g\left(M_{min}^{(xT)}\right)^{1/4} K_{min} \right] \times \left(\frac{B_{xT}}{B_{1T}} \right)^{1/4} \tag{2.13}$$

At each fracture probability, Equation (2.14) sums the errors between the scaled fracture toughness data of high constraint and the low constraint specimens, and also the errors between the scaled fracture toughness data of high/low constraint specimens and toughness data of the 1T plane strain SSY model [24].

$$Error\left(m, K_{min}\right) = \sum_{i=1}^{n_{LC}+n_{HC}} \left| K_{JC(i)}^{xC-1TSSY} - K_{JC(i)}^{1TSSY} \right| WF_{(i)} + \sum_{i=1}^{\min\left(n_{LC}, n_{HC}\right)} \left| K_{JC(i)}^{HC-1TSSY} - K_{JC(i)}^{LC-1TSSY} \right| WF_{(i)} \tag{2.14}$$

where WF is the weight factor $\left(\sum WF = 1\right)$. The calibrated parameters m and K_{min} will give the minimum error in Equation (2.14). In the current study, m is tested from 1 to 30 with the step of $\Delta m = 1$ and K_{min} value is tested from 1 to 80 $\mathrm{MPa}\sqrt{\mathrm{m}}$ with the step of $\Delta K_{\min} = 1\,\mathrm{MPa}\sqrt{\mathrm{m}}$ to calibrate the m and K_{min} in the Weibull model.

2.2 Concept of *T*-Stress

For a crack in an isotropic elastic material subjected to plane strain Mode I loading, if the origin of the coordinate system is defined at the crack tip, and the x axis locates along the crack plane, the stress terms of the Williams solution [2] can be written as Equation (2.15):

$$\sigma_{ij} = \frac{K_I}{\sqrt{2\pi r}} f_{ij}(\theta) + \begin{bmatrix} T & 0 & 0 \\ 0 & 0 & 0 \\ 0 & 0 & \upsilon T \end{bmatrix} + \text{H.O.T.} \tag{2.15}$$

where H.O.T. denotes the 'higher order terms'. The above equation shows that the stress field surrounding the crack tip consists of a singular term, a constant term and the higher order terms. At the position very close to the crack tip ($x \to 0$), the higher order terms are negligible. The constant term, T is called *T*-stress, which acts parallel with the crack plane. The zero *T*-stress refers to the small scale yielding condition. The non-zero *T*-stress has profound effect on the stress distribution ahead of the crack tip (Figures 2.1 and 2.2) and the shape of the plastic zone (Figure 2.3). The positive *T*-stress increases the crack opening stress. The crack tip is under high plastic constraint condition and the plastic zone concentrates behind the crack tip (see Figure 2.3(a)). The negative *T*-stress decreases the crack opening stress and the crack tip is under low plastic constraint condition. The yield zone is concentrated ahead of the crack tip (see Figure 2.3(b)), which may sustain a higher load at the fracture failure.

For elastic plane strain problems, the strain components accounting for *T*-stress can be written according to Hooke's law as follows,

$$\varepsilon_x = \frac{1+\upsilon}{E}\left[(1-\upsilon)\sigma_x - \upsilon\sigma_y\right] = \frac{1-\upsilon^2}{E}T \tag{2.16}$$

$$\varepsilon_y = \frac{1+\upsilon}{E}\left[(1-\upsilon)\sigma_y - \upsilon\sigma_x\right] = -\frac{(1+\upsilon)\upsilon}{E}T \tag{2.17}$$

$$\gamma_{xy} = \frac{\tau_{xy}}{G} = 0 \tag{2.18}$$

Note that

$$\varepsilon_x = \frac{\partial u}{\partial x};\ \varepsilon_y = \frac{\partial v}{\partial y};\ \gamma_{xy} = \frac{\partial u}{\partial y} + \frac{\partial v}{\partial x} \tag{2.19}$$

the displacement can be obtained by integrating Equation (2.19),

$$u_{ij} = \delta_{ij} T_i x_j \tag{2.20}$$

where $T_i = \frac{1-\upsilon^2}{E}T$ for $x_j = x$ or $-\frac{\upsilon(1+\upsilon)}{E}T$ for $x_j = y$.

Equation (2.20) implies that displacements due to *T*-stress effect are proportional to the distance from the crack tip.

The total elastic displacement fields including *T*-stress effects for the plane strain condition are

$$u(r,\theta) = \frac{K_I(1+\upsilon)}{E}\sqrt{\frac{r}{2\pi}}\cos\left(\frac{\theta}{2}\right)\left(3-4\upsilon-\cos\theta\right) + \frac{1-\upsilon^2}{E}Tr\cos\theta \tag{2.21}$$

$$v(r,\theta) = \frac{K_I(1+\upsilon)}{E}\sqrt{\frac{r}{2\pi}}\sin\left(\frac{\theta}{2}\right)\left(3-4\upsilon-\cos\theta\right) - \frac{\upsilon(1+\upsilon)}{E}Tr\sin\theta \tag{2.22}$$

The in-plane stress components around the crack tip are

$$\sigma_x = \frac{K_I}{\sqrt{2\pi r}}\cos\frac{\theta}{2}\left(1-\sin\frac{\theta}{2}\sin\frac{3\theta}{2}\right) + T + \text{H.O.T} \tag{2.23}$$

$$\sigma_y = \frac{K_I}{\sqrt{2\pi r}}\cos\frac{\theta}{2}\left(1+\sin\frac{\theta}{2}\sin\frac{3\theta}{2}\right) + \text{H.O.T} \tag{2.24}$$

$$\tau_{xy} = \frac{K_I}{\sqrt{2\pi r}}\cos\frac{\theta}{2}\sin\frac{\theta}{2}\cos\frac{3\theta}{2} + \text{H.O.T} \tag{2.25}$$

Near the crack tip, the higher order terms of the stress can be ignored, the principal stress components in the elastic field are,

$$\sigma_1 = \frac{K_I}{\sqrt{2\pi r}}\cos\frac{\theta}{2} + \frac{1}{2}T + \frac{1}{2}\sqrt{\frac{K_I^2}{2\pi r}\sin^2\theta + T^2 - \frac{2K_I T}{\sqrt{2\pi r}}\sin\theta\sin\frac{3\theta}{2}} \tag{2.26}$$

$$\sigma_2 = \frac{K_I}{\sqrt{2\pi r}}\cos\frac{\theta}{2} + \frac{1}{2}T - \frac{1}{2}\sqrt{\frac{K_I^2}{2\pi r}\sin^2\theta + \sigma_{0x}^2 - \frac{2K_I T}{\sqrt{2\pi r}}\sin\theta\sin\frac{3\theta}{2}} \tag{2.27}$$

$$\sigma_3 = \sigma_z = \upsilon\left(\frac{2K_I}{\sqrt{2\pi r}}\cos\frac{\theta}{2} + T\right) \tag{2.28}$$

By the von Mises equation,

$$\sigma_e = \sqrt{\frac{1}{2}\left[\left(\sigma_1 - \sigma_2\right)^2 + \left(\sigma_2 - \sigma_3\right)^2 + \left(\sigma_1 - \sigma_3\right)^2\right]} \tag{2.29}$$

the von Mises equation including the *T*-stress effect can be written as

$$\sigma_e = \sqrt{\frac{1}{2}\frac{3}{2}\left[\frac{K_I^2}{2\pi r}\sin^2\theta + T^2 - \frac{2K_I T}{\sqrt{2\pi r}}\sin\theta\sin\frac{3\theta}{2}\right] + 2\left[\left(1-2\upsilon\right)\frac{K_I}{\sqrt{2\pi r}}\cos\frac{\theta}{2} + \left(\frac{1}{2} - \upsilon\right)T\right]^2} \tag{2.30}$$

Neglecting the effect of *T*-stress and the stress redistribution at the crack tip, the radius of the plastic zone is [2],

$$r_y\left(\theta\right) = \frac{1}{4\pi}\left(\frac{K_I}{\sigma_y}\right)^2\left[\left(1-2\upsilon\right)^2\left(1+\cos\theta\right) + \frac{3}{2}\sin^2\theta\right] \tag{2.31}$$

Let the ratio of *T*-stress and material yield stress to be a constant n ($n = T/\sigma_y$), the von Mises stress at $\theta = 0^{\mathrm{o}}$ equals

$$\sigma_e = \sqrt{\left\{\left[\left(1-2\upsilon\right)\frac{K_I}{\sqrt{2\pi r}} + \left(\frac{1}{2} - \upsilon\right)n\sigma_y\right]^2 + \frac{3}{4}\left(n\sigma_y\right)^2\right\}} \tag{2.32}$$

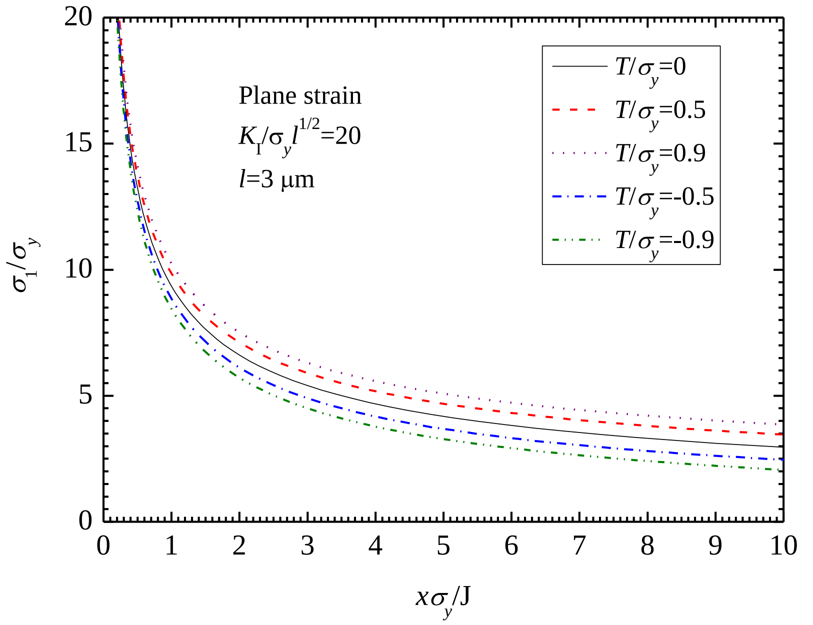

Figure 2.1 The maximum principal stress distribution along the symmetric crack plane at $T/\sigma_y = 0, \ \pm 0.5, \text{ and } \pm 0.9$ from elastic solutions

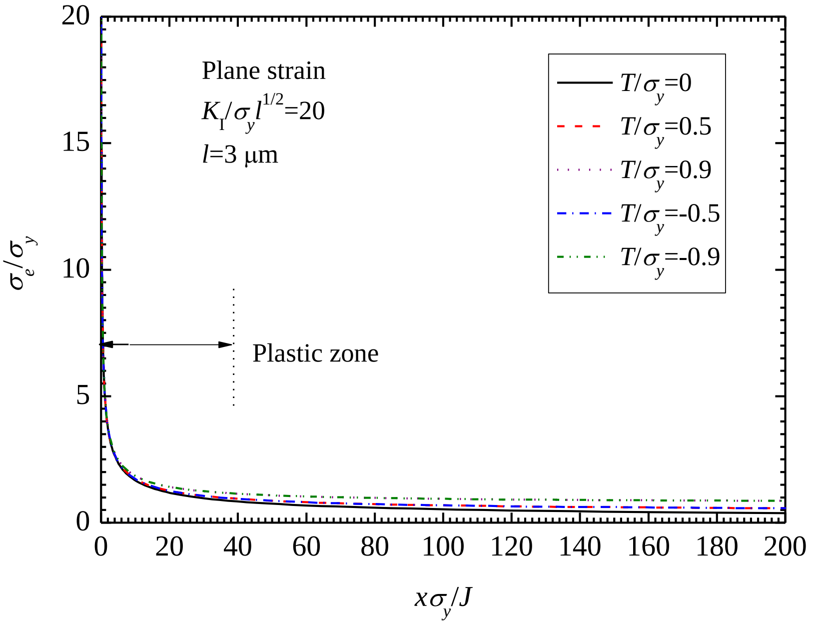

Figure 2.2 The von Mises stress distribution along the symmetric crack plane at $T/\sigma_y = 0, \ \pm 0.5, \text{ and } \pm 0.9$ from elastic solutions

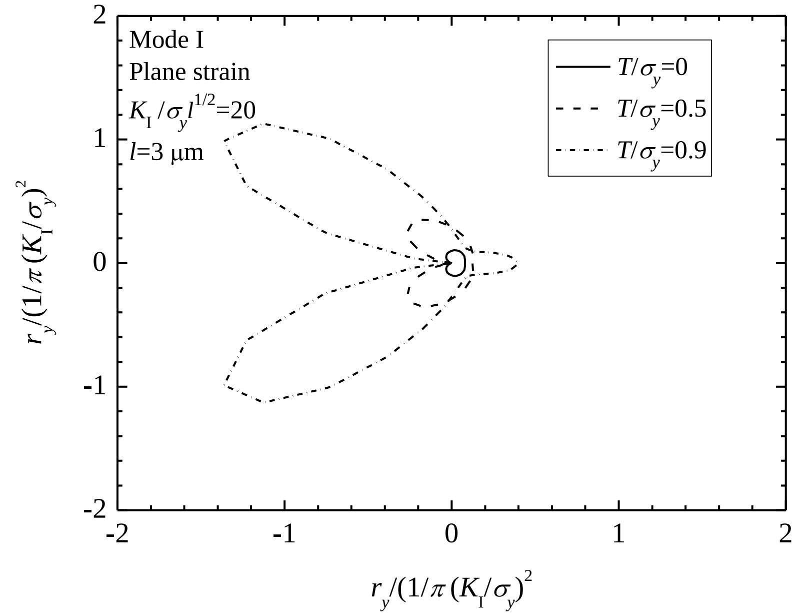

(a)

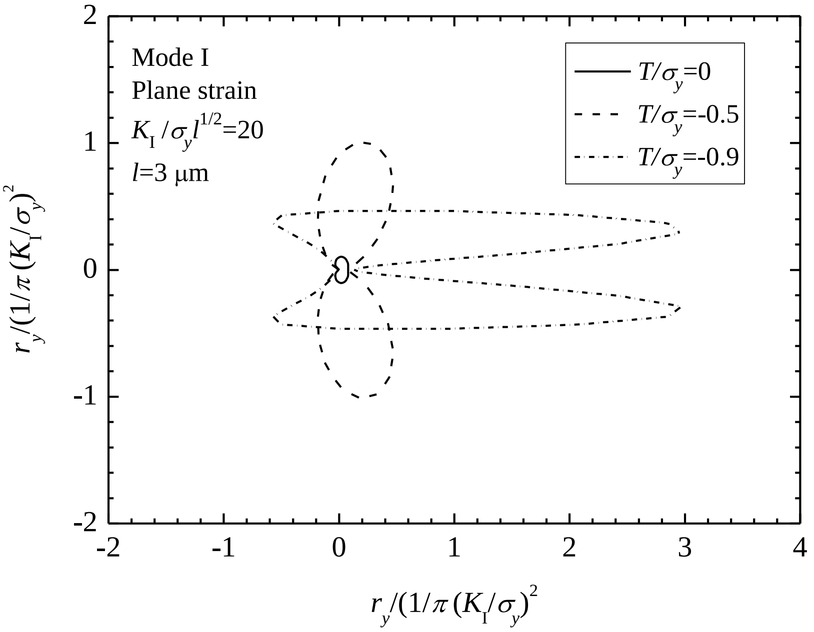

(b)

Figure 2.3 *T*-stress effect on the plastic zone estimated from elastic solutions for plane strain mode I (a) $T/\sigma_y = 0,\ 0.5,\ \text{and}\ 0.9$; (b) $T/\sigma_y = 0,\ -0.5,\ \text{and} -0.9$

2.3 Conventional Mechanism-based Stain Gradient Plasticity (CMSG) Theory

2.3.1 Constitutive Model in CMSG Plasticity Theory

Gao *et al*. [46] and Huang *et al*. [47] propose a multi-scale constitutive model to account for micro scale plasticity based on the Taylor dislocation theory. The proposed mechanism-based strain gradient (MSG) plasticity involves higher-order stress terms that require significantly computational efforts. Huang *et al*. [4] later develop the conventional mechanism-based strain gradient (CMSG) plasticity theory containing the higher-order stress only in the constitutive model and no additional higher order terms are required in the analysis. Therefore, the CMSG plasticity theory is substantially more convenient to be implemented than the MSG theory and provides results that are sufficiently accurate in most part of the domain except those in the vicinity of the boundary [5, 60].

The CMSG plasticity model obeys the Taylor hardening theory. The shear flow stress is [61]

$$\tau = \alpha\mu\bar{b}\sqrt{\rho_T} \tag{2.33}$$

where $\bar{b}$ is the magnitude of Burgers vector; μ is the shear modulus; α is the empirical constant, ranging from 0.2-0.5 depending on the material property; and the total dislocation density ρ_T is the sum of density of statistically stored dislocation ρ_S and geometrically necessary dislocation ρ_G.

The tensile flow stress can be related to the shear flow stress by Taylor factor M (M = 3.06 [62] for face-centered material and $\sqrt{3}$ for isotropic solids based on von-Mises rule [63]) as,

$$\sigma_f = M\tau \tag{2.34}$$

Under the uni-axial tension, only uniform plastic deformation exists. Thus, the strain gradient is absent. The geometrically necessary dislocation density therefore vanishes. Hence, under the uni-axial tension condition, the flow stress follows the macroscale stress-strain relationship as,

$$\sigma = M\tau = M\alpha\mu \bar{b}\sqrt{\rho_S} = \sigma_y f\left(\varepsilon^p\right) \tag{2.35}$$

where σ_y denotes the yield stress and the $f\left(\varepsilon^p\right)$ function is the material's constitutive relation in uni-axial tension. It follows that,

$$f\left(\varepsilon^p\right) = \left(1 + \frac{\varepsilon^p}{\varepsilon_y}\right)^N \tag{2.36}$$

where ε^p is the effective plastic strain, ε_y is the yield strain and equals σ_y / E, and N is strain hardening exponent. This constitutive model is suitable for ductile materials.

According to Equation (2.35), the statistically stored dislocation density can be written as

$$\rho_S = \left[\frac{\sigma_y f\left(\varepsilon^p\right)}{M\alpha\mu \bar{b}}\right]^2 \tag{2.37}$$

The geometrically necessary dislocations density is proposed by Ashby [2] as,

$$\rho_G = \frac{\bar{r}\eta^p}{\bar{b}} \tag{2.38}$$

where $\bar{r}$ is the Nye factor [64] ($\bar{r}$ =1.85 for bending or 1.93 for torsion), and η^p is the effective plastic strain gradient.

Combining Equation (2.33)-(2.38), the flow stress of Taylor dislocation model is obtained in Equation (2.39).

$$\sigma_f = \sigma_y\sqrt{f^2(\varepsilon^p) + l\eta^p} \tag{2.39}$$

where l is the material length scale, and

$$l = \bar{r}\,\bar{b}\left(\frac{M\alpha\mu}{\sigma_y}\right)^2 \tag{2.40}$$

Usually, M=3.06 and $\bar{r}$ =1.90, so the length scale is simplified to $l = 18\bar{b}\left(\alpha\mu \big/ \sigma_y\right)^2$. For typical steel materials, the length scale l is in the order of micron [65].

The effective plastic strain gradient tensor is given by Gao *et al.* [3] as,

$$\eta^p = \sqrt{\eta^p_{ijk}\eta^p_{ijk}}\,/\,2 \tag{2.41}$$

where η^p_{ijk} is the plastic strain gradient tensor and equals $\eta^p_{ijk} = \varepsilon^p_{ik,j} + \varepsilon^p_{jk,i} - \varepsilon^p_{ij,k}$, $\varepsilon^p_{ij} = \int \dot{\varepsilon}^p_{ij} dt$ is the plastic strain tensor, and the super-dot denotes the differentiation with respect to time. The effective plastic strain rate can be derived from the effective strain rate:

$$\dot{\varepsilon}^p = \dot{\varepsilon}\left[\frac{\sigma_e}{\sigma_y\sqrt{f^2\left(\varepsilon^p\right) + l\eta^p}}\right]^n \tag{2.42}$$

where n is the rate-sensitive coefficient and σ_e refers to the effective stress. The effective strain rate is derived from the deviatoric strain tensor as follows,

$$\dot{\varepsilon} = \sqrt{\frac{3\dot{\varepsilon}'_{ij}\,\dot{\varepsilon}'_{ij}}{2}} \tag{2.43}$$

The deviatoric strain tensor equals,

$$\dot{\varepsilon}'_{ij} = \frac{\dot{\sigma}'_{ij}}{2\mu} + \frac{3\dot{\varepsilon}^p}{2\sigma_e}\sigma'_{ij} \tag{2.44}$$

The total strain rate thus becomes,

$$\dot{\varepsilon}_{ij} = \frac{\dot{\sigma}_{kk}}{9K}\delta_{ij} + \frac{\dot{\sigma}'_{ij}}{2\mu} + \frac{3\dot{\varepsilon}^p}{2\sigma_e}\sigma'_{ij} = \frac{\dot{\sigma}_{kk}}{9K}\delta_{ij} + \frac{\dot{\sigma}'_{ij}}{2\mu} + \frac{3\dot{\varepsilon}}{2\sigma_e}\left[\frac{\sigma_e}{\sigma_y\sqrt{f^2\left(\varepsilon^p\right) + l\eta^p}}\right]^n \sigma'_{ij} \tag{2.45}$$

where K defines the bulk modulus. Therefore, the constitutive relationship including the strain gradient effect is calculated as follows [4],

$$\dot{\sigma}'_{ij} = K\dot{\varepsilon}_{kk}\delta_{ij} + 2\mu\left\{\dot{\varepsilon}'_{ij} - \frac{3\dot{\varepsilon}}{2\sigma_e}\left[\frac{\sigma_e}{\sigma_y\sqrt{f^2\left(\varepsilon^p\right)+l\eta^p}}\right]^n \sigma'_{ij}\right\} \tag{2.46}$$

The above derivation has been implemented as a user subroutine [53] in the general purpose finite element software ABAQUS [66].

2.3.2 FEM Formulation

For C^0 solid elements with n nodes, the displacements u, v, w, and coordinates x, y, z can be expressed as [5],

$$u = \sum_{i=1}^{n} N_i(g,h,r)u_i \qquad v = \sum_{i=1}^{n} N_i(g,h,r)v_i \qquad w = \sum_{i=1}^{n} N_i(g,h,r)w_i \tag{2.47}$$

$$x = \sum_{i=1}^{n} N_i(g,h,r)x_i \qquad y = \sum_{i=1}^{n} N_i(g,h,r)y_i \qquad z = \sum_{i=1}^{n} N_i(g,h,r)z_i \tag{2.48}$$

where g, h , and r are the natural coordinates, and N_i is the shape function.

The Jacobian matrix is

$$J = \frac{\partial(x,y,z)}{\partial(g,h,r)} = \begin{bmatrix} x_{,g} & x_{,h} & x_{,r} \\ y_{,g} & y_{,h} & y_{,r} \\ z_{,g} & z_{,h} & z_{,r} \end{bmatrix} \tag{2.49}$$

The inverse of Jacobian matrix is,

$$J^{-1} = \frac{\partial(g,h,r)}{\partial(x,y,z)} = \begin{bmatrix} g_{,x} & g_{,y} & g_{,z} \\ h_{,x} & h_{,y} & h_{,z} \\ r_{,x} & r_{,y} & r_{,z} \end{bmatrix} \tag{2.50}$$

The strain matrix is,

$$\{\varepsilon\}=\begin{bmatrix}\frac{\partial u}{\partial x} & \frac{\partial v}{\partial y} & \frac{\partial w}{\partial z} & \frac{\partial u}{\partial y}+\frac{\partial v}{\partial x} & \frac{\partial v}{\partial z}+\frac{\partial w}{\partial y} & \frac{\partial w}{\partial x}+\frac{\partial u}{\partial z}\end{bmatrix}^T=[B]\{\delta\} \qquad (2.51)$$

here,

$$[B]=\begin{bmatrix}B_1 & B_2 & \ldots & B_n\end{bmatrix} \qquad [\delta]=\begin{bmatrix}\delta_1^T & \delta_2^T & \ldots & \delta_n^T\end{bmatrix}^T$$

$$[B_i]=\begin{bmatrix}N_{i,x} & 0 & 0\\ 0 & N_{i,y} & 0\\ 0 & 0 & N_{i,z}\\ N_{i,y} & N_{i,x} & 0\\ 0 & N_{i,z} & N_{i,y}\\ N_{i,z} & 0 & N_{i,x}\end{bmatrix} \qquad \{\delta_i\}=\begin{Bmatrix}u_i\\ w_i\end{Bmatrix}, i=1, 2, 3, ..., \text{n}$$

The derivative of the strain vector with respect to x can be written as,

$$\{\varepsilon\}_{,x}=\begin{bmatrix}\frac{\partial^2 u}{\partial x^2} & \frac{\partial^2 v}{\partial y\partial x} & \frac{\partial^2 w}{\partial z\partial x} & \frac{\partial^2 u}{\partial y\partial x}+\frac{\partial^2 v}{\partial x^2} & \frac{\partial^2 v}{\partial z\partial x}+\frac{\partial^2 w}{\partial y\partial x} & \frac{\partial^2 w}{\partial x^2}+\frac{\partial^2 u}{\partial z\partial x}\end{bmatrix}^T=[B]_{,x}\{\delta\} \quad (2.52)$$

where $$[B_i]_{,x}=\begin{bmatrix}N_{i,xx} & 0 & 0\\ 0 & N_{i,yx} & 0\\ 0 & 0 & N_{i,zx}\\ N_{i,yx} & N_{i,xx} & 0\\ 0 & N_{i,zx} & N_{i,yx}\\ N_{i,zx} & 0 & N_{i,xx}\end{bmatrix}$$

According to the chain rule of derivatives,

$$N_{i,xx}=\frac{\partial N_{i,x}}{\partial g}\frac{\partial g}{\partial x}+\frac{\partial N_{i,x}}{\partial h}\frac{\partial h}{\partial x}+\frac{\partial N_{i,x}}{\partial r}\frac{\partial r}{\partial x}=N_{i,xg}g_{,x}+N_{i,xh}h_{,x}+N_{i,xr}r_{,x} \qquad (2.53)$$

$$\begin{bmatrix}N_{i,xx} & N_{i,xy} & N_{i,xz}\\ N_{i,yx} & N_{i,yy} & N_{i,yz}\\ N_{i,zx} & N_{i,zy} & N_{i,zz}\end{bmatrix}=\begin{bmatrix}N_{i,xg} & N_{i,xh} & N_{i,xr}\\ N_{i,yg} & N_{i,yh} & N_{i,yr}\\ N_{i,zg} & N_{i,zh} & N_{i,zr}\end{bmatrix}\begin{bmatrix}g_{,x} & g_{,y} & g_{,z}\\ h_{,x} & h_{,y} & h_{,z}\\ r_{,x} & r_{,y} & r_{,z}\end{bmatrix} \qquad (2.54)$$

$$\frac{\partial(N_{i,x},N_{i,y},N_{i,z})}{\partial(x,y,z)}=\frac{\partial(N_{i,x},N_{i,y},N_{i,z})}{\partial(g,h,r)}\frac{\partial(g,h,r)}{\partial(x,y,z)}=\frac{\partial(N_{i,x},N_{i,y},N_{i,z})}{\partial(g,h,r)}J^{-1} \qquad (2.55)$$

$$N_{i,gg}=N_{i,gx}x_{,g}+N_{i,gy}x_{,g}+N_{i,gz}x_{,g} \qquad (2.56)$$

$$\frac{\partial(N_{i,g}, N_{i,h}, N_{i,r})}{\partial(g,h,r)} = \frac{\partial(N_{i,g}, N_{i,h}, N_{i,r})}{\partial(x,y,z)} \frac{\partial(x,y,z)}{\partial(g,h,r)} = \frac{\partial(N_{i,g}, N_{i,h}, N_{i,r})}{\partial(x,y,z)} J \tag{2.57}$$

$$\frac{\partial(N_{i,x}, N_{i,y}, N_{i,z})}{\partial(x,y,z)} = \frac{\partial(N_{i,g}, N_{i,h}, N_{i,r})}{\partial(g,h,r)} J^{-1} \tag{2.58}$$

$$\frac{\partial(N_{i,x}, N_{i,y}, N_{i,z})}{\partial(x,y,z)} = J^{-T} \frac{\partial(N_{i,g}, N_{i,h}, N_{i,r})}{\partial(g,h,r)} J^{-1} \tag{2.59}$$

For a plane isoparametric element with n nodes, the variables in above equations along z direction diminish. The strain gradient matrices based on the above equations have been implemented in the finite element package, ABAQUS as user subroutines by Swaddiwudhipong et al. [53] The subroutines compute the effective plastic strain gradient for each Gauss point at each increment in the formulation of the stiffness equations. More details on the finite element formulations and implementation were reported earlier in [53].

CHAPTER 3 STRESS ANALYSIS FOR A CRACK IN PLANE STRAIN MODE I LOADING

3.1 Introduction

Fracture specimens can be idealized as plane stress or plane strain problems. The difference is that plane strain condition constrains the displacement in the out-of-plane direction while the stress vanishes on the free surface for a plane stress condition. Under the plane strain condition, the triaxial stress state limits the plastic deformation around the crack tip so that the material is prone to brittle failure. Therefore, the crack under plane strain conditions causes more concern.

This chapter uses a modified boundary layer (MBL) model to study the stress field of a crack under plane strain, mode I loadings by imposing a remote K_I loading ($K_I / \sigma_y l^{1/2} = 20$) on the boundary of MBL model. The material properties follow the parameters reported by Swaddiwudhipong *et al*. [5], with the Young's modulus, $E = 205\,\text{GPa}$; yield stress and Young's modulus ratio, $\sigma_y / E = 0.002$; the plastic work hardening exponent, $N = 2$ (see Equation (2.36)); Poisson ratio $\upsilon = 0.3$, and the material length scale, $l = 3$ μm. As the load, K_I satisfying the equation $K_I / \sigma_y l^{1/2} = 20$ is about 14.2 $\text{MPa}\sqrt{\text{m}}$ and not enough to cause the failure of steel specimen, small strain formulation is applied to all numerical analyses reported in this chapter.

3.2 Finite Element Modeling

3.2.1 Modified Boundary Layer Model

The MBL model as shown in Figure 3.1 is for modeling the crack that locates on the symmetric plane of the cracked-body. The outer circumference of the MBL model experiences a plane strain K_I displacement field [2]:

$$u(r,\theta)=\frac{K_I(1+\upsilon)}{E}\sqrt{\frac{r}{2\pi}}\cos\left(\frac{\theta}{2}\right)\left(3-4\upsilon-\cos\theta\right) \tag{3.1}$$

$$v(r,\theta)=\frac{K_I(1+\upsilon)}{E}\sqrt{\frac{r}{2\pi}}\sin\left(\frac{\theta}{2}\right)\left(3-4\upsilon-\cos\theta\right) \tag{3.2}$$

The plane perpendicular to the y-axis (at $y=0$) plane in Figure 3.1 is the symmetric plane. The outer radius of the finite element model is more than 20 times the radius of the plastic zone at the maximum load to ensure that the small scale yielding condition prevails at the crack tip [24].

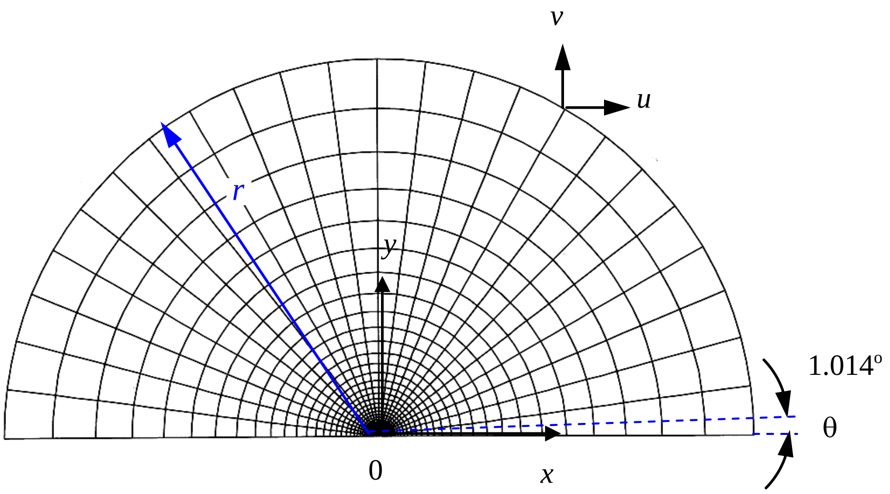

Figure 3.1 Modified boundary layer model

3.2.2 Crack Tip Modeling

To simulate the deformation and the stress field near the crack tip correctly under both low and high load levels, this section adopts two types of crack tip modeling. One is to model the crack tip as a sharp crack by using two elements at the crack tip, as shown in Figure 3.2(a). The two elements sharing the crack tip node initially locate on the symmetric plane (Figure 3.2(a)); after loading, the tip element on the free surface is pulled to leave the crack plane, another tip element which locates ahead of the crack tip deforms along the symmetric plane. With the increasing of loading, the two elements at the crack tip are severely distorted (Figure 3.2(b)). This type of modeling normally encounters the convergence problems during the numerical computation when the load increases to certain levels. In order to solve the convergence problem, a modified crack-tip modeling that contains an initial root radius at the crack tip as depicted in Figure 3.3 is used. At large load level, the elements on the symmetric plane of the crack are elongated in the opening stress direction, and shortened along the horizontal direction. The numerical performance of the latter model affected by the deformation of the elements around the crack tip is significantly healthier compared to that of the model shown in Figure 3.2.

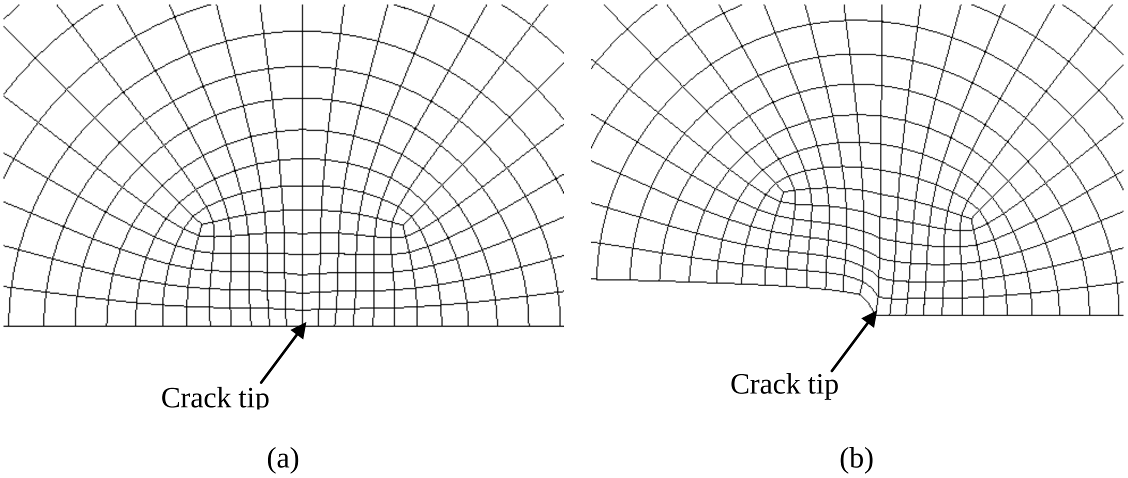

Figure 3.2 Crack model with sharp crack tip mesh (a) Before loading; (b) After loading

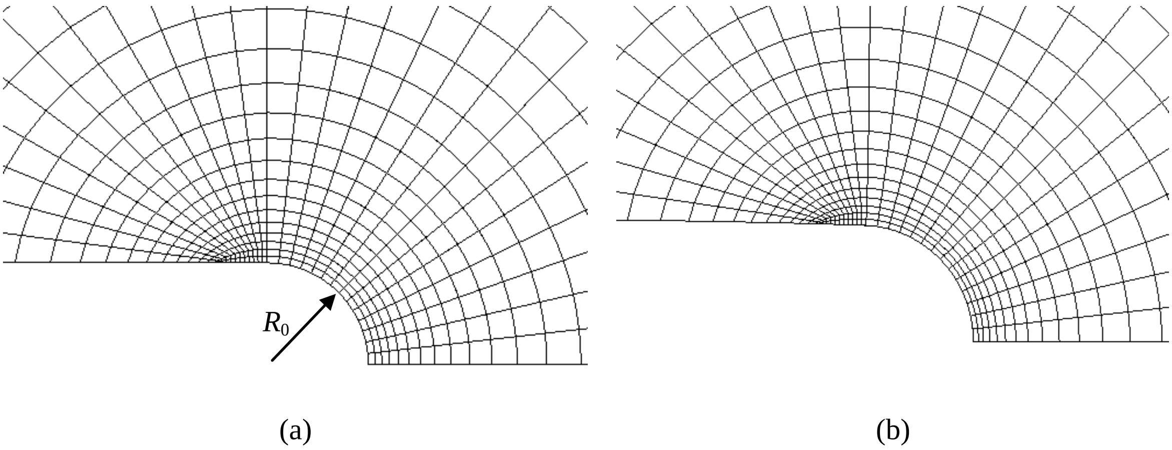

(a) (b)

Figure 3.3 Crack model with initial root (a) Before loading; (b) After loading

3.2.3 Small Scale Yielding Model with Zero *T*-Stress

In the linear elastic solution of the crack tip stress, the first term (see Equation (2.15)) approaches an infinite value when the distance r from the crack tip approaches to zero. The second constant term '*T*-stress' and the other higher order terms can be ignored compared to the first term. This results in a single-parameter (K_I or G) controlled crack tip stress field. This section presents the single-parameter, K_I controlled stress field by using the MBL model.

3.2.3.1 Comparison of Normalized Von Mises Stress Distribution by the Classical Plasticity and the CMSG Plasticity Analyses

In the small scale yielding model as shown in Figure 3.1, the magnitude of the non-dimensional loading K_I satisfies the equation $K_I / \sigma_y l^{1/2} = 20$ and is about 14.2 $\text{MPa}\sqrt{\text{m}}$. The outer radius of the model is 3 mm which is 20 times greater than the plastic zone size ($0 < r/l < 10$) with the maximum load of K_I =14.2 $\text{MPa}\sqrt{\text{m}}$. In finite element model, the crack tip is modeled as a mathematically sharp crack. Along the radius direction, bias mesh has been taken. The detail of mesh is listed in table 3.1. The total number of the CPE8 elements in the FE model is around 2280 and the minimum element size near the crack tip is around 2 nm. At various nodes along the circular boundary of the model, the displacements obtained from Equations (3.1) and (3.2) are imposed on the finite element model as shown in Figure 3.1.

Table 3.1 Mesh design for SSY model with R=3 mm and R_0=0

Radial distance (μm)	Bias ratio	Number of elements
0~2	1	7
2~30	10	22
30~300	10	17
300~3000	10	17
Number of seeds along circular edge	24	
Minimum element size (nm)	2	
Total Number of elements	2280	

The current work adopts the plastic strain gradient user subroutine written by Swaddiwudhipong *et al*. [53]. Figure 3.4 compares the normalized von Mises stress distribution along the path at $\theta = 1.014^{\circ}$ direction incline to the crack plane (see Figure 3.1) between the current study and Swaddiwudhipong *et al*. [5]. The normalized von Mises stress distribution curve in the current study coincides with Swaddiwudhipong *et al*. [5] results. Figure 3.4 also shows that the plastic strain gradient introduced by the CMSG plasticity theory does not change the plastic zone size. Both the CMSG plasticity analysis and the classical plasticity analysis show the same size of plastic zone ($0 < r/l < 10$). However, at the distance $0.09 < r < 0.3$ μm ahead of the crack tip, the magnitude of von Mises stress obtained from the CMSG plasticity analysis is more than 3 times that from the classical plasticity analysis. This is due to the fact that the CMSG plasticity theory includes the high plastic strain gradient at the crack tip.

3.2.3.2 Comparison of Normalized Von Mises Stress Distribution by Different Elements

Both 2-D model with 8-node (CPE8) plane selements and 3D model with 20-node (C3D20) elements are used in the simulation of the crack under plane strain condition.

The two models have the same in-plane mesh design. In the 3D model, there is one layer of elements along the thickness direction. In order to simulate the stress and strain fields for plane stain condition by 3D model, all the nodes' out-of-plane displacements are constrained. The total number of elements is 2280. The minimum element size is 2 nm. The symmetric boundary condition is applied to the crack plane. The elastic, plane strain displacement field with $K_I / \sigma_y l^{1/2} = 20$ is applied to the outer radius of the MBL model. The material properties follow those presented in Swaddiwudhipong *et al.* [5]. The current work uses the plastic strain gradient program and validates it.

Figure 3.5 plots the normalized von Mises stress distribution along $\theta = 0^{\circ}$ (measured from the horizontal x axis in Figure 3.1) by models with CPE8 elements and C3D20 elements. Apparently, the two types of modeling show the same von Mises stress distribution in either the classical plasticity analysis or the CMSG plasticity analysis. This verifies that the C3D20 elements can also simulate the stress field near a crack tip under the plane strain condition provided that all the nodes' out-of-plane displacements are constrained.

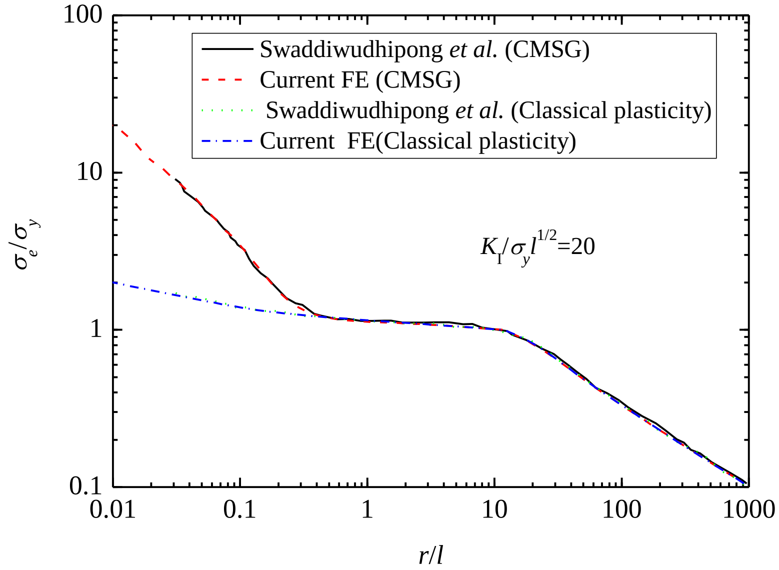

Figure 3.4 Normalized von Mises stress distribution along $\theta = 1.014^{\circ}$

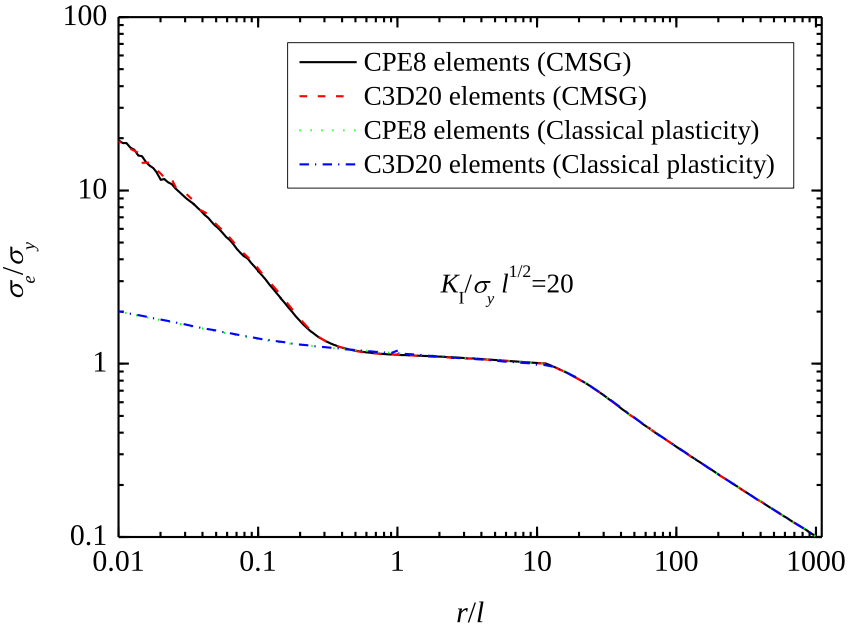

Figure 3.5 Normalized von Mises stress distribution along $\theta = 0^{\circ}$

3.2.3.3 Material Length Scales Effect on the Normalized Maximum Principal Stress Distribution along the Crack Plane by SSY Model

Figure 3.6 illustrates the effect of the values of the material length scale ($l = 3$, 5, 7, and 10 μm) on the normalized principal stress distribution along the crack plane by the small scale yielding (SSY) model with the crack tip mesh in Figure 3.2. The 20-node brick elements are used in the analyses, and the applied load is $K_I = 14.2\ \text{MPa}\sqrt{\text{m}}$.

The values of maximum principal stress at the crack tip region ($0.01 \le x\sigma_y / J \le 1$) for material length scales of $l = 3$, 5, 7, and 10 μm are significantly higher than that computed from the classical plasticity analysis. The magnitude of the maximum principal stress curves computed from $l = 5$, 7, and 10 μm do not show significant differences. This implies that maximum principal stress is not so sensitive to the material length scale value when the length is in the range of 5-10 μm.

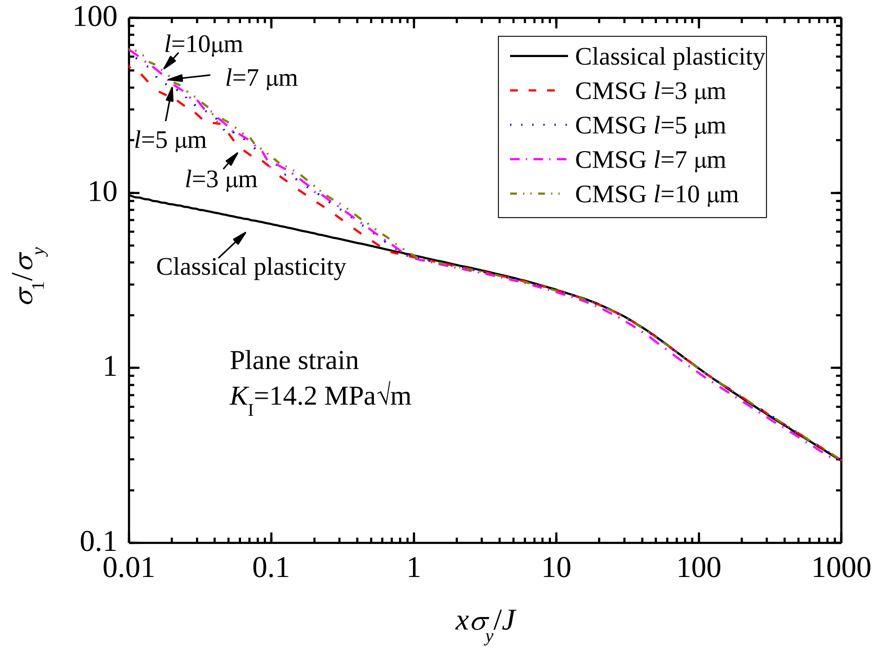

Figure 3.6 Comparison of normalized maximum principal stress distribution along θ = 0° by two crack tip modeling ($R_0 = 0$ and 0.1)

3.2.3.4 Comparison of Stress Distribution by Different Crack Tip Modeling

Two types of crack tip modeling shown in Figures 3.2 and 3.3 are used in the FE computations. Both models use the C3D20 elements, and the applied load is $K_I / \sigma_y l^{1/2} = 20$.

Figure 3.7 shows the opening stress distribution along the $\theta = 0^\circ$ (measured from the horizontal x axis in Figure 3.1) by MBL models with different radius of initial root under classical plasticity. The mathematically sharp crack tip modeling ($R_0/l = 0$) captures the singular stress at the crack tip, while with the increasing of the initial root radius ($R_0/l = 0.01, 0.1$, and 1), the stress singularity at the crack tip is gradually removed and the opening stresses along the crack plane redistribute. According to Wasiluk *et al.* [24], the size of initial root radius is acceptable if the deformed root radius exceeds 3 times the undeformed root radius. At the load of $K_I/\sigma_y l^{1/2} = 20$, the deformed radius for $R_0/l = 0.01, 0.1$, and 1 are around 7.5, 2, and 1 times of undeformed radii, respectively. Therefore, the model with initial root of $R_0/l = 0.01$ is acceptable to simulate the stress field of the crack.

Figure 3.8 compares the normalized maximum principal stress distribution of the models with different radii of initial root ($R_0/l = 0$ and 0.01) under both classical plasticity and the CMSG plasticity analyses. In the results of classical plasticity analyses, the initial root radius removes the stress singularity at the crack tip. Therefore, crack tip stress computed by the models with the initial root radius of $R_0/l = 0.01$ is lower than that from $R_0/l = 0$. However, under the CMSG plasticity analyses, the initial root radius does not show significant effect on the magnitude of the stress at the crack tip due to the high plastic strain gradient at the crack tip.

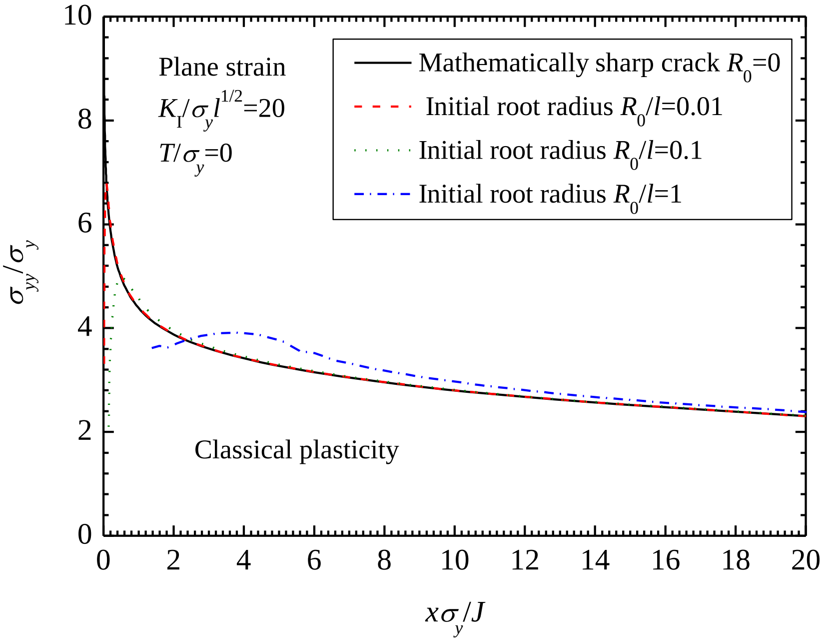

Figure 3.7 Comparison of Normalized opening stress distribution along $\theta = 0^o$ by two crack tip modeling ($R_0 = 0$ and 0.1)

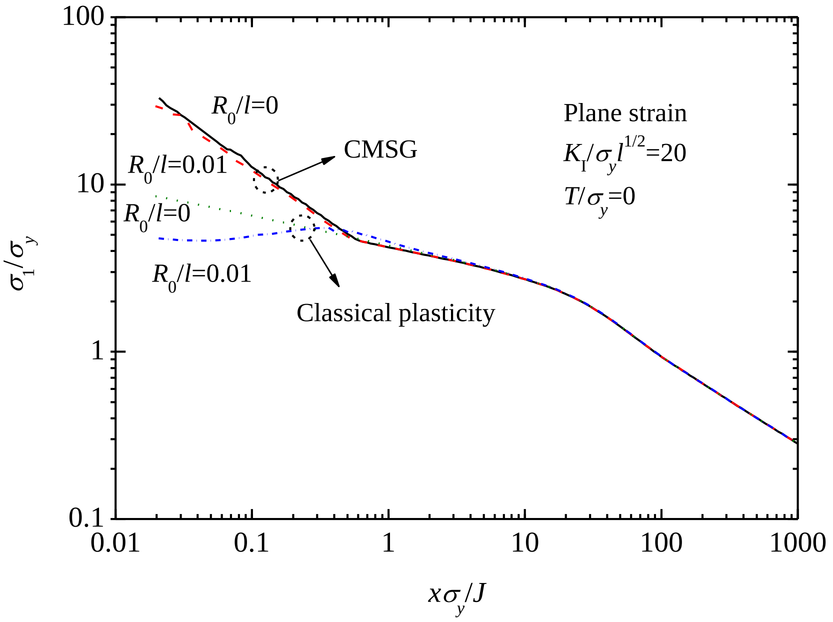

Figure 3.8 Comparison of normalized von Mises distribution along $\theta = 0^{\circ}$ by two crack tip modeling ($R_0 / l = 0$ and 0.1)

3.2.4 Small Scale Yielding Model with Nonzero *T*-Stresses

This section uses the MBL model with zero root radius $R_0 = 0$ to model the crack under small scale yielding and non-zero *T*-stresses conditions. The model contains 2280 20-node brick elements with 161513 nodes. Only one layer of elements locates in the thickness direction of the model. The smallest element near the crack tip is 2 nm. The material properties follow those reported by Swaddiwudhipong *et al.* [5].

The numerical procedure imposes the K_I controlled displacement field (see Equations (3.1) and (3.2)) together with the displacement field caused by *T*-stress loading (see Equations (3.3)) and (3.4)) to the circumference of the semi-circle boundary,

$$u(r,\theta) = T\frac{1-\upsilon^2}{E} r\cos\theta \tag{3.3}$$

$$v(r,\theta) = -T\frac{\upsilon(1+\upsilon)}{E} r\sin\theta \tag{3.4}$$

The out-of-plane displacement at all nodes are constrained. The K_I loading satisfies with the equation $K_I / \sigma_y l^{1/2} = 20$ and the *T*-stress equals $T / \sigma_y = 0,\ \pm 0.5,$ or ± 0.9.

Figures 3.9(a) and 3.9(b) show the normalized opening stress along the crack plane, $\theta = 0^{\text{o}}$ direction (measured from the horizontal x axis in Figure 3.1) under five different levels of *T*-stresses by the classical plasticity and the CMSG plasticity analyses. At the position close to the crack tip ($0 < x\sigma_y / J < 10$), the opening stresses with positive *T*-stress ($T / \sigma_y = 0.5$ and 0.9) are higher than those in the small scale yielding limit (zero *T*-stress) as the crack plane undergoes high constraint. However, the negative *T*-stress significantly decreases the opening stress ahead of the crack tip as the crack plane experiences low constraint.

Figures 3.10(a) and 3.10(b) compare the normalized opening stress distribution along the crack plane between the CMSG plasticity and classical plasticity analyses for five different levels of *T*-stress ($T / \sigma_y = 0,\ \pm 0.5,$ or ± 0.9) conditions. By using the strain gradient plasticity, the opening stress within 6 μm ahead of the crack tip ($0 < x\sigma_y / J < 3$) decreases compared with that using the classical plasticity theory. This illustrates that the plastic strain gradient hardens the material at the crack front and causes the lost of the plastic constraint in the material.

Figures 3.11(a) and 3.11(b) plot the normalized von Mises stress distribution at five levels of *T*-stresses ($T / \sigma_y = 0,\ \pm 0.5,$ or ± 0.9) by the classical plasticity and the CMSG plasticity analyses. The results based on both theories show that the *T*-stress has lower effect on the magnitude of von Mises stress near the crack tip ($0 < x\sigma_y / J < 3$) than the region far away from the crack tip ($x\sigma_y / J > 60$).

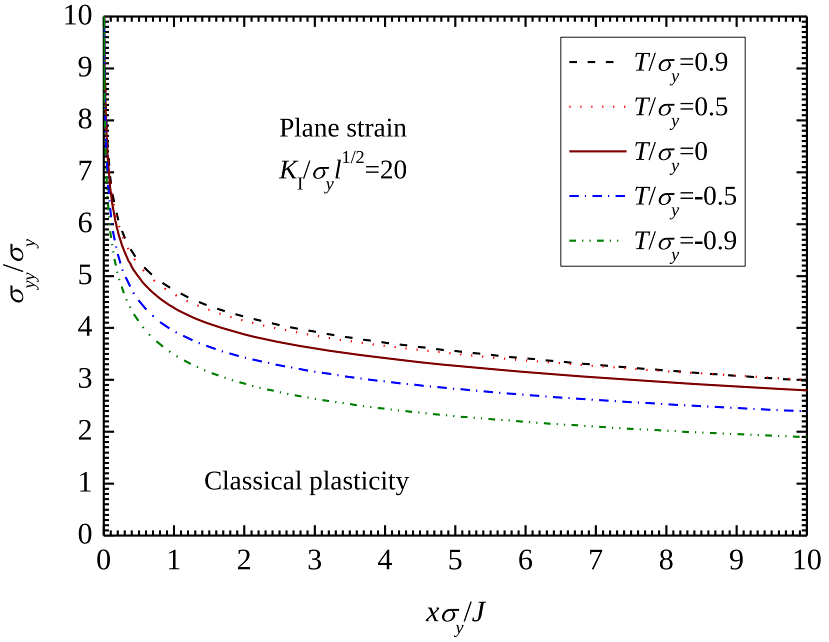

(a)

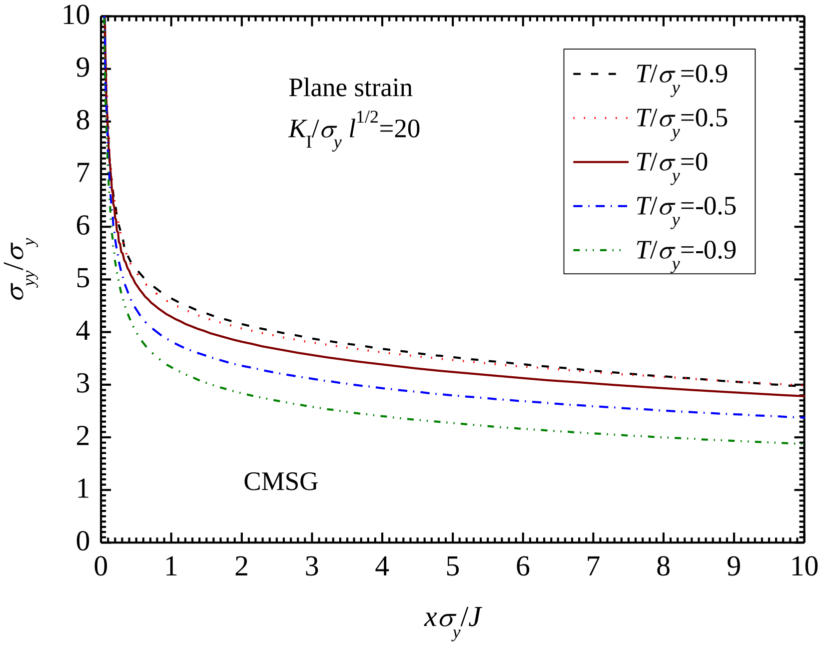

(b)

Figure 3.9 Normalized opening stress distribution along symmetric plane at various *T*-stresses ($T/\sigma_y = 0, \pm 0.5$ and ± 0.9) (a) Classical plasticity; (b) CMSG plasticity

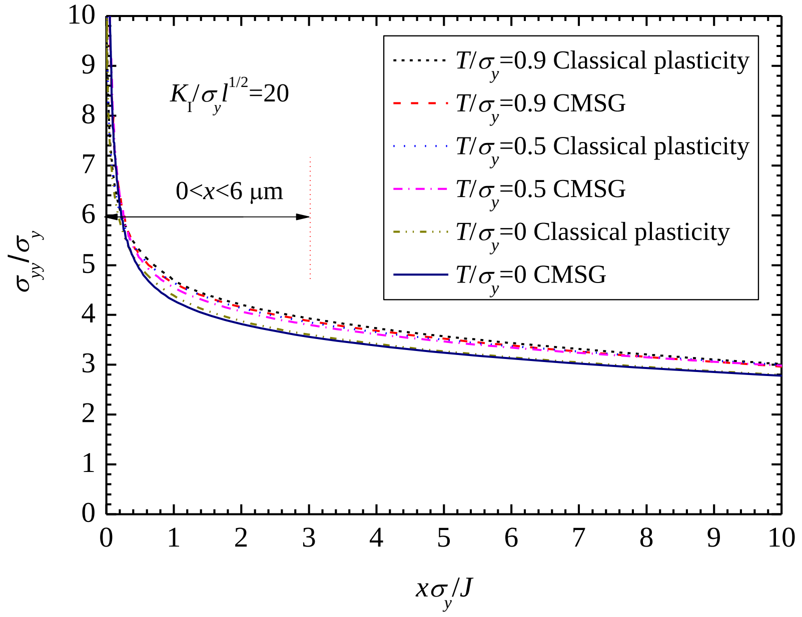

(a)

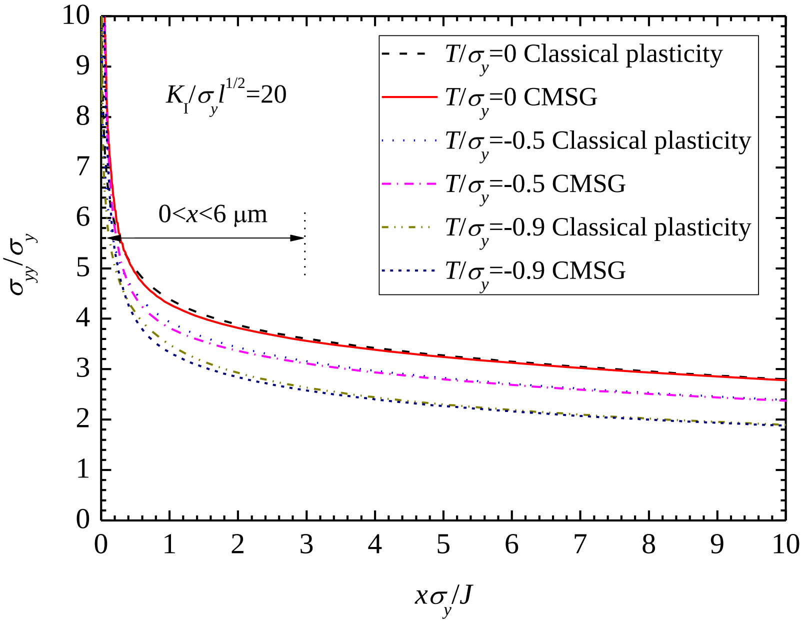

(b)

Figure 3.10 Comparison of normalized opening stress distribution between classical plasticity and CMSG plasticity analysis (a) $T/\sigma_y = 0, 0.5$ and 0.9 ;(b) $T/\sigma_y = 0, -0.5$ and -0.9

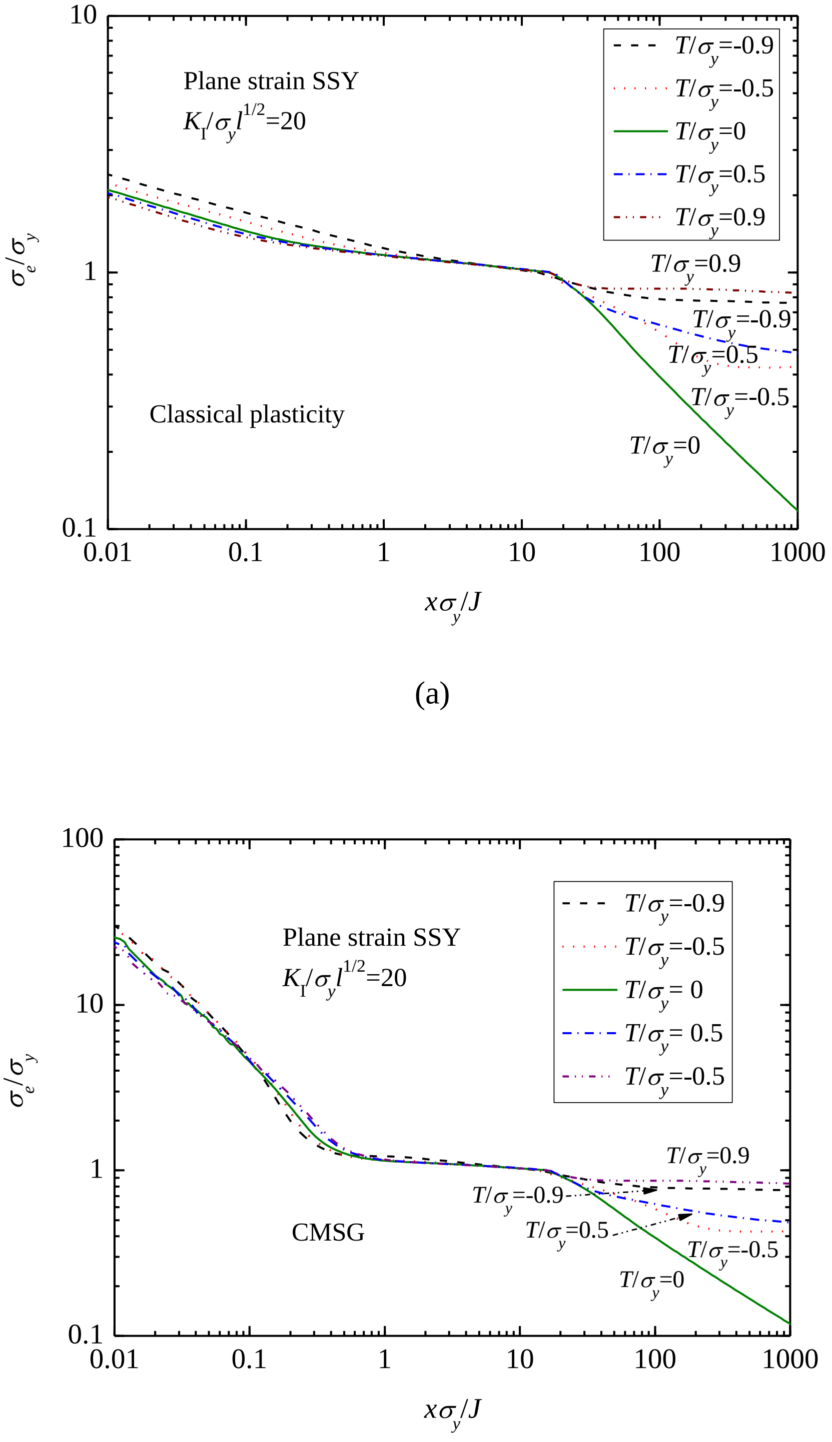

(a)

(b)

Figure 3.11 Normalized von Mises stress distribution under five levels of *T*-stresses $T/\sigma_y = 0, \ \pm 0.5$ and ± 0.9 (a) Classical plasticity; (b) CMSG plasticity

3.2.5 Weibull Stress Calculations

The modified boundary layer model as shown in Figure 3.2 is used for modeling the crack under plane strain and small scale yielding conditions. The material properties reported by Swaddiwudhipong *et al*. [5] are as follows: *E* = 205 GPa; σ_y = 410 GPa; plastic strain hardening exponent, $N = 0.2$; $K_I / \sigma_y l^{1/2} = 20$. The Weibull-stress values are computed according to the numerical solutions of the classical and the CMSG plasticity theories. The reference volume V_0 =1 mm^3.

3.2.5.1 Plastic Strain Gradient Effect on Weibull Stress Values

In this study, the size of fracture process zone is defined as the region that the maximum principal stress is greater than twice of the yield strength $\sigma_1 \geq 2\sigma_y$ [24].

Figure 3.12 plots the normalized maximum principal stress distribution along the crack plane. At the distance around 0.3 μm ($x\sigma_y / J = 0.13$) ahead of the crack tip, the maximum principal stress from the CMSG plasticity analysis is more than 2 times of that from the classical plasticity analysis. As the Weibull stress is the maximum principal stress integrating over the fracture process zone, the magnitude of Weibull stress from the CMSG plasticity analysis is also higher than that from the classical plasticity analysis as shown in Figure 3.13. The value of Weibull stress at the maximum load obtained from the CMSG plasticity analysis is about 10 times higher than that obtained from the classical plasticity analysis for *m*=10.

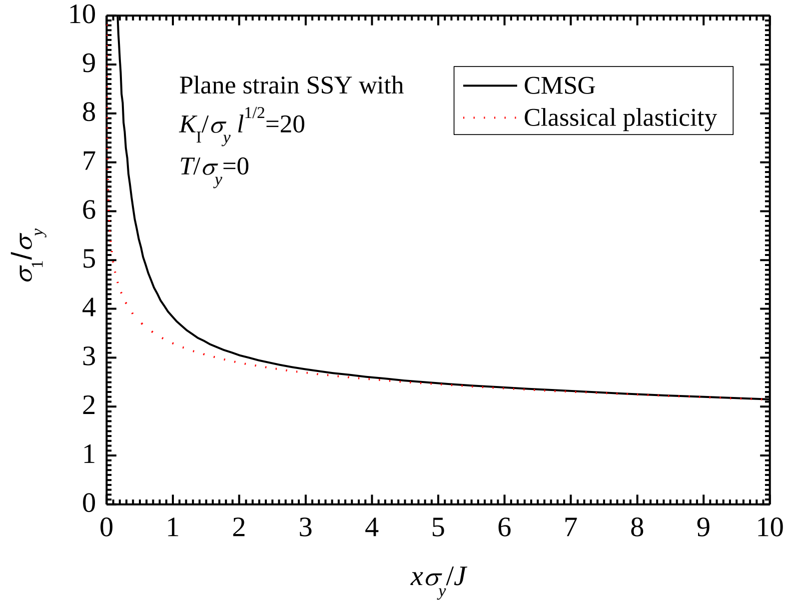

Figure 3.12 Comparison of normalized maximum principal stress distribution along the crack plane at load $K_I / \sigma l^{1/2} = 20$ and zero *T*-stress based on classical plasticity and CMSG plasticity analyses

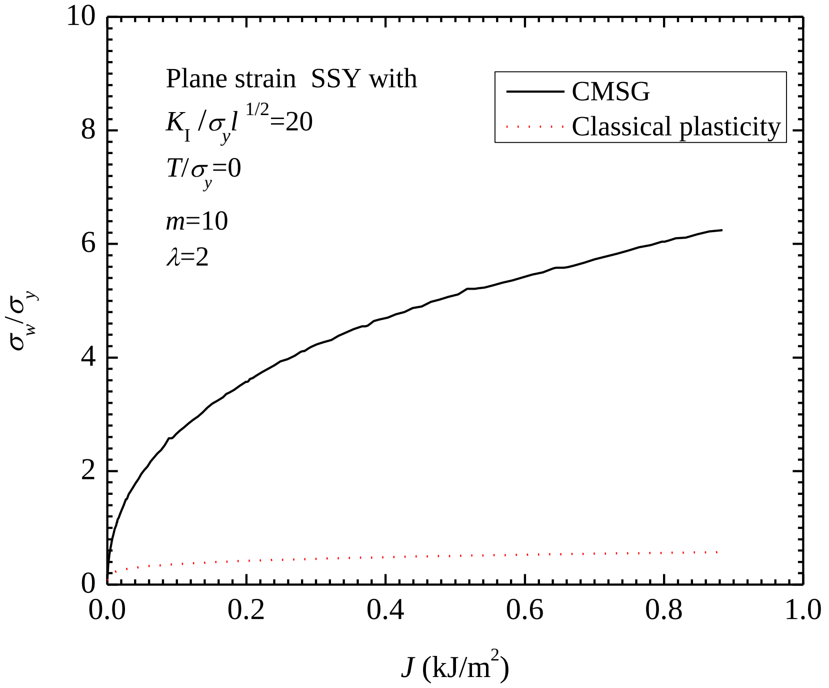

Figure 3.13 Comparison of Weibull stress in the loading of $K_I / \sigma l^{1/2} = 20$ and zero *T*-stress based on classical plasticity and CMSG plasticity analyses

3.2.5.2 Initial Root Radius Effect on Weibull Stress Values

Figures 3.14(a) and 3.14(b) present the Weibull stress curves from the models with different initial root radius $R_0 / l = 0$ and 0.01 by the classical plasticity and the CMSG plasticity analyses. Under both analyses, the Weibull stress values computed from the model with initial root radius of $R_0 / l = 0.01$ is lower than that without initial root. The reason is that the introducing of initial root removes the stress singularity at the crack tip in the loading history. In the results of classical plasticity analysis (see Figure 3.14(a)), the difference of Weibull stress values between initial root radius $R_0 / l = 0.01$ and $R_0 / l = 0$ is around 7% at the load of 14.2 $\mathrm{MPa}\sqrt{\mathrm{m}}$ while in the CMSG plasticity analysis, the difference is around 56% (see Figure 3.14(b)). However, this load level is less than the threshold fracture toughness 20 $\mathrm{MPa}\sqrt{\mathrm{m}}$ of the steels [11]. Hence the current maximum load is not sufficient to initiate the fracture failure. Dodds *et al.* [67] find that at a large load level, the size of the initial root radius does not have profound effect on the crack tip field. Therefore, the initial root will not significantly affect the magnitude of Weibull stress at high loads which will be illustrated in Chapter 4.

3.2.5.3 The Size of Fracture Process Zone Effect on Weibull Stress Values

The stress cutting parameter, λ defines the size of fracture process zone. High value of λ means that more elements are included in the fracture process zone (FPZ), and Weibull stress value is averaged over more elements at certain load levels. Therefore, the Weibull stress curve downshifts with the increasing of λ. This can be seen from Figure 3.15(a) which is plotted based on the classical plasticity analysis.

After including the plastic strain gradient effect, the stress field near the crack tip is significantly elevates. The value of λ does not affect the Weibull stress values as shown in Figure 3.15(b).

3.2.5.4 Weibull Modulus Effect on Weibull Stress Values

The magnitude of Weibull stress is also affected by the parameter, m. The higher values of m induce higher values of Weibull stress (see Equation (2.6)). Figures 3.16(a) and 3.16(b) plot the Weibull stress curves with Weibull modulus m at 5, 10 and 15 from both the classical plasticity and the CMSG ($l = 3$ μm) plasticity analyses. Based on classical plasticity analyses, the Weibull stress values at m=10 and m=15 are around 6 and 15 times that at $m = 5$ under the maximum load K_I=14.2 $\text{MPa}\sqrt{\text{m}}$. However, after including the plastic strain gradient effect, the Weibull stress values at $m = 10$ and $m = 15$ are around 18 and 65 times that at $m = 5$ under the maximum load K_I=14.2 $\text{MPa}\sqrt{\text{m}}$.

3.2.5.5 *T*-Stresses Effect on Weibull Stress Values

From the classical plasticity analyses, as shown in Figure 3.17(a), the positive *T*-stress increases the opening stress. Therefore, the Weibull stress value is higher. On the contrary, the negative *T*-stress decreases the opening stress, the crack plane undergoes low constraint, and therefore, the Weibull stress is lower. The results from the CMSG plasticity analysis also show that the positive *T*-stresses generate higher Weibull stress value than that by the negative *T*-stresses (see Figure 3.17(b)). However, these differences in Weibull stress values induced by *T*-stresses are less from the CMSG plasticity analysis than that from the classical plasticity analyses.

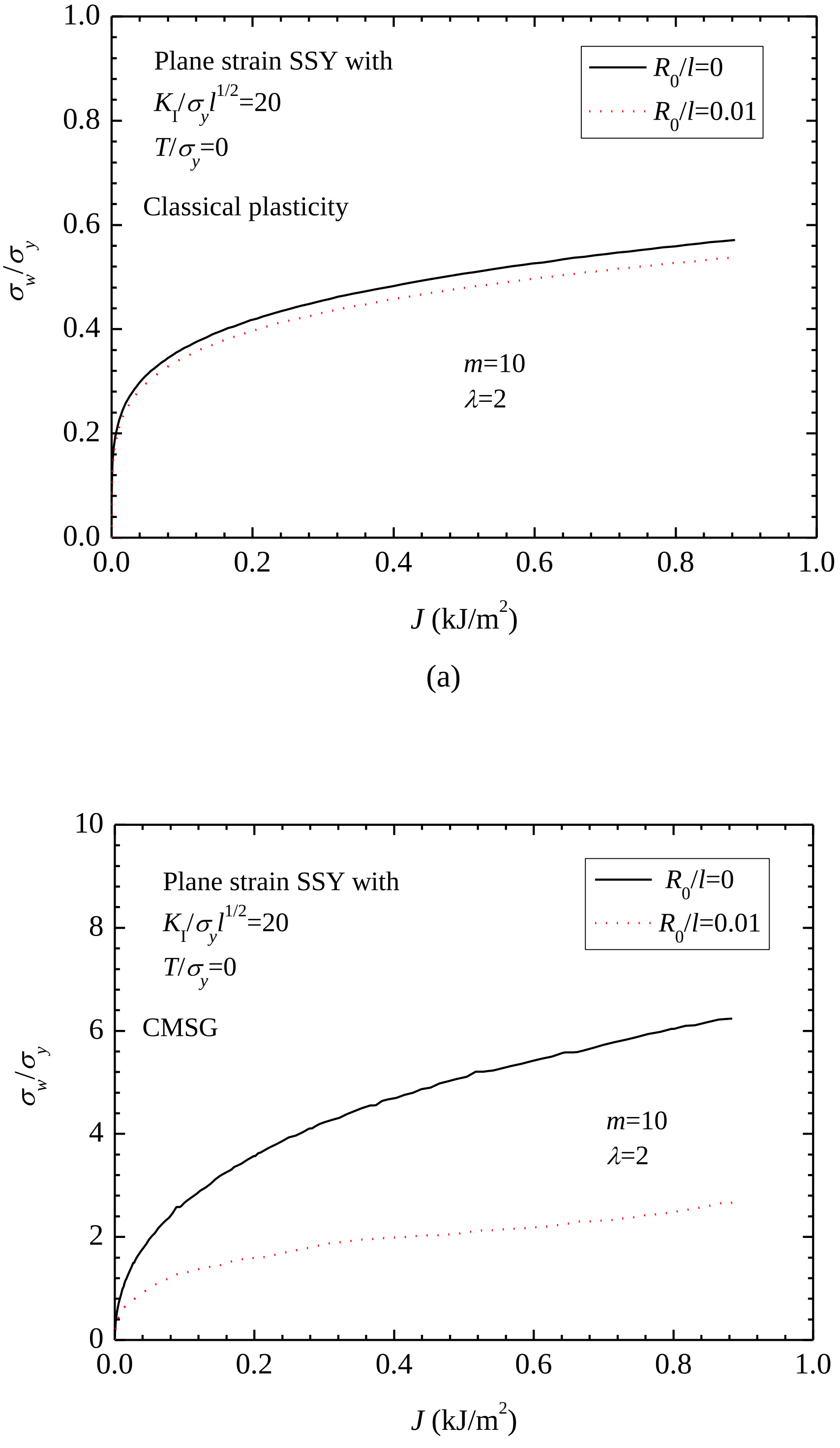

(a)

(b)

Figure 3.14 The effect of initial root radius on the magnitude of Weibull stress ($K_I / \sigma l^{1/2} = 20$) (a) Classical plasticity; (b) CMSG plasticity

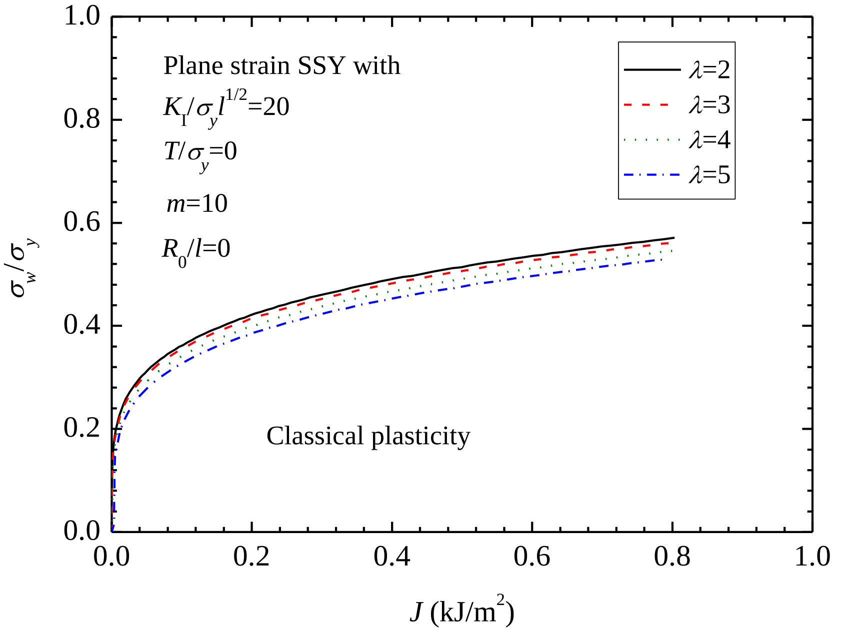

(a)

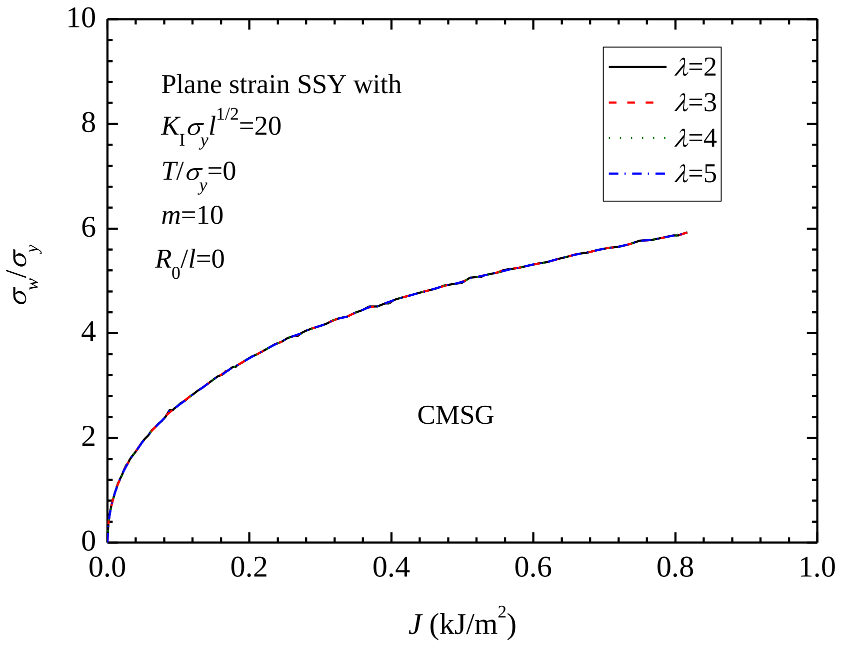

(b)

Figure 3.15 The cutting parameter, λ effect on the magnitude of Weibull stress ($K_I / \sigma l^{1/2} = 20$)
(a) Classical plasticity; (b) CMSG plasticity

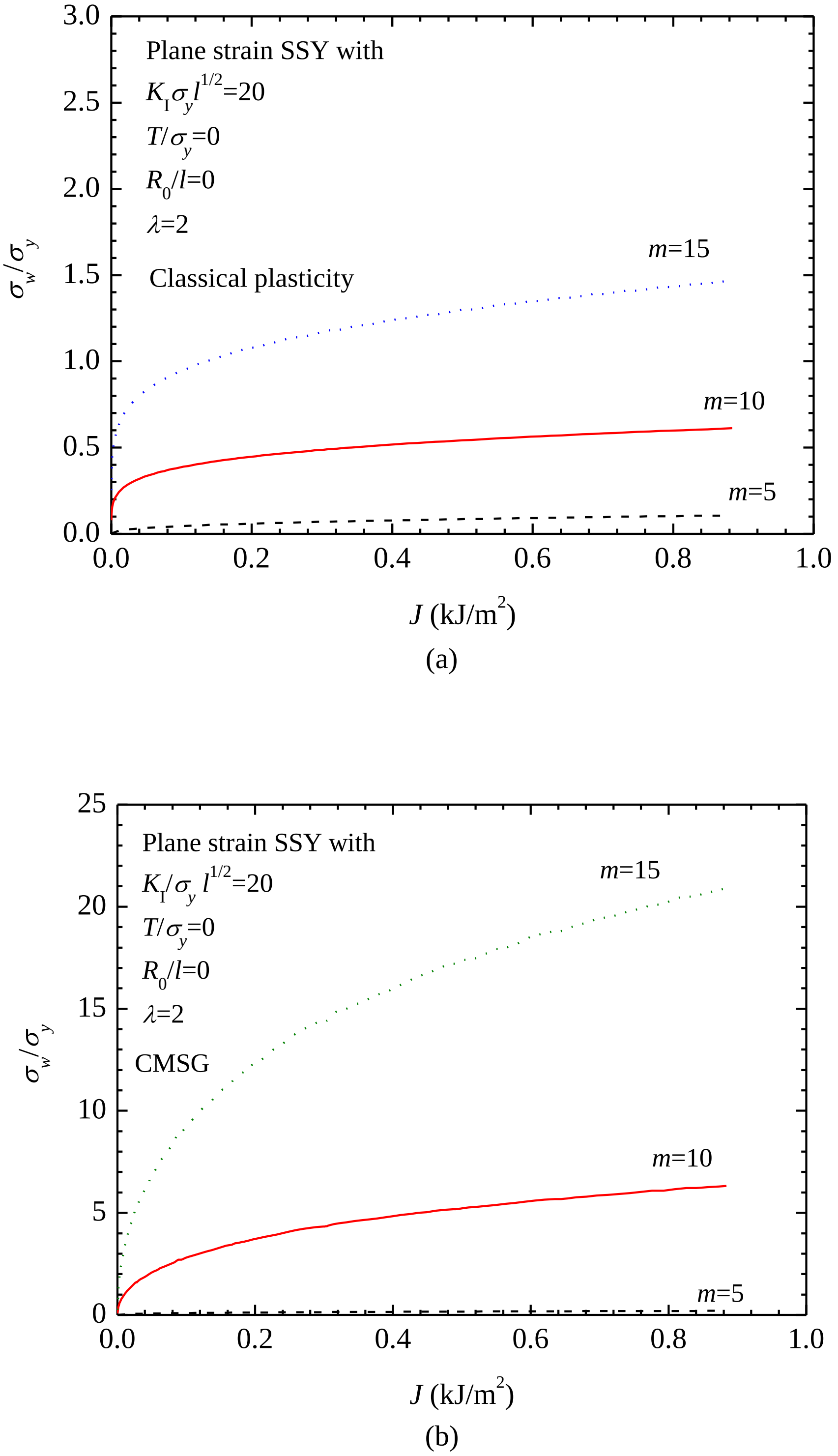

Figure 3.16 The Weibull modulus, m effect on the magnitude of Weibull stress ($K_I / \sigma l^{1/2} = 20$)
(a) Classical plasticity (b) CMSG plasticity

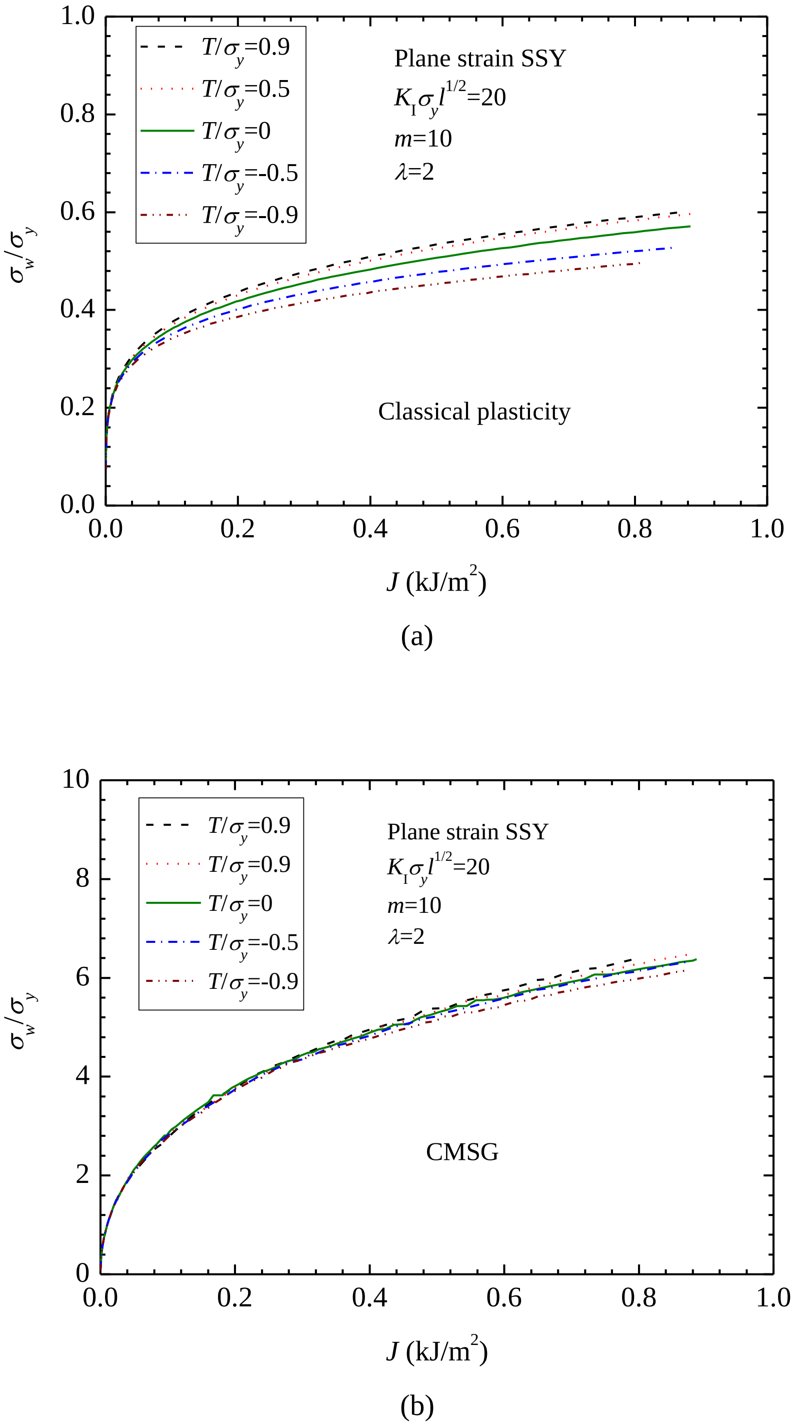

(a)

(b)

Figure 3.17 The *T*-stress ($T / \sigma_y = 0, \ \pm 0.5, \text{ and } \pm 0.9$) effect on the magnitude of Weibull stress (a) Classical plasticity; (b) CMSG plasticity

3.3 Summary

This chapter discusses the stress field near the crack tip in plane strain small scale yielding model. The numerical results indicate that the CMSG plasticity theory is able to predict the significantly high stress values at the crack tip compared with these from the classical plasticity analysis as it includes the plastic strain gradient.

In the crack tip modeling, two types of models are introduced. The mathematically sharp tip modeling is suitable for small deformation computation. For crack tip under finite deformation, the introducing of the initial root radius in the FE model helps convergence in the numerical computation.

This chapter also discusses the *T*-stress effect on the crack tip stress field. The crack with the positive *T*-stress experiencing high constraint and the opening stress is higher than that of the small scale yielding limit. Negative *T*-stress decreases the opening stress along the crack plane, and the crack experiences low plastic constraint condition.

In this chapter, the Weibull stress is also computed based on the classical plasticity and CMSG plasticity theories by a small scale yielding model. The effect of plastic strain gradient in the crack tip gives high Weibull stress values. The initial root removes the stress singularity at the crack tip, thus, decreases the magnitude of the Weibull stress at the low load levels. The variation of the values of λ does not affect the Weibull stress values computed by the CMSG plasticity theory. The high value of the Weibull modulus m generates large magnitude of Weibull stress and indicates that m is a sensitive factor for the computation of the Weibull stress. The *T*-stress also has effect on the Weibull stress, positive *T*-stress gives higher values of Weibull stress than that of negative *T*-stress.

The high Weibull stress values computed from the CMSG plasticity theory motivates the necessity to re-calibrate the Weibull stress material parameters using the CMSG plasticity theory for the experimental fracture toughness data of 22-Ni-MoCr steels developed in the Euro project.

CHAPTER 4 CALIBRATION OF WEIBULL PARAMETERS BASED ON CLASSICAL PLASTICITY AND CMSG PLASTICITY THEORY

4.1 Introduction

Chapter 3 has demonstrated that plastic strain gradient plasticity can significantly raise the near-tip stress field. This chapter including the work of Qian *et al*. [68] further examines the impact of the plastic strain gradient effect on the Weibull parameters (Weibull modulus, *m*, and the threshold fracture toughness, K_{min}) in the three-parameter Weibull stress model for the Euro steels (22-Ni-MoCr37). The fracture toughness data for the 22-Ni-MoCr37 steels at three different temperatures ($\Theta = -20\ ^{\mathrm{o}}\mathrm{C}$, $-40\ ^{\mathrm{o}}\mathrm{C}$, and $-110\ ^{\mathrm{o}}\mathrm{C}$) reported in European Union project [8] are used in the calibration. The calibration follows the procedure proposed by Wasiluk *et al*. [24]. Besides the calibration, the numerical procedure ascertains the effect of plastic strain gradient on the magnitude of the Weibull stress and the constraint-correction function, under various $K_I + T$ loads.

4.2 Finite Element Modeling

The finite element modeling uses the C^0 solid element formulation with strain gradient model described by the CMSG plasticity theory [5] to study the stress field around the crack tip. Figure 4.1 shows the typical finite element models used in the current study for the compact tension, C(T) specimen, single-edge-notched bend, SE(B) specimen with a side groove, and the modified boundary layer (MBL) model. All the C(T) specimens in Figure 4.1(a) follow geometrically similar dimensions, with $W/B = 2$ and $a/W = 0.56$. The SE(B) specimen in Figure 4.1(b) has a crack size of $a/W = 0.5$.

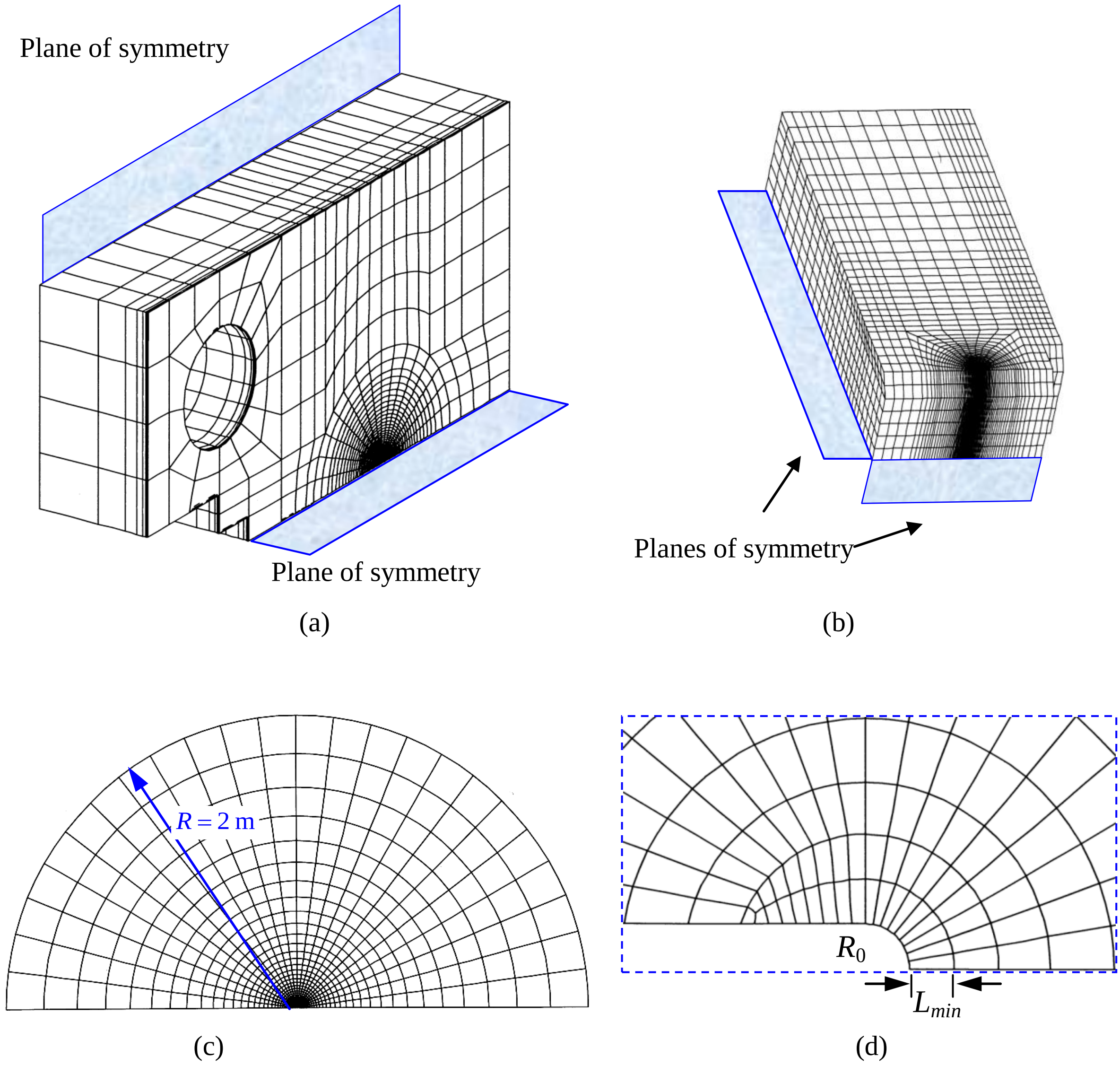

Figure 4.1 Typical FE meshes (a) A quarter-symmetric C(T) specimen; (b) A quarter-symmetric SE(B) specimen; (c) A half-symmetric MBL model with an initial root radius and an outer radius $R = 2\ \mathrm{m}$; and (d) The close-up view of the crack-tip showing the initial root radius and the minimum element size

The MBL model (see Figure. 4.1(c)) contains a single layer of elements, with the out-of-plane displacements for all nodes constrained to simulate the plane strain condition. The C(T) and SE(B) specimens utilize 3D quarter-symmetric models due to the presence of two planes of symmetry in each specimen. The number of nodes varies from 4000-21000, 27000-31000, 18000-48000, and 37000-4000 for the plane strain modified boundary layer model, 0.5T C(T) model, 1T C(T) model, and 0.4T SE(B) model, respectively, with the number of elements in the range of 600-2900, 5700-6600, 3700-11000, and 7800-8900 for the four respective models.

The mathematically sharp crack-tip models for these specimens fail to converge at a very small load level, much lower than the specified K_{min} value ($K_{min} = 20\ \mathrm{MPa}\sqrt{\mathrm{m}}$) in ASTM E 1921 [11]. To facilitate numerical convergence at large deformations, the FE models include an initial root radius, R_0, at the crack tip, as shown in Figure 4.1(d). The Weibull stress for a single specimen thus computes from multiple FE models with the R_0 varying from 0.05 μm to 15 μm. The C3D20 elements shown in Figure 4.1 employ a reduced integration scheme. The element response follows the finite deformation theory.

The strain hardening exponent, N, that describes the material true stress versus plastic strain relationship is obtained from a regression analysis of the experimentally measured data at three different temperatures ($\Theta = -20\ ^{\mathrm{o}}\mathrm{C},\ -40\ ^{\mathrm{o}}\mathrm{C}$, and $-91\ ^{\mathrm{o}}\mathrm{C}$) as shown in Figure 4.2. The hardening exponent for all three temperatures, derived from the curve fitting of the experimental stress-strain data, equals about 0.13, while the material yield stress follows the fitted constant in the regressed reference stress in the power-law hardening rule.

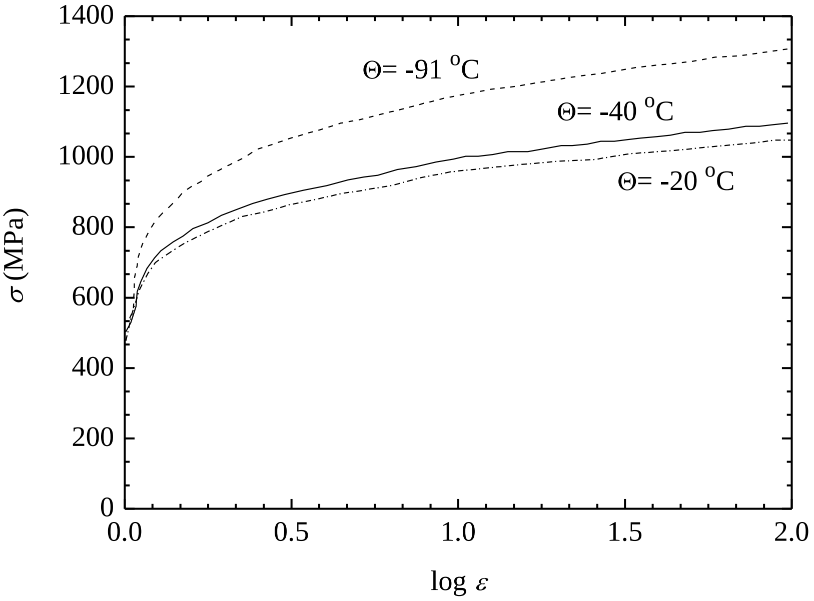

Figure 4.2 Uniaxial true stress-strain curves for the 22-Ni-MoCr37 steels measured at three temperatures over the ductile-to-brittle transition

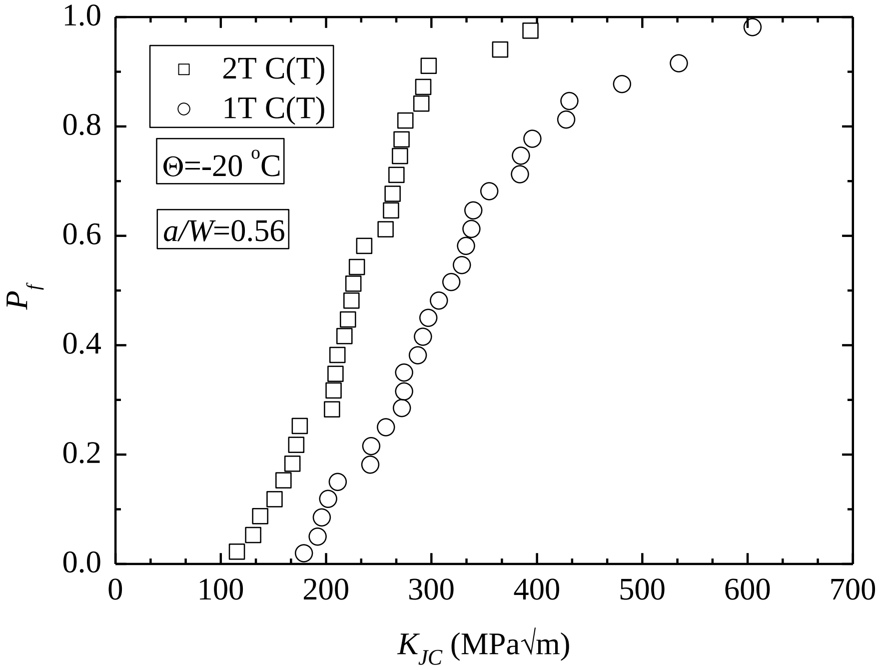

(a)

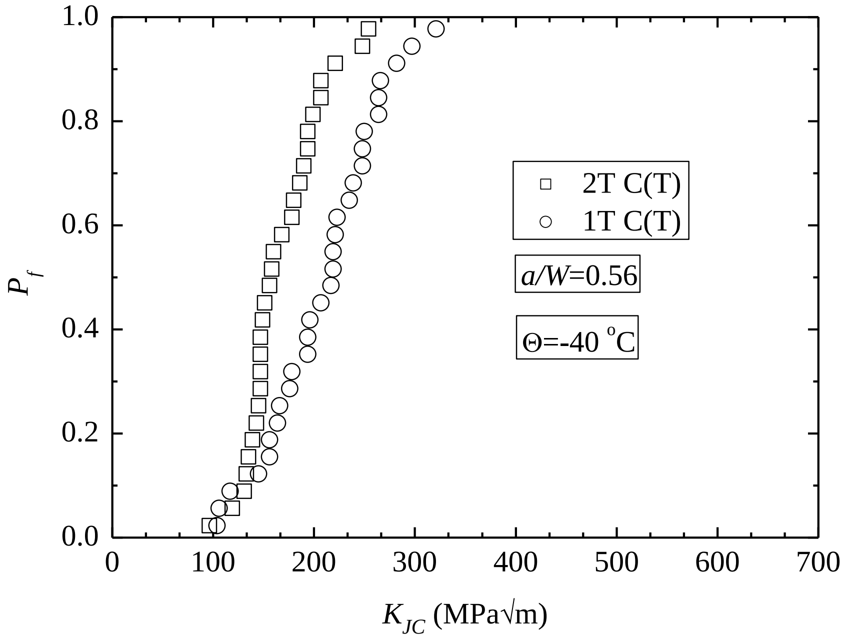

(b)

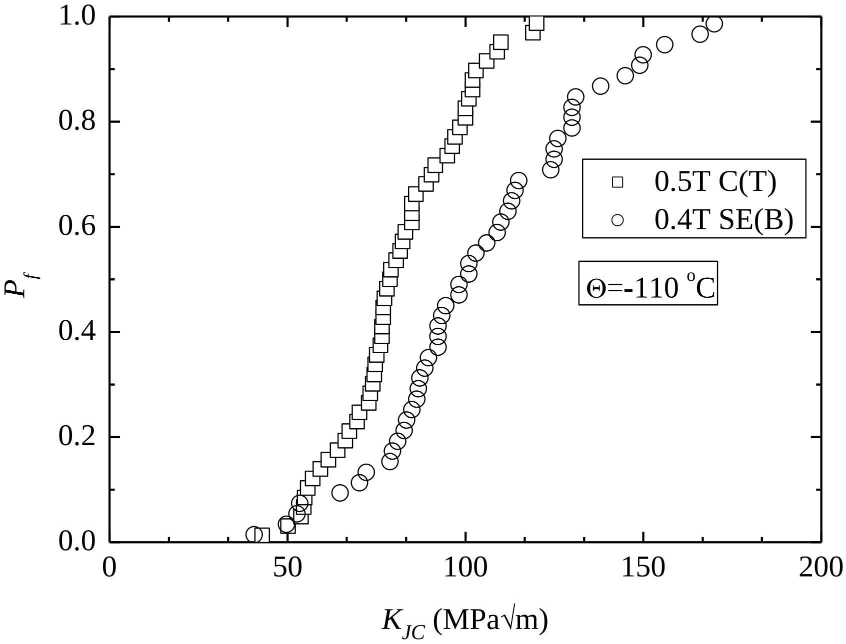

(c)

Figure 4.3 The rank probability of the fracture toughness data (a) 2T and 1T C(T) specimens at $\Theta = -20\ ^\circ\mathrm{C}$; (b) 2T and 1T C(T) specimens at $\Theta = -40\ ^\circ\mathrm{C}$; and (c) 0.5T C(T) and 0.4T SE(B) specimens at $\Theta = -110\ ^\circ\mathrm{C}$

Figures 4.3(a)-(c) show the fracture probability of the experimentally measured fracture toughness data at $\Theta = -20\ ^{\mathrm{o}}\mathrm{C},\ \ -40\ ^{\mathrm{o}}\mathrm{C},$ and $-110\ ^{\mathrm{o}}\mathrm{C}$, respectively. At each test temperature, the fracture toughness data shown in Figures 4.3(a)-(c) include two sets of specimens with contrast differences in the crack front constraints. At $\Theta = -20\ ^{\mathrm{o}}\mathrm{C}$ and $-40\ ^{\mathrm{o}}\mathrm{C}$, the high constraint toughness data refer to the experimental results measured from the thicker 2T C(T) specimens, while at a lower temperature, $\Theta = -110\ ^{\mathrm{o}}\mathrm{C}$, the thin 0.5T C(T) specimens experience small scale yielding, high constraint conditions near the crack front. Since the stress-strain data at $\Theta = -110\ ^{\mathrm{o}}\mathrm{C}$ is not available, the numerical procedure employs the stress-strain data at $\Theta = -91\ ^{\mathrm{o}}\mathrm{C}$ which is most close to $\Theta = -110\ ^{\mathrm{o}}\mathrm{C}$ reported by Heerens and Hellmann [69] to calibrate the Weibull parameters at $\Theta = -110\ ^{\mathrm{o}}\mathrm{C}$.

Figure 4.4(a) illustrates the effect of the initial root radius, R_0, and the minimum element size, L_{min}, near the crack tip, on the Weibull stress values, integrated over the fracture process zone around the crack tip of the modified boundary layer model shown in Figure 4.1(c). The Weibull stress values ($m = 10$) in Figure 4.4(a) are computed from multiple MBL models with the same initial root radius, R_0, but five different minimum element sizes, L_{min}, ranging from 50 nm to 10 μm. The material properties follow the true stress-strain data measured at $\Theta = -40\ ^{\mathrm{o}}\mathrm{C}$, with the strain-gradient hardening described by the CMSG plasticity theory using $l = 5$ μm. This value of material length scale is assumed according to that the material length scale of steel should be greater than that of the copper which is around 3 μm [45, 70] comparing the diameter of the atoms of the two metals (steel and copper). The integration of the maximum principal stresses over the fracture process zone demonstrates hardly any dependence on the mesh sizes near the crack tip for the range of element sizes considered. Figure 4.4(b) shows the Weibull stress values computed from MBL models with a varying initial root radius, R_0, which ranges from 0 to 2 μm. The initial root radius alleviates the singular stress field near the crack tip, and varies the stress distribution/redistribution within a small volume of material ahead of the crack tip. The change in the initial root radius leads to marginal differences in the computed Weibull stress magnitude only at very small load levels, as shown in Figure 4.4(b).

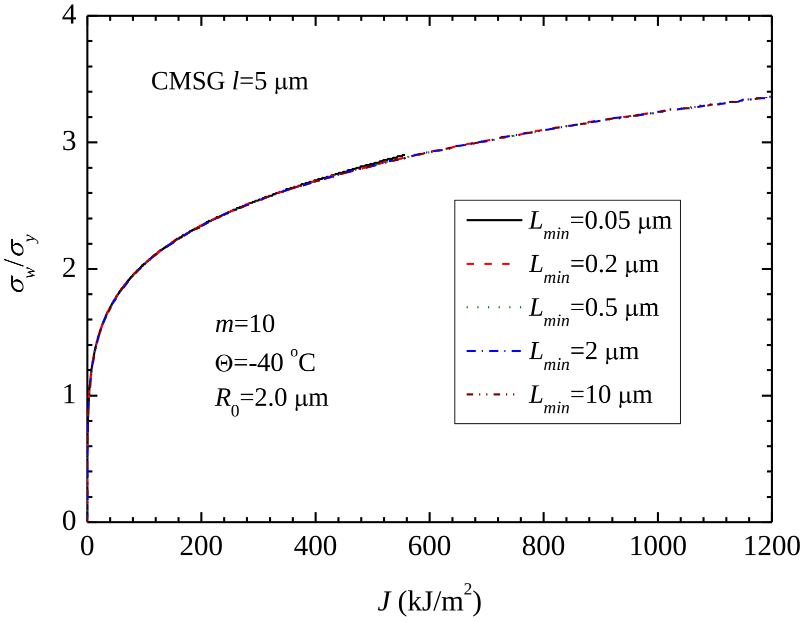

(a)

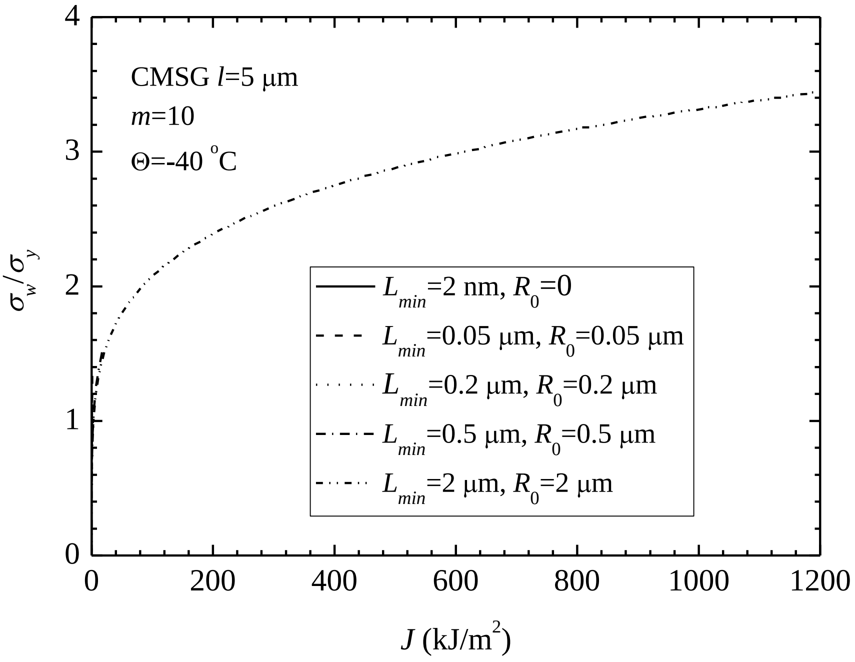

(b)

Figure 4.4 Effect of the minimum element size and the initial root radius on the σ_w values computed from the MBL model at $\Theta = -40\ ^{\circ}\mathrm{C}$ (a) Minimum element size L_{min}; (b) Initial root radius R_0

4.3 Effect of CMSG Plasticity on the Weibull Stress Model

The strain-gradient dependent material hardening elevates the near-tip stresses compared to the stress values computed using the classical plasticity theory, which prescribes the dependence of the material hardening on strains only. This section examines the effect of the CMSG plasticity on both the Weibull stress values and the crack front constraints, exemplified by the numerical computation for the 22-Ni-MoCr37 Euro steel at $-20\ ^{\circ}\mathrm{C}$, $-40\ ^{\circ}\mathrm{C}$, and $-110\ ^{\circ}\mathrm{C}$.

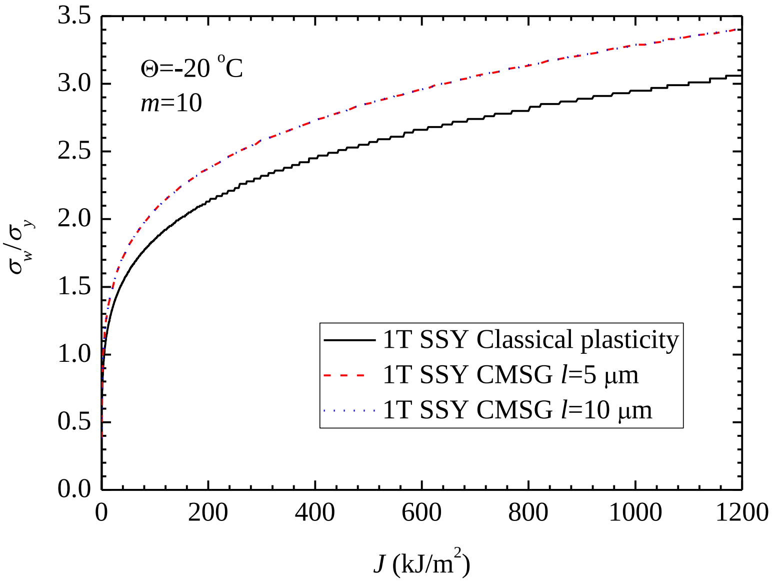
Θ=-20 °C
m=10
1T SSY Classical plasticity
1T SSY CMSG l=5 μm
1T SSY CMSG l=10 μm
σw/σy
J (kJ/m2)
0.0
0.5
1.0
1.5
2.0
2.5
3.0
3.5
0
200
400
600
800
1000
1200

(a)

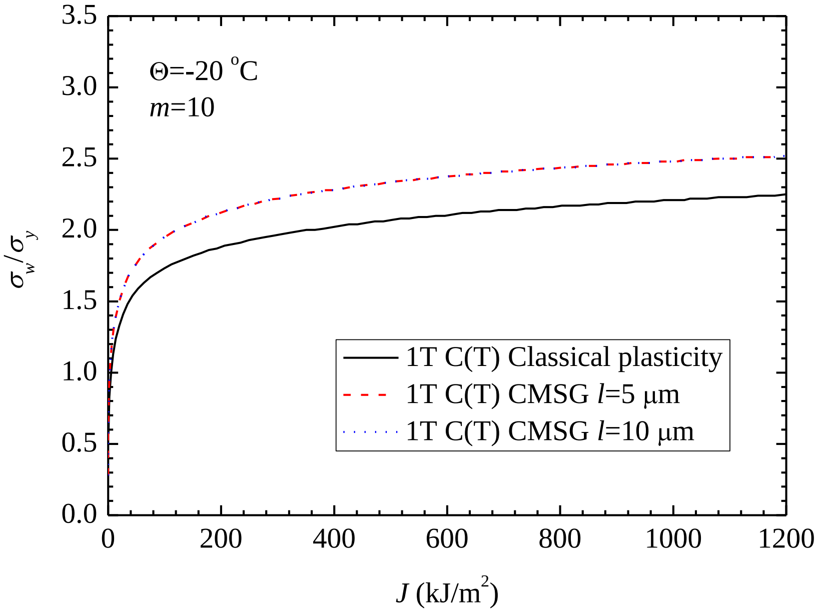
Θ=-20 °C
m=10
1T C(T) Classical plasticity
1T C(T) CMSG l=5 μm
1T C(T) CMSG l=10 μm
σw/σy
J (kJ/m2)
0.0
0.5
1.0
1.5
2.0
2.5
3.0
3.5
0
200
400
600
800
1000
1200

(b)

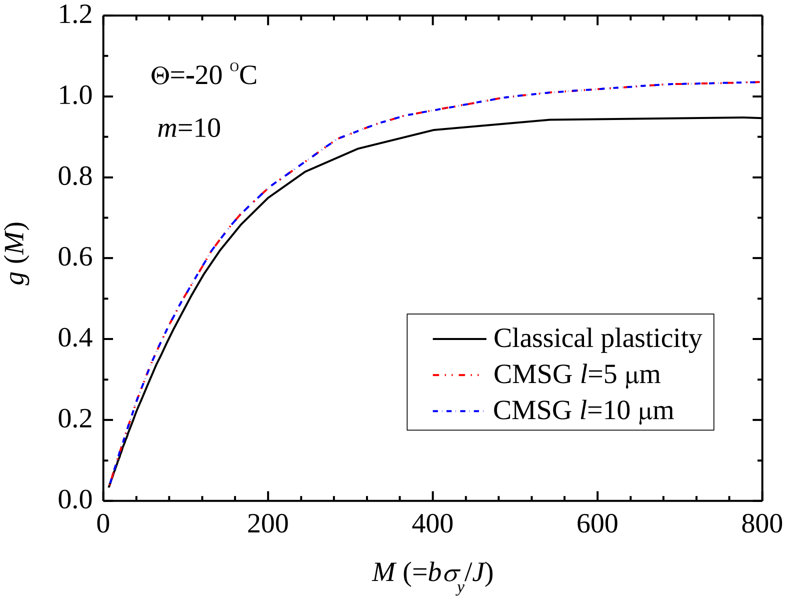

(c)

Figure 4.5 The evolution of σ_w and the constraint-correction function computed using the classical plasticity and the CMSG plasticity (a) σ_w for MBL models ;(b) σ_w for 1T C(T) ; and (c) Constraint-correction $g\left(M\right)$ for 1T C(T) at $\Theta = -20^{\mathrm{o}}\mathrm{C}$

Figure 4.5(a) compares the Weibull stress values with respect to the remotely applied J loading for the plane strain, MBL model computed using the Euro steel material properties at $-20\ ^{\mathrm{o}}\mathrm{C}$ under both the CMSG plasticity and the classical plasticity analyses, for a Weibull modulus, $m = 10$. The Weibull stress values computed from the CMSG plasticity theory with the material length scale of $l = 5$ μm and 10 μm, show about 10-11% increase compared to the σ_w values calculated from the classical theory of plasticity. The 3D C(T) model demonstrates a similar increase in the Weibull stress values computed from the CMSG plasticity theory in contrast to those calculated from the classical plasticity theory as shown in Figure 4.5(b). Figure 4.5(c) illustrates the $g(M)$ function with respect to the nondimensional loading parameter, $M = b\sigma_y / J$, at $m = 10$ for the C(T) specimens. The inclusion of the CMSG plasticity theory in the numerical procedure apparently increases the contribution to the Weibull stress from the very high stresses in the immediate vicinity of the crack tip. Consequently, the constraint-correction $g(M)$ function based on the CMSG plasticity theory becomes higher than the $g(M)$ function based on the classical theory of plasticity (see Figure 4.5(c)). This implies that the strong hardening triggered by plastic deformations at the material length scale level elevates the crack front constraints.

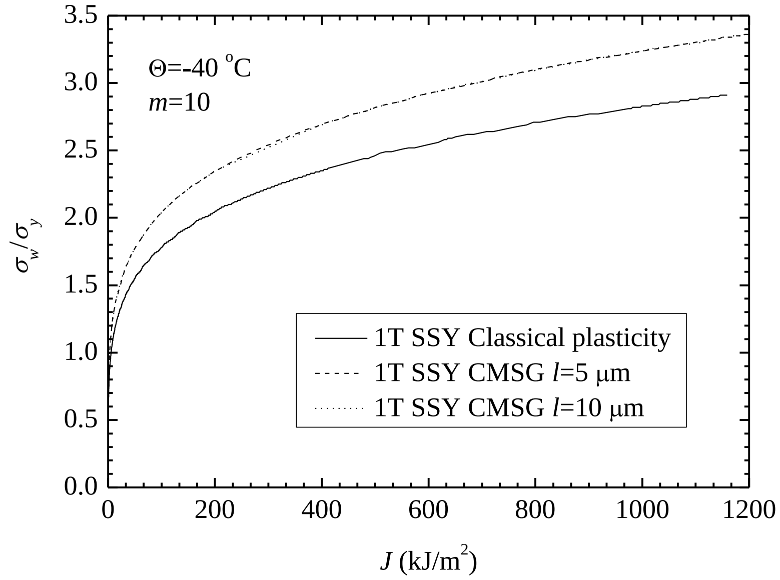

(a)

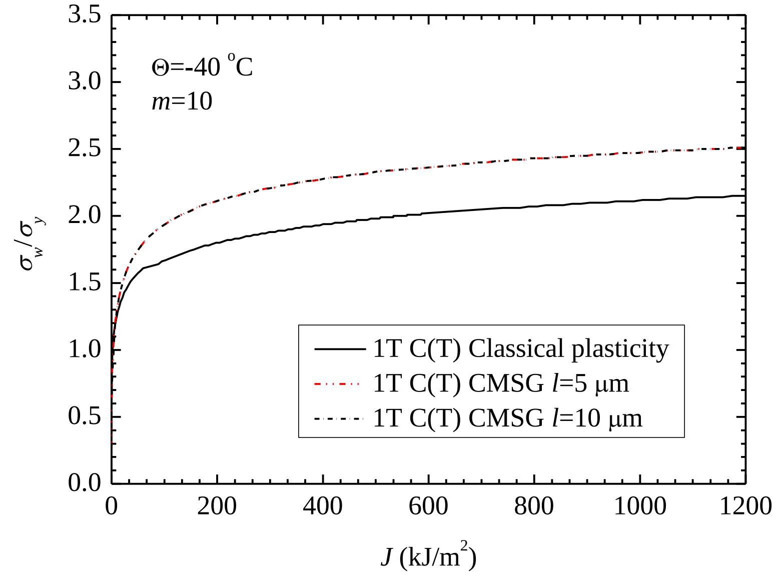

(b)

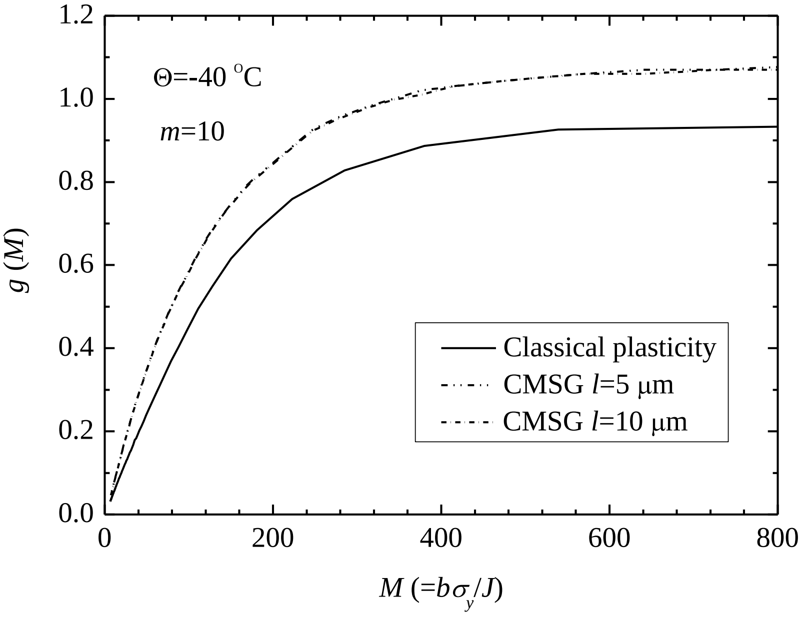

(c)

Figure 4.6 The evolution of σ_w and the constraint-correction function computed using the classical plasticity and the CMSG plasticity (a) σ_w for MBL models; (b) σ_w for 1T C(T); and (c) Constraint-correction $g(M)$ for 1T C(T) at $\Theta = -40^{\circ}\mathrm{C}$

Figure 4.6(a) compares the Weibull stress, σ_w vs. load, J curves of the plane strain small scale yielding (SSY) model by using the Euro steel material properties at -40 °C under both the CMSG plasticity and the classical plasticity analyses, with the Weibull modulus of $m = 10$. The Weibull stress values computed from the CMSG plasticity theory also show about 10-15% higher than those calculated from the classical plasticity theory. Similarly, the Weibull stress vs. J curves from the CMSG plasticity analysis of the 1T C(T) is 10-15% higher than that calculated from the classical plasticity theory (see Figure 4.6(b)). Figure 4.6(c) shows that the $g(M)$ function at -40 °C and $m = 10$ for the C(T) specimens with including the plastic strain gradient effect is around 8% higher than the $g(M)$ function based on the classical plasticity implying that the plastic deformations at the material length scale level elevates the crack front constraints.

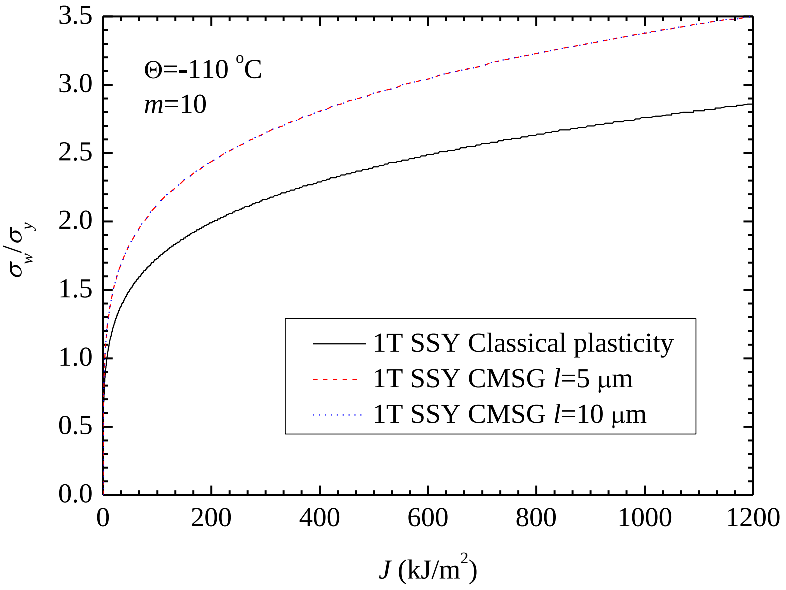
Θ=-110 °C
m=10
1T SSY Classical plasticity
1T SSY CMSG l=5 μm
1T SSY CMSG l=10 μm
σw/σy
0.0
0.5
1.0
1.5
2.0
2.5
3.0
3.5
0
200
400
600
800
1000
1200
J (kJ/m2)

(a)

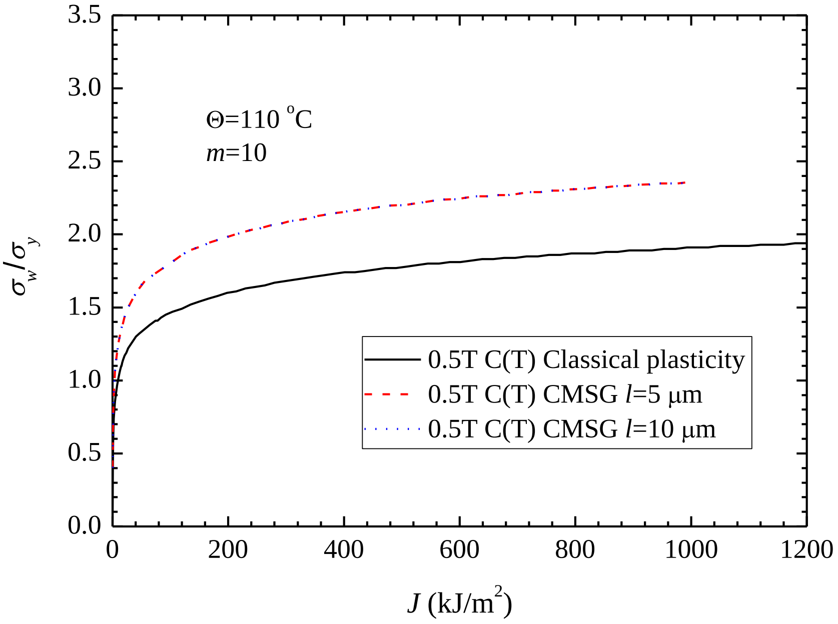
Θ=110 °C
m=10
0.5T C(T) Classical plasticity
0.5T C(T) CMSG l=5 μm
0.5T C(T) CMSG l=10 μm
σw/σy
0.0
0.5
1.0
1.5
2.0
2.5
3.0
3.5
0
200
400
600
800
1000
1200
J (kJ/m2)

(b)

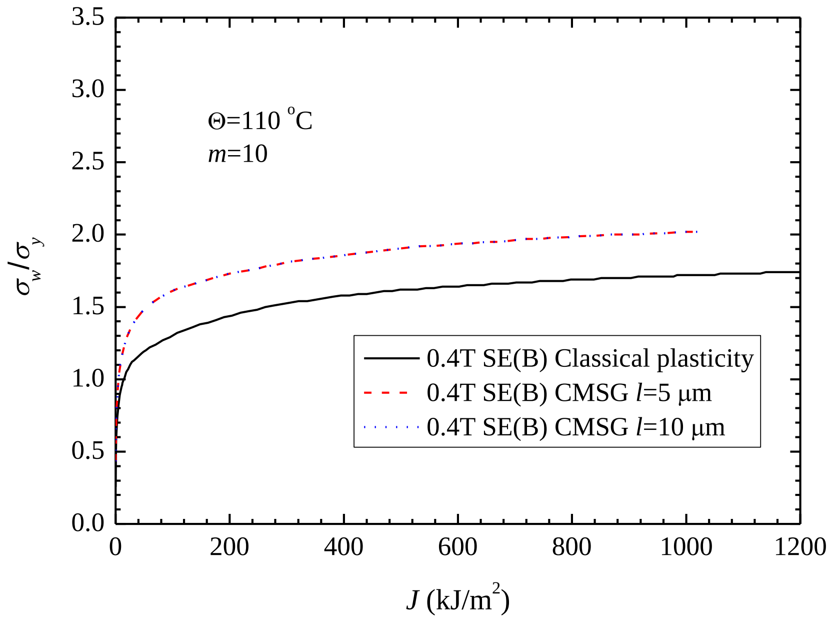
Θ=110 °C
m=10
0.4T SE(B) Classical plasticity
0.4T SE(B) CMSG l=5 μm
0.4T SE(B) CMSG l=10 μm
σ_w/σ_y
J (kJ/m²)
0.0
0.5
1.0
1.5
2.0
2.5
3.0
3.5
0
200
400
600
800
1000
1200

(c)

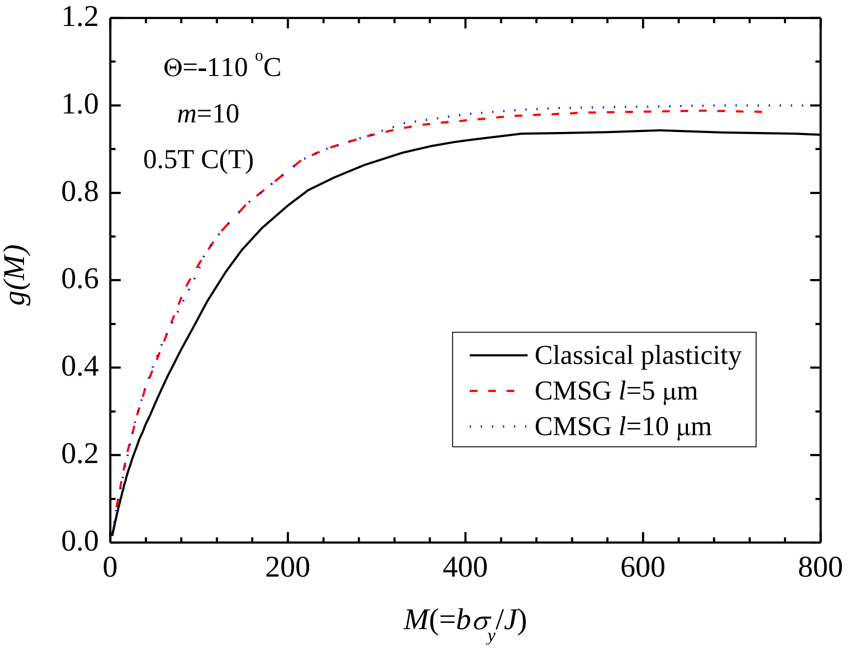
Θ=-110 °C
m=10
0.5T C(T)
Classical plasticity
CMSG l=5 μm
CMSG l=10 μm
g(M)
M(=bσ_y/J)
0.0
0.2
0.4
0.6
0.8
1.0
1.2
0
200
400
600
800

(d)

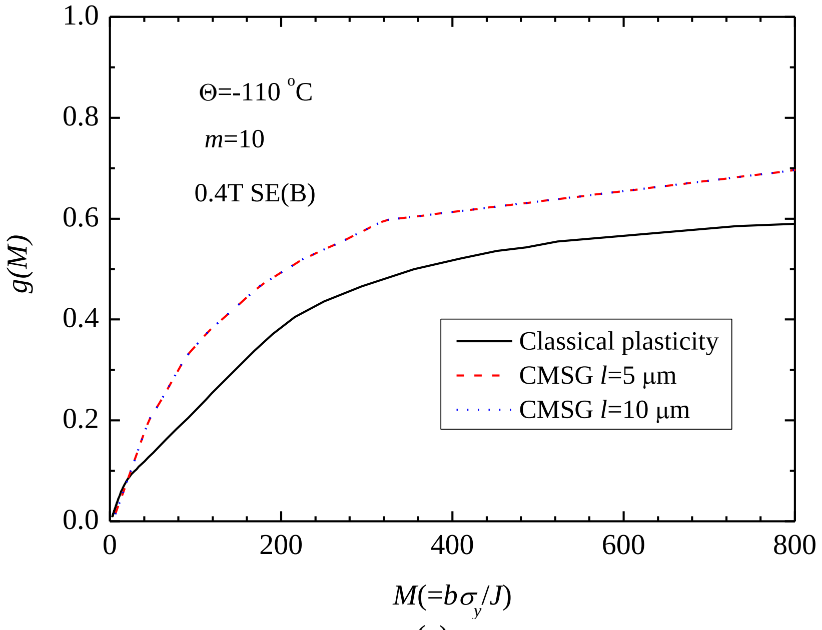

(e)

Figure 4.7 The evolution of σ_w and the constraint-correction function computed using the classical plasticity and the CMSG plasticity (a) σ_w for MBL models (b) σ_w for 0.5T C(T) (c) σ_w for 0.4SE(B) (d) Constraint-correction $g\left(M\right)$ for 1T C(T); and (e) constraint-correction function $g\left(M\right)$ for 0.4T SE(B) specimens at $\Theta = -110^{\circ}\mathrm{C}$

Figures 4.7(a)-(c) plot the Weibull stress vs. J curves of the small scale yielding (SSY) model, 0.5T C(T) model and the 0.4T SE(B) models by using the Euro steel material properties at $-110\ ^{\circ}\mathrm{C}$ under both the CMSG plasticity and the classical plasticity analyses, with the Weibull modulus of $m = 10$. The Weibull stress values for the three models computed from the CMSG plasticity theory show around 22%, 24%, and 15% increase compared to the σ_w values calculated from the classical theory of plasticity, respectively. Both Figures 4.7(d) and 4.7(e) show that the $g(M)$ function at $m = 10$ for the C(T) model and SE(B) model with the plastic strain gradient effect is higher than the $g(M)$ function based on the classical theory of plasticity further implying that the plastic strain gradient raises the crack front constraints.

4.4 Effect of *T*-Stress

The elastic *T*-stress refers to the second term in the classical Williams' solution [71] for the crack-tip stress field derived from small-displacement assumptions. The *T*-stress represents a stress field parallel to the crack plane, imposing a strong effect on the stress triaxiality very near the crack tip [72]. The direction and magnitude of the *T*-stress, therefore, characterizes the plasticity constraints experienced by the crack tip. A crack tip under a compressive (negative) *T*-stress often experiences very low plasticity constraints, while a crack tip with a zero or positive *T*-stress represents a high constraint condition.

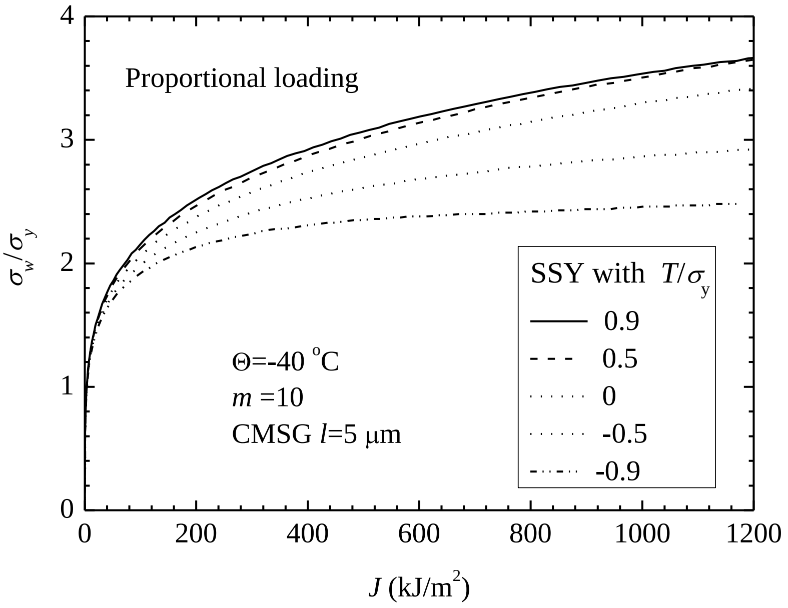

(a)

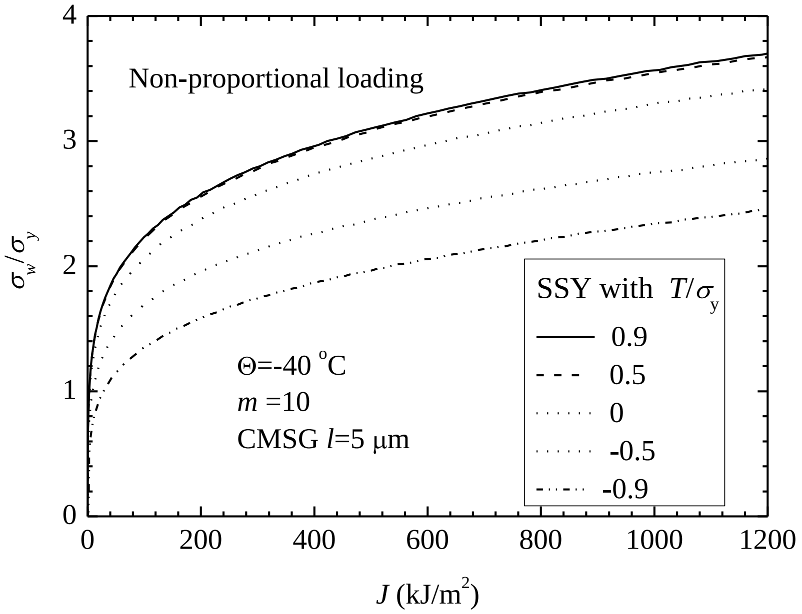

(b)

Figure 4.8 The variation of the σ_w values in MBL models subjected to different T-stresses (a) Proportional loading; (b) Non-proportional loading

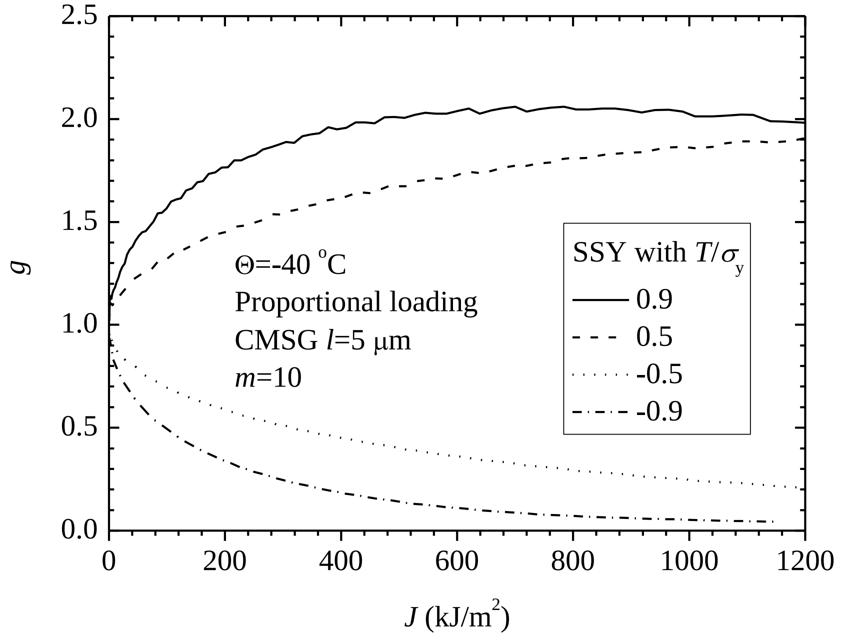

(a)

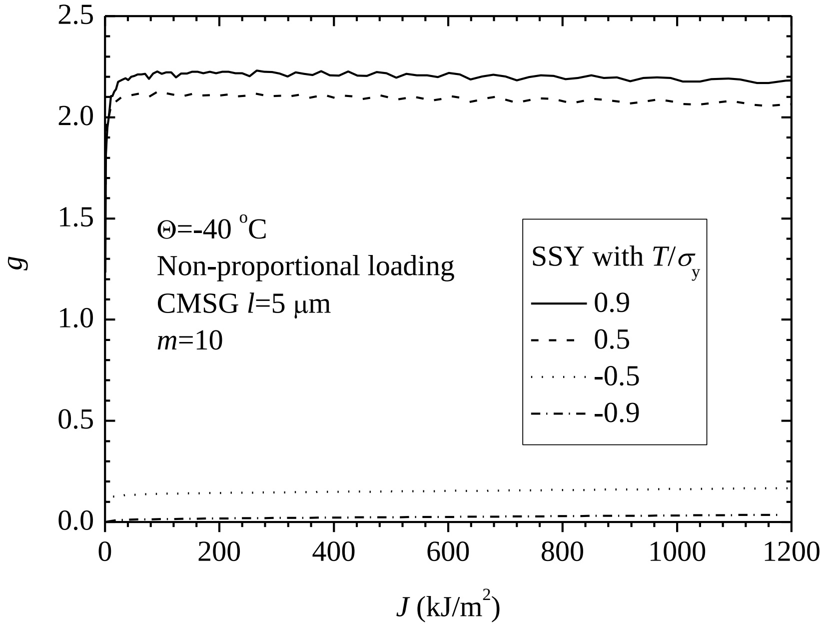

(b)

Figure 4.9 The variation of the constraint-correction function in MBL models (a) Proportional loading; (b) Non-proportional loading

Figure 4.8 illustrates the effect of crack front constraints, quantified the linear-elastic *T*-stresses, on the σ_w values and the constraint-correction function, g, in Equation (2.8), for a plane strain MBL model with the CMSG plasticity hardening ($l = 5$ μm). The numerical procedure imposes the displacement-controlled loading caused the elastic *T*-stress, together with the K_I loading described in Equations (3.1) and (3.2), to the circumference of the semi-circular MBL model. The MBL model here has an outer radius of $R = 2$ m and an initial root radius of $R_0 = 2$ μm.

The numerical procedure examines two types of applications of the $K_I + T$ loading, namely the proportional loading and the non-proportional loading. The proportional loading applies the K_I displacements in Equations (3.1) and (3.2) simultaneously with the *T*-stress displacements in Equations (3.3) and (3.4) on the plane strain MBL model.

The non-proportional loading, in contrast, separates the loading procedure into two steps, with the *T*-stress applied in the first step followed by the K_I loading in the second step.

Figures 4.8(a) and 4.8(b) compare the σ_w values computed from Equation (2.6) with $m = 10$ for these two loading cases under five different levels of *T*-stresses, $T / \sigma_y =$ -0.9, -0.5, 0, 0.5, and 0.9. A positive *T*-stress leads to slightly higher σ_w values than the Weibull stresses at a zero *T*-stress, while a negative *T*-stress generates more severe reductions in the σ_w values compared to the Weibull stress corresponding to a zero *T*-stress. O'Dowd and Shih [72] demonstrate that the negative *T*-stress causes significantly lower maximum principal stresses within the plastic zone around the crack tip than does the zero *T*-stress condition, while a positive *T*-stress leads to slightly higher maximum principal stress values around the crack tip. The application of *T*-stresses prior to the K_I in the non-proportional loading initiates a more severe deviation in the σ_w values with nonzero *T*-stresses from those with a zero *T*-stress at a low loading, J, compared to the proportional loading. Figures 4.9(a) and 4.9(b) show the constraint-correction function *g* in Equation (2.8) for $m = 10$, computed from the ratio of the Weibull stress with a nonzero *T*-stress over the σ_w values with a zero *T*-stress, both corresponding to the same crack-opening load, J,

$$g = \left(\frac{\sigma_w (T \neq 0)}{\sigma_w (T = 0)} \right)^m \tag{4.1}$$

The *T*-stress increases from 0 to the designated value in the proportional loading case, which shows a g value of 1.0 at $J = 0$ with a continuously increasing g value for the positive *T*-stresses and a continuously decreasing g-value for the negative *T*-stresses. In contrast, the non-proportional loading reflects the effect of the non-zero *T*-stress by showing a very large g value for the positive *T*-stress and a very small g value for the negative *T*-stress, even at a small load level. The g value in the non-proportional loading condition maintains an approximately constant magnitude with the increasing load, implying that the constraint change is primarily driven by the constant *T*-stress.

The results in Figures 4.8 and 4.9 prove that the correct estimation of the Weibull stress magnitudes, requires accurately evaluating the ratio of the *T*-stress with respect to the crack-opening load K_I (often measured by the biaxiality ratio, $\beta = T\sqrt{\pi a}K_I$).

4.5 Calibration at –20 $^{\mathrm{o}}$C

The calibration procedure in the current study scans through m value from 1 to 30 at a step of $\Delta m = 1$ and the K_{min} value from 1 to 80 $\mathrm{MPa}\sqrt{\mathrm{m}}$ at a step of $\Delta K_{min} = 1\ \mathrm{MPa}\sqrt{\mathrm{m}}$. Tables 4.1 list the calibrated m and K_{min} values at three different temperatures ($\Theta = -20\ ^{\mathrm{o}}\mathrm{C},\ -40\ ^{\mathrm{o}}\mathrm{C},$ and $-110\ ^{\mathrm{o}}\mathrm{C}$), based on the minimum calibration error computed in Equation (2.14). At $-110\ ^{\mathrm{o}}\mathrm{C}$, two material curves ($\sigma - \varepsilon$ at $-91\ ^{\mathrm{o}}\mathrm{C}$ and $-110\ ^{\mathrm{o}}\mathrm{C}$), are used to calibrate the Weibull parameters.

For all three temperatures, the numerical procedure examines three types of strain-hardening behavior: the classical plasticity, the CMSG plasticity with the material length scale of 5 μm and the CMSG plasticity with the material length scale of 10 μm. These material length scales correspond to an α value from 0.2 to 0.3, assuming the Burgers vector lies in the range from 0.1 nm to 0.2 nm. At $\Theta = -20\ ^{\mathrm{o}}\mathrm{C}$, the calibrated m equals 17 for the classical plasticity theory and 19 for the CMSG plasticity theory with $l = 5$ μm and 10 μm, while the K_{min} value equals 47 $\mathrm{MPa}\sqrt{\mathrm{m}}$ for all three strain-hardening properties.

Table 4.1 Calibrated m and K_{min} for the Weibull stress model for 22-Ni-MoCr37 steels at three different temperatures

Θ (°C)	Material Hardening	Calibrated Weibull Stress Parameters	
		m	K_{min} ($\mathrm{MPa}\sqrt{\mathrm{m}}$)
–20 °C	Classical plasticity	17	47
	CMSG l = 5 μm	19	47
	CMSG l = 10 μm	19	47
–40 °C	Classical plasticity	17	48
	CMSG l = 5 μm	19	47
	CMSG l = 10 μm	19	47
–110 °C ($\sigma-\varepsilon$ at -91 °C)	Classical plasticity	15	20
	CMSG l = 5 μm	19	20
	CMSG l = 10 μm	19	20
–110 °C ($\sigma-\varepsilon$ at -110 °C)	Classical plasticity	15	23
	CMSG l = 5 μm	19	23
	CMSG l = 10 μm	19	23

Table 4.2 Weibull stresses based on the classical plasticity theory and the CMSG plasticity theory at the calibrated m values for $\Theta = -20\ ^{\circ}\mathrm{C}$, computed from an MBL model under zero T-stress

J (kJ/m^2)	σ_w / σ_y	$\sigma_w^{CMSG} / \sigma_w^{classical}$	
	Classical plasticity (m = 17)	CMSG (l = 5 μm, m = 19)	CMSG (l = 10 μm, m = 19)
10	1.67	1.20	1.20
100	2.20	1.20	1.20
300	2.51	1.15	1.15
500	2.66	1.15	1.15
1000	2.89	1.14	1.14

Table 4.2 shows the ratio between Weibull stress and yield stress, and the Weibull stress ratio between the classical plasticity and the CMSG plasticity analyses at -20 ^{o}C. The ratio from the classical plasticity analysis implies that the Weibull stress increases with the load *J*. The difference in the Weibull stress values computed from the CMSG plasticity and the classical plasticity is around 14%-20% and at small load level the difference is bigger, and then keeps constant at higher load levels. Figure 4.8(a) shows the evolution of the normalized calibration error with respect to the m value corresponding to $K_{min} = 47 \text{ MPa}\sqrt{\text{m}}$ for the three types of hardening behavior. The normalized error refers to the ratio of the error in Equation (2.14) computed for a given m value over the maximum error computed for all m values, for each series of calibration. The change in the material length scale in the CMSG plasticity causes insignificant variation in the error function, as shown in Figure 4.10. The calibrations based on both the classical plasticity and the CMSG plasticity theories indicate distinctive minimum errors with respect to the m value, as shown in Figure 4.10(a). In contrast, Figure 4.8(b) shows a plateau near the minimum errors ($K_{min} = 47 \text{ MPa}\sqrt{\text{m}}$) for both the classical plasticity and the CMSG plasticity theory. This implies that the minimum error remains much less sensitive to the selection of the K_{min} value than to the choice of an m value. The K_{min} value represents a threshold below which the cleavage fracture failure does not take place. The K_{min} value introduces a less significant effect on the constraint scaling, implemented in Equation (2.13), than the constraint-correction function, $g\left(M\right)$, especially for fracture toughness data with $K_{JC} \geq K_{min}$. The $g\left(M\right)$ function depends directly on the Weibull modulus, m, as shown in Equation (2.8).

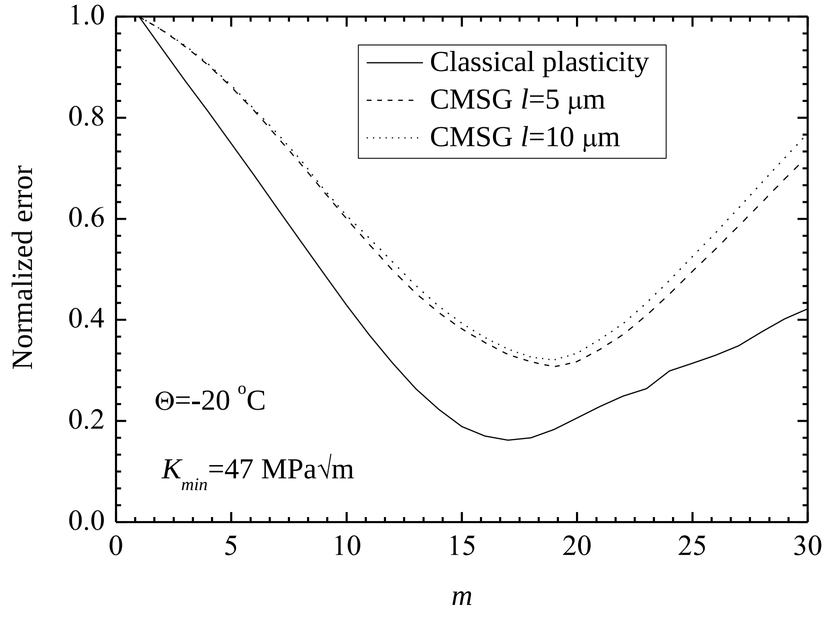

(a)

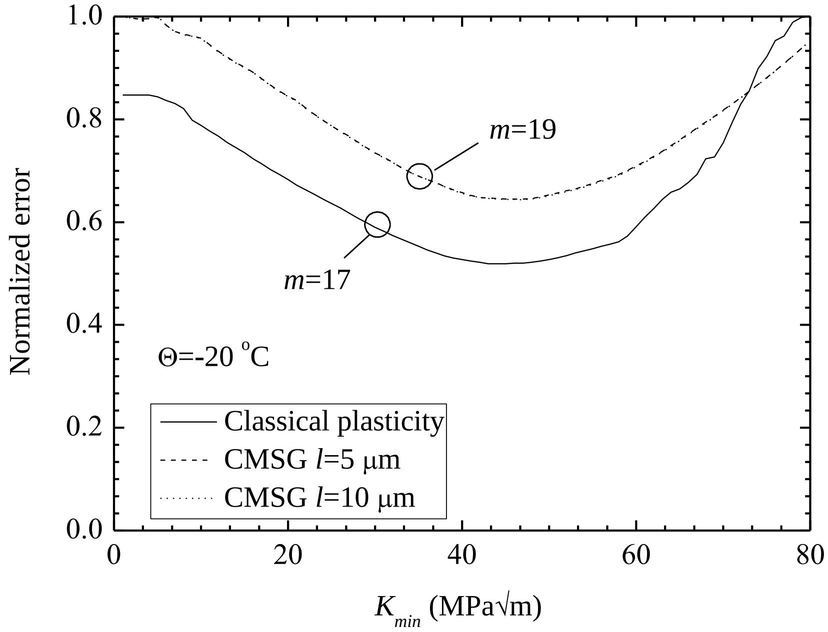

(b)

Figure 4.10 The variation of the normalized calibration error with respect to the *m* values and the K_{min} values for fracture toughness data measured at $\Theta = -20\ ^{\circ}\mathrm{C}$ (a) *m* values; (b) K_{min} values

Figure 4.11 compares the fracture toughness data scaled to the 1T SSY condition based on Equation (2.13) with the probability of fracture predicted by the Weibull stress model in Equation (2.9) using the calibrated m and K_{min} value. The calibrated Weibull parameters based on the CMSG plasticity hardening properties yield slightly better predictions of the scaled experimental data, than do the Weibull parameters calibrated using the classical theory of plasticity.

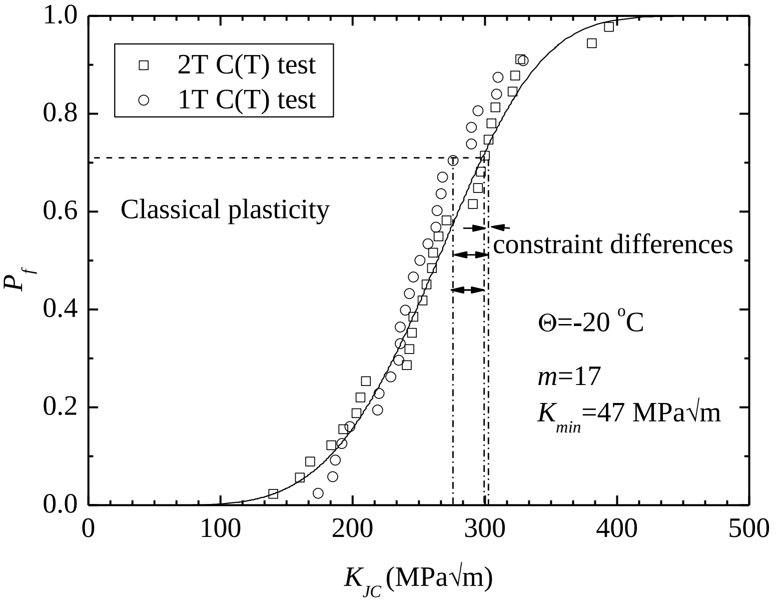

(a)

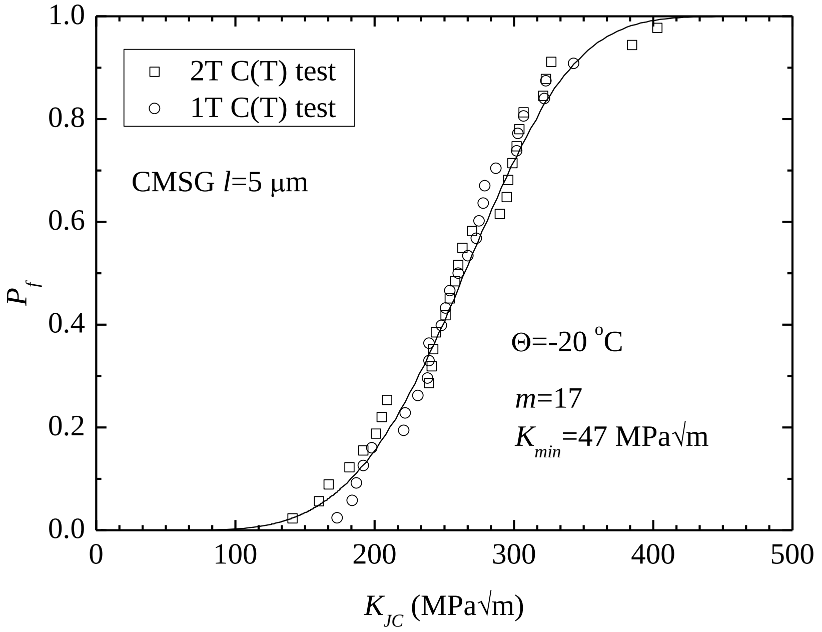

(b)

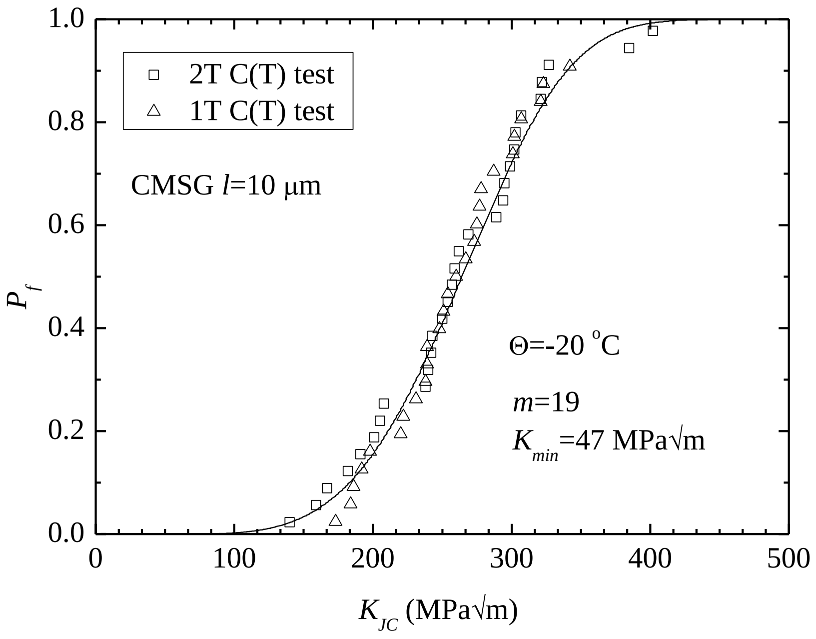

(c)

Figure 4.11 The comparison between the constraint-scaled fracture toughness data at $\Theta = -20$ °C and the probability prediction by the Weibull stress model (a) Classical plasticity; (b) CMSG plasticity theory with $l = 5\,\mu\text{m}$; and (c) CMSG plasticity theory with $l = 10\,\mu\text{m}$

4.6 Calibration at –40 ^{o}C

At $\Theta = -40$ ^{o}C, the calibration procedure yields an *m* value of 17 at the minimum error for the classical theory of plasticity and an *m* value of 19 for the CMSG plasticity theory. The calibrated K_{min} value equals 48 $\text{MPa}\sqrt{\text{m}}$ for the classical theory of plasticity and 47 $\text{MPa}\sqrt{\text{m}}$ for the CMSG plasticity theory. Table 4.3 shows the ratio between Weibull stress and yield stress, and the Weibull stress ratio between the CMSG plasticity and the classical plasticity analyses at 40 ^{o}C. The difference in the Weibull stress values computed from the CMSG plasticity and the classical plasticity is around 24%-25% at small load level the difference, and then keeps 18%-19% at higher load levels.

Figure 4.12 illustrates the variation of the normalized calibration error with respect to the *m* value and K_{min} value. Similar to the calibration for $\Theta = -20$ ^{o}C, the calibration error shows a distinctive minimum value with respect to the variation of the *m* value, and a plateau near $K_{min} = 47\ \mathrm{MPa}\sqrt{\mathrm{m}}$ for the calibration based on the CMSG plasticity theory and near $K_{min} = 48\ \mathrm{MPa}\sqrt{\mathrm{m}}$ for the calibration based on the classical plasticity. For the calibration with respect to the *m* value, the normalized error based on the CMSG plasticity theory shows a slightly more gentle variation near the minimum value than the normalized error based on the classical plasticity theory.

Figure 4.13 compares the cumulative probability of fracture predicted by the Weibull stress model using Equation (2.9) and the fracture toughness at $-40\ ^{\mathrm{o}}\mathrm{C}$ scaled to the 1T SSY condition. Both predictions based on the CMSG plasticity and the classical plasticity theories demonstrate close agreement with the experimental data.

Table 4.3 Weibull stresses based on the classical plasticity theory and the CMSG plasticity theory at the calibrated *m* values for $\Theta = -40\ ^{\mathrm{o}}\mathrm{C}$, computed from an MBL model under zero *T*-stress

J (kJ/m^2)	σ_w / σ_y	$\sigma_w^{CMSG} / \sigma_w^{classical}$	
	Classical plasticity (*m* = 17)	CMSG (*l* = 5 μm, *m* = 19)	CMSG (*l* = 10 μm, *m* = 19)
10	1.61	1.24	1.25
100	2.11	1.21	1.21
300	2.41	1.19	1.20
500	2.56	1.19	1.19
1000	2.77	1.18	1.18

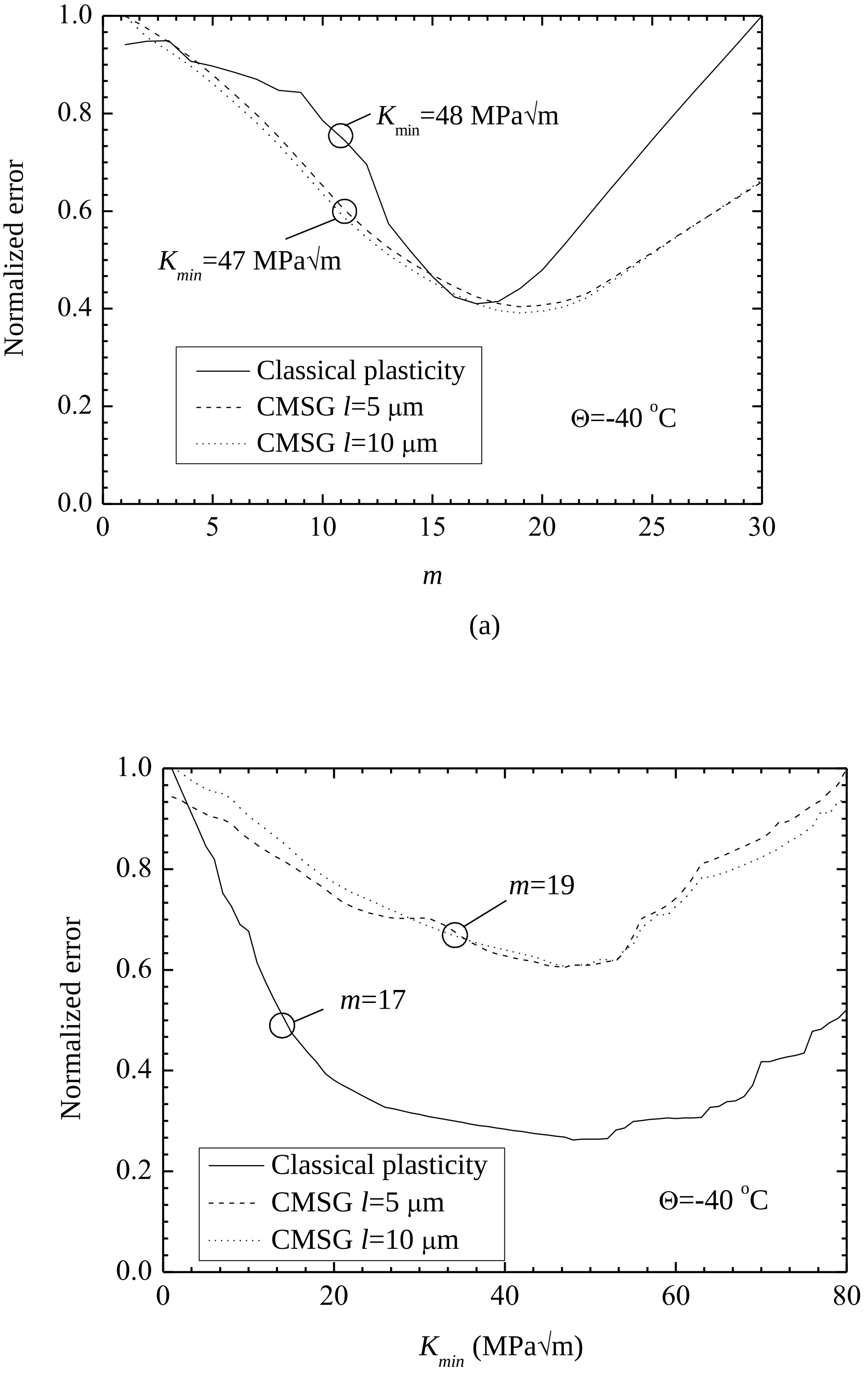

(a)

(b)

Figure 4.12 The variation of the normalized calibration error with respect to the *m* values and the K_{min} values for fracture toughness data measured at $\Theta = -40$ °C (a) *m* values; (b) K_{min} values

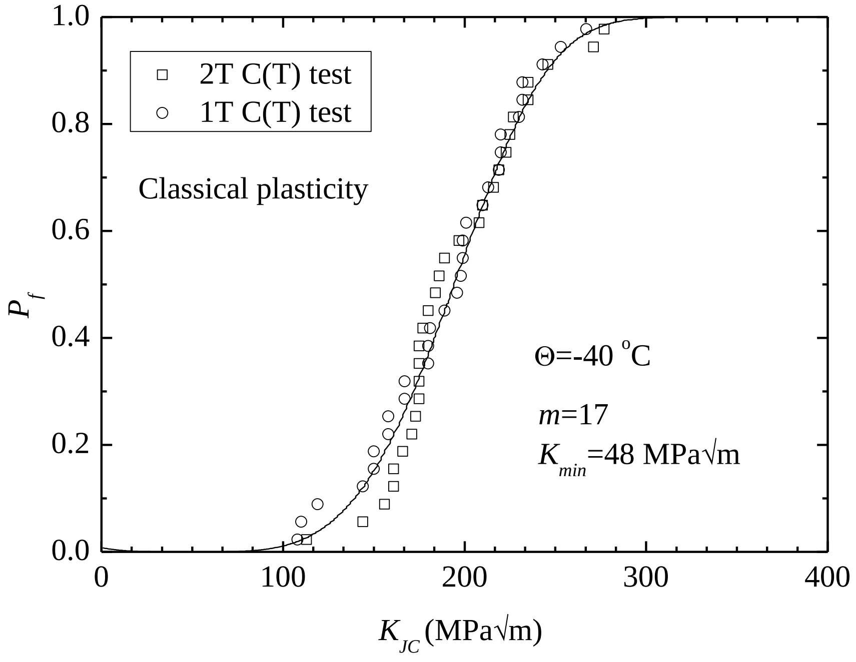
□ 2T C(T) test
○ 1T C(T) test
Classical plasticity
Θ=-40 °C
m=17
K_min=48 MPa√m
P_f
K_JC (MPa√m)
0.0
0.2
0.4
0.6
0.8
1.0
0
100
200
300
400

(a)

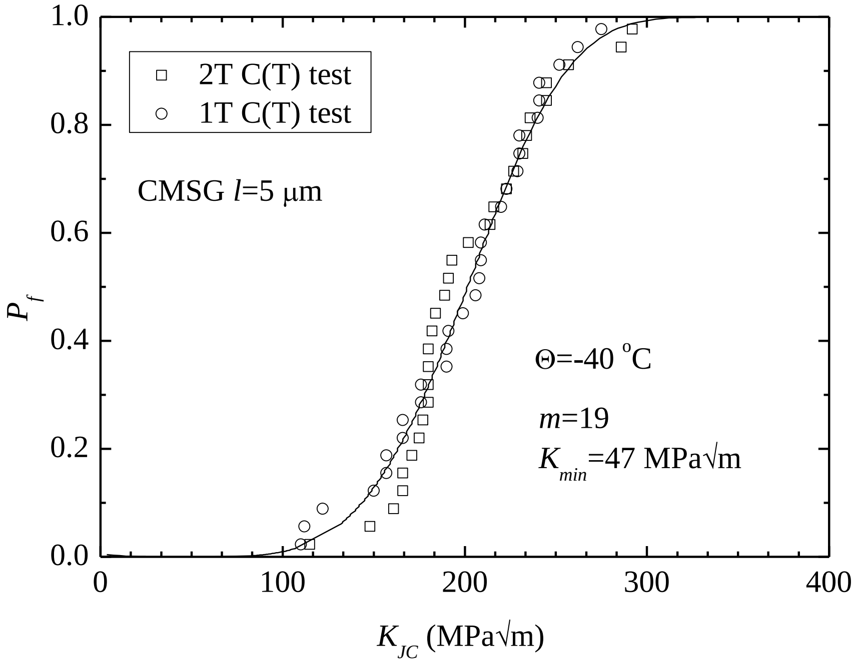
□ 2T C(T) test
○ 1T C(T) test
CMSG l=5 μm
Θ=-40 °C
m=19
K_min=47 MPa√m
P_f
K_JC (MPa√m)
0.0
0.2
0.4
0.6
0.8
1.0
0
100
200
300
400

(b)

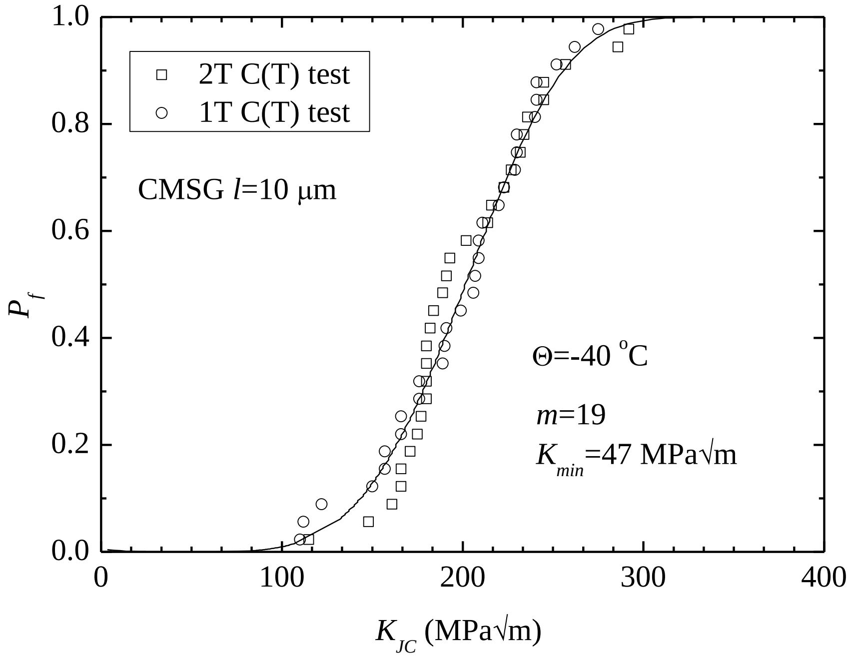

(c)

Figure 4.13 The comparison between the constraint-scaled fracture toughness data at $\Theta = -40\ ^{\mathrm{o}}\mathrm{C}$ and the probability prediction by the Weibull stress model (a) classical plasticity; (b) CMSG plasticity theory with $l = 5\ \mu\mathrm{m}$; and (c) CMSG plasticity theory with $l = 10\ \mu\mathrm{m}$

4.7 Calibration at –110 °C

The calibration of the Weibull parameters at $-110\ ^{\mathrm{o}}\mathrm{C}$ initially uses the material property at –91 °C as Wasiluk *et al.* [24] due to the material property for –91 °C is currently unavailable.

4.7.1 Calibration using material property at -91 °C

The calibrated *m* value equals 15 based on the classical plasticity and 19 based on the CMSG plasticity theory for the fracture toughness data measured at $-110\ ^{\mathrm{o}}\mathrm{C}$. The K_{min} value calibrates to be 20 $\mathrm{MPa}\sqrt{\mathrm{m}}$ for both the classical plasticity and the CMSG plasticity theory. Table 4.4 shows the ratio between Weibull stress and yield stress, and the Weibull stress ratio between the CMSG plasticity and the classical plasticity analysis at 110 °C. The difference in the Weibull stress values computed from the CMSG plasticity and the classical plasticity is around 49% at small load level the difference, and then keeps 28%-31% at higher load levels.

Figure 4.14 shows the variation of the normalized error with respect to the *m* value and the K_{min} value. The calibration error based on the CMSG plasticity theory shows a more gentle variation near the minimum value around $m = 19$ than the calibration error around $m = 15$ based on the classical plasticity theory. For both the classical plasticity and the CMSG plasticity theory, the calibration error shows a plateau near the minimum value where $K_{min} = 20\ \mathrm{MPa}\sqrt{\mathrm{m}}$. Figure 4.15 demonstrates the close agreement between the cumulative probabilities of fracture predicted using Equation (2.9) and the constraint-scaled fracture toughness for $\Theta = -110\ ^{\mathrm{o}}\mathrm{C}$.

Table 4.4 Weibull stresses based on the classical plasticity theory and the CMSG plasticity theory at the calibrated *m* values for $\Theta = -110\ ^{\mathrm{o}}\mathrm{C}$, computed from an MBL model under zero *T*-stress

J (kJ/m^2)	σ_w / σ_y	$\sigma_w^{CMSG} / \sigma_w^{classical}$	
	Classical plasticity (*m* = 15)	CMSG (*l* = 5 μm, *m* = 19)	CMSG (*l* = 10 μm, *m* = 19)
10	1.43	1.49	1.49
100	2.0	1.38	1.38
300	2.34	1.33	1.33
500	2.51	1.31	1.31
1000	2.76	1.28	1.28

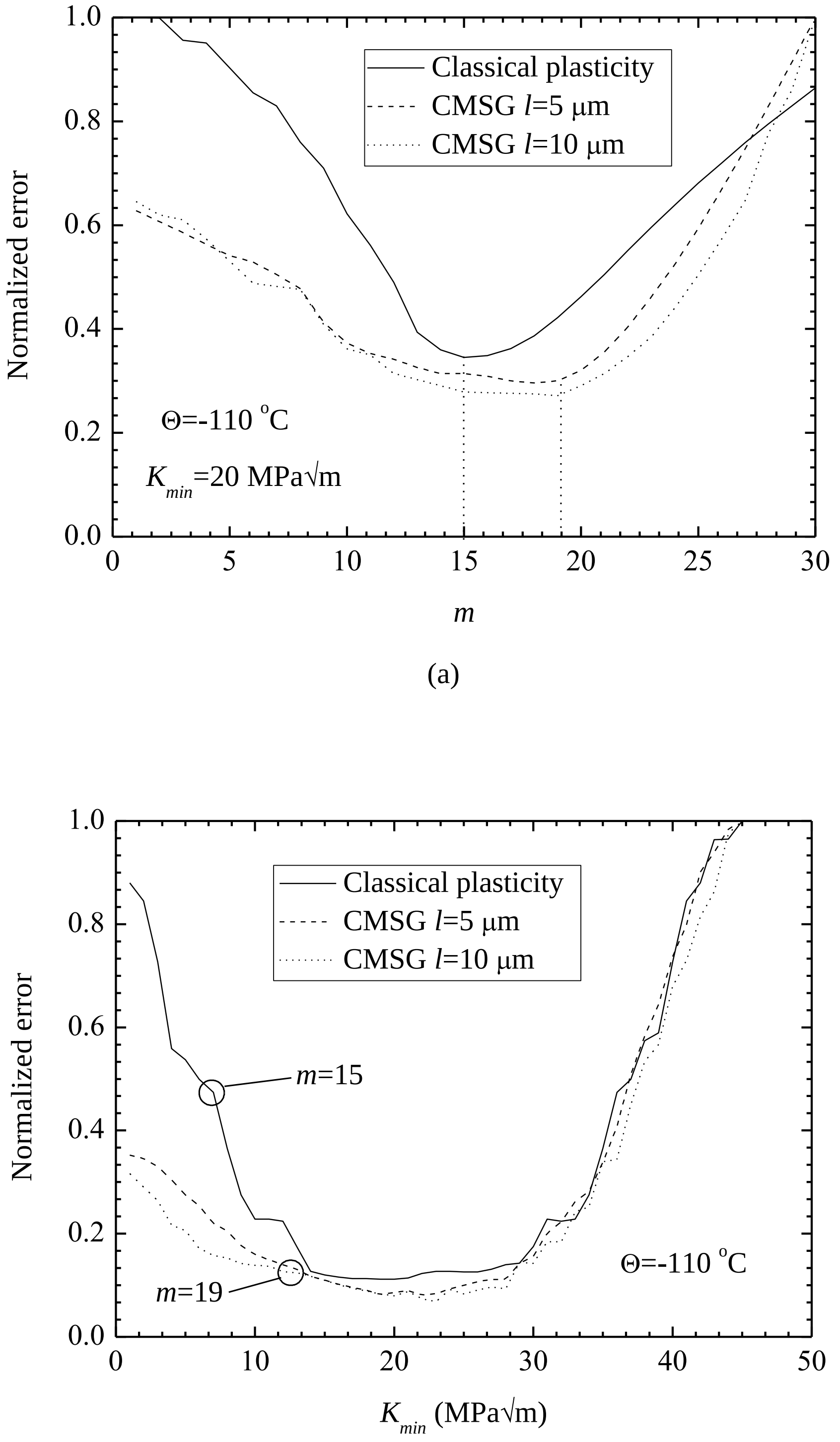

(a)

(b)

Figure 4.14 The variation of the normalized calibration error with respect to *m* values and the K_{min} values for fracture toughness data measured at $\Theta = -110$ °C (a) *m* values; (b) K_{min} values

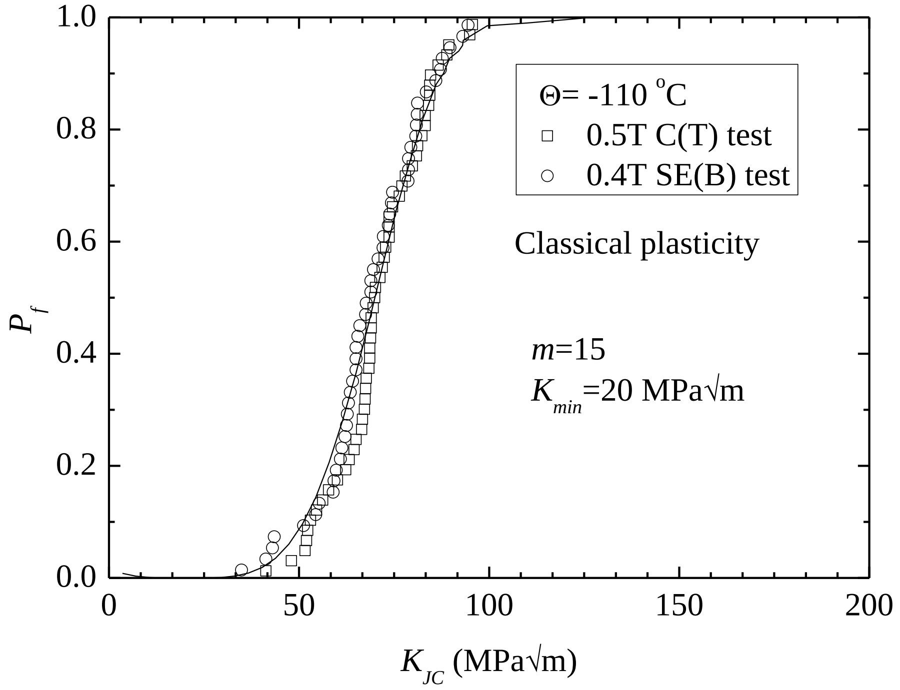
1.0
0.8
0.6
0.4
0.2
0.0
P_f
0
50
100
150
200
K_{JC} (MPa√m)
Θ= -110 °C
□ 0.5T C(T) test
○ 0.4T SE(B) test
Classical plasticity
m=15
K_{min}=20 MPa√m

(a)

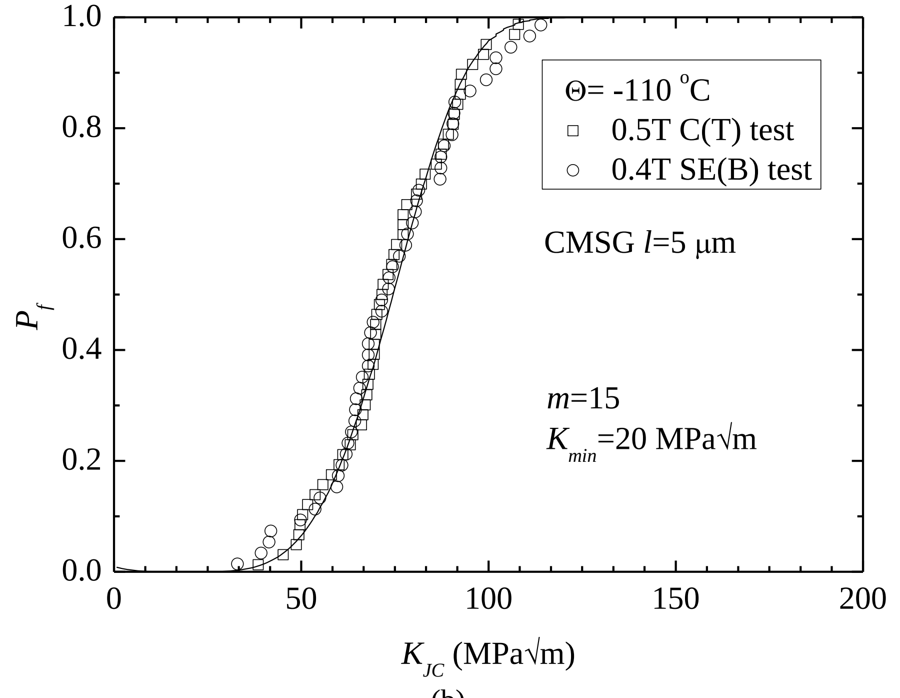
1.0
0.8
0.6
0.4
0.2
0.0
P_f
0
50
100
150
200
K_{JC} (MPa√m)
Θ= -110 °C
□ 0.5T C(T) test
○ 0.4T SE(B) test
CMSG l=5 μm
m=15
K_{min}=20 MPa√m

(b)

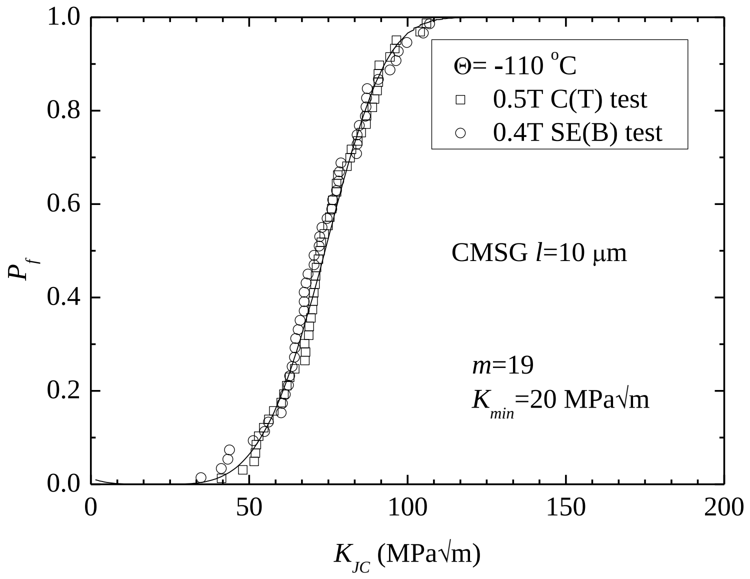

(c)

Figure 4.15 The comparison between the constraint-scaled fracture toughness data at $\Theta = -110\ ^{\circ}\mathrm{C}$ and the probability prediction by the Weibull stress model (a) Classical plasticity; (b) CMSG plasticity theory with $l = 5\ \mu\mathrm{m}$; and (c) CMSG plasticity theory with $l = 10\ \mu\mathrm{m}$

4.7.2 Calibration using interpolated material property at -110 °C

The available stress-strain data for Euro steels (22 Ni-MoCr37) from [73] covers the DBT transition temperature from $-20\ ^{\circ}\mathrm{C}$ to $-154\ ^{\circ}\mathrm{C}$ and now is plotted in Figure 4.16. The

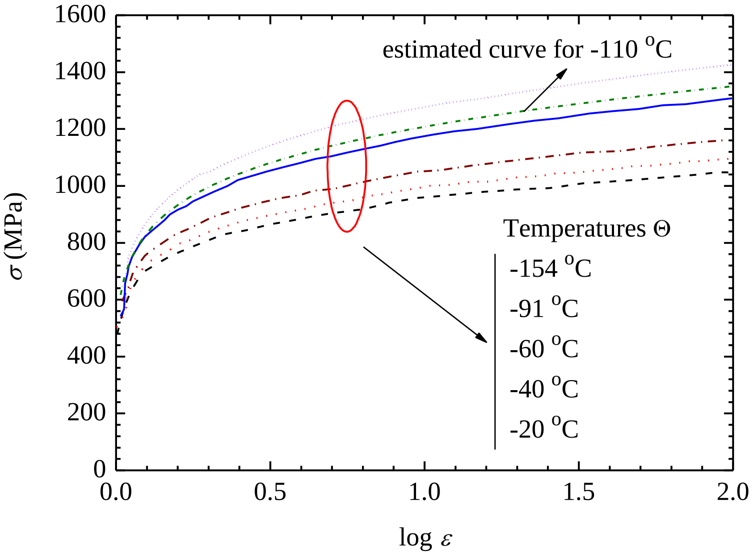

Figure 4.16 Euro-steel true stress-strain curves at different temperatures

yield stress at $-110\ ^{\circ}\mathrm{C}$ is computed from the yield stress vs. temperature function reported by Walllin [74],

$$\sigma_y = 450 + 1294 \times \exp\left[-0.0147 \times \Theta(K)\right] \tag{4.2}$$

According to this equation, the yield stress at $-110\ ^{\circ}\mathrm{C}$ is about 567 MPa and 5% higher than that at $-91\ ^{\circ}\mathrm{C}$. The hardening exponent interpolated between the values of the hardening exponent at $-91\ ^{\circ}\mathrm{C}$ and $-154\ ^{\circ}\mathrm{C}$ is around 0.16. Based on the hardening power law in Equation (2.36), the true stress-strain curve for Euro steels (22 Ni-MoCr37) at $-110\ ^{\circ}\mathrm{C}$ can be estimated as shown in Figure 4.16. In this section, the estimated material property is used to re-calibrate the Weibull parameters at $-110\ ^{\circ}\mathrm{C}$.

Figures 4.17 (a) and (b) compare the Weibull stress computed based on material curves at $-110\ ^{\circ}\mathrm{C}$ and $-91\ ^{\circ}\mathrm{C}$ for 1T SSY model and 0.5T C(T) model. The Weibull stress curve computed from $\Theta = -110\ ^{\circ}\mathrm{C}$ is around 2%-5% higher than that from $\Theta = -91\ ^{\circ}\mathrm{C}$, while the load-constraint function as shown in Figure 4.17 (c) from both temperature are slightly different, therefore produce the similar Weibull parameters.

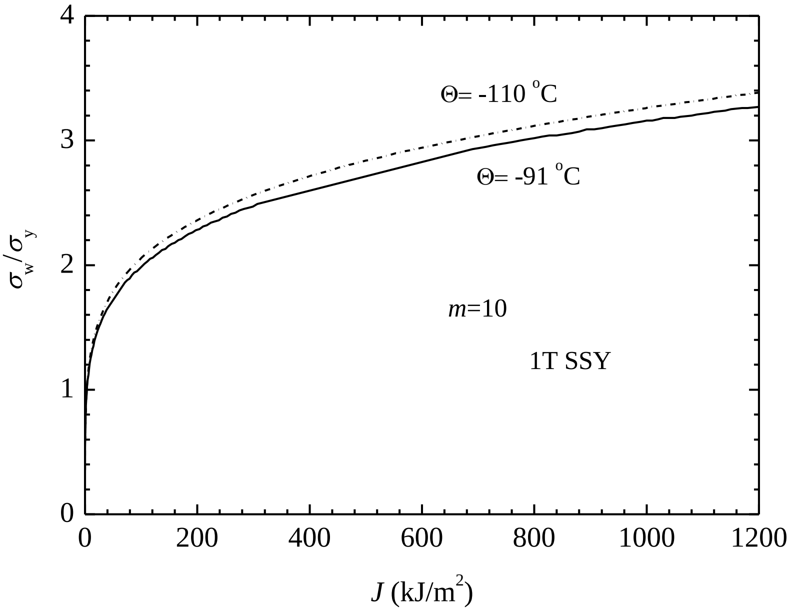

(a)

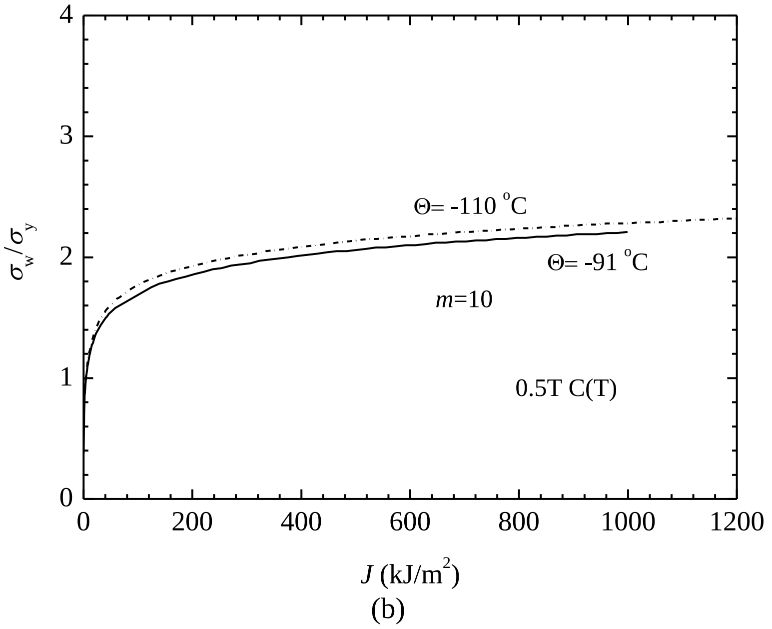

(b)

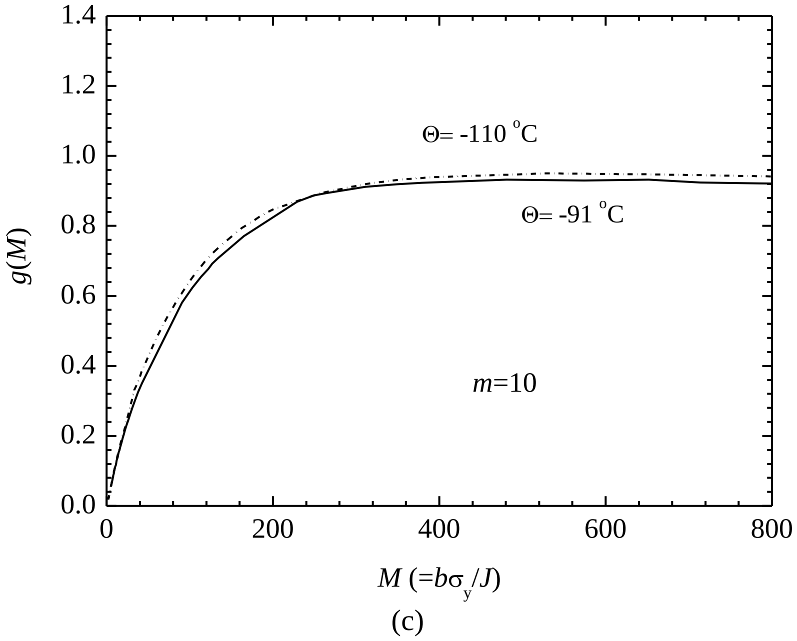

(c)

Figure 4.17 The evolution of σ_w and the constraint-correction function computed using the CMSG plasticity (a) σ_w for MBL models; (b) σ_w for 0.5T C(T); and (c) Constraint-correction $g(M)$ for C(T) at $\Theta = -91^{\circ}\mathrm{C}$ and $-110^{\circ}\mathrm{C}$

Figures 4.18 (a) and (b) show the error distribution curves computed using the interpolated stress-strain curve at $\Theta = -110\ ^{\circ}\mathrm{C}$. We also find the calibrated Weibull modulus and K_{min} are also similar as that using stress-strain curve at $\Theta = -91\ ^{\circ}\mathrm{C}$. The two parameters computed from classical plasticity are around 15 for m and 23 $\text{MPa}\sqrt{\text{m}}$ for K_{min}. Weibull moduls m equal 19 and K_{min} equal 23 $\text{MPa}\sqrt{\text{m}}$ from the CMSG plasticity analyses using the interpolated stress-strain curve for $\Theta = -110\ ^{\circ}\text{C}$.

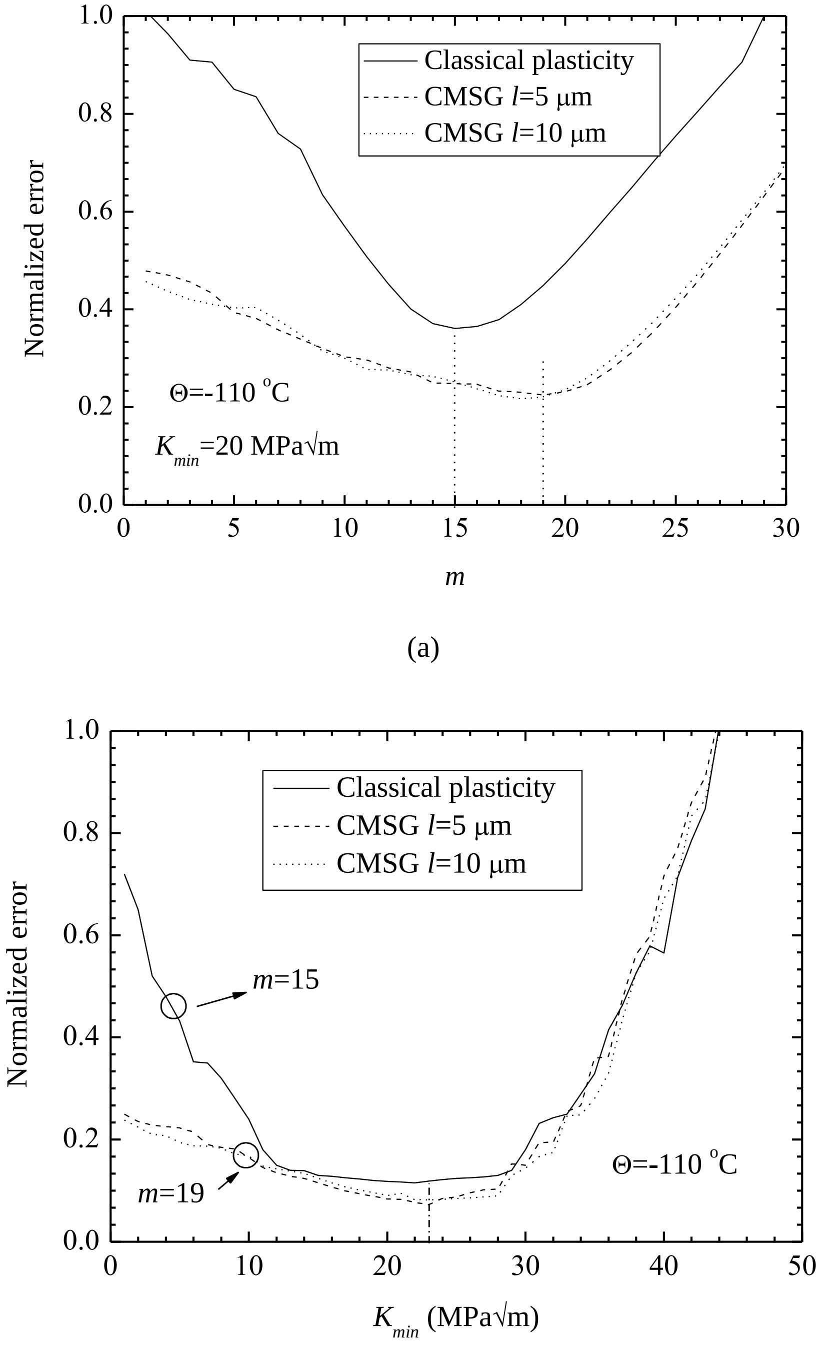

(a)

(b)

Figure 4.18 The variation of the normalized calibration error with respect to the m values and the K_{min} values for fracture toughness data measured at $\Theta = -110\ ^{\circ}\text{C}$ (a) m values; (b) K_{min} values using the interpolated material curve for $\Theta = -110\ ^{\circ}\text{C}$

Figures 4.19 (a-c) plot both the fracture probability curves using the material curve at $\Theta = -110\ ^{\circ}\mathrm{C}$ and $\Theta = -91\ ^{\circ}\mathrm{C}$, the fracture probability curves from both temperatures are also slightly different. Therefore, using the material stress-strain curve at $\Theta = -91\ ^{\circ}\mathrm{C}$ to calibrate the Weibull parameters does not affect the calibrated results significantly.

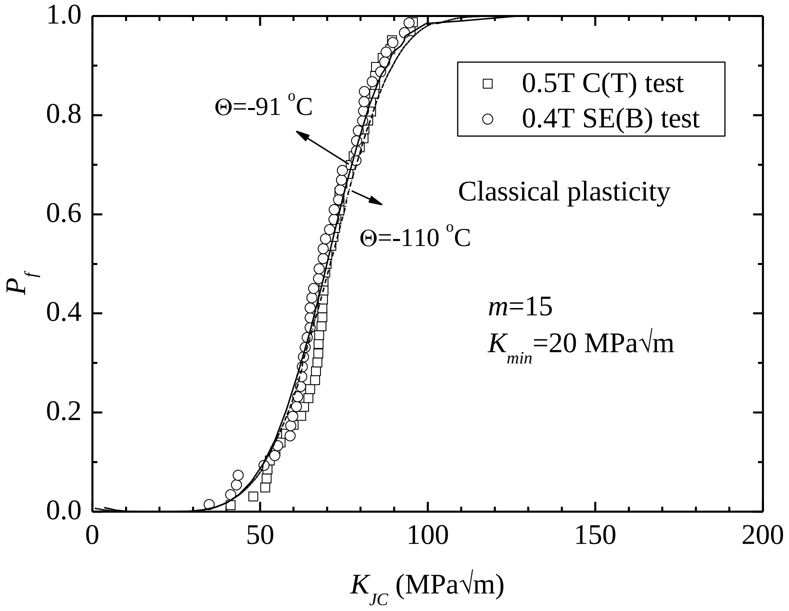

(a)

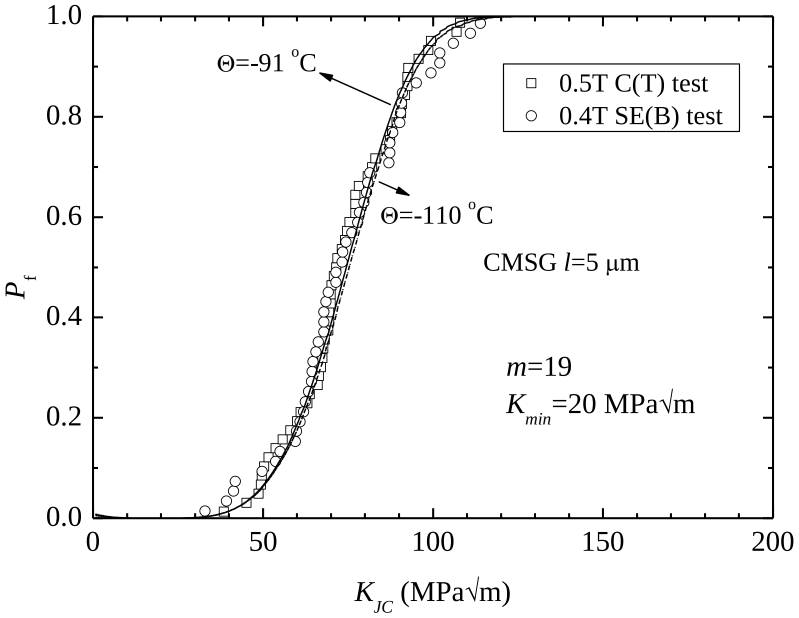

(b)

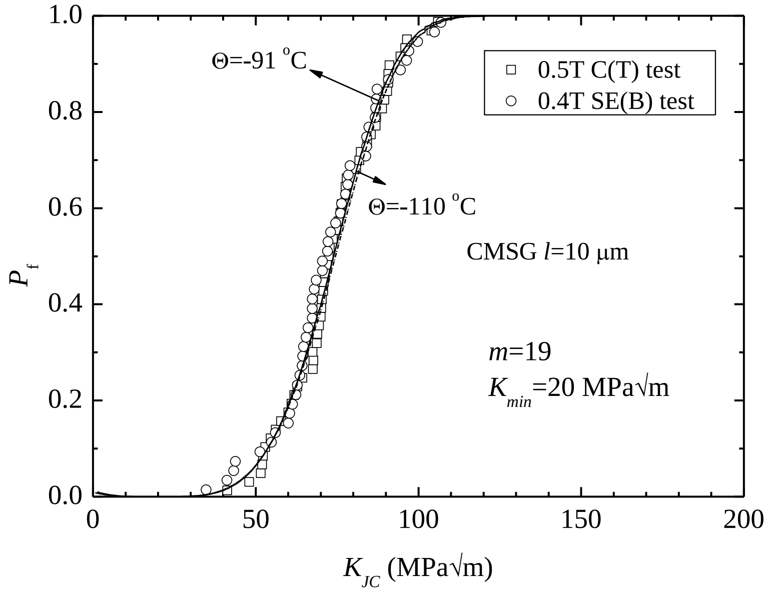

(c)

Figure 4.19 The comparison between the constraint-scaled fracture toughness data at $\Theta = -110\ ^{\circ}\mathrm{C}$ and the probability prediction by the Weibull stress model using the material curves from $\Theta = -91\ ^{\circ}\mathrm{C}$ and $-110\ ^{\circ}\mathrm{C}$ (a) Classical plasticity; (b) CMSG plasticity theory with $l = 5\ \mu\mathrm{m}$; and (c) CMSG plasticity theory with $l = 10\ \mu\mathrm{m}$

4.8 Discussions

The Weibull stress model, described by Equation (2.9), provides a unified approach to predict the cumulative probability of cleavage fracture for crack fronts under both high plasticity constraints and low plasticity constraints. The CMSG plasticity theory provides the much-needed description of the micro scale hardening of the material well within the plastic zone around the crack tip. The inclusion of the CMSG plasticity in the material constitutive description predicts increased σ_w values, and varies subsequently the calibrated Weibull material parameters, m and K_{min} compared to the conventional approach based on the classical theory of plasticity. These variations lead consequently to a different estimate of the cumulative probability of fracture, based on the microscopic crack driving force σ_w.

This section compares the probability of fracture estimated using the Weibull stress model based on the classical theory of plasticity and that based on the CMSG plasticity theory for two realistic situations: 1) an assumed m value, and 2) the calibrated m values, both utilizing the calibrated K_{min} values. The first case corresponds to a practical situation where insufficient experimental data is available to support the calibration of the Weibull parameters m, while the second case exemplifies a situation where extensive experimental data are available to calibrate the m value using both the CMSG plasticity and the classical plasticity theories.

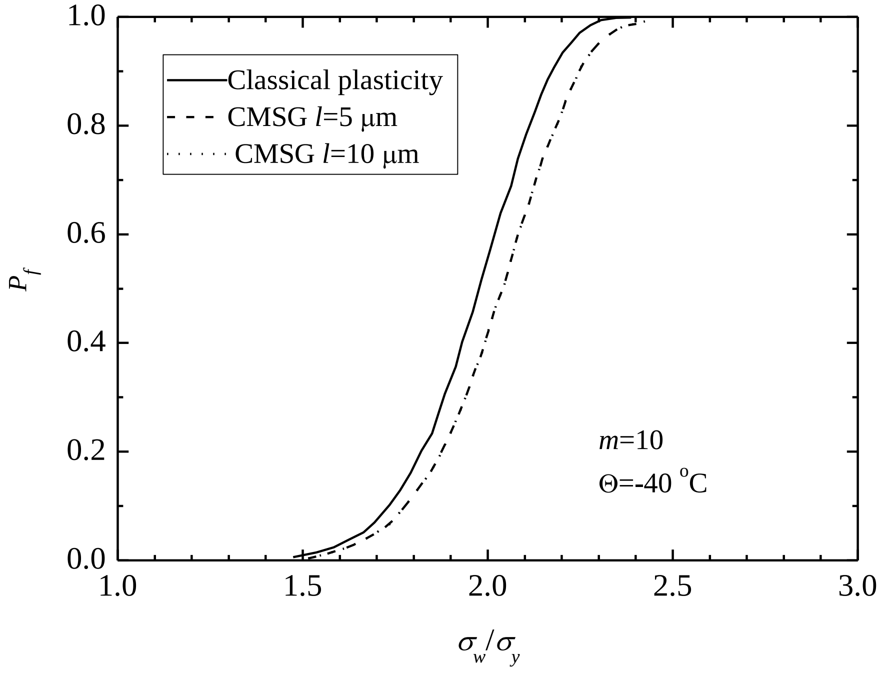

(a)

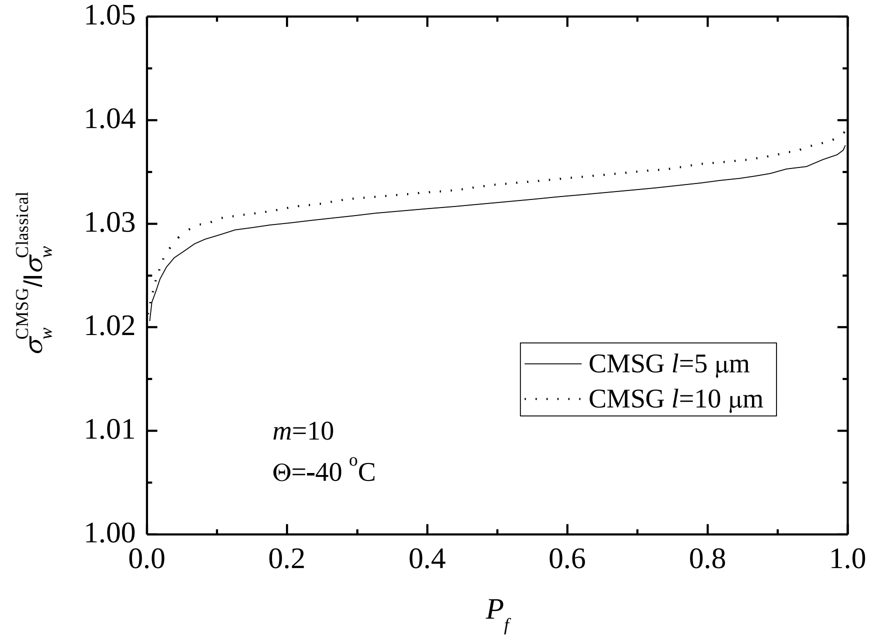

(b)

Figure 4.20 The cumulative probability of fracture and the ratio of $\sigma_w^{CMSG} / \sigma_w^{Classical}$ (a) Fracture probability by the classical plasticity and the CMSG plasticity theories using m =10; (b) Ratio of $\sigma_w^{CMSG} / \sigma_w^{Classical}$ corresponding to the same P_f in (a)

Figure 4.16(a) shows the cumulative probability of fracture, P_f , with respect to the microscopic crack driving force, σ_w, computed from Equation (2.9) using the σ_u and σ_w values determined from the classical plasticity and the CMSG plasticity theory at $\Theta = -40$ °C for a common Weibull modulus, $m = 10$. The P_f values for the CMSG plasticity with two material length scales, $l = 5$ μm and 10 μm, show very close predictions, but considerable differences compared to the P_f value based on the classical plasticity theory. Figure 4.16(a) implies that the classical plasticity theory yields a higher probability of fracture than the CMSG plasticity for the same microscopic crack driving force, σ_w. However, the CMSG plasticity often leads to a more than 10% higher estimate on the Weibull stress values than does the classical theory of plasticity, at the same macroscopic crack driving force (J), as shown in Figure 4.5. Figure 4.16(b) illustrates the ratio of the σ_w value computed from the CMSG plasticity theory over the σ_w value calculated using the classical plasticity to predict the same cumulative probability of fracture, P_f . The same probability of cleavage fracture failure requires the σ_w value computed by the CMSG plasticity theory to exceed the σ_w value based on the classical plasticity by 2-4%. However, the CMSG plasticity theory leads to an increased Weibull stress magnitude by more than 10% compared to the classical theory of plasticity under the same crack-opening loading, J , for $m = 10$, as shown in Figure 4.5. The Weibull stress model based on the CMSG plasticity theory, therefore, leads to an increased probability of fracture compared to that based on the classical plasticity with the same Weibull modulus, *m*, for fracture specimens subjected to the same macroscopic crack-opening load, J .

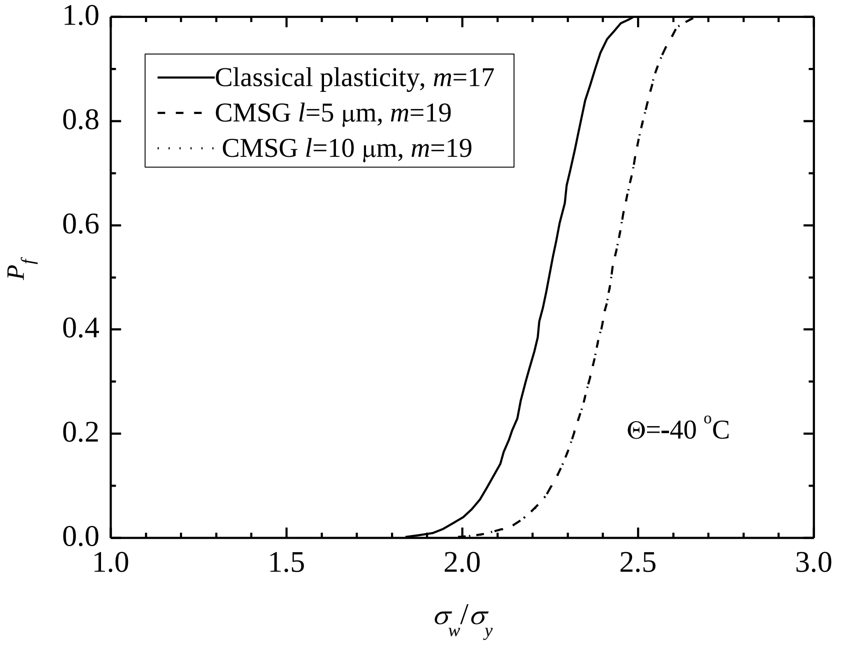

(a)

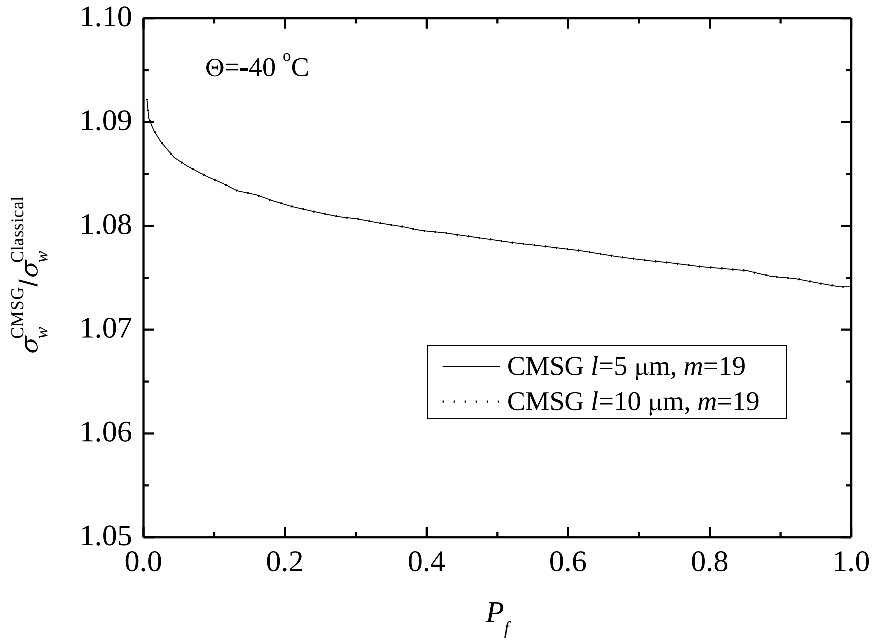

(b)

Figure 4.21 The cumulative probability of fracture and the ratio of $\sigma_w^{CMSG} / \sigma_w^{Classical}$ (a) Fracture probability by the classical plasticity and the CMSG plasticity theories using the calibrated *m* values; (b) Ratio of $\sigma_w^{CMSG} / \sigma_w^{Classical}$ corresponding to the same P_f in (a)

Figure 4.17(a) shows the predicted cumulative probability of cleavage fracture using Equation (2.9) based on the calibrated m values for the classical plasticity ($m = 17$) and the CMSG plasticity theory ($m = 19$) at $\Theta = -40\ ^{\text{o}}\text{C}$. Equal probabilities of failure require the σ_w values computed using the CMSG plasticity theory (with $m = 19$) to exceed those calculated from the classical plasticity (with $m = 17$) by 7-10%, as shown in Figure 4.17(b). The material hardening following the CMSG plasticity constitutive model description ($m = 19$), however, leads to an 18-25% increase in the σ_w values compared to the σ_w values based on the classical plasticity ($m = 17$), computed from an MBL model under a zero *T*-stress (see Table 4.3). These pronounced increases in the σ_w values caused by the strain-gradient dependent material hardening lead to a considerably higher cumulative probability of fracture than the P_f value predicted based on the classical plasticity, when implemented in the P_f - σ_w curve with a very sharp slope as shown in Figure 4.17(a). At temperature $\Theta = -20\ ^{\mathrm{o}}\mathrm{C}$ and $\Theta = -110\ ^{\mathrm{o}}\mathrm{C}$, we also obtain the similar trends that the Weibull stress computed from CMSG plasticity (with $m = 19$) is around 7%-10% higher than that computed from classical plasticity (with $m = 19$) at the same fracture probability as shown in Figure 4.18 (a) and (b). However, the Weibull stress based on CMSG plasticity is almost 14%-20% (for $\Theta = -20\ ^{\mathrm{o}}\mathrm{C}$) and 28%-50% (for $\Theta = -110\ ^{\mathrm{o}}\mathrm{C}$) higher than that computed from classical plasticity based on the calibrated *m* value at the same load. Therefore, if we consider the strain gradient effect, a higher fracture probability can be achieved.

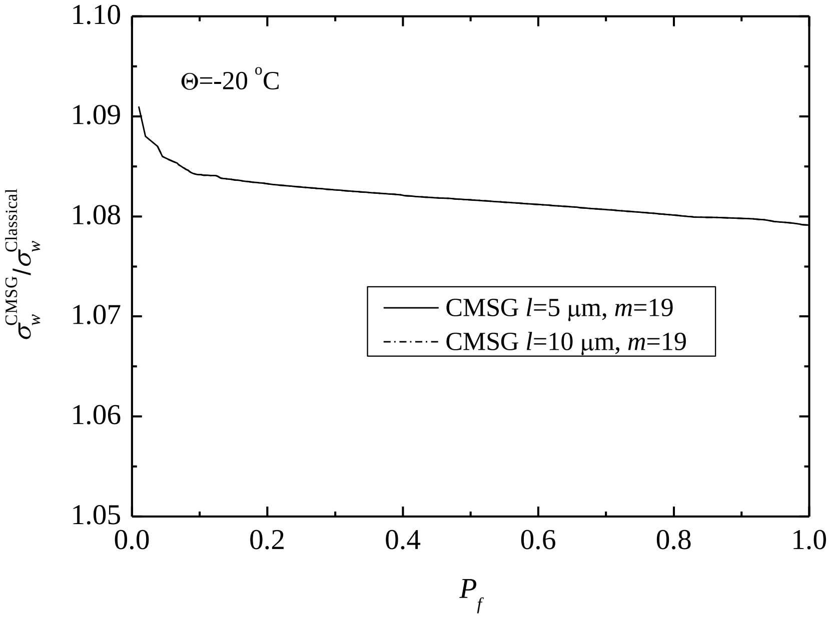

(a)

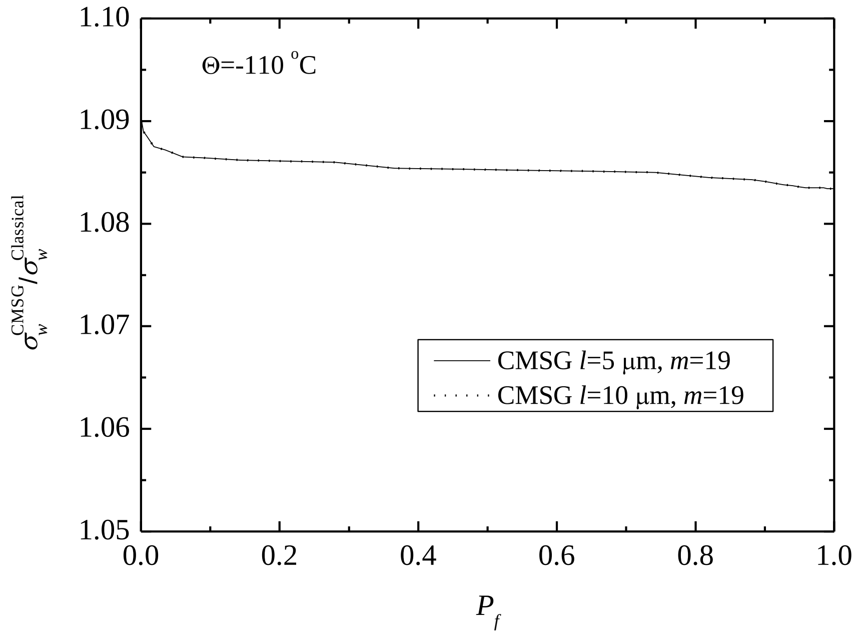

(b)

Figure 4.22 The cumulative probability of fracture and the ratio of $\sigma_w^{CMSG} / \sigma_w^{Classical}$ using the calibrated *m* values; (a) Θ =-20 °C (b) Θ =-110 °C

4.9 Summary and Conclusion

This study recalibrates the Weibull modulus *m* and the threshold fracture toughness K_{min} in a three-parameter Weibull stress model for the 22-Ni-MoCr37 steel tested in a five-year European Union project involving 11 countries [8]. The calibration exercise utilizes more than 220 fracture toughness data measured at three temperatures over the ductile-to-brittle transition regime: $\Theta = -20\ ^{\circ}\mathrm{C},\ -40\ ^{\circ}\mathrm{C},\ \text{and}\ -110\ ^{\circ}\mathrm{C}$. The calibration procedure, following a similar approach presented by Wasiluk *et al.* [24], examines the effect of strain hardening caused by the plastic deformations at microscopic levels through the CMSG plasticity theory, implemented in the C^0 solid element formulation [5]. The results presented above support the following conclusions:

(1) The strain-gradient dependent material hardening described by the CMSG plasticity theory leads to significant increases in the Weibull stress magnitudes compared to the predictions based on the classical plasticity for fracture specimens under the same macroscopic crack-opening load, J. The implementation of the CMSG plasticity theory in the calibration procedure generates slightly larger values of the Weibull modulus, m, than the values calculated using the classical theory of plasticity. The threshold fracture toughness value, K_{min}, which generates a very small plastic zone around the crack tip, in contrast, exhibits very little dependence on the material strain hardening properties.

(2) This study assumes two typical values of the material length scales, $l = 5$ μm and $l = 10$ μm, in the CMSG plasticity theory for the calibration of Weibull stress parameters. Both the magnitudes of the Weibull stress and the calibrated m and K_{min} values indicate hardly noticeable dependence on these two values of the material length scales. Hence, it can be deduced that any material length scales that between $l = 5$ μm and $l = 10$ μm, e.g., $l = 7$ μm should produce the similar magnitudes of Weibull stress, Weibull modulus and minimum fracture toughness K_{min}.

(3) The crack front constraints, characterized by the elastic *T*-stresses impose a strong effect on the magnitude of the Weibull stresses, especially for crack fronts experiencing low plasticity constraints. The non-proportional loading and proportional loading cause significant differences in both the Weibull stress values and the constraint-correction function. An accurate estimation of the Weibull stress, based on the MBL model, thus requires an accurate evaluation of the biaxiality ratio ($\beta = T\sqrt{\pi a}K_I$) near the crack tip.

(4) The calibrated Weibull modulus, *m*, based on the CMSG plasticity theory, shows the same value $m = 19$ for all three temperatures considered. The temperature

independence of the *m*-value asserts that the magnitude of *m* characterizes the distribution of the micro crack sizes in the material, which should not rely on the environmental temperature. This study also confirms the temperature dependence of the threshold fracture toughness, K_{min} , which shows a substantially lower calibrated value at $\Theta = -110\ ^{\circ}\mathrm{C}$ than the K_{min} value calibrated at $\Theta = -40\ ^{\circ}\mathrm{C}$ or $\Theta = -20\ ^{\circ}\mathrm{C}$.

(5) The calibrated Weibull stress model, shown in Equation (2.9), predicts a higher probability of fracture for materials exhibiting strain-gradient dependent material hardening than the P_f value for materials following the classical plasticity theory for a macro crack under the same opening load measured by the domain integral, J , if the same Weibull modulus m is assumed or if the calibrated *m* values are used.

The values of material length scale are assumed to be 5 and 10 μm in this chapter. They are common values of the materials length scale for the metallic materials. The more accurate values of the material length scale for the structural steel studied in this thesis will be quantified through the indentation tests described in Chapter 5.

CHAPTER 5 MATERIAL CHARACTERIZATION OF STRUCTURAL STEELS

5.1 Introduction

By assuming the values of the material length scale for the structural steels, Chapter 4 has demonstrated that the plastic strain gradient can significantly increase the magnitudes of the Weibull stress curves and predict high fracture probability. As the material length scale for the structural steels is currently not available, it is necessary to find the material length scale of the structural steels through the indentation tests which have been popularly used for characterizing the material properties of the metals and metallic alloys [70, 75-79]. This chapter attempts to evaluate the appropriate values of the material length scale of two commonly used structural steels for offshore structures (S355 and S690) at different temperatures through the indentation tests and the corresponding simulations by the CMSG plasticity theory. As the indentation test at temperatures below the room temperature is not feasible in Singapore due to the constraint in the experimental setting up. Therefore, the indentation tests are performed at two different temperatures (20 ^{o}C and 300 ^{o}C) to examine the effect of temperature on the variation of the material length scales. In the simulations of indentation tests by the CMSG plasticity theory, three mechanical properties parameters, the Young's modulus E, the hardening exponent N and the yield stress σ_y are determined from the uni-axial tensile tests at the two temperatures (20 ^{o}C and 300 ^{o}C). The uni-axial tensile test at –40 ^{o}C and corresponding simulations of indentation test are also performed for future study.

5.2 Uniaxial Tensile Test for S355 and S690 at Three Temperatures

5.2.1 Sample Preparation

In the uni-axial tensile tests, the S355 coupon specimens are fabricated from a circular hollow section member with an outer diameter of 406 mm and wall thickness of 12.5 mm. The specimens for S690 are cut from a plate with the thickness of 12 mm. At each temperature, three specimens are prepared for each types of steel. The gauge length (60 mm) of all the specimens are in accordance with ASTM E8 [80] as shown in Figure 5.1. At temperature 300 ^{o}C, the specimens are designed as shown in Figure 5.1(b) longer than those for room temperature (20 ^{o}C) tests in Figure 5.1(a) for heating the specimen by the high temperature Instron Severn-Furnace-Limited (SFL) furnace presented in Figure 5.2. Due to space limitation between the two legs of the clevis, the thickness of the specimen is kept as 12 mm. The strain gauges are used to measure the engineering strain for tests at room temperature while the extensometer with the gauge length of 25 mm is used to measure the elongation of the materials at 300 ^{o}C since most of the strain gauges are unable to measure the strain at 300 ^{o}C, only the extensometer with the gauge length of 25 mm is used to measure the elongation of the materials at 300 ^{o}C. In the heating process, the heating rate is set to 1 ^{o}C / min to heat the specimens to 300 ^{o}C and the temperature is held at 300 ^{o}C for 1 hour before conducting the tensile test.

The specimens for the tensile test at –40 ^{o}C are much shorter than those for 20 ^{o}C and 300 ^{o}C tensile tests (see Figure 5.1 (c)) due to the limitation in the height of the cold chamber which is around 56 cm high (see Figure 5.3) and the height of clevises which are totally around 24 cm high. The gauge length is also designed as the specimens for testing at room temperature. Also due to most of the strain gauges are unable to measure the strain at below –20 ^{o}C, only the extensometer with the gauge length of 50 mm is used to measure the elongation of the materials at –40 ^{o}C. In the cooling process, the cooling rate is set to 1 °C / min to cool the specimens to –40 °C and the temperature is held at –40 °C for 1 hour before conducting the tensile test. All the tensile tests are performed by the displacement rate of 0.1 mm/min.

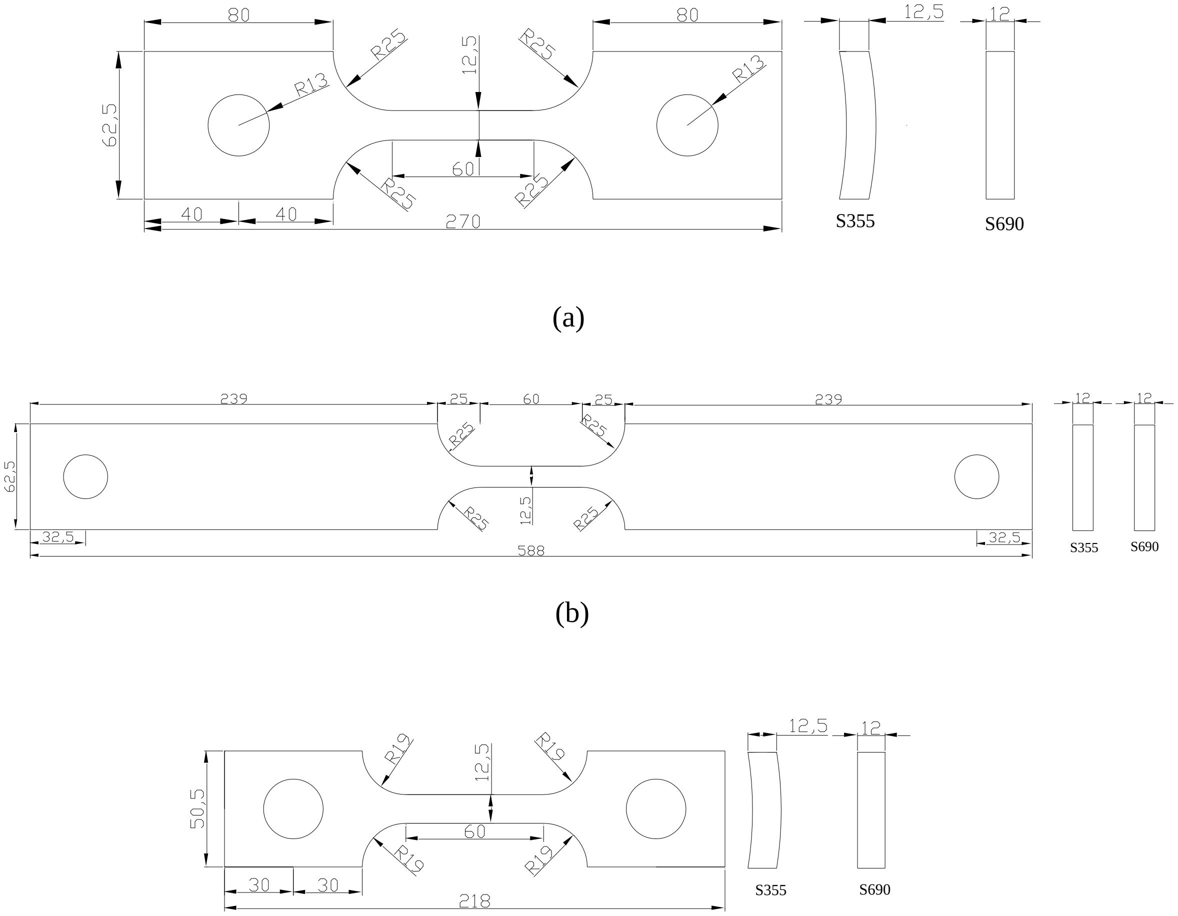

(a)

(b)

(c)

Figure 5.1 Samples S355 and S690 for uniaxial-tension test (a) 20 °C; (b) 300 °C; and (c) -40 °C

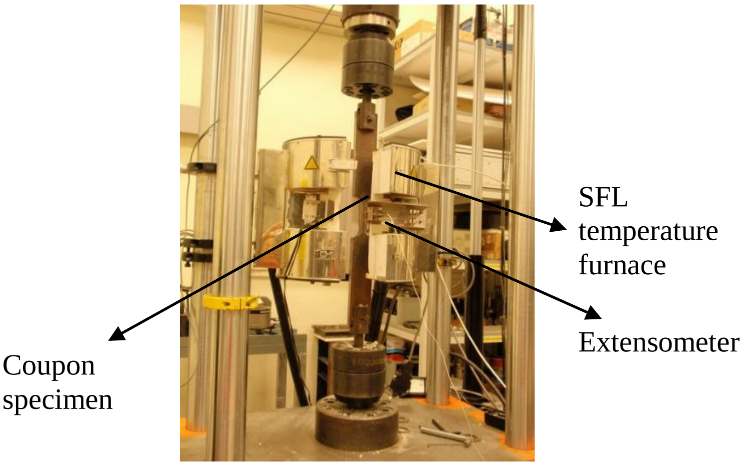

Figure 5.2 Instron SFL high temperature furnace for high temperature tensile test

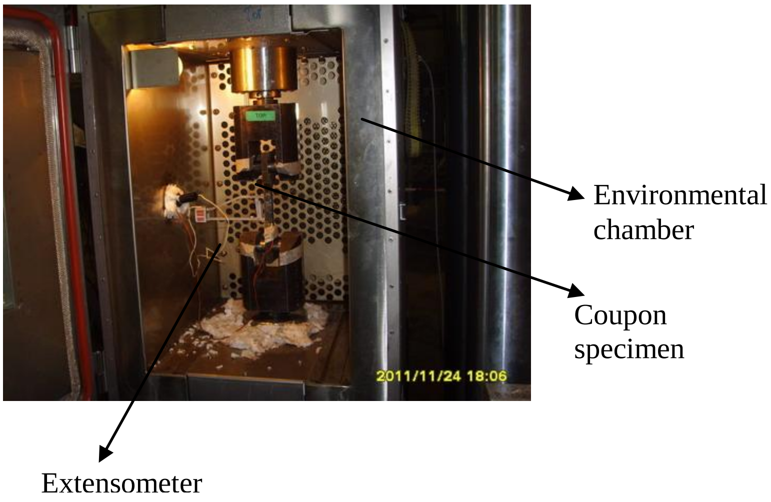

Figure 5.3 Environmental chamber for low temperature tensile test

5.2.2 Stress-Strain Curves from Coupon Tests

We use the average slope of the linear-elastic portion of the recorded engineering stress-strain curves to determine the Young's modulus and adopt the 0.2% offset method to determine the yield stress [80].

Figures 5.4(a) and 5.4(b) present the engineering stress-strain curves for S355 and S690 (20 ^{o}C, 300 ^{o}C, and –40 ^{o}C). The true stress-strain data are converted from engineering stress-strain data. The power law (Equation 2.36) is used to fit the hardening exponent N of the stress-strain data. Table 5.1 compiles the values of Young's modulus E, yield stress σ_y, and hardening exponent N for steel S355 and S690 at two different temperatures (20 °C and 300 °C). Apparently, the Young's modulus and yield stress decrease as the temperature escalates from –40 °C to 300 °C for both S355 and S690.

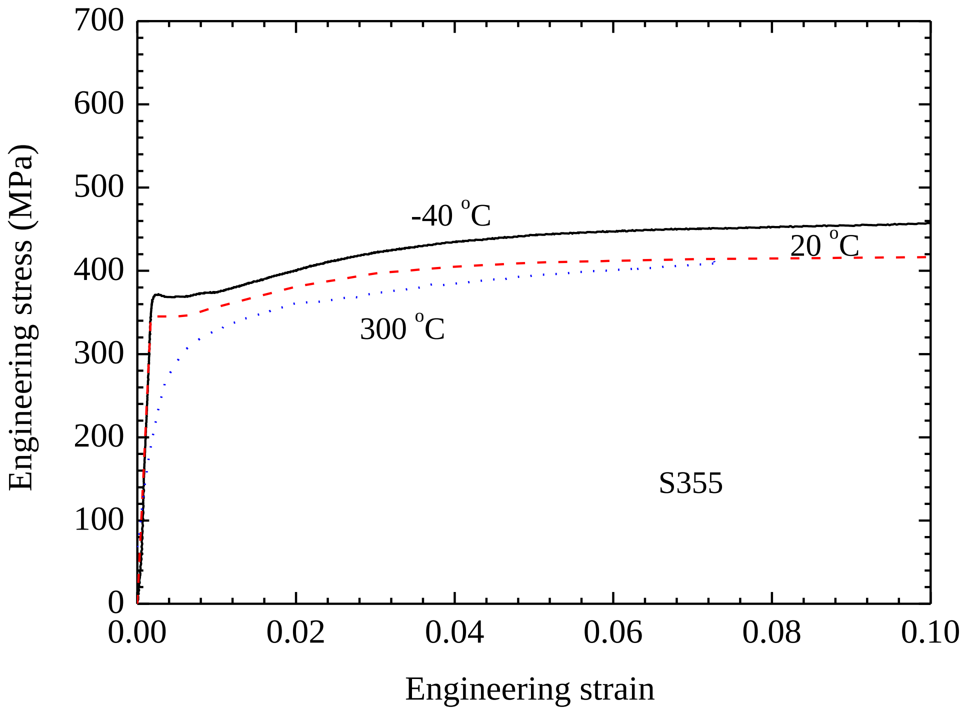

(a)

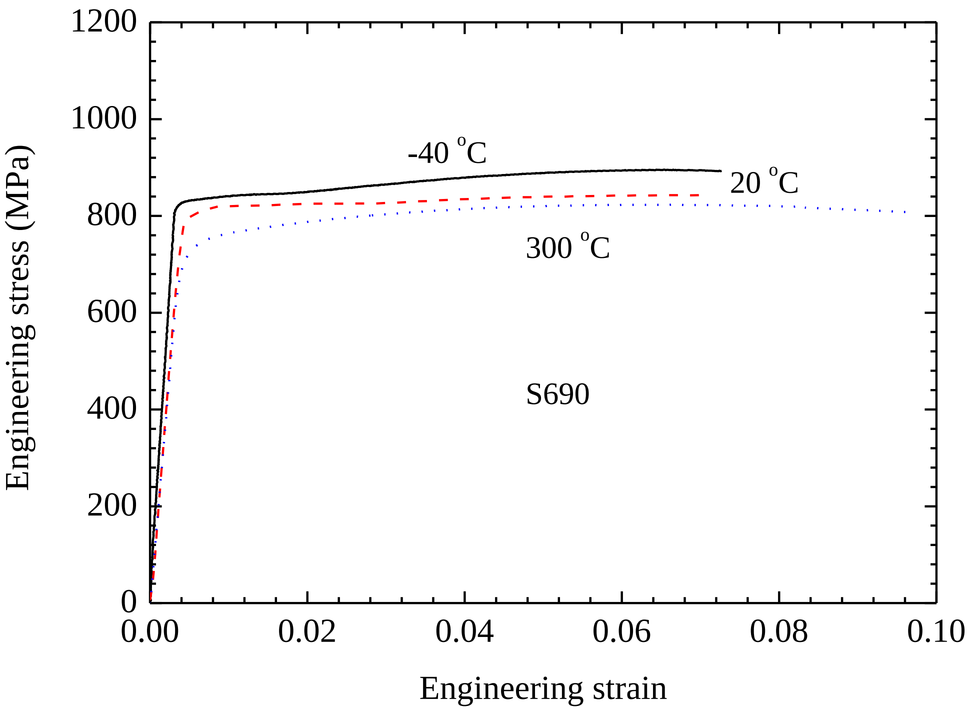

(b)

Figure 5.4 Uniaxial stress-strain curves for structural steels at temperatures –40 °C, 20 °C, and 300 °C (a) S355; (b) S690

Table 5.1 Material properties for S355 and S690 steels

Material	Temperature (°C)	Young's modulus E (GPa)	Yield stress σ_y (MPa)	Hardening exponent N
S355	–40	218	368	0.1
	20	203	345	0.1
	300	153	300	0.15
S690	–40	231	830	0.06
	20	200	760	0.07
	300	184	600	0.07

5.3 Indentation Tests for S355 and S690 at Temperatures 20 ^{o}C and 300 ^{o}C

5.3.1 Test Preparation

For the indentation tests, one sample is required for each type of steels S355 and S690. Each sample has to be polished before testing as the roughness of the surface can affect significantly the accuracy of the test results. The surfaces of the samples are firstly ground by sandpaper with the grit number of 500, 2400 and 4000, and then mechanically polished by 6 μm, 3 μm, and 1 μm diamond suspensions. Finally, 0.1 μm silica solution is used for final polishing. Figure 5.5(a) shows the samples for S355 and S690. Figure (b) is the indentation machine. Figure 5.5(c) illustrates the indented surface of the sample S355 obtained from the scanning electron microscope (SEM) machine. As the surface of steel sample can be oxide easily, the sample has to be re-polished just before the testing if it is left untested for a few weeks.

The MTS Nano-XP system with maximum loading capacity of 500 mN is used to indent S355 and S690 samples at room temperature (20 ^{o}C), while the compatible Agilent Nano Indenter G200 system is used for 300 ^{o}C test. For both systems, we use the standard Berkovich indenter with the tips of total angle of 142.3^{o} as shown in Figure 5.6(a) for all indentation tests. The corresponding finite element is depicted in Figure 5.6(b).

Each specimen is tested with five sets of indentation load rages (30 mN, 100 mN, 200 mN, 350 mN, and 500 mN) repeating ten times for each load level. The operation is carried out automatically once the first indentation location and spaces between two indentation positions are specified.

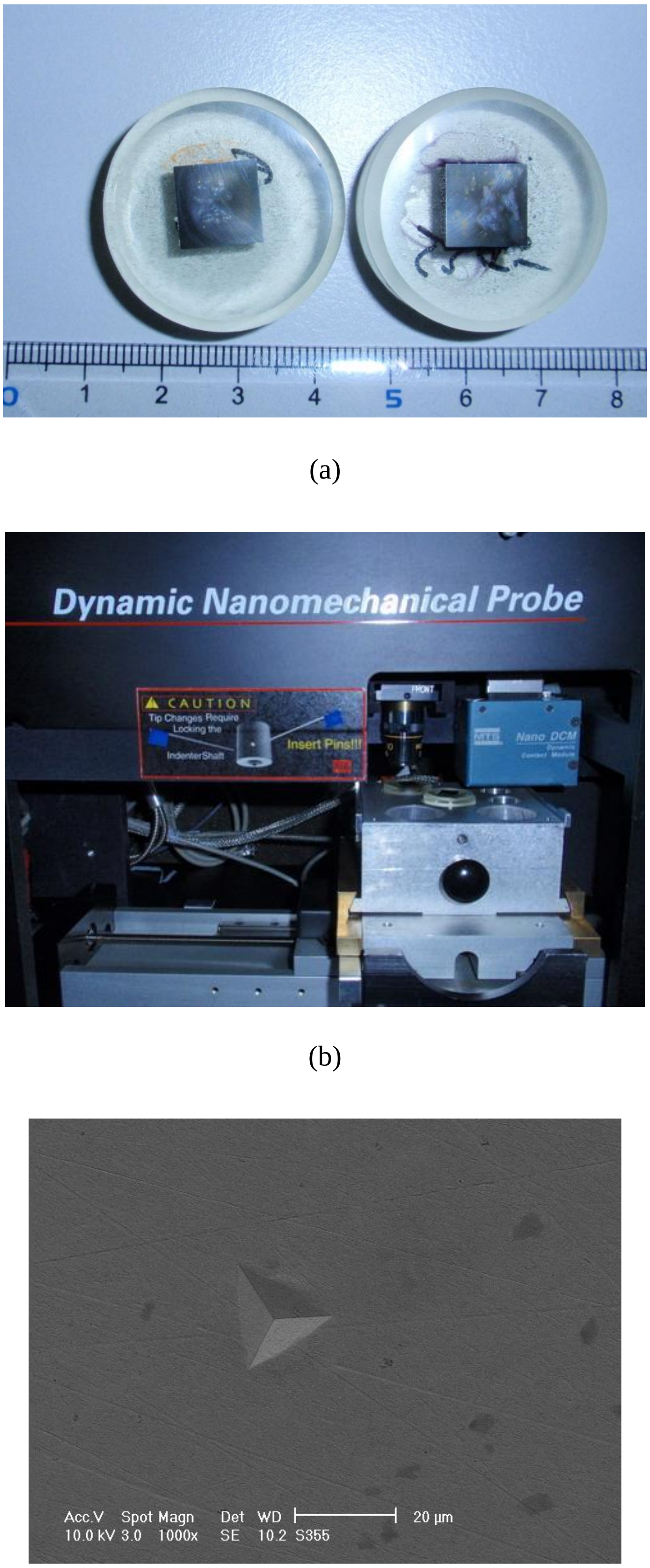

(a)

(b)

(c)

Figure 5.5 Indentation test samples and machine (a) Samples S355 and S690; (b) Indentation machine; (c) Indented surface of S355

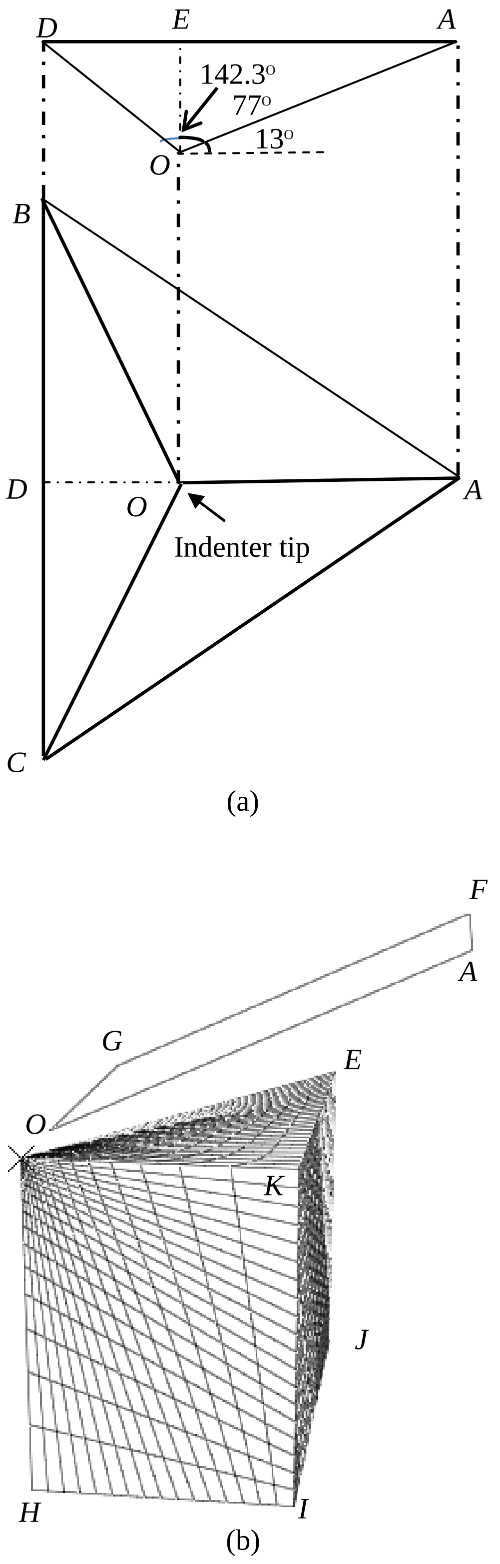

Figure 5.6 Schematics of Berkovich indenter and FE model (a) Geometry of indenter; (b) FE model for indentation test

5.3.2 Indentation Experimental Results and Simulations at 20 ^{o}C

The indentation load-displacement curves scatter as the indenter presses randomly either on the grain or its boundary and the indentation machine is incapable of identifying the surface property during the indentation. Simultaneously, as indentation depth is very small at micron level, variation of test results is unavoidable. A few curves in a set are normally deviated substantially from the majority of the curves at each lead level of indentation tests as shown in Figures 5.7 (a)-5.11(a) for S355 and Figures 5.12 (a)-5.16(a) for S690. In each set of data, we discard the outliners with maximum indentation depths deviating from the average value by two-standard-deviation method (i.e., only the data with 95% confidence interval are kept for further analyses). Only the remaining curves (about 10% of 10 sets of tested data) are presented as shown in Figures 5.7(b)-5.11(b) for S355 and 5.12(b)-5.16(b) for S690.

5.3.3 Numerical Analysis of Indentation Tests at Temperature 20 ^{o}C

As Berkovich indenter tip is a three-sided symmetric pyramid, only one-sixth of the problem is modelled and a rigid surface (one-sixth of the indenter tip) is adopted for the rigid indenter as illustrated in Figure 5.6. The angle between the rigid surface and the contacted surface of the material is 13^{o}. The analysis assumes no friction between the indenter and the target material during the indentation process. The material properties for S355 and S690 as tabulated in Table 5.1 are used in numerical simulations. The Young’s modulus for the indenter is 1100 GPa, and the effect of temperature variation on the Young’s modulus of the indenter is neglected. The finite element model as shown in Figure 5.6 contains 7600 20-node brick elements. The total number of the nodes is 33822. The minimum size of element in the contact region is around 2 nm. The finite deformation formulations are used in the simulations of the indentation tests.

At each load level, the finite element model is displacement-controlled load up to the average values of the maximum indentation depth of each set of test data. The maximum indentation depths for S355 are around 0.69, 1.4, 1.97, 2.69, and 3.26 μm at above five load levels.

The finite element simulated results based on both classical plasticity and CMSG plasticity theories with material length scales of $l = 5$, 7 and 10 μm at five different load levels are included in Figure 5.7(b)-5.11(b) . The CMSG simulations with the compare the material length scale of $l = 7$ μm seems to produce the load-displacement curves that are in close agreement with the experimental observations for S355 at all load levels under room temperature of 20 ^{o}C. Apparently, the classical plasticity theory underestimates the value of applied loads, especially at the indentation depths of micron or submicron level. This implies that classical plasticity is unable to capture the size effect of material hardening for indentation at micron level when finite elements incorporating strain gradient plasticity have to be adopted. It is observed that with the increasing of the indent depth, the difference between the CMSG plasticity results and the classical plasticity values decreases, implying that the size effect diminishes with the increasing indentation depth.

In the simulation of indentation tests on steel S690 at room temperature of 20 ^{o}C, the maximum indentation depth imposed on the finite element model are around 0.52, 1.03, 1.48, 2.04, and 2.45 μm at the five load levels, respectively. Figures 12(b)-16(b) also shows that the load-displacement curves from the CMSG plasticity analyses with the material length scale of $l = 7$ μm seems to match the experimental curves at almost all load levels..

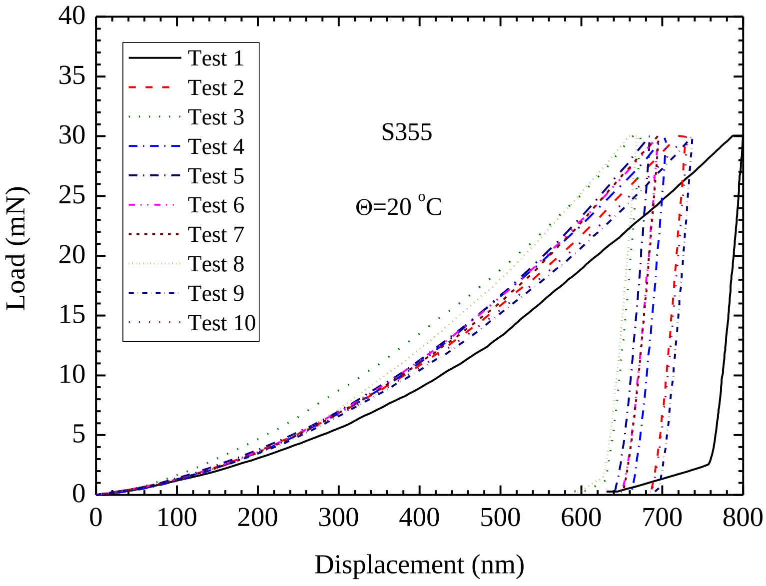

(a)

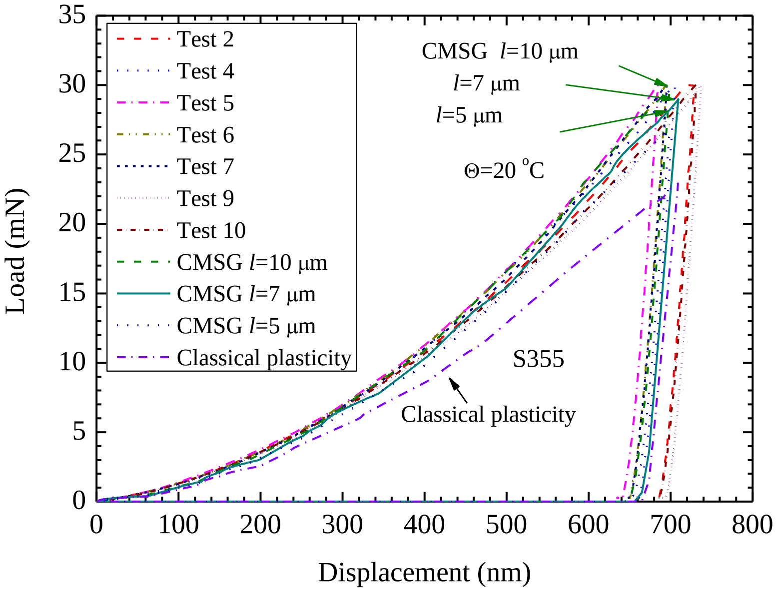

(b)

Figure 5.7 Load-displacement indentation curves for S355 with maximum load of 30 mN at 20 °C (a) Test results; (b) Comparison between FE and screened test results

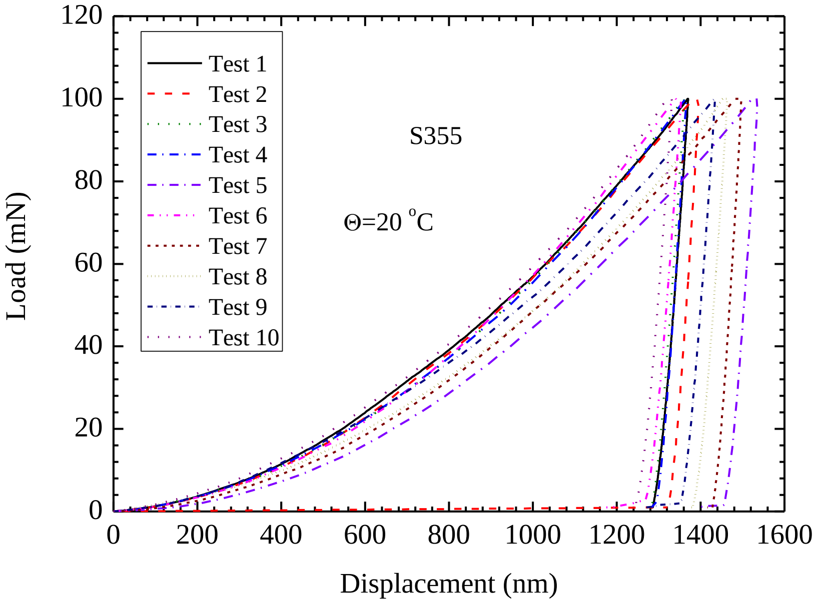

(a)

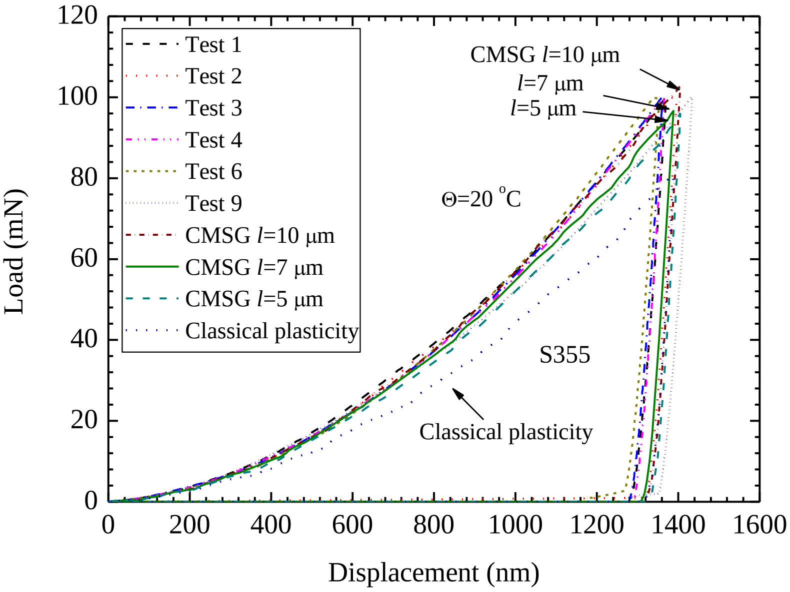

(b)

Figure 5.8 Load-displacement indentation curves for S355 with maximum load of 100 mN at 20 °C (a) Test results; (b) Comparison between FE and screened test results

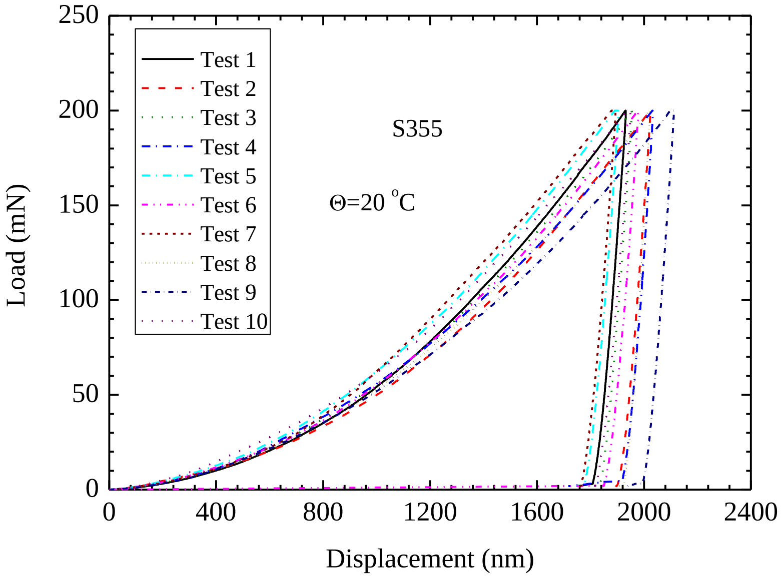

(a)

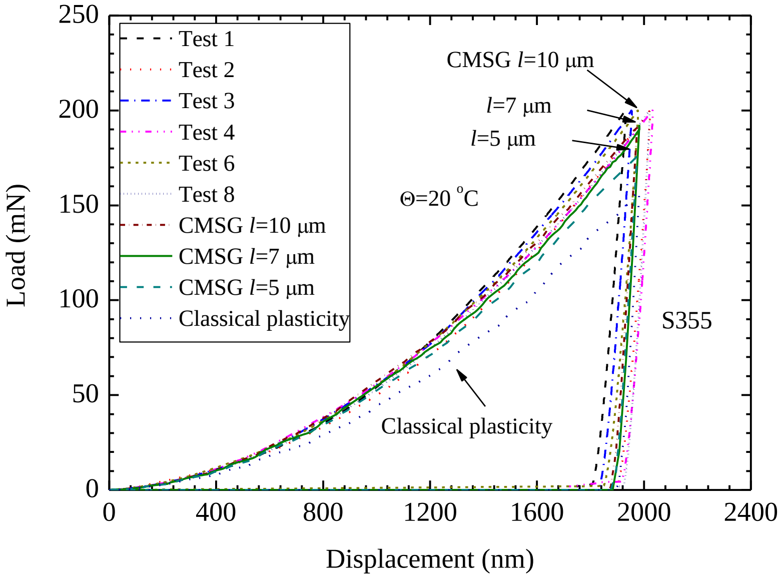

(b)

Figure 5.9 Load-displacement indentation curves for S355 with maximum load of 200 mN at 20 °C (a) Test results; (b) Comparison between FE and screened test results

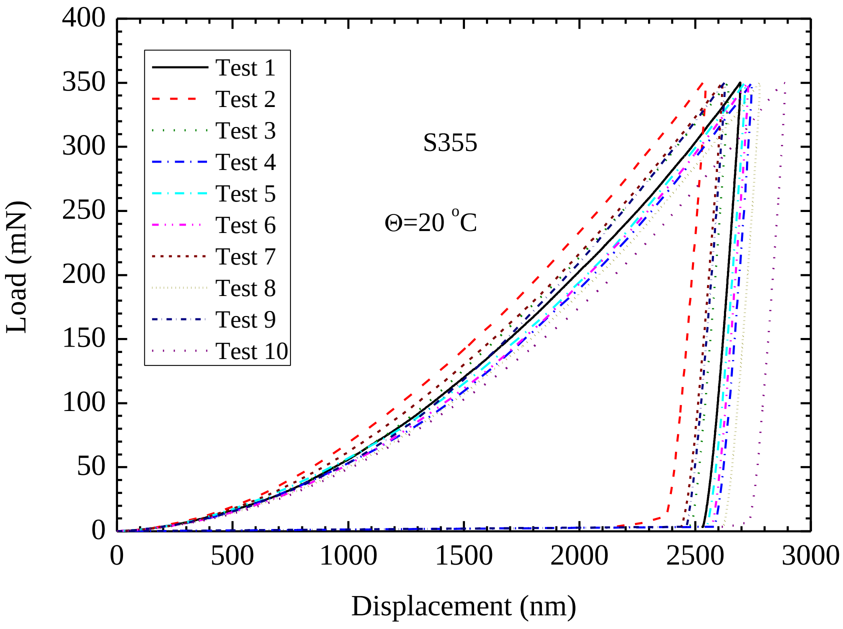

(a)

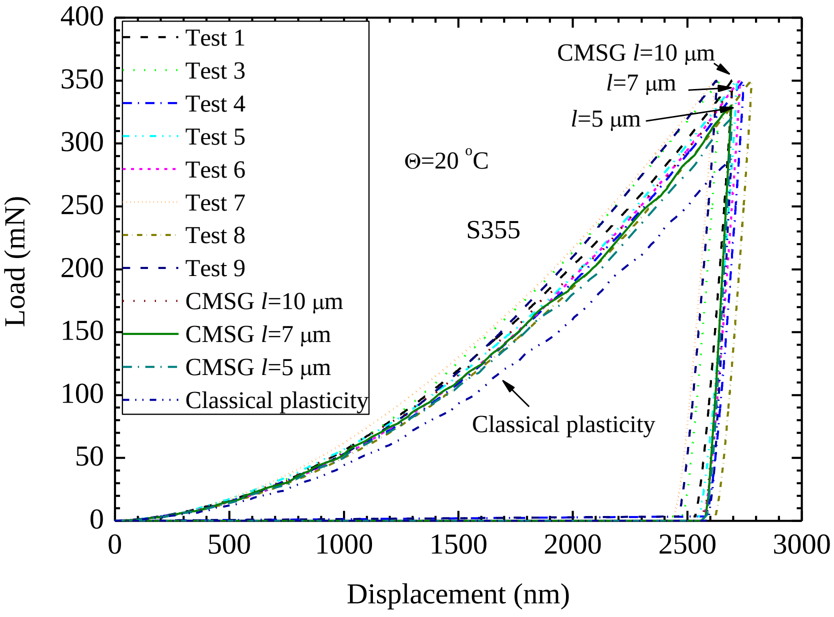

(b)

Figure 5.10 Load-displacement indentation curves for S355 with maximum load of 350 mN at 20 °C (a) Test results; (b) Comparison between FE and screened test results

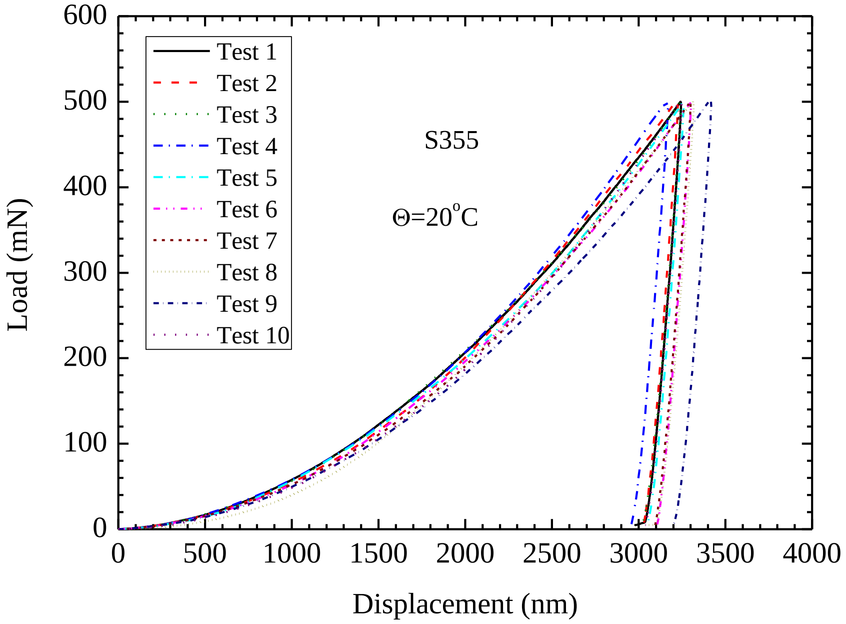

(a)

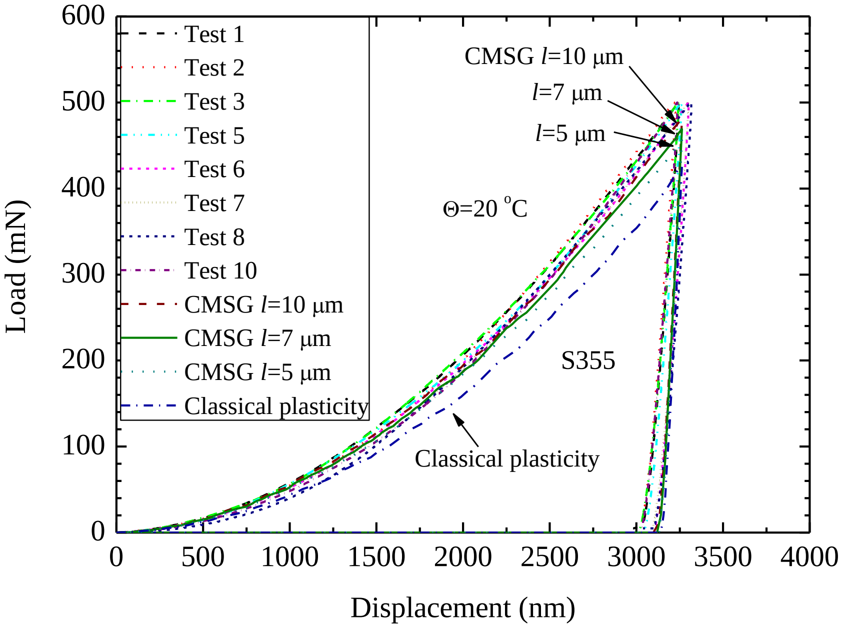

(b)

Figure 5.11 Load-displacement indentation curves for S355 with maximum load of 500 mN at 20 °C (a) Test results; (b) Comparison between FE and screened test results

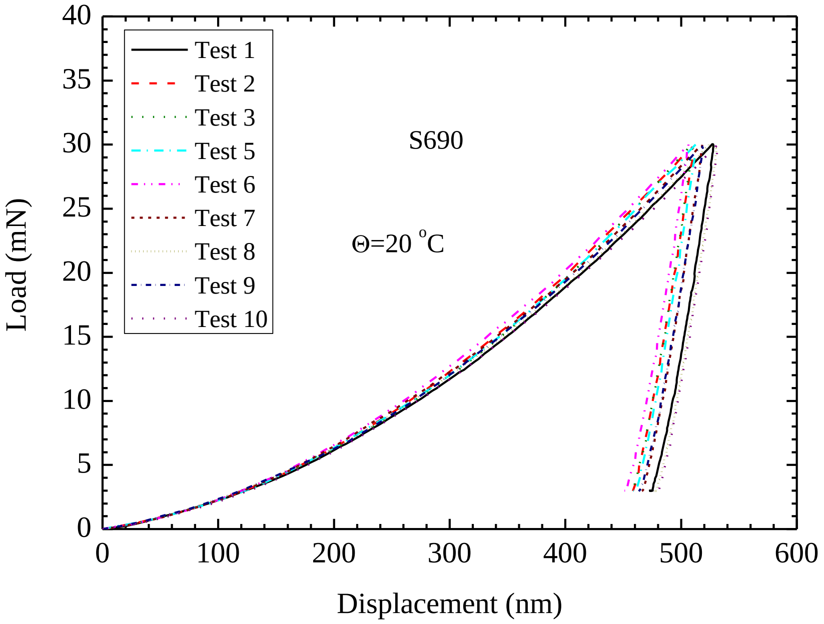

(a)

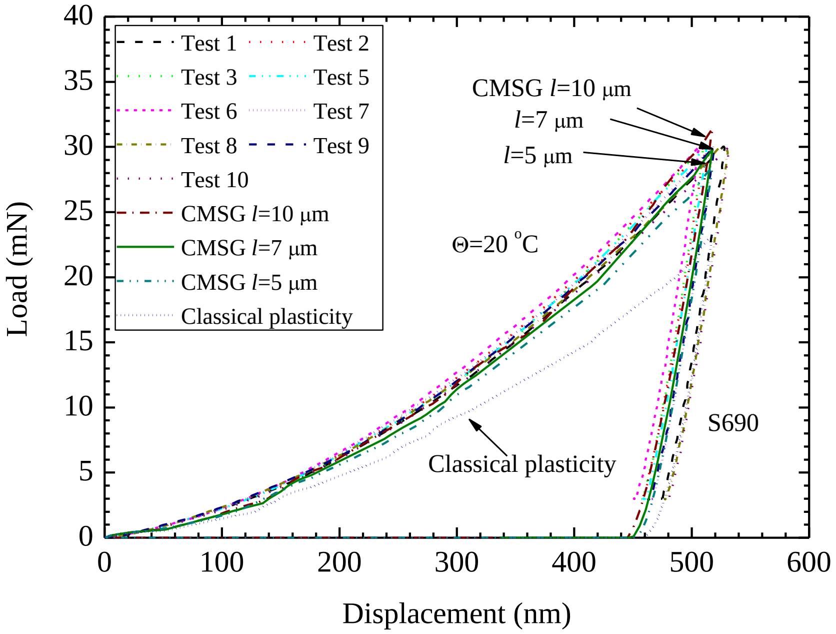

(b)

Figure 5.12 Load-displacement indentation curves for S690 with maximum load of 30 mN at 20 °C (a) Test results; (b) Comparison between FE and screened test results

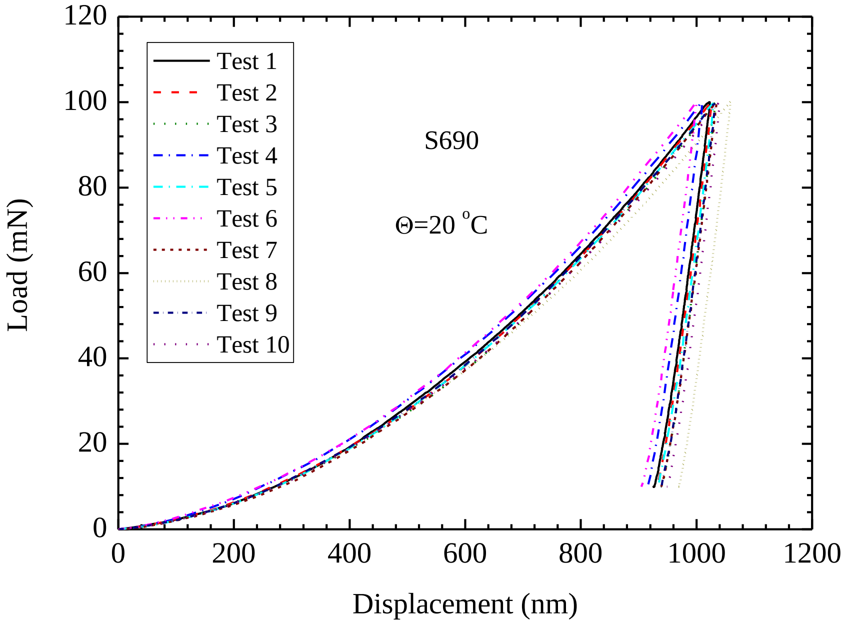

(a)

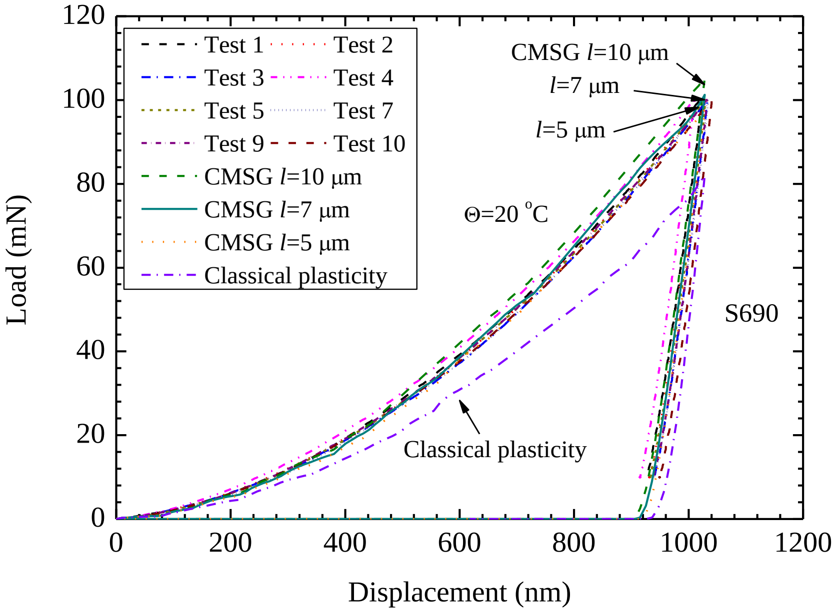

(b)

Figure 5.13 Load-displacement indentation curves for S690 with maximum load of 100 mN at 20 °C (a) Test results; (b) Comparison between FE and screened test results

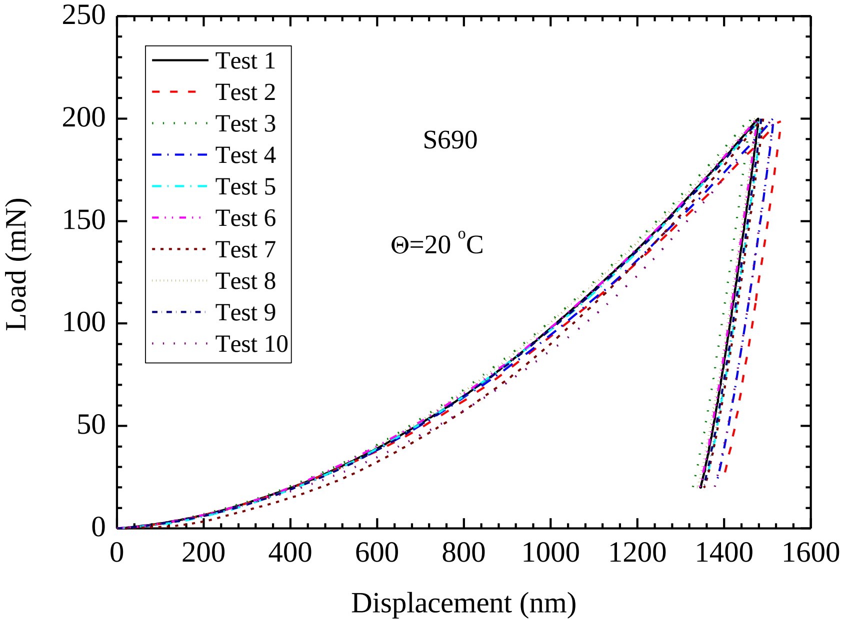

(a)

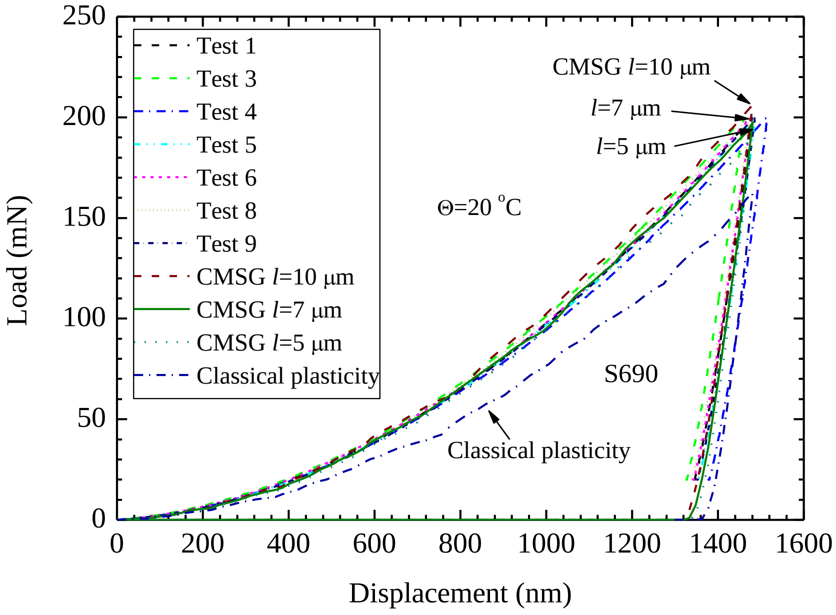

(b)

Figure 5.14 Load-displacement indentation curves for S690 with maximum load of 200 mN at 20 °C (a) Test results; (b) Comparison between FE and screened test results

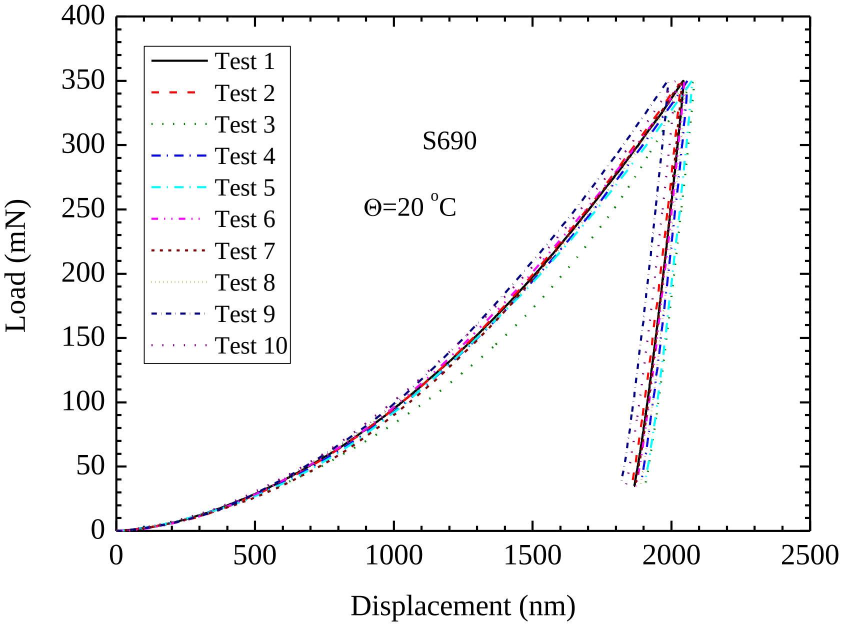

(a)

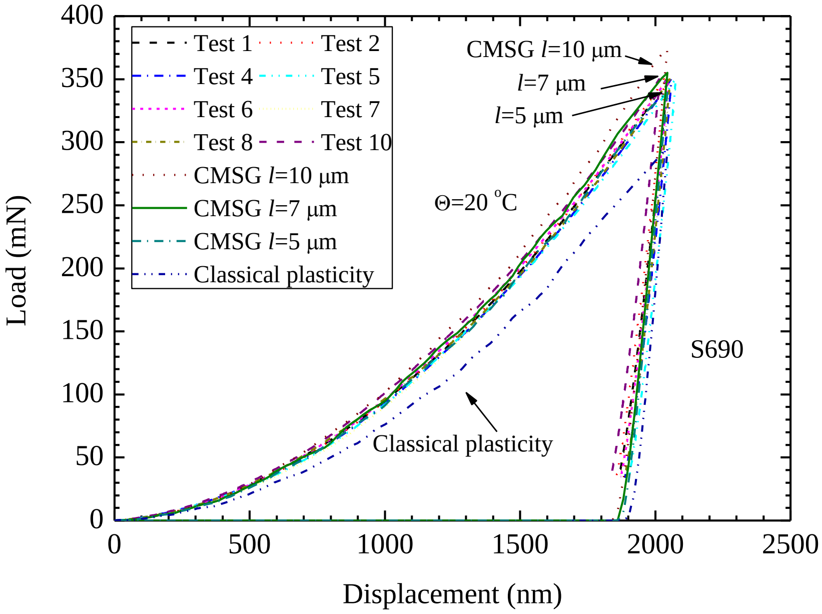

(b)

Figure 5.15 Load-displacement indentation curves for S690 with maximum load of 350 mN at 20 °C (a) Test results; (b) Comparison between FE and screened test results

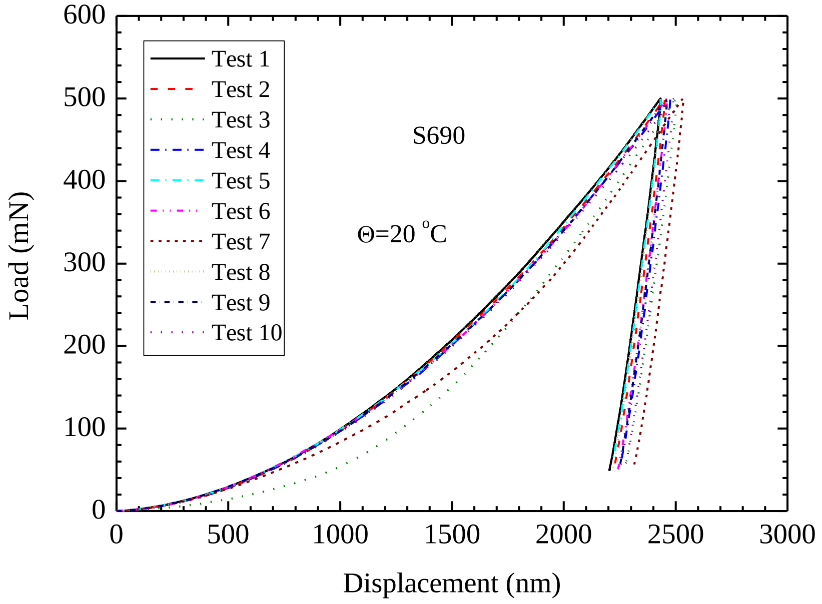

(a)

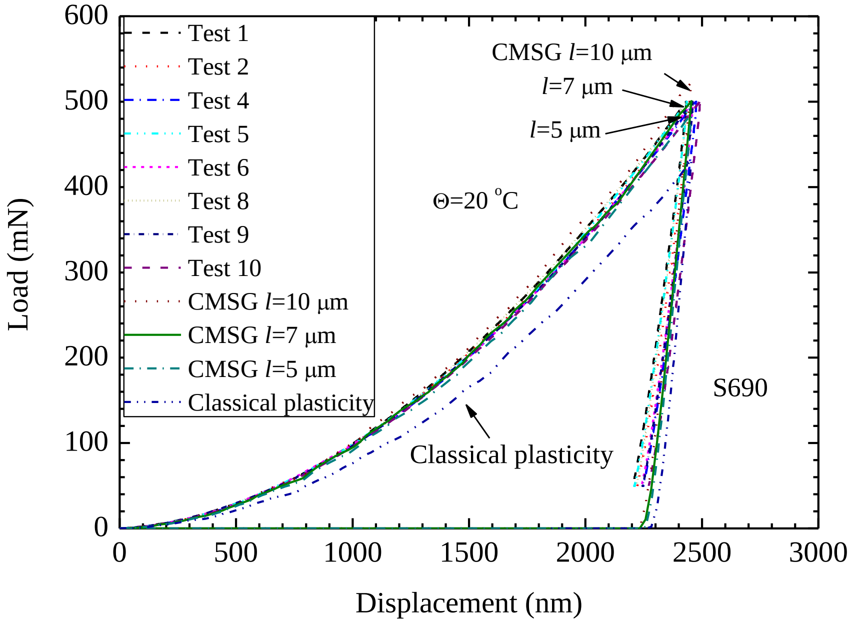

(b)

Figure 5.16 Load-displacement indentation curves for S690 with maximum load of 500 mN at 20 °C (a) Test results; (b) Comparison between FE and screened test results

5.3.4 Numerical Analysis of Indentation Tests at Temperature 300 ^{o}C

In the simulations of the tests at 300 ^{o}C, we adopt the same method as that used at 20 ^{o}C. The displacements applied to the finite element model for S355at each load level (30 mN, 100 mN, 200 mN, 350 mN, and 500 mN) are about 0.66, 1.34, 1.97, 2.68, and 3.22 μm, while for S690, the displacements imposed are around 0.6, 1.1, 1.65, 2.17, and 2.64 μm at the five load levels. Figures 17(a)-21(a) and Figures 22(a)-26(a) presenting the tested curves for S355 and S690. .Figures 17(b)-21(b) and Figures 22(b)-26(b) present the screened tested curves for S355 and S690 and the corresponding finite element simulation results from the classical plasticity and the CMSG plasticity analyses with material length scales of $l = 5$, 7, and 10 μm at each load level. The material length scale of $l = 7$ μm still produces the similar load-indentation curves as the experimental curves for S355 and S690 at temperature 300 ^{o}C. The load-displacement curves computed from the classical plasticity theory are lower than those computed by the CMSG theory as the constitutive model of the classical plasticity does not contain the material length scale.

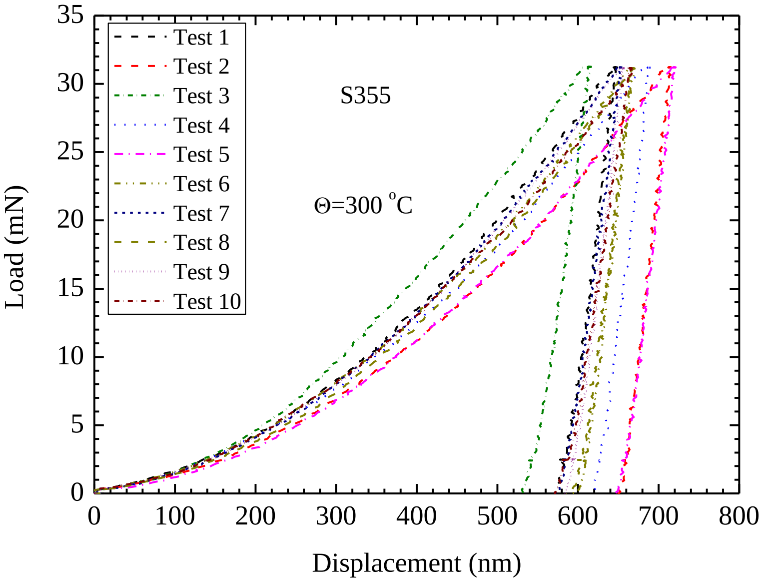

(a)

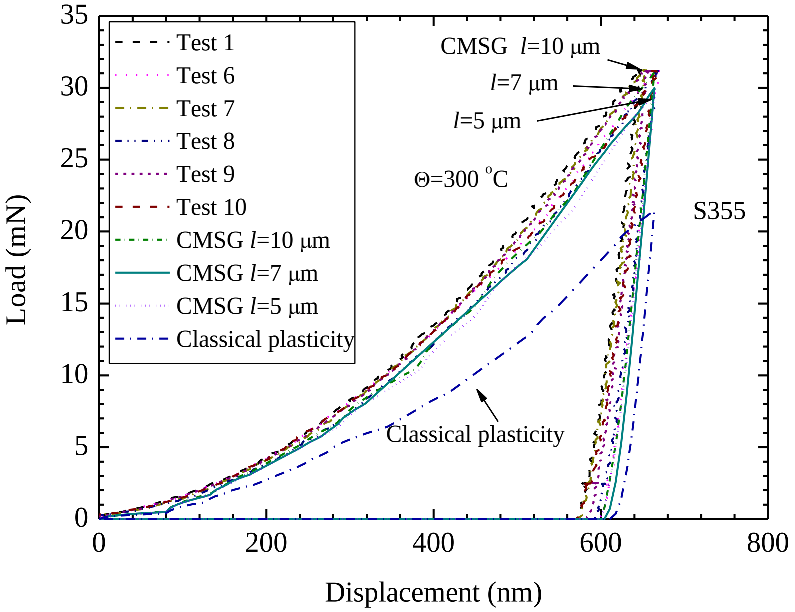

(b)

Figure 5.17 Load-displacement indentation curves for S355 with maximum load of 30 mN at 300 °C (a) Test results; (b) Comparison between FE and screened test results

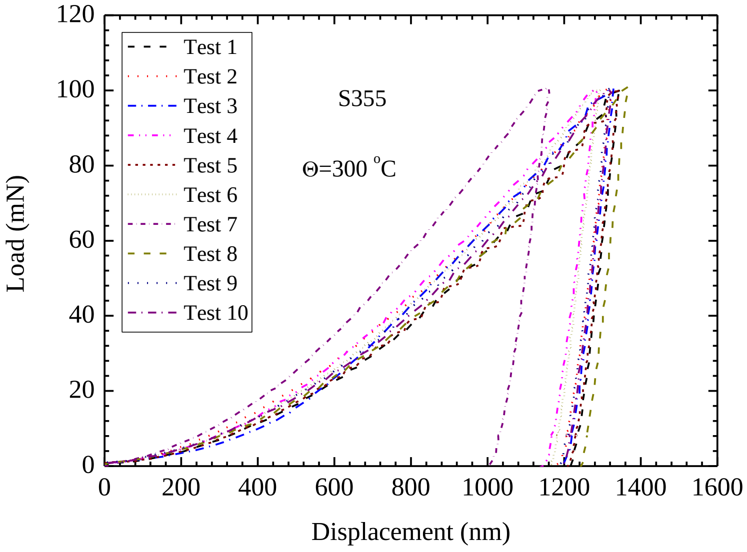

(a)

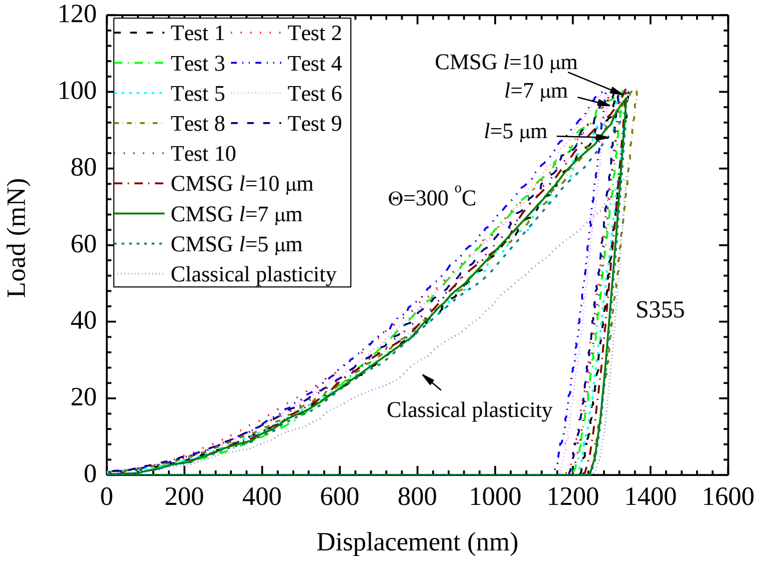

(b)

Figure 5.18 Load-displacement indentation curves for S355 with maximum load of 100 mN at 300 °C (a) Test results; (b) Comparison between FE and screened test results

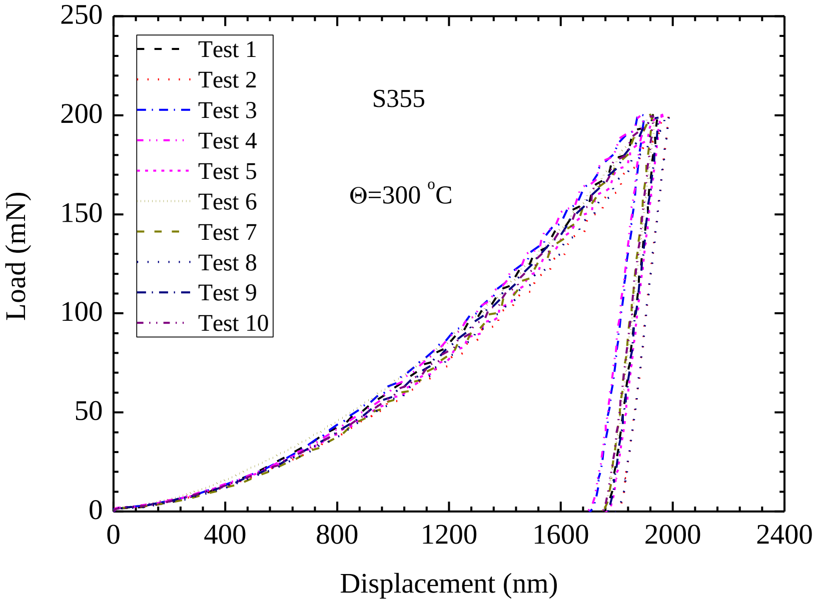

(a)

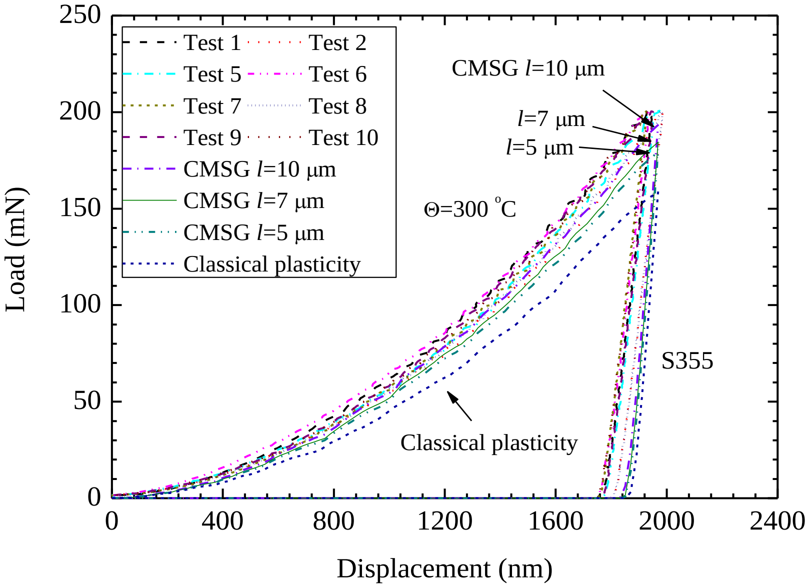

(b)

Figure 5.19 Load-displacement indentation curves for S355 with maximum load of 200 mN at 300 °C (a) Test results; (b) Comparison between FE and screened test results

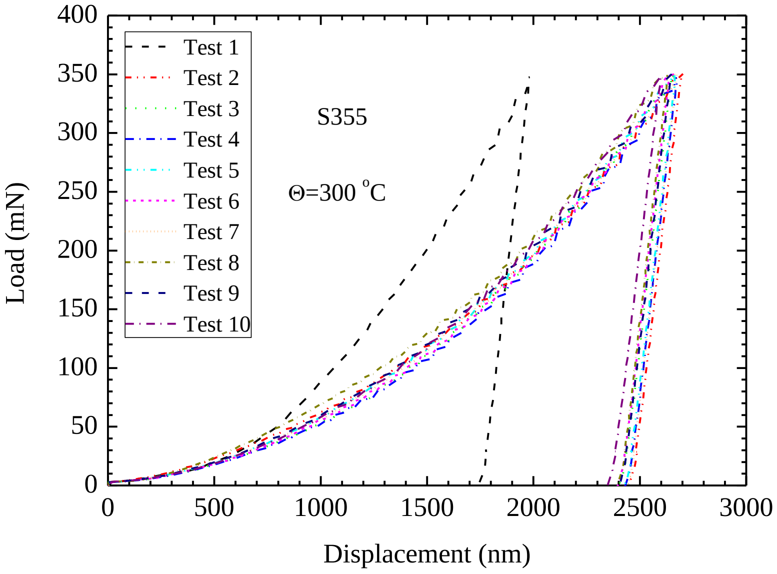

(a)

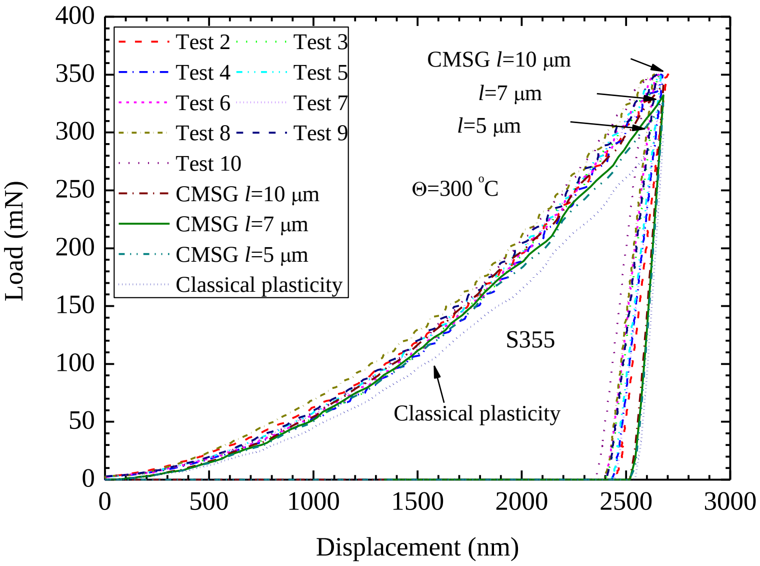

(b)

Figure 5.20 Load-displacement indentation curves for S355 with maximum load of 350 mN at 300 °C (a) Test results; (b) Comparison between FE and screened test results

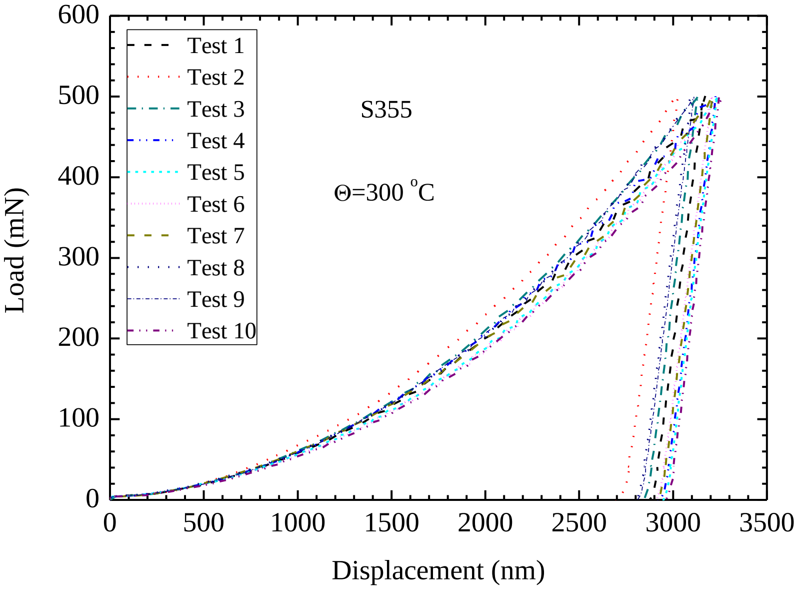

(a)

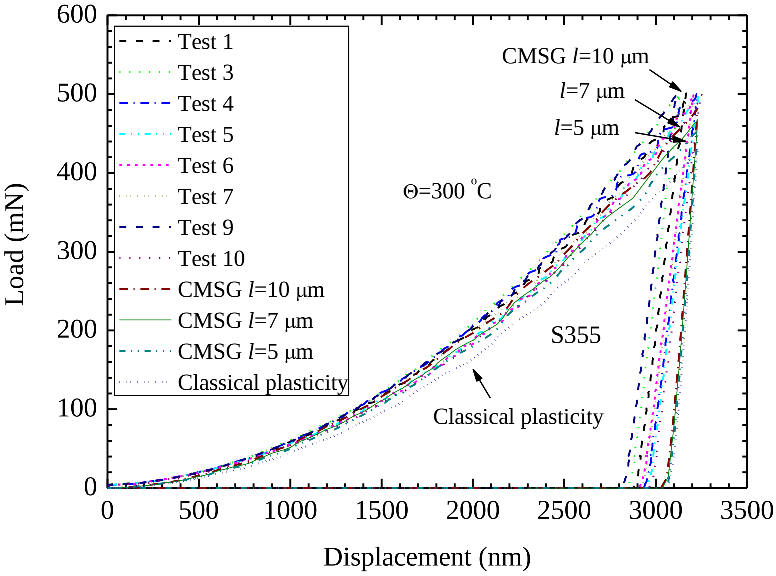

(b)

Figure 5.21 Load-displacement indentation curves for S355 with maximum load of 500 mN at 300 °C (a) Test results; (b) Comparison between FE and screened test results

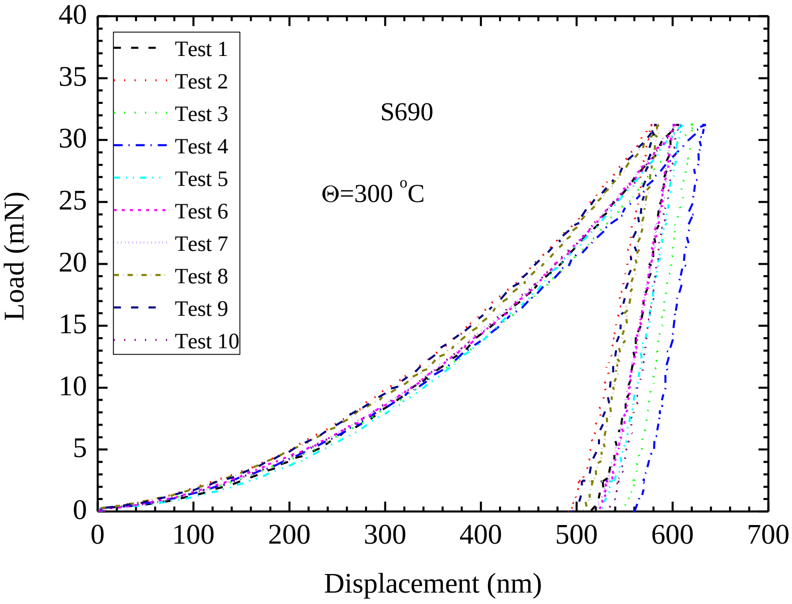

(a)

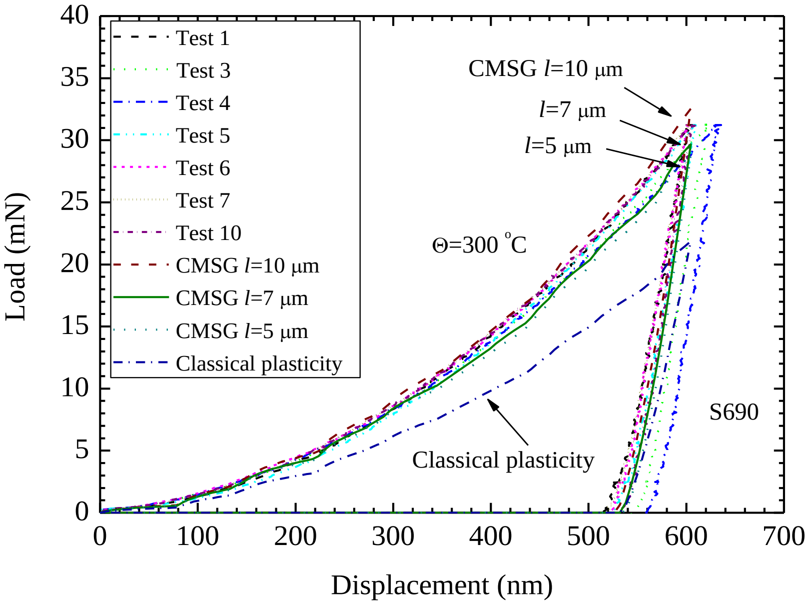

(b)

Figure 5.22 Load-displacement indentation curves for S690 with maximum load of 30 mN at 300 °C (a) Test results; (b) Comparison between FE and screened test results

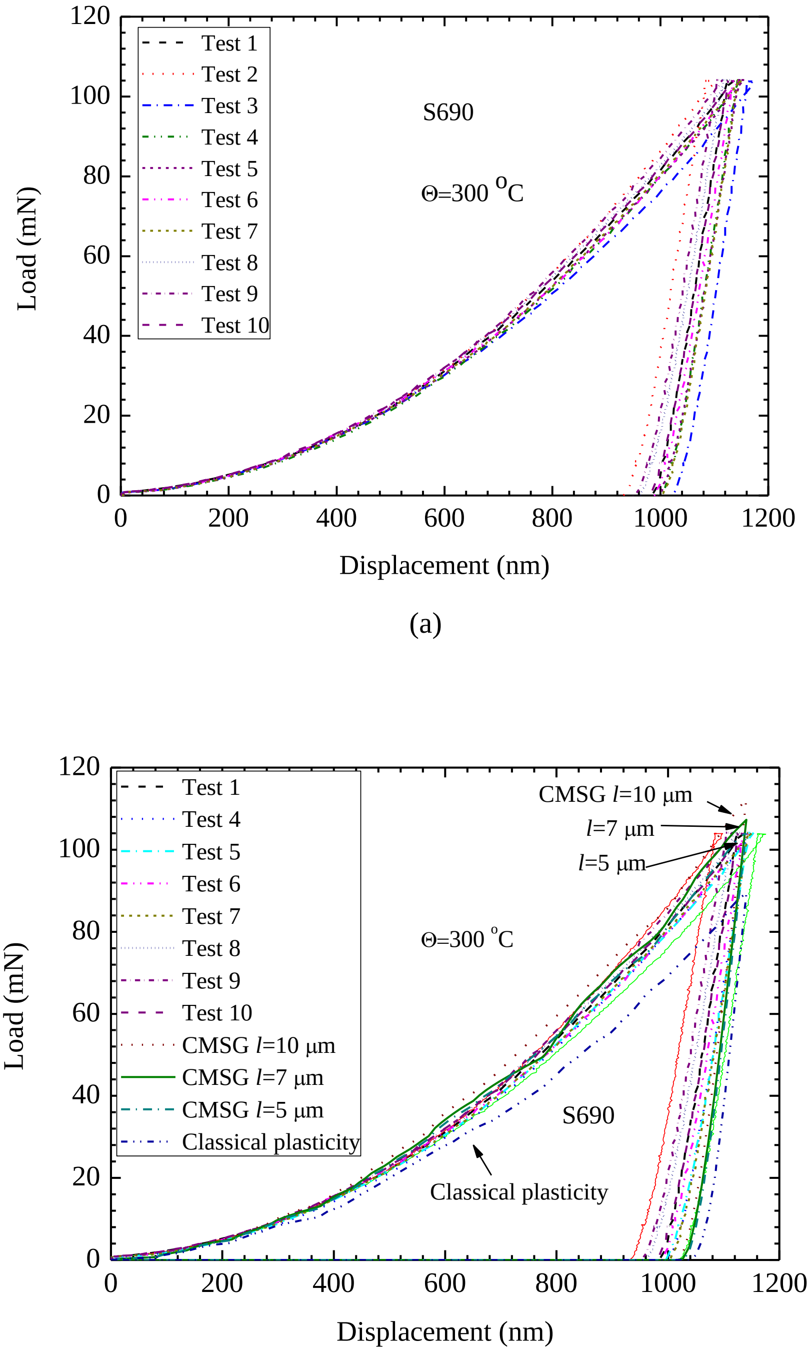

Figure 5.23 Load-displacement indentation curves for S690 with maximum load of 100 mN at 300 °C (a) Test results; (b) Comparison between FE and screened test results

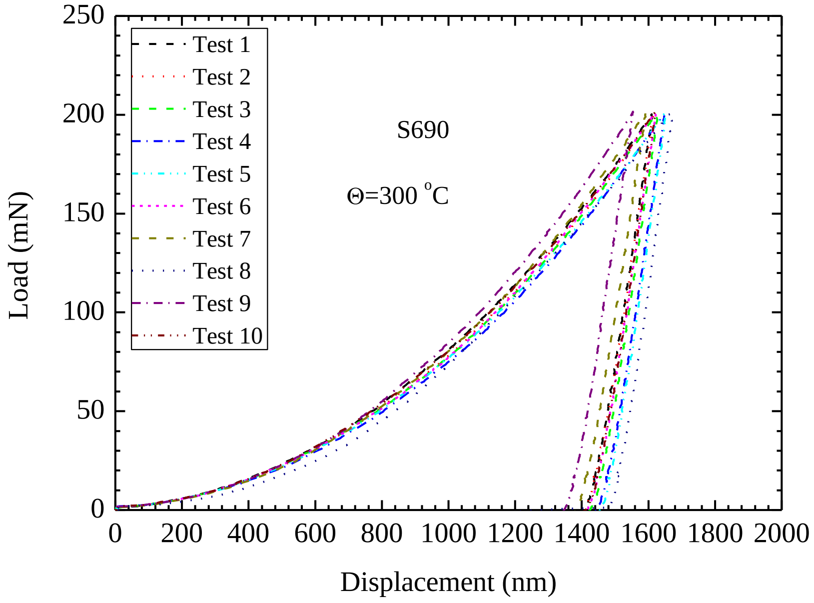

(a)

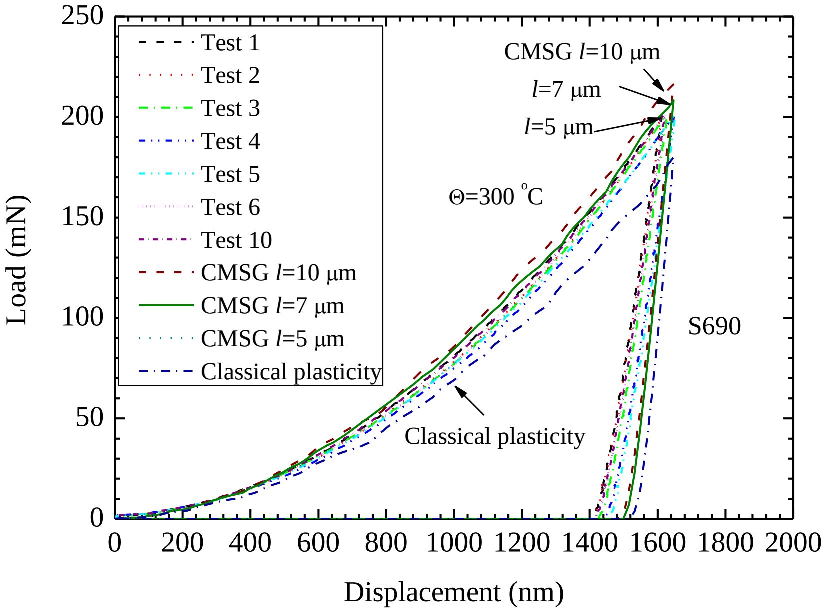

(b)

Figure 5.24 Load-displacement indentation curves for S690 with maximum load of 200 mN at 300 °C (a) Test results; (b) Comparison between FE and test results

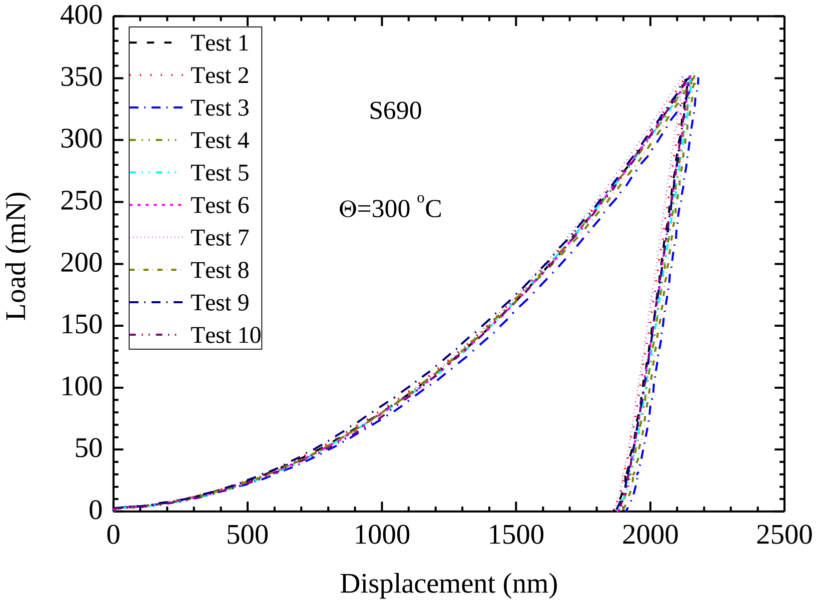

(a)

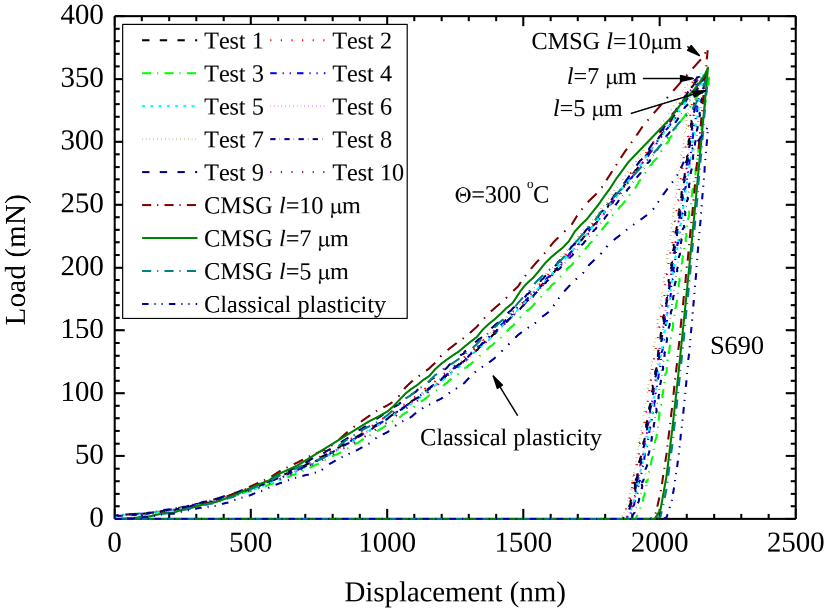

(b)

Figure 5.25 Load-displacement indentation curves for S690 with maximum load of 350 mN at 300 °C (a) Test results; (b) Comparison between FE and screened test results

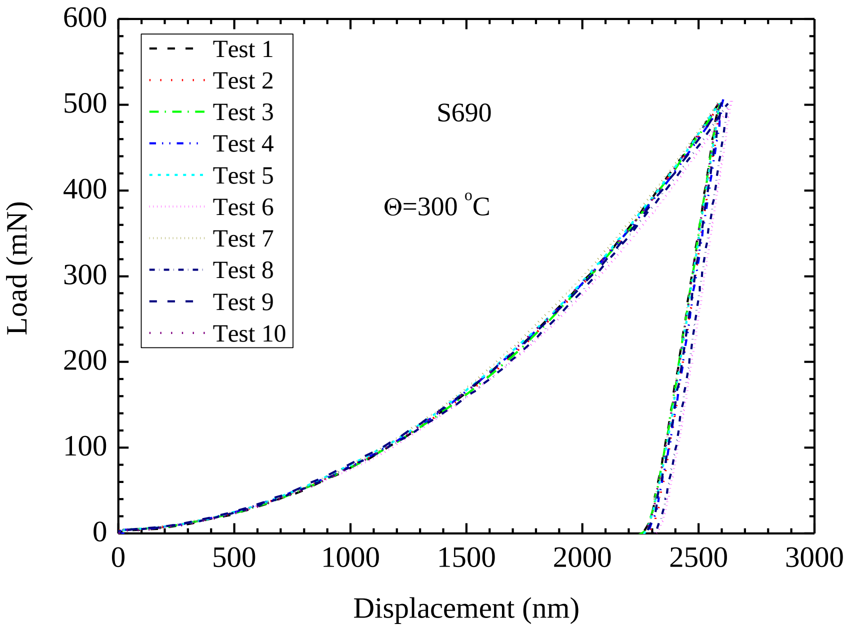

(a)

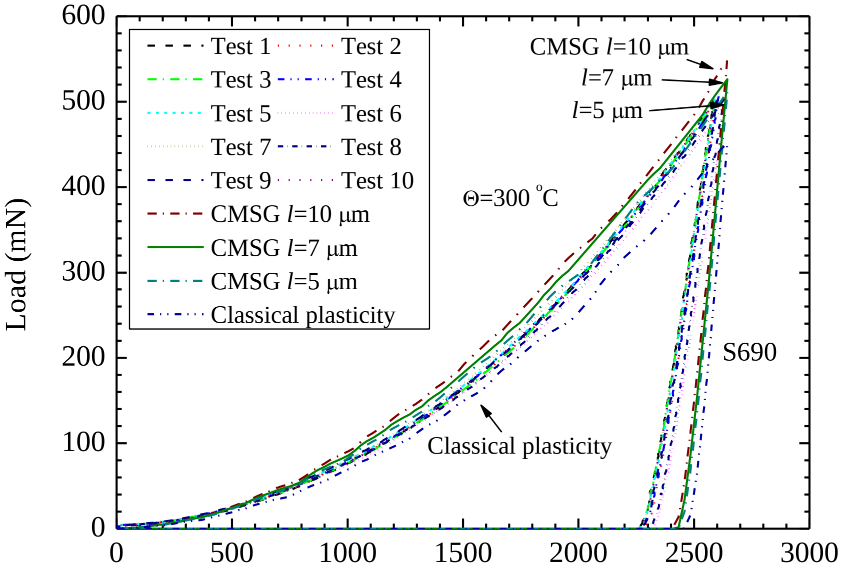

(b)

Figure 5.26 Load-displacement indentation curves for S690 with maximum load of 500 mN at 300 °C (a) Test results; (b) Comparison between FE and screened test results

5.4 Simulations of Indentation Tests for S355 and S690 at Temperature –40 °C

As currently, it has difficulty in the experimental setting up for the low temperature indentation tests in Singapore. In this section, the simulations for the low temperature indentation are performed for the references of future experiments at –40 °C. The finite element model is the same as that used for 20 °C and 300 °C, which has contains 7600 20-node brick elements with the minimum element size of 2 nm in the contact region. The material properties for S355 and S690 adopt the stress-strain curve at –40 °C in Figure 5.4. The material length scale in the simulations uses 7 μm which is obtained from the indentation tests at temperature 20 °C and 300 °C.

Figures 5.27(a)-(e) show the numerical results of the indentation test for S355 at –40 °C with various load levels based on classical plasticity and CMSG plasticity theories with three different values of material length scale, $l = 5$, 7 and 10 μm. The simulations of the indentation tests use the displacement-controlled method to apply the load. The five levels reaction forces are about 30, 100, 200, 350, and 500 mN, and the corresponding imposed of displacements at are around 0.6, 1.3, 1.95, 2.6, and 3.3 μm for each load level. Comparing the load-displacement curves with the same displacement-imposed, the differences of the maximum reaction force between material length scale of $l = 10$ μm and $l = 7$ μm and between material length scale $l = 10$ μm and $l = 7$ μm are around 3.3% at load of 30 mN, and decreases to 2% for load case of 500 mN. The differences between the load-displacement curves from the CMSG plasticity analyses and the classical plasticity analyses also decrease with the load increasing, implying the diminishing of the material size effect at the higher load levels.

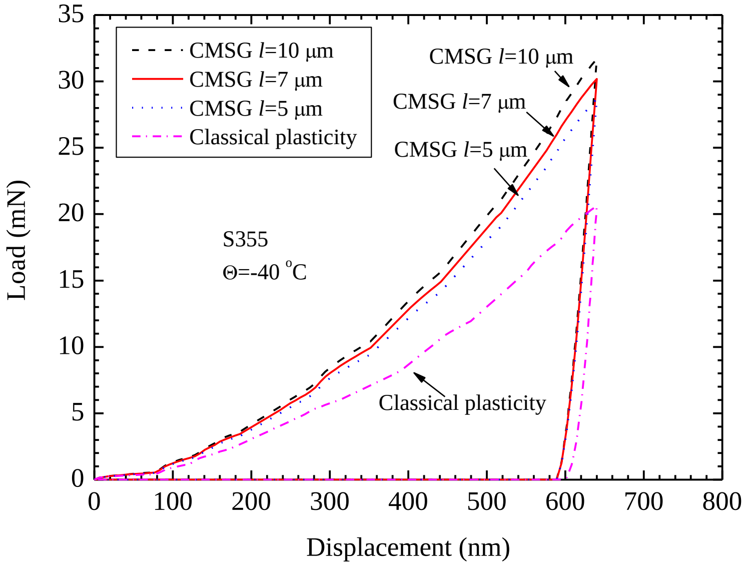
35
30
25
20
15
10
5
0
0
100
200
300
400
500
600
700
800
Load (mN)
Displacement (nm)
CMSG *l*=10 μm
CMSG *l*=7 μm
CMSG *l*=5 μm
Classical plasticity
S355
Θ=-40 °C
CMSG *l*=10 μm
CMSG *l*=7 μm
CMSG *l*=5 μm
Classical plasticity

(a)

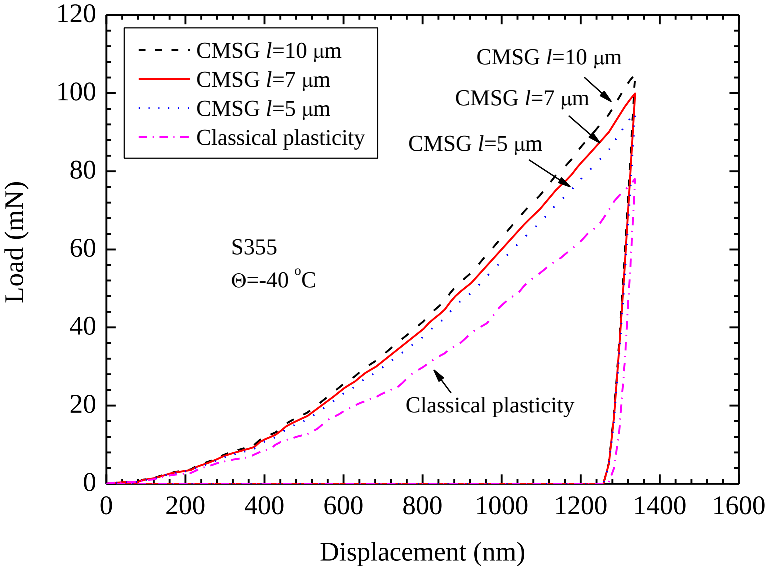
120
100
80
60
40
20
0
0
200
400
600
800
1000
1200
1400
1600
Load (mN)
Displacement (nm)
CMSG *l*=10 μm
CMSG *l*=7 μm
CMSG *l*=5 μm
Classical plasticity
S355
Θ=-40 °C
CMSG *l*=10 μm
CMSG *l*=7 μm
CMSG *l*=5 μm
Classical plasticity

(b)

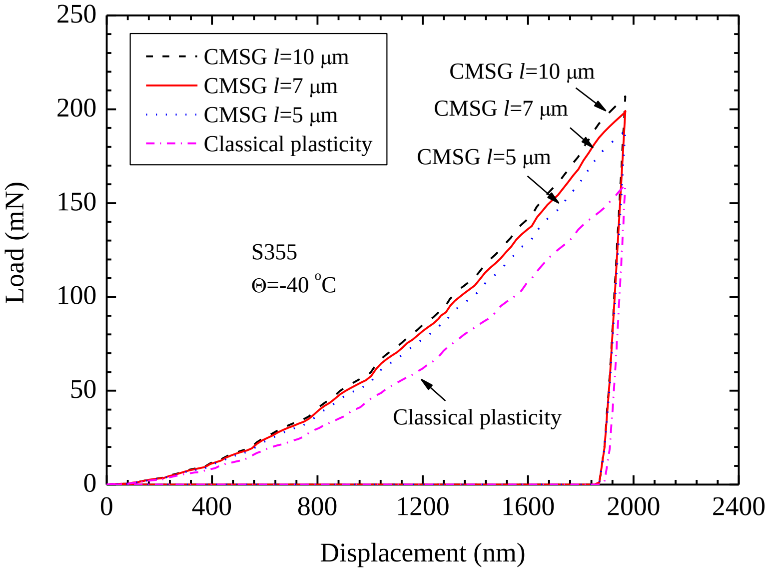
CMSG l=10 μm
CMSG l=7 μm
CMSG l=5 μm
Classical plasticity
CMSG l=10 μm
CMSG l=7 μm
CMSG l=5 μm
S355
Θ=-40 °C
Classical plasticity
Load (mN)
Displacement (nm)
0
50
100
150
200
250
0
400
800
1200
1600
2000
2400

(c)

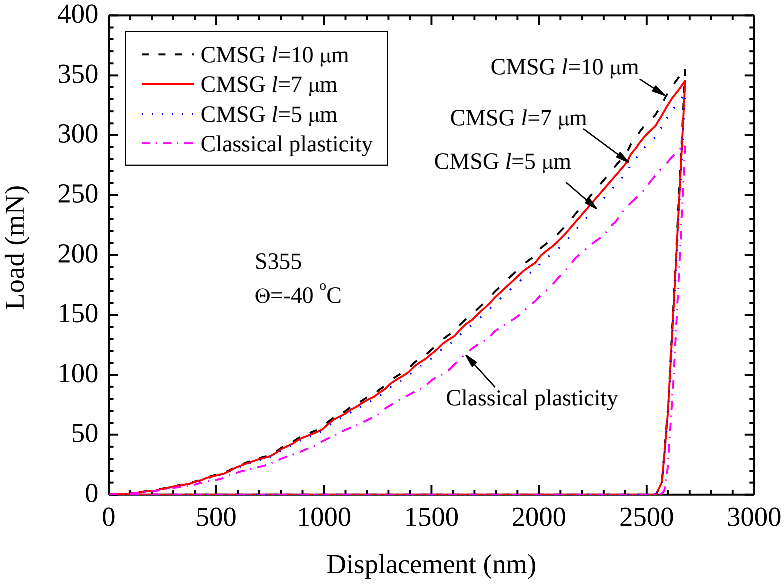
CMSG l=10 μm
CMSG l=7 μm
CMSG l=5 μm
Classical plasticity
CMSG l=10 μm
CMSG l=7 μm
CMSG l=5 μm
S355
Θ=-40 °C
Classical plasticity
Load (mN)
Displacement (nm)
0
50
100
150
200
250
300
350
400
0
500
1000
1500
2000
2500
3000

(d)

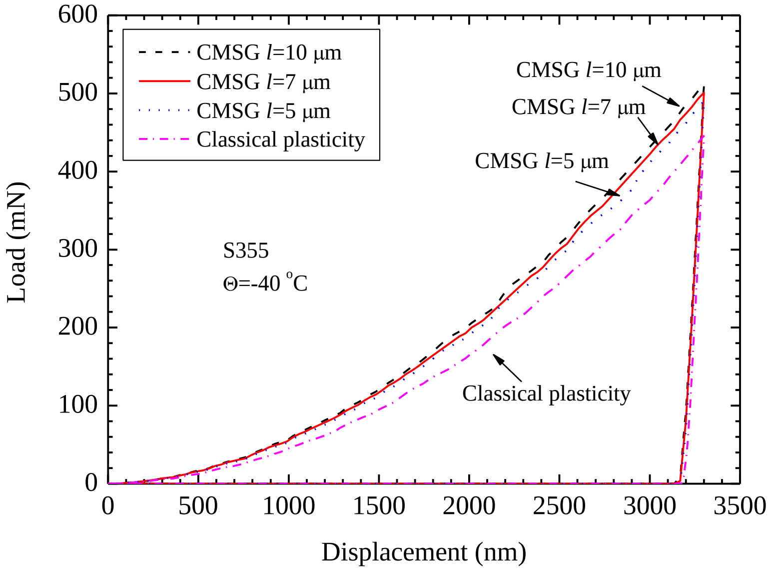

(e)

Figure 5.27 FE simulations of load-displacement indentation curves for S355 with maximum load of 350 mN at –40 °C at load levels (a) 30 mN; (b) 100 mN; (c) 200 mN; (d) 350 mN; (e) 500 mN

Compared with the indentation load-displacement curve for S355 at temperature 20 °C (see Figures 5.7-5.11) and 300 °C (see Figure 5.17-5.21), at the same maximum load, the maximum displacement at –40 °C is less than that at 20 °C and 300 °C. At the maximum load levels of 30 mN, 100 mN, 200 mN, 350 mN, and 500 mN, the maximum displacement at –40 °C is around 0.3% less than that at 20 °C and 300 °C for each load levels. This difference is not much, but very significant for steel S690.

Figures 5.28(a)-(e) show the simulations of the indentation test for S690 at –40 °C with various load levels (30 mN, 100 mN, 200 mN, 350 mN, and 500 mN). The imposed displacements at each load level are around 0.49, 0.96, 1.34, 1.89, and 2.3 μm at the five load levels, respectively. Comparing the load-displacement curves with the same displacement-imposed, the differences of the maximum reaction force between material length scale of $l = 10$ μm and $l = 7$ μm and between material length scale $l = 10$ μm and $l = 7$ μm are around 3.3% at load of 30 mN, and gradually decrease to 2% for load case of 500 mN. The differences between the load-displacement curves from the CMSG plasticity analyses and the classical plasticity analyses also decrease with the load increasing, implying the diminishing of the material size effect in the higher load levels.

Compared with the indentation load-displacement curve for S690 at temperature 20 ^{o}C (see Figure 5.7-5.11) and 300 ^{o}C (see Figures 5.17-5.21), at the same maximum load, the maximum displacement at –40 ^{o}C is less than that at 20 ^{o}C and 300 ^{o}C. If the curves with material length scale of $l = 7$ μm for –40 ^{o}C are used for comparison, at the maximum load level of 30,100, 200, 350, and 500 mN, the maximum displacement is 4-6% less than that the tested curves at 20 ^{o}C and 12-14% less than those at 300 ^{o}C, respectively. The smaller indent displacement at 20 ^{o}C reflects that the steel is harder than 20 ^{o}C and 300 ^{o}C.

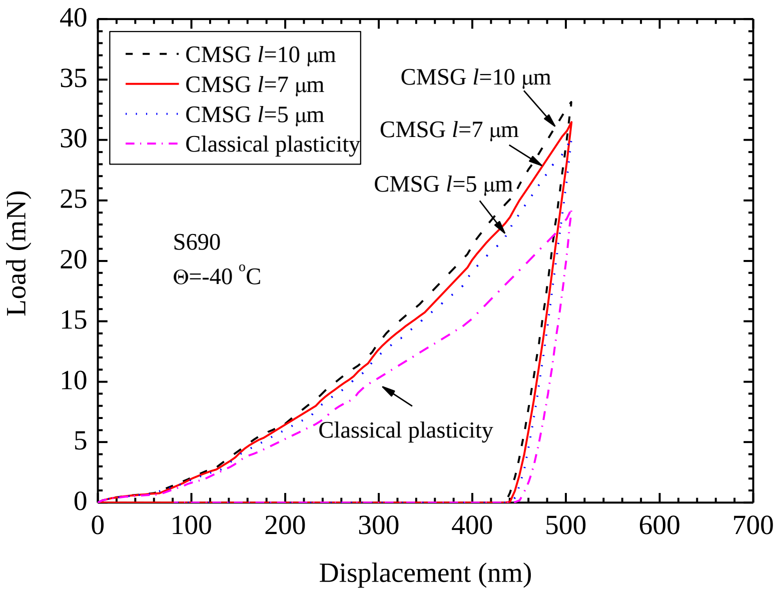

(a)

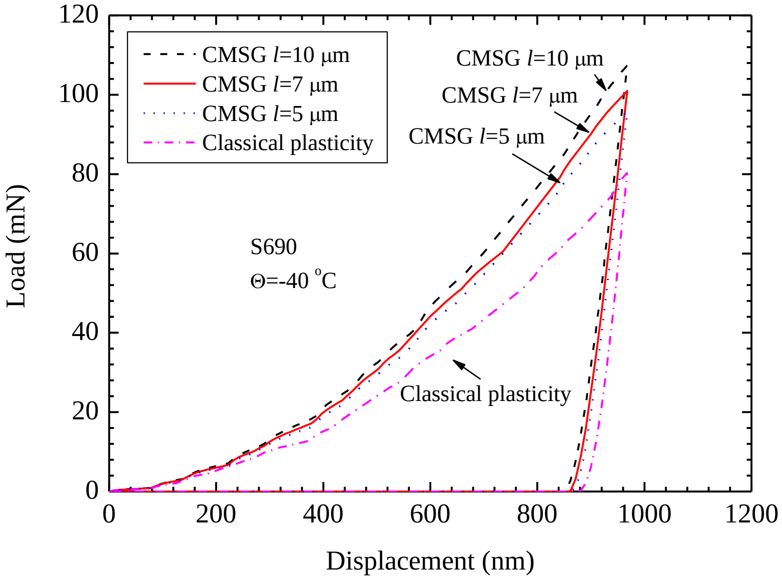
CMSG l=10 μm
CMSG l=7 μm
CMSG l=5 μm
Classical plasticity
CMSG l=10 μm
CMSG l=7 μm
CMSG l=5 μm
Classical plasticity
S690
Θ=-40 °C
Load (mN)
Displacement (nm)
0
20
40
60
80
100
120
0
200
400
600
800
1000
1200

(b)

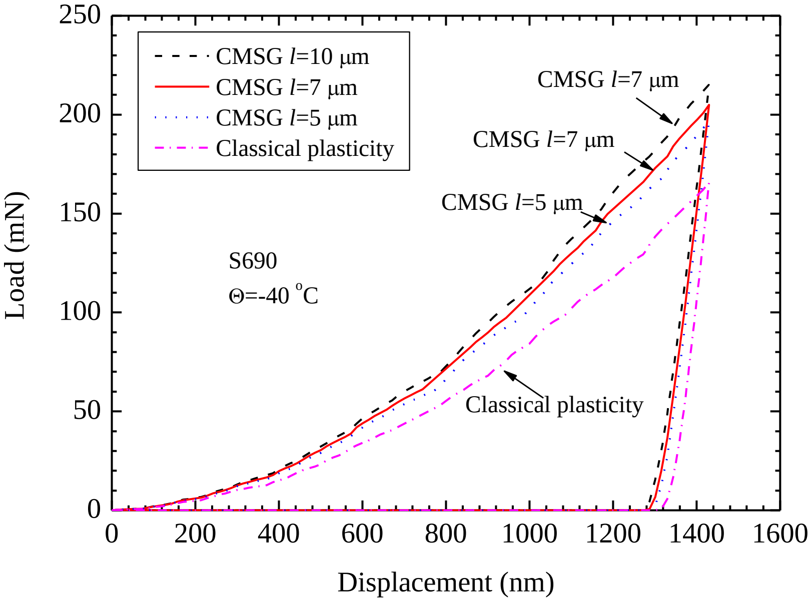
CMSG l=10 μm
CMSG l=7 μm
CMSG l=5 μm
Classical plasticity
CMSG l=7 μm
CMSG l=7 μm
CMSG l=5 μm
Classical plasticity
S690
Θ=-40 °C
Load (mN)
Displacement (nm)
0
50
100
150
200
250
0
200
400
600
800
1000
1200
1400
1600

(c)

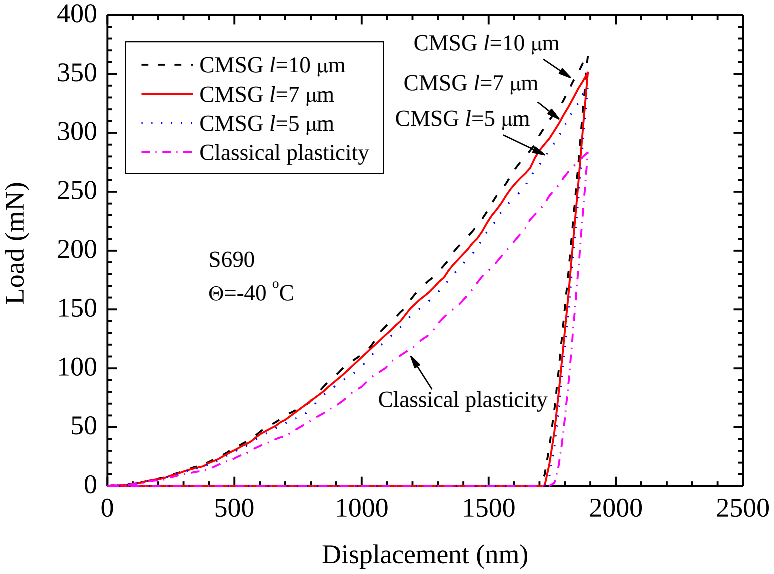

(d)

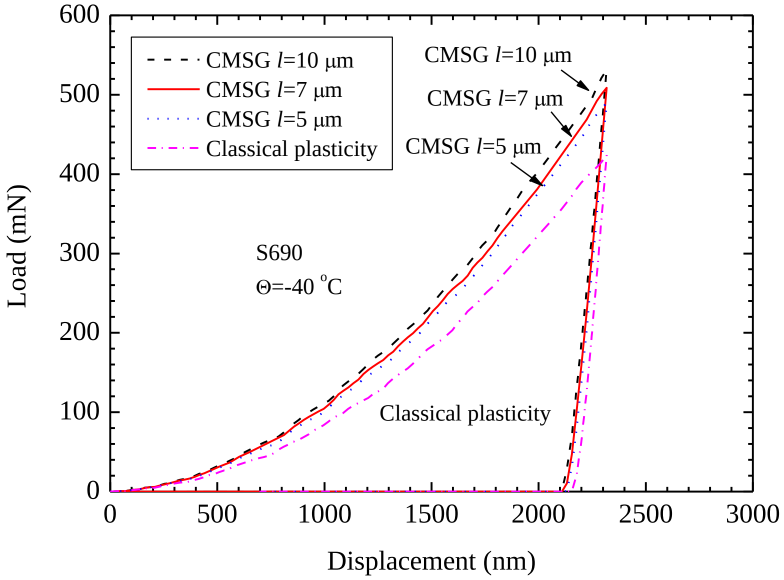

(e)

Figure 5.28 FE simulations of load-displacement indentation curves for S690 with maximum load of 350 mN at -40 ^{o}C at load levels (a) 30 mN; (b) 100 mN; (c) 200 mN; (d) 350 mN; (e) 500 mN

5.5 Summary

This chapter quantifies the material length scale of the steels (S355 and S690) at two temperatures (20 ^{o}C and 300 ^{o}C) by comparison of the indentation load-displacement curves and the numerical results from CMSG plasticity analyses. The results show that the material length scale for steel S355 and S690 is around 7 μm. Through the evaluation of the material length scale at two distinct temperatures (20 °C and 300 °C), this study shows that values of the material length of the structural steels at the two temperatures do not vary, implying that the material length scale is independent of the temperature in the range of 20 °C ~ 300 °C.

This chapter also shows that even at the maximum loading capacity of the indentation machine, the maximum indent depth is still lower than 3.5 μm for both types of steels, and is also lower than the intrinsic material length scale as the steel is very hard. Therefore, at the maximum loading level, 500 mN, the difference between the CMSG plasticity and the classical plasticity curves is still large. We may infer that the load-displacement curve from the classical plasticity and the CMSG plasticity will converge to one curve at the load level higher than 500 mN, that is, when the indentation size effect diminishes.

The current results of the indentation test for S355 and S690 at –40 °C based on the classical plasticity and the CMSG plasticity analyses with material length scale of $l = 5$, 7 and 10 μm show that the maximum displacement at this low temperature is less than that at temperatures 20 °C and 300 °C with the same maximum displacement load applied, implying the two types of steel at –40 °C are harder than at 20 °C and 300 °C. The simulations results for S355 and S690 at –40 °C will be used for justifying the indentation tests at –40 °C in the future. The material length scale obtained from this chapter will be continuously used in Chapter 6 to study the plastic strain gradient effect on the crack opening displacement which is an important parameter for describe the crack tip conditions.

CHAPTER 6 EFFECT OF PLASTIC STRAIN GRADIENT ON THE NEAR-TIP DISPLACEMENT

6.1 Introduction

The crack tip opening displacement (CTOD) is one of the parameters that can be used to describe the crack tip conditions for elastic-plastic materials. The most common definition of CTOD is the displacement at the 90^{o} intersection vertex with crack flanks [2] (see Figure 6.1). According to this definition, the location for measuring the CTOD moves further away from the original crack tip with the crack opening up. As the plastic strain gradient acts on the crack-tip stress field when the plastic deformation is in micron or submicron level, thus, this chapter numerically studies the effect of the strain gradient plasticity on the near-tip opening displacement by selecting the positions which are around tens of micron behind the crack tip to measure the near-tip crack opening displacement. The compact tension with thickness of half inch, 0.5T C(T) model is used to verify the effect of the plastic strain gradient on the CTOD values and its influence range behind the crack tip. Then, this chapter adopts the plane strain small scale yield model (SSY) and further studies the effect of the plastic strain gradient on the near-tip opening displacement.

6.2 Effect of the Plastic Strain Gradient on the Near-tip Displacement

The near-tip locations of 2.5, 10, and 50 μm behind the crack tip are used in the 0.5T C(T) models to quantify the plastic strain gradient effect on the near-tip crack opening displacement and all the analyses in this chapter are based on the finite deformation formulations.

6.2.1 Effect of Plastic Strain Gradient on the Near-tip opening Displacement for the C(T) model

Figure 6.2(a) presents the full FE model of a 0.5T C(T) model specimen as the crack is not exactly on the symmetric plane of the specimen. This specimen is from one of fracture tests performed in current research. The dimensions are also shown in Figure 6.2 (a). The initial crack length is around 19 mm. It is supposed to have a crack length ratio of $a / W = 0.5$ after the precrack process. After precracking, monotonic load is applied on the specimen until it fails. In the FE modeling, the crack front follows the extended crack front measured in the post-test examination, which connects 9 uniformly distributed upper triangular as shown in Figure 6.2(b). In the FE model, along the thickness direction there locates 8 layers of 20-node elements (C3D20). The total number of elements is 13952. The total number of nodes is 64367. This model also contains an initial root radius of 2.5 μm to help the convergence in the numerical computation. The material properties follow the S355 at room temperature (20 ^{o}C). Young’s modulus is 203 GPa, yield stress is 345 MPa and the plastic hardening exponent is 0.1. In the CMSG plasticity analyses, the material length scale is adopted as 7 μm.

Figure 6.3 shows the load–CTOD curves from the classical plasticity and the CMSG plasticity analyses. The values of CTOD are obtained according to the common definition of the CTOD, that is, measured at various locations of 90^{o} intersect vertex during the process of the crack opening. Apparently, the two curves are coincided and show that the plastic strain gradient does not affect the CTOD values. However, if the locations behind the crack tip for measuring the CTOD values are fixed, the plastic strain gradient can be seen. Figure 6.4(a) plots load–CTOD curves, in which the CTOD values are measured at the mid-thickness of the specimen and 2.5 μm behind the crack tip ($Z / B = 0.5$). The difference of the CTOD values computed from the classical plasticity and the CMSG plasticity analyses is around 46% at the load of 25 kN (i.e., 91 $\mathrm{MPa}\sqrt{\mathrm{m}}$). The difference increases to 63.6% at the load of 30 kN (i.e., 109 $\mathrm{MPa}\sqrt{\mathrm{m}}$). Figure 6.4(b) shows the difference of the CTOD values between the classical plasticity and the CMSG plasticity analyses is around 10% at 25 kN when the CTOD values are measured at the location of 10 μm behind the original crack tip ($Z/B = 0.5$), which is smaller compared to the difference measured at the location of 2.5 μm. At the location of 50 μm behind the crack tip, the CTOD curve from classical plasticity agrees with that from the CMSG plasticity results. This verifies that the plastic strain gradient affects the values of CTOD only at the locations very near the crack tip. Beyond certain distance away from the crack tip, the effect of the plastic strain gradient on the near-tip opening displacement fades away. The CTOD values computed from the CMSG plasticity theory are much lower than those from the classical plasticity at the distance very near to the crack tip (< 50 μm), implying that the plastic strain gradient hardens the material and reduces the materials' plastic flow so that the values of CTOD are smaller. At the distance further away from the crack tip, the CTOD values are not influenced by the plastic strain gradient.

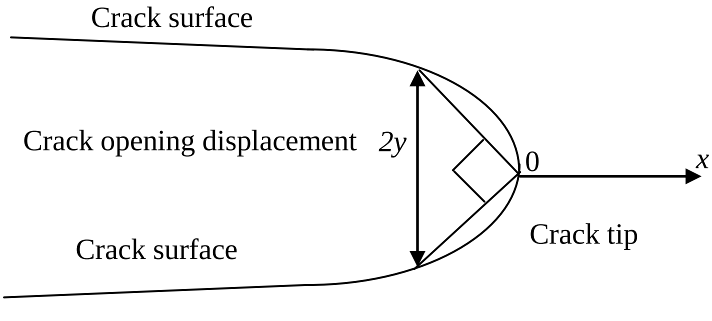

Figure 6.1 Crack tip opening displacement

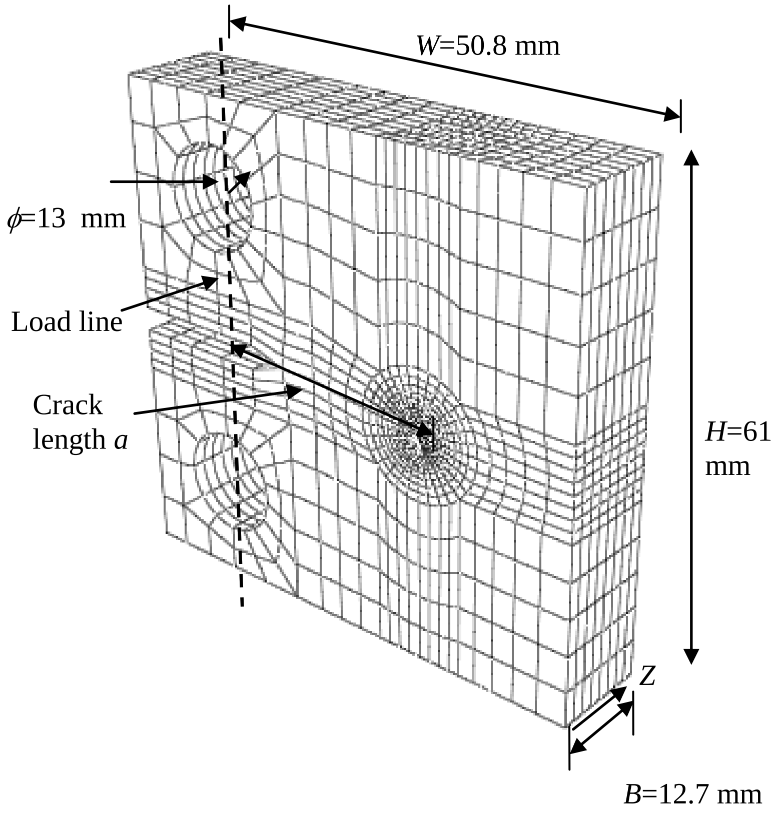

(a)

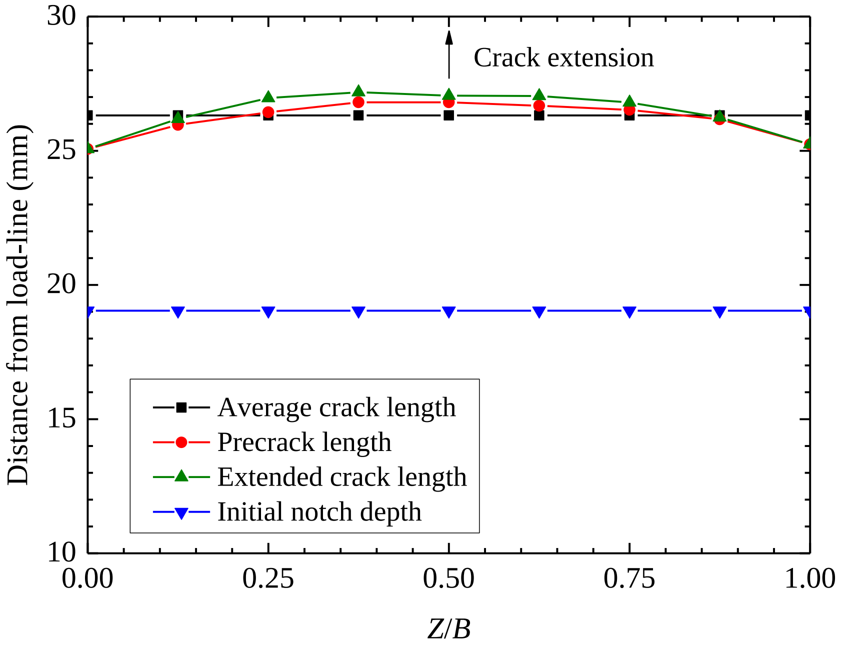

(b)

Figure 6.2 0.5TC(T) specimen (a) FE model; (b) The crack front measurement

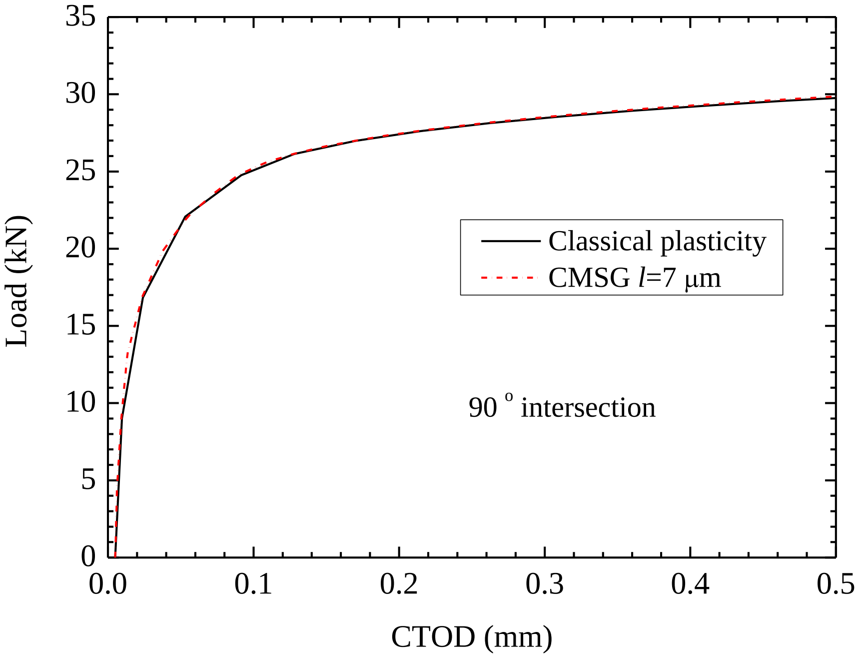

Figure 6.3 The load vs. CTOD curves from classical plasticity and CMSG plasticity analyses

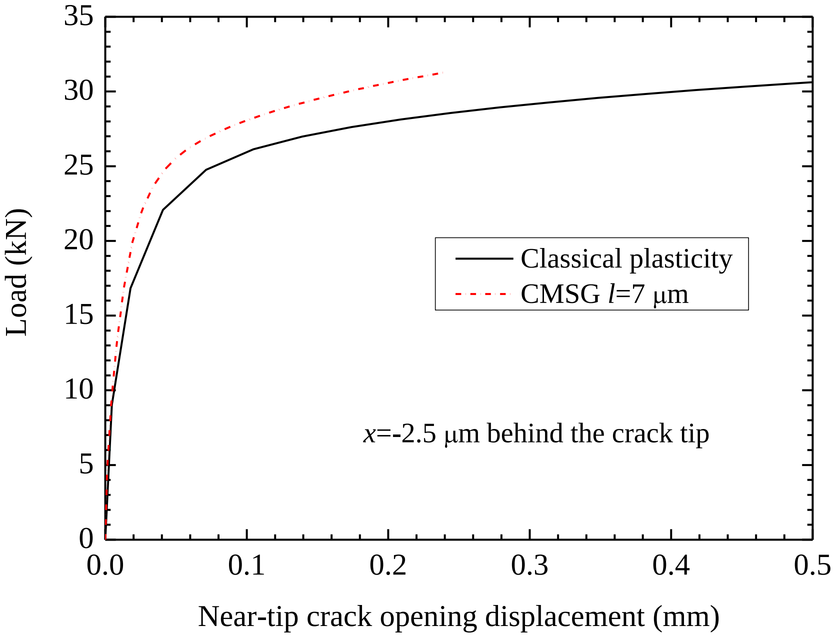

(a)

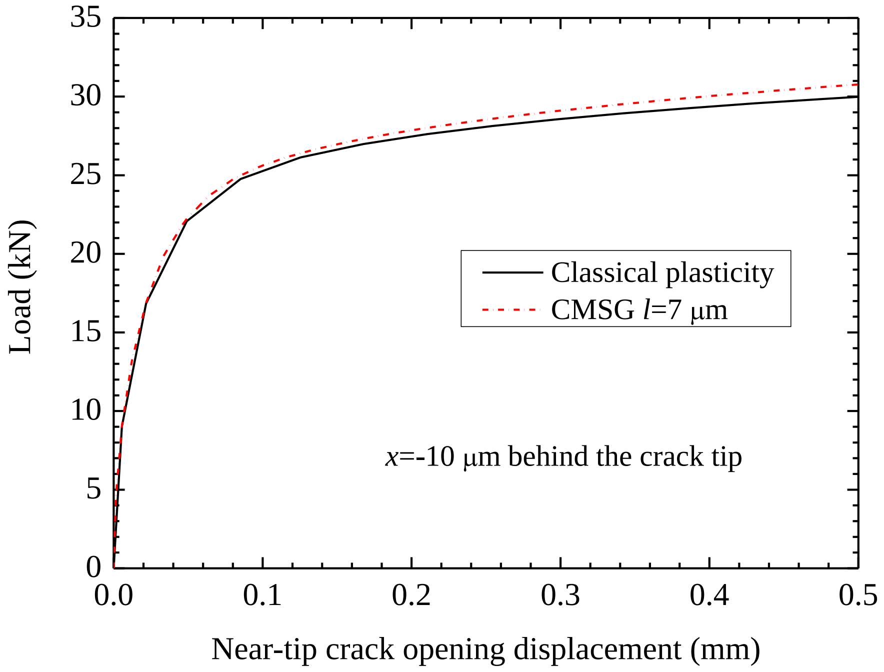

(b)

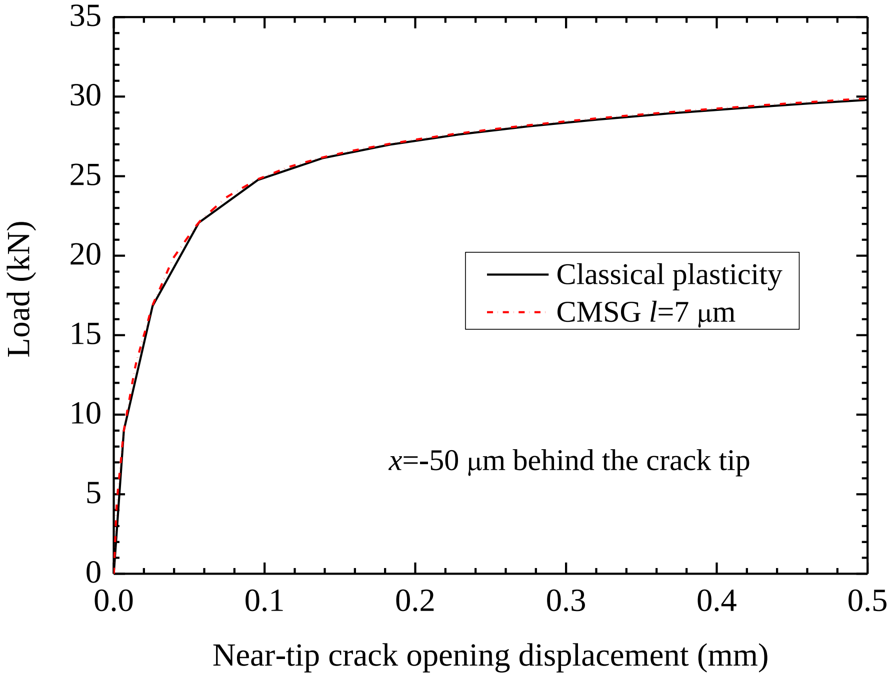

(c)

Figure 6.4 Load-near-tip opening displacement from classical plasticity and CMSG plasticity analyses for 0.5T C(T) model at different locations behind the crack tip (a) 2.5 μm; (b) 10 μm; (c) 50 μm

6.2.2 Effect of Plastic Strain Gradient on the Near-tip Opening Displacement for the SSY Model with Zero T-stress

The above section quantifies the distance behind the crack tip that the plastic strain gradient can affect on the near-tip opening displacement of the 0.5T C(T) model which is less than 50 μm away from the crack tip. This section adopts a plane strain SSY model and further studies the plastic strain gradient effect on the near-tip opening displacement. The CTOD values are determined at 2.5 μm behind the crack tip. The mesh of the SSY model is the same as presented in Figure 4.1(c) of Chapter 4. The total numbers of elements and nodes are 2839 and 20681, respectively. The initial root and the minimum element size are both 2.5 μm. The material properties are the same as the steel S355 at the room temperature (20 ^{o}C). Young's modulus is 203 GPa, yield stress is 345 MPa and the plastic hardening exponent is 0.1. The material length scale is 7 μm.

Originally only the plane strain, K_I loading with zero *T*-stress is imposed on the outer radius of the SSY model. Figures 6.5(a) and 6.5(b) compare the normalized von Mises stress and strain distribution along the crack plane by the classical plasticity and the CMSG plasticity analyses for the SSY model. At load of $K_I = 300\ \mathrm{MPa}\sqrt{\mathrm{m}}$, the normalized von Mises stress computed from the CMSG plasticity analysis is higher than that from the classical plasticity analysis in the range of $x\sigma_y / J \le 0.08$, which is around of 10 μm ahead of the crack tip while the strain is lower than that from the classical plasticity analysis. This implies that the plastic strain gradient stiffens the material so that the strain at the crack tip is lower while the stress is significantly higher.

Figure 6.6 presents the load K_I versus the opening displacement at a location, 2.5 μm behind the crack tip. Initially, the initial root affects the stress field near the crack tip, and removes the stress singularity ahead of the crack tip. Thus, the plastic strain gradient effect on the near-tip opening displacement is insignificant. As the load and the plastic deformation of the crack tip increase, the effect of the initial root radius on the deformation of the crack tip gradually diminishes and the plastic strain gradient on the near-tip opening displacement can be observed. At the load of $K_I = 300\ \text{MPa}\sqrt{\text{m}}$, the near-tip opening displacement at $x = -2.5\ \mu\text{m}$ computed from the CMSG plasticity analysis is 8% lower than that computed from the classical plasticity. The plastic strain gradient hardens the material and reduces the near-tip opening displacement simultaneously.

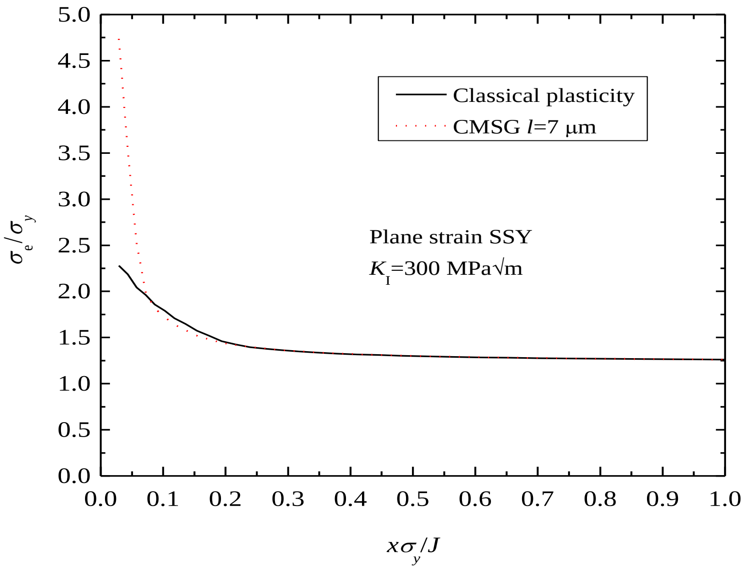

(a)

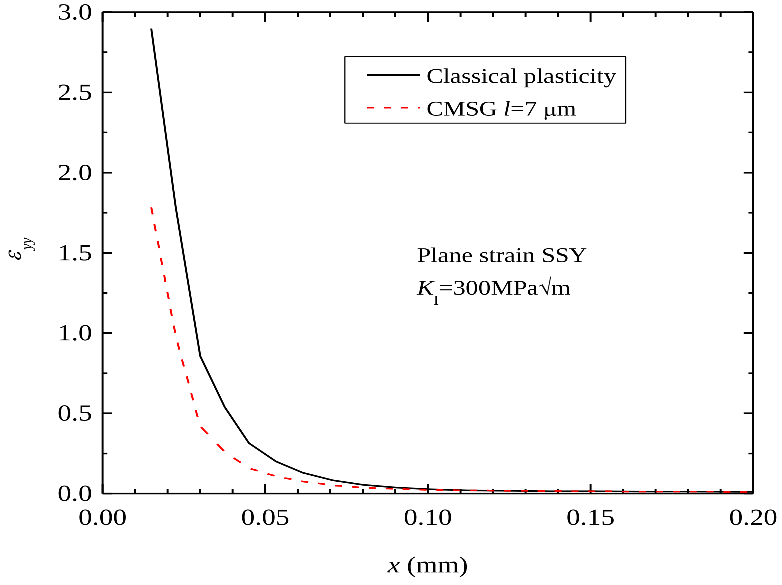

(b)

Figure 6.5 The comparison of normalized von Mises stress and strain ε_{yy} distribution along the crack plane for plane strain SSY model by the classical plasticity and CMSG plasticity analyses (a) Normalized von Mises; (b) Strain ε_{yy}

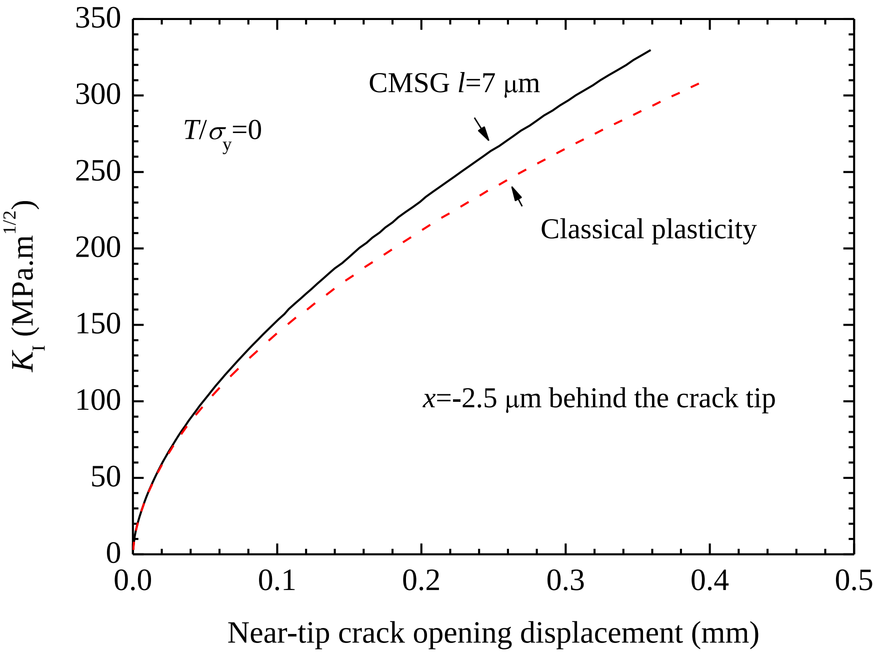

Figure 6.6 Load-opening displacement at location of 2.5 μm behind the crack tip from classical plasticity and CMSG plasticity analyses for SSY model with zero T-stress

6.2.3 Effect of Plastic Strain Gradient on the Near-tip Opening Displacement for the SSY model with Non-zero T-stress

In this section, the SSY model with non-zero *T*-stress is used to study the plastic strain gradient effect on the near-tip opening displacement. The mesh of the SSY model is the same as section 6.2.3 and contains 2.5 μm root radius at the crack tip. The location for measuring the opening displacement is defined at 2.5 μm behind the crack tip. The plane strain, K_I with different levels of *T*-stress, $T/\sigma_y = \pm 0.5, \pm 0.9$ displacement fields are applied on the SSY model.

Two different methods, proportional loading and non-proportional loading are used for applying the *T*-stress. Proportional loading applies the load $K_I + T$ proportionally on the outer radius of the SSY model in one step while the non-proportional loading applies the *T*-stress in the first step followed by K_I loading in the second step. Figures 6.7(a) and 6.7(b) show that under proportional $K_I + T$ loading with two different positive *T*-stresses, $T/\sigma_y = 0.5, 0.9$. The differences of the opening displacement between the CMSG plasticity results and classical plasticity results are trivial at small load for both cases as the initial root removes the stress singularity at the crack tip. As the load increases, the initial root presents less significant effect on the stress field near the crack tip and the plastic strain gradient gradually shows the effect on the CTOD values. At the load of $K_I = 300 \text{ MPa}\sqrt{\text{m}}$, the near-tip opening displacement at $x = -2.5$ μm computed from the CMSG plasticity analysis is around 17% and 18% lower than that computed from the classical plasticity for $T/\sigma_y = 0.5 \text{ and } 0.9$, respectively. For the two different levels of positive *T*-stress, the CMSG plasticity reduces the opening displacement compared with the classical plasticity.

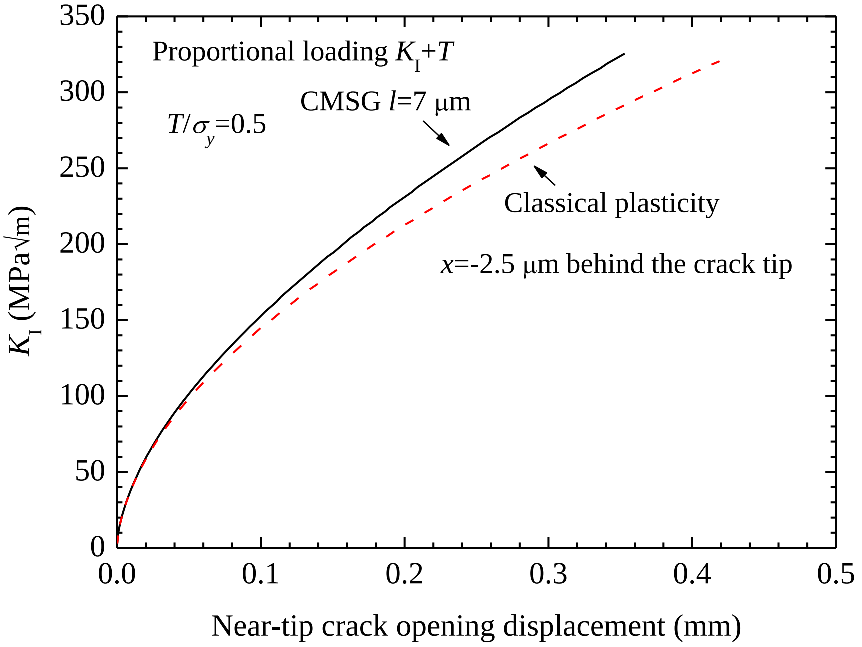
Proportional loading K_I+T
$T/\sigma_y=0.5$
CMSG l=7 μm
Classical plasticity
x=-2.5 μm behind the crack tip
K_I (MPa√m)
0
50
100
150
200
250
300
350
0.0
0.1
0.2
0.3
0.4
0.5
Near-tip crack opening displacement (mm)

(a)

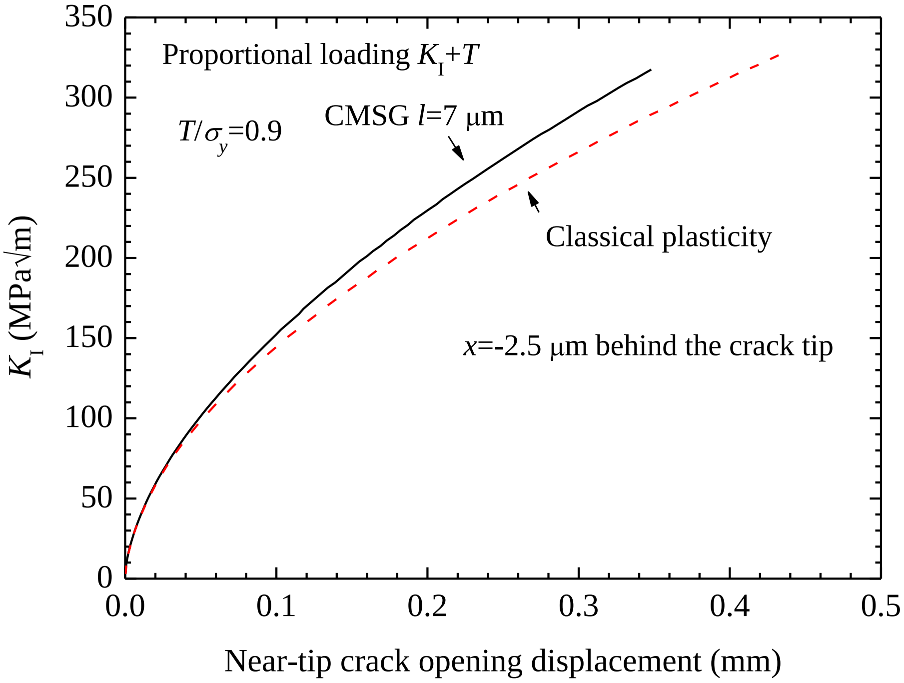
Proportional loading K_I+T
$T/\sigma_y=0.9$
CMSG l=7 μm
Classical plasticity
x=-2.5 μm behind the crack tip
K_I (MPa√m)
0
50
100
150
200
250
300
350
0.0
0.1
0.2
0.3
0.4
0.5
Near-tip crack opening displacement (mm)

(b)

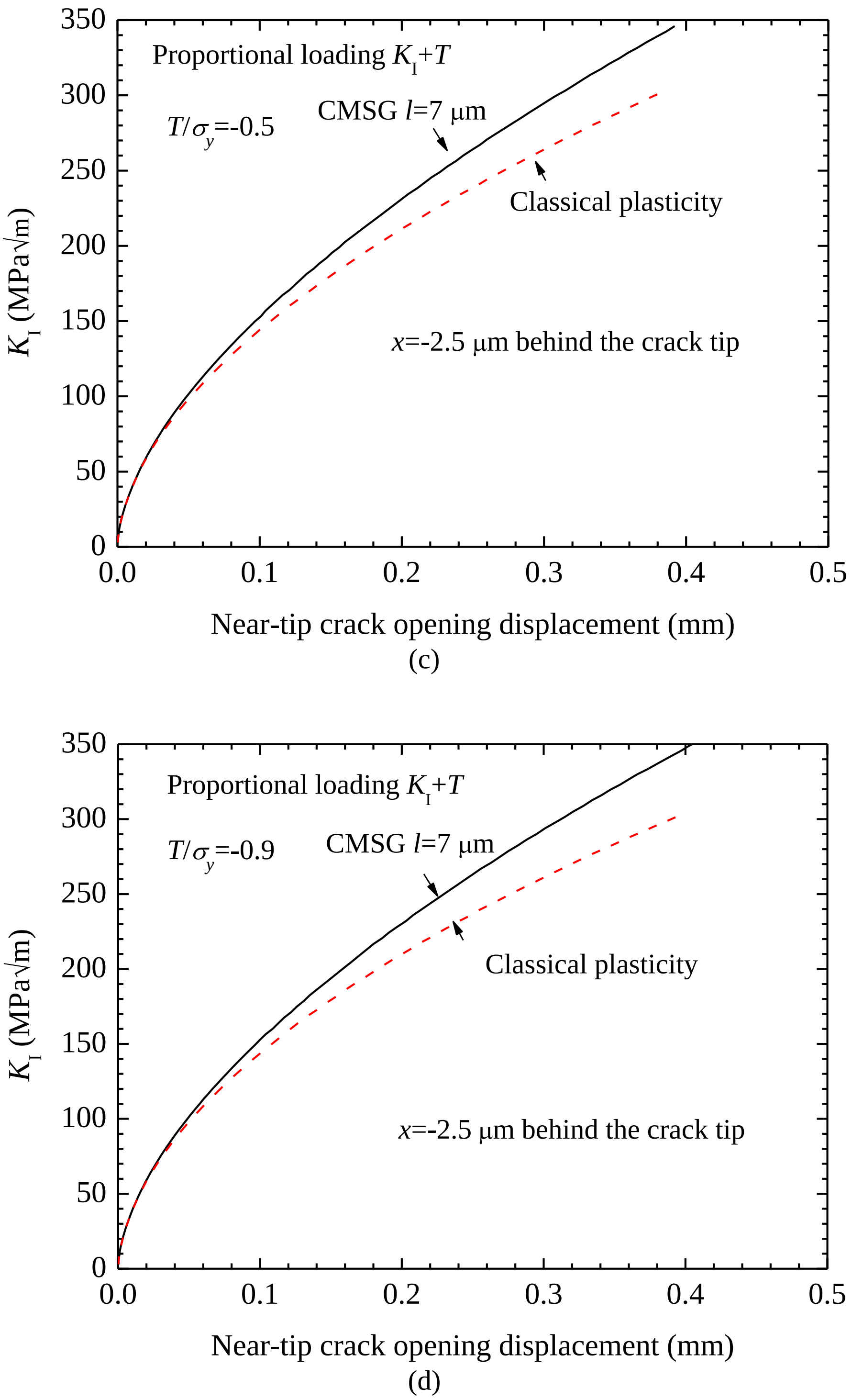

Figure 6.7 Load-opening displacement at location of 2.5 μm behind the crack tip from classical plasticity and CMSG plasticity analyses for SSY model with different level of T-stress (a) $T/\sigma_y = 0.5$; (b) $T/\sigma_y = 0.9$; (c) $T/\sigma_y = -0.5$; (d) $T/\sigma_y = -0.9$

Figures 6.7(c) and 6.7(d) also present that under proportional $K_I + T$ loading with the negative T-stresses, $T/\sigma_y = -0.5$, and -0.9, the near-tip opening displacement with including plastic strain gradient effect has less opening displacement compared with that computed from the classical plasticity. At the load of $K_I = 300\ \mathrm{MPa}\sqrt{\mathrm{m}}$, the near-tip opening displacement at $x = -2.5\ \mu\mathrm{m}$ computed from the CMSG plasticity analysis is around 15% and 16% lower than that computed from the classical plasticity for $T / \sigma_y = -0.5$ and -0.9, respectively. For the two different levels of negative *T*-stress, the CMSG plasticity reduces the CTOD values compared with the classical plasticity.

Figure 6.8(a) plots load K_I versus the near-tip opening displacement curves at different of *T*-stress $T / \sigma_y = \pm 0.5$ and ± 0.9 from the CMSG plasticity analysis. The load-near-tip opening displacement for positive *T*-stress ($T > 0$) is slightly higher than that for negative *T*-stress ($T \leq 0$). Initially, the *T*-stress does not affect the crack opening displacement. As the load increases, crack tip with positive T-stress keeps the small scale yield and high constraint conditions, while the negative *T*-stresses ($T / \sigma_y = -0.5$ and -0.9) relax the material constraint ahead of the crack tip, therefore, generate large opening displacement. The results of the classical plasticity analyses (see Figure 6.8(b)) also provide the same conclusions that the crack tip with the negative *T*-stress induces less near-tip opening displacement than positive *T*-stress, and the higher *T*-stress has less opening displacement. This phenomenon agree well with Hancock *et al.* [81] in the condition of non-extension crack. If the crack extends, negative *T*-stress can relax more material constraint and causes larger CTOD.

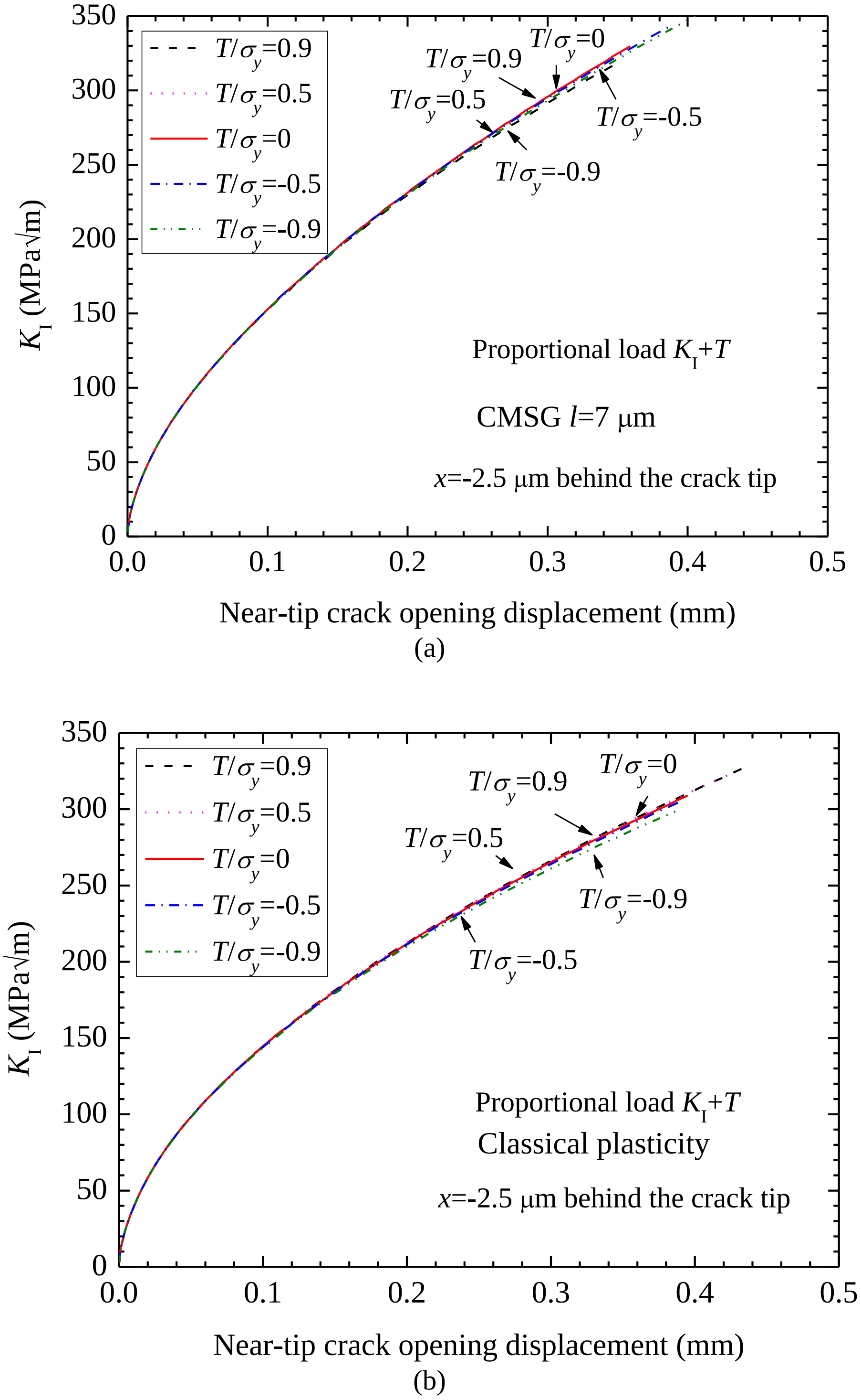

Figure 6.8 Load-opening displacements at location of 2.5 μm behind the crack tip for SSY model with proportional loading ($T / \sigma_y = 0, \ \pm 0.5$, and ± 0.9) (a) CMSG plasticity; (b) Classical plasticity

Under the non-proportional $K_I + T$ loading, the model is applied T in the first step, and followed by K_I in the second step. The first step load, *T*-stress has slight effect on the CTOD value. Figures 6.9(a) and 6.9(b) show that under the load of $K_I = 300\ \text{MPa}\sqrt{\text{m}}$, the CTOD value at $x = -2.5\ \mu\text{m}$ computed from the CMSG plasticity is 18% and 17% lower than that computed from the classical plasticity for $T/\sigma_y = 0.5 \text{ and } 0.9$, respectively. For negative *T*-stresses (see Figures 6.9(c) and (d), $T/\sigma_y = -0.5 \text{ and} -0.9$), at the load of $K_I = 300\ \text{MPa}\sqrt{\text{m}}$, the CTOD values from the CMSG plasticity analysis are also around 18% and 17% lower than those from the classical plasticity.

Comparing the load-CTOD curves computed from non-proportional load, $K_I + T$, $T/\sigma_y = 0.5,\ 0.9,\ -0.5, \text{ and} -0.9$ by the CMSG plasticity and the classical plasticity analyses (see Figures 6.10(a) and 6.10(b)), the CTOD values at $x = -2.5\ \mu\text{m}$ behind the crack tip for positive *T*-stress ($T > 0$) are slightly higher than that for negative *T*-stress ($T \leq 0$). The crack tip with positive *T*-stress keeps the small scale yielding, high constraint conditions as the load increases. However, the negative *T*-stresses ($T/\sigma_y = -0.5 \text{ and} -0.9$) relax the material constraint ahead of the crack tip, therefore, has slightly larger opening displacements. The results of the classical plasticity analyses (see Figure 6.8(b)) also can conclude that the crack tip with high *T*-stress experiencing high plastic constraint has less opening displacement and the negative *T*-stress induces less near-tip opening displacement.

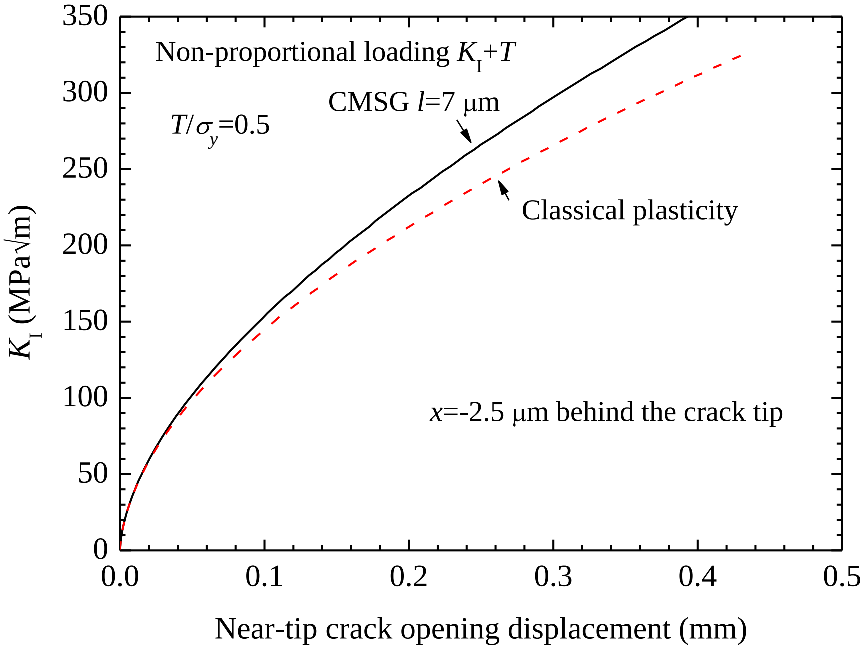
Non-proportional loading K_I+T
T/σ_y=0.5
CMSG l=7 μm
Classical plasticity
x=-2.5 μm behind the crack tip
K_I (MPa√m)
0
50
100
150
200
250
300
350
0.0
0.1
0.2
0.3
0.4
0.5
Near-tip crack opening displacement (mm)

(a)

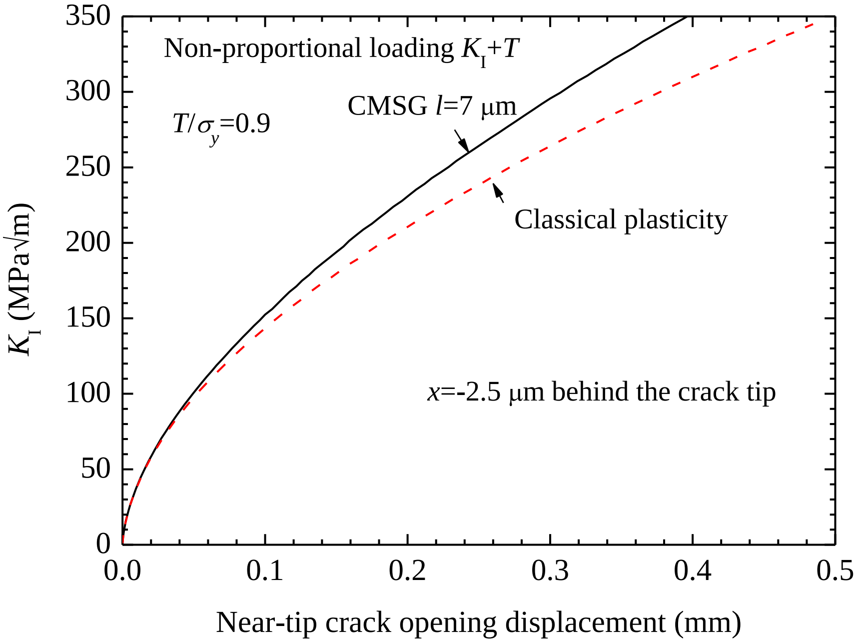
Non-proportional loading K_I+T
T/σ_y=0.9
CMSG l=7 μm
Classical plasticity
x=-2.5 μm behind the crack tip
K_I (MPa√m)
0
50
100
150
200
250
300
350
0.0
0.1
0.2
0.3
0.4
0.5
Near-tip crack opening displacement (mm)

(b)

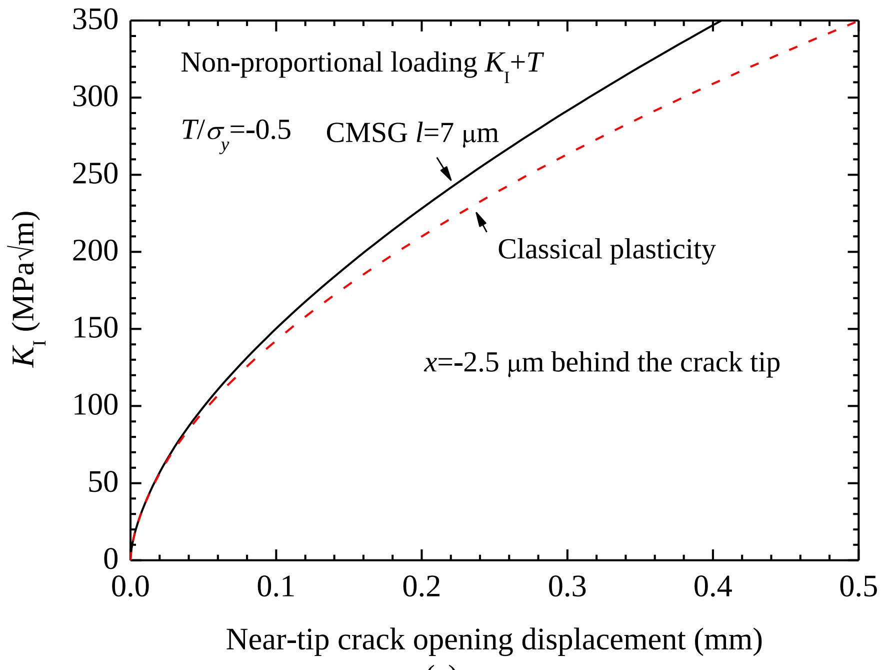

(c)

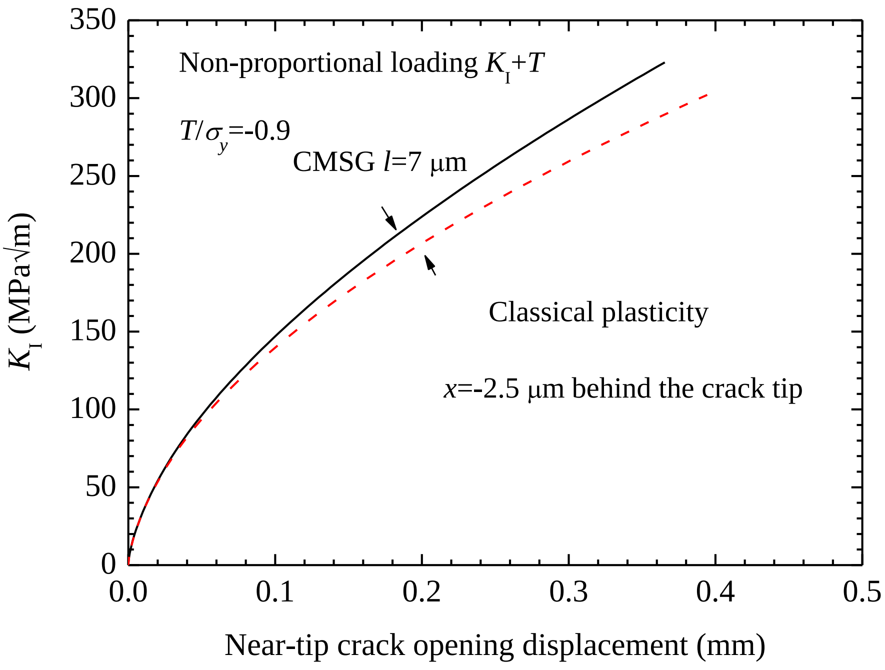

(d)

Figure 6.9 Load-opening displacement at location of 2.5 μm behind the crack tip from classical plasticity and CMSG plasticity analyses for SSY model under non-proportional loadings (a) $T/\sigma_y = 0.5$; (b) $T/\sigma_y = 0.9$; (c) $T/\sigma_y = -0.5$; (d) $T/\sigma_y = -0.9$

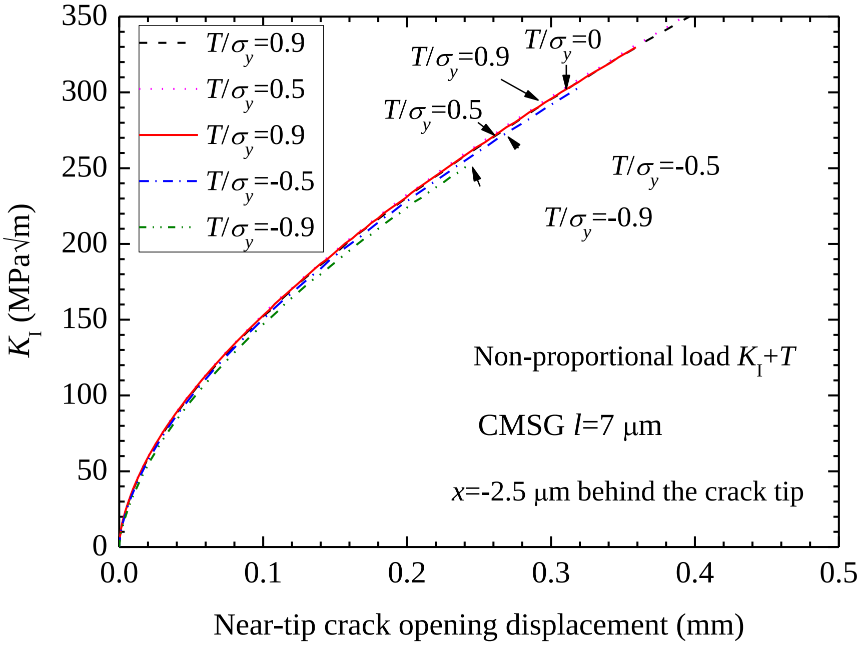

(a)

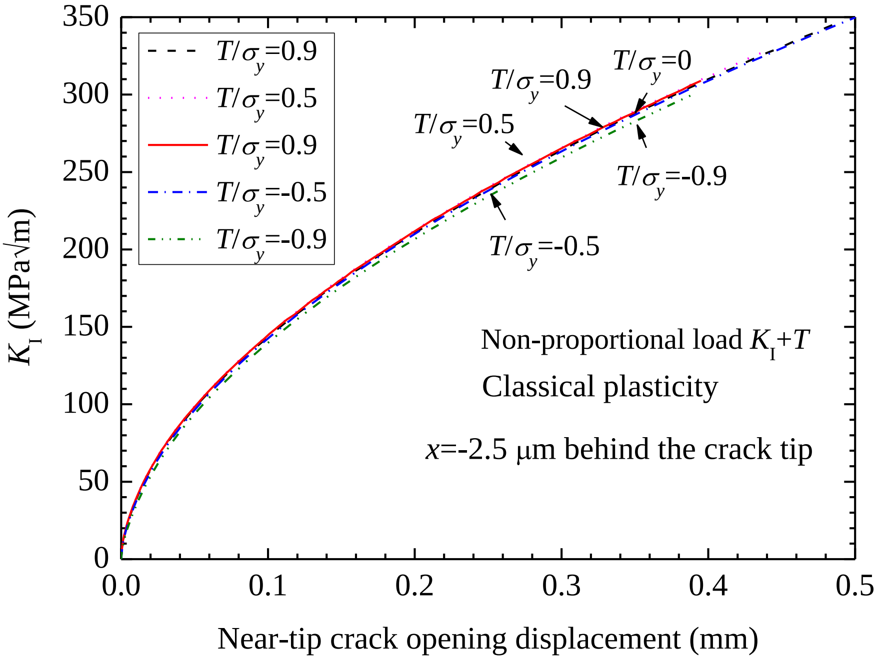

(b)

Figure 6.10 Load-opening displacements at location of 2.5 μm behind the crack tip for SSY model with nonproportional loadings ($T / \sigma_y = 0, \pm 0.5$, and ± 0.9) (a) CMSG plasticity; (b) Classical plasticity

6.3 Summary

This chapter numerically investigates the plastic strain gradient effect on the near-tip opening displacement by the 0.5T C(T) model and the SSY model. The results from the

0.5T C(T) model show that the incorporation of the plastic strain gradient reduces the near-tip opening displacement compared with that from classical plasticity if the location of the measured CTOD is less than 10 μm behind the crack tip. The effect of plastic strain gradient on the opening displacement diminishes as the position moves gradually away from the crack tip,

In the study of plane strain SSY model, we find that the CMSG plasticity effect also reduces the near-tip opening displacement under the proportional and non-proportional $K_I + T$ loading. The crack tip with low *T*-stress ($T < 0$) experiencing the low constraint has slightly larger crack tip opening displacements than the crack tip subjected to positive *T*-stresses from both the CMSG plasticity and the classical plasticity analyses under the condition of no crack extension.

Practically, the SEM (scanning electron microscope) technique has been popularly used for measuring crack opening displacement for several types of metals [82-85]. In the current work, due to lack of the necessary equipment, the fracture tests for verifying the plastic strain gradient effect on the near-tip opening displacement has not been done and is suggested to be done in the future.

CHAPTER 7 CONCLUSIONS AND FUTURE WORK

7.1 Conclusions

The study involves the cleavage fracture by incorporating the conventional mechanism-based strain gradient (CMSG) plasticity theory. The detailed work includes the investigation of the plastic strain gradient effect on the crack tip stress field by the small yielding model, and the recalibration of the Weibull parameters, the Weibull modulus m and the threshold fracture toughness K_{min}, in a three-parameter Weibull stress model for the 22-Ni-MoCr37 steel at three temperatures over the ductile-to-brittle transition under three different temperature: $\Theta = -20\ ^{o}\mathrm{C},\ -40\ ^{o}\mathrm{C}$ and $-110\ ^{o}\mathrm{C}$. As the material length scale is the most important parameter in the CMSG plasticity theory, this work also quantifies the material length scales of the two types of structural steels (S355 and S690) through the indentation tests and the corresponding simulations at the two temperatures 20 ^{o}C and 300 ^{o}C. The simulations for indentation test on the two types of steel at –40 ^{o}C are also performed for the reference of the future indentation tests at this temperature. The plastic strain gradient effect on the crack tip opening displacement by the 0.5T C(T) model and the plane strain small scale yielding model is studied as well.

Based on the above work done, the following conclusions are made.

1. The results from the study of fracture model by small scale yielding model show that the CMSG plasticity can capture the asymptotic stress fields near the crack tip more accurately than the classical plasticity because the CMSG plasticity theory defines the material hardening not only on the strain but also on the gradient of strain. The result agrees well with previous research work [5, 49].

2. The calibration results of the Weibull modulus m and the threshold fracture toughness K_{min} for the 22-Ni-MoCr37 steel at three temperatures $\Theta = -20\ ^{o}C$, $-40\ ^{o}C$, and $-110\ ^{o}C$ over the ductile-to-brittle transition regime show that the CMSG plasticity theory significantly increases the Weibull stress magnitudes compared to those obtained from the classical plasticity for fracture specimens under the same macroscopic crack-opening load. The CMSG plasticity theory generates slightly larger values of the Weibull modulus than those from the classical plasticity theory. The threshold fracture toughness values exhibit less dependence on the material strain hardening properties. By assuming two typical values of the material length scales, $l = 5$ μm and $l = 10$ μm, in the CMSG plasticity theory for the calibration of Weibull stress parameters, the magnitudes of the Weibull stress and the calibrated m and K_{min} values indicate negligible dependence on these two values of the material length scales. The calibrated Weibull stress model predicts a higher probability of the fracture for the plastic strain-gradient dependent hardening material than that for the materials following the classical plasticity theory for a macro-crack under the same opening load, if the same Weibull modulus m is assumed or if the calibrated m values are used in the Weibull stress model. The study from the small scale yielding model also shows that the crack front constraints, characterized by the linear-elastic T-stress, impose a strong effect on the magnitude of the Weibull stresses, especially when the crack front experiences low plasticity constraints. Both proportional and non-proportional loads cause significant differences in the Weibull stress values and the constraint-correction function.
3. The simulations of the indentation test for structural steels S355 and S690 using the CMSG plasticity theory with the trial values of the material length scale show

that the material length scale of the structural steel is around 7 μm under the two temperatures (20 °C and 300 °C).

4. Finite element analyses from the 0.5T C(T) model show that the plastic strain gradient effect on the crack tip opening displacement, CTOD is negligible since the location to determine the CTOD moves further away from the crack tip with increasing loads. However, the crack opening displacement measured near (less than 10 μm) the true crack tip depends strongly on the plastic strain gradient. The values of near-tip crack opening displacement computed using the CMSG plasticity behind the crack tip are lower than using the classical plasticity, indicating that the strain gradient stiffens the material deformation near the crack tip and hence reduces the values of near-tip crack opening displacement. The SSY model imposed with different *T*-stresses shows that the negative *T*-stress can relax the material constraint and induce slightly higher values of near-tip crack opening displacement while the positive *T*-stress constrains the crack tip material and induces slightly lower values of near-tip crack opening displacement.

7.2 Future Work

The current research numerically shows the plastic strain gradient is very important to capture the crack tip stress field and also can affect the values of near-tip crack opening displacement. Therefore, it is necessary to determine the important parameter, the material length scale, which induces the plastic strain gradient into the CMSG plasticity constitutive model. For the steels, S355 and S690, the material length scale currently is quantified as 7 μm through the simulation of indentation tests at two temperatures of $20\ ^{\circ}\mathrm{C}$ and $300\ ^{\circ}\mathrm{C}$. The indentation tests at $-40\ ^{\circ}\mathrm{C}$ have not been done. It is necessary to carry out the indentation test at low temperature to verify the effect of the temperatures on the material length scale for the steels which may undergo the tremendously cold environment in the arctic zone.

The current finite element results show that the CMSG plasticity affects on the crack opening displacement only at the position very close to the crack tip. In the future work, the SEM method is recommended to measure the near-tip crack opening displacement and verify the plastic strain gradient effect on the magnitude of near-tip opening displacement in the near-tip field.

REFERENCES

[1] Chang JI, Lin CC. A study of storage tank accidents. J Loss Prevention in the Process Industries 2006;19:51-59.

[2] Anderson T. Fracture mechanics: fundamentals and applications.3rd edition. Taylor & Francis 2005.

[3] Huang Y, Zhang L, Gao TF, Hwang KC. Mixed mode near-tip fields for cracks in materials with strain-gradient effects. J Mech Phys Solids 1997;45:439-465.

[4] Huang Y, Qu S, Hwang KC, Li M, Gao H. A conventional theory of mechanism-based strain gradient plasticity. Int J Plasticity 2004;20:753-782.

[5] Swaddiwudhipong S, Hua J, Tho KK, Liu Z. Finite element modelling for materials with size effect. Model Simul Mater Sci Eng 2006;14:1127-1137.

[6] Wallin K, Saario T, Torronen K. Statistical model for carbide induced brittle fracture in steel. Metal Sci 1984;18:13-16.

[7] Mudry F. A local approach to cleavage fracture. Nucl Eng Des 1987;105:65-76.

[8] Heerens J, Pfuff M, Hellmann D, Zerbst U. The lower bound toughness procedure applied to the Euro fracture toughness dataset. Eng Fract Mech 2002;69:483-495.

[9] Neale B. An assessment of fracture toughness in the ductile to brittle transition regime using the Euro fracture toughness dataset. Eng Fract Mech 2002;69:497-509.

[10] Petti JP, Dodds RH. Calibration of the Weibull stress scale parameter, σ_u, using the Master Curve. Eng Fract Mech 2005;72:91-120.

[11] ASTM E 1921 A. Test method for the Determination of Reference Temperature for Ferritic Steels in the Transition Range. American Society for Testing and Materials Philadelphia. 2002.

[12] Beremin FM. A local criterion for cleavage fracture of a nuclear pressure vessel steel. Met Trans 1983;14A:2277-2287.

[13] Bakker A, Koers R. Preduction of cleavage fracture events in the brittle-ductile transition region of a ferrtic steel. In: Blauel, Schwalbe, editors. Defect assessment in components-fundamentals and applications. London: Mechanical Engineering Publications 1991:613-632.

[14] Wallin K. Fracture toughness transition curve shape for ferritic steels. Fract Eng Mater Struct. 1991;55:83-88.

[15] Wallin K. Irradiation damage effects on the fracture toughness transition curve shape for reactor pressure vessel steels. Int J Pressure Ves Piping 1993;55:61-79.

[16] Minami F, Bruckner-Foit A, Munz D, Trolldenier B. Estimation procedure for the Weibull parameters used in the local approach. Int J Fract 1992;54:191-197.

[17] Ruggieri C, Dodds RH. Numerical evaluation of probabilistic fracture parameters with WSTRESS. Eng Comp 1998;15:49-73.

[18] Ruggieri C, Gao X, Dodds RH. Transferability of elastic-plastic fracture toughness using the Weibull stress approach: significance of parameter calibration. Eng Fract Mech 2000;67:101-117.

[19] Gao X, Ruggieri C, Dodds RH. Calibration of Weibull stress parameters using fracture toughness data. Int J Fract 1998;92:175-200.

[20] Gao X, Dodds RH. Constraint effects on the ductile-to-brittle transition temperature of ferritic steels: A Weibull stress model. Int J Fract 2000;102:43-69.

[21] Heerens J, Hellmann D. Development of the Euro fracture toughness dataset. Eng Fract Mech 2002;69:421-449.

[22] Bernauer G, Brocks W. Micro-mechanical modelling of ductile damage and tearing-results of a European round robin. Fatigue Fract Eng Mater Struct 2002;25:363-383.

[23] Petti JP, Dodds RH. Coupling of the Weibull stress model and macroscale models to predict cleavage fracture. Eng Fract Mech 2004;71:2079-2103.

[24] Wasiluk B, Petti JP, Dodds RH. Temperature Dependence of Weibull Stress Parameters: Studies Using the Euro-Material Similar to ASME A508 Class-3 Steel. United States; 2007. p. 63.

[25] Moorman JE. A statistical model of cleavage fracture. Eng Fract Mech 2008;75:1587-1604.

[26] Bernauer G, Brocks W, Schmitt W. Modifications of the Beremin model for cleavage fracture in the transition region of a ferritic steel. Eng Fract Mech 1999;64:305-325.

[27] O’Dowd NP, Lei Y, E.P. B. Prediction of cleavage failure probabilities using the Weibull stress. Eng Fract Mech 2000;67:87-100.

[28] Bordet SR, Karstensen AD, Knowles DM, Wiesner CS. A new statistical local criterion for cleavage fracture in steel. Part I: model presentation. Eng Fract Mech 2005;72:435-452.

[29] Bordet SR, Karstensen AD, Knowles DM, Wiesner CS. A new statistical local criterion for cleavage fracture in steel. Part II: application to an offshore structural steel. Eng Fract Mech 2005;72:453-474.

[30] Rathbun HJ, Odette GR, He MY, Yamamoto T. Influence of statistical and constraint loss size effects on cleavage fracture toughness in the transition-A model based analysis. Eng Fract Mech 2006;73:2723-2747.

[31] Smith DJ, Hadidi-Moud S, Mahoudi AH, Sisan AM, C.E.Truman. Experiments and predictions of the effects of load history on cleavage fracture in steel. Eng Fract Mech 2010;77:631-645.

[32] Bostjan B, Anuradha B. A local approach model for cleavage fracture and crack extension direction of functionally graded materials. Eng Fract Mech 2010;77:3394-3407.

[33] Jorg H, Valerie F, Jan W, Dieter S. Assessment of the role of micro defect nucleation in probabilistic modeling of cleavage fracture. Eng Fract Mech 2008;75:3306-3327.

[34] Jorg H, Volker H, Sabrina L, Dieter S. An enhanced probabilistic model for cleavage fracture assessment accounting for local constraint effects. Eng Fract Mech 2010;77:3573-3591.

[35] Elssner G, Korn D, Ruehle M. The influence of interface impurities on fracture energy of UHV diffusion bonded metal-ceramic bicrystals. Scripta Metall et Mater 1994;31:1037-1042.

[36] Korn D, Elssner G, Cannon RM, Ruhle M. Fracture properties of interfacially doped Nb-Al_2O_3 bicrystals. I. Fracture characteristics. Acta Metall et Mater 2002;50:3881-3901.

[37] Korn D, Elssner G, Fischmeister HF, Rühle M. Influence of interface impurities on the fracture energy of UHV bonded niobium sapphire bicrystals. Acta Metall et Mater 1992;40:355-360.

[38] Beltz GE, Wang JS. Crack direction effects along copper sapphire interfaces. Acta Metall et Mater 1992;40:1675-1683.

[39] O’Dowd NP, Stout MG, Shih CF. Fracture-toughness of alumina niobium interfaces-experiments and analyses. Philosophical Magazine A 1992;66:1037-1064.

[40] Fleck NA, Hutchinson JW. A phenomenological theory for strain gradient effects in plasticity. J Mech Phys Solids 1994;41:1825-1857.

[41] Ma Q, Clark DR. Size-dependent hardness in silver single crystals. J Mater Res 1995;10:853-863.

[42] Nix WD. Elastic and plastic properties of thin films on substrates: nano-indentation techniques. Mater Sci Eng A 1997:234-236.

[43] Ashby MF. The deformation of plastically non-homogeneous alloys. Philosophical Magazine A 1970;21:399-424.

[44] Xia ZC, Hutchinson JW. Crack tip fields in strain gradient plasticity. J Mech Phys Solids 1996;44:1621-1648.

[45] Gao H, Huang Y, Nix WD. Modeling plasticity at the micrometer scale. Naturwissenschaflen 1999;86:507-515.

[46] Gao H, Huang Y, Nix WD, Hutchinson JW. Mechanism-based strain gradient plasticity-I. Theory. J Mech Phys Solids 1999;47:1239-1263.

[47] Huang Y, Gao H, Nix WD, Hutchinson JW. Mechanism-based strain gradient plasticity-II. Analysis. J Mech Phys Solids 2000;48:99-128.

[48] Chen JY, Wei Y, Huang Y, Hutchinson JW, Hwang KC. The crack tip fields in strain gradient plasticity: the asymptotic and numerical analyses. Eng Fract Mech 1999;64:625-648.

[49] Jiang H, Huang Y, Zhuang Z, Hwang KC. Fracture in mechanism-based strain gradient plasticity. J Mech Phys Solids 2001;49:979-993.

[50] Wei Y, Qiu X, Hwang KC. Steady-state crack growth and fracture work based on the theory of mechanism-based strain gradient plasticity. Eng Fract Mech 2004;71:107-125.

[51] Qu S, Huang Y, Jiang H, Liu C, Wu PD, Hwang KC. Fracture analysis in the conventional theory of mechanism-based strain gradient (CMSG) plasticity. Int J Fract 2004;129:199-220.

[52] Qiu X, Huang Y, Wei Y, Gao H, Hwang KC. The flow theory of mechanism-based strain gradient plasticity. Mech Mater 2003;35:245-258.

[53] Swaddiwudhipong S, Hua J, Tho KK, Liu Z. C^0 solid elements for materials with strain gradient effects. Int J Numer Meth Eng 2005;64:1400-1414.

[54] Swaddiwudhipong S, Tho KK, Hua J, Liu Z. Mechanism-based strain gradient plasticity in C^0 axisymmetric element. Int J Solids Struct 2006;43:1117-1130.

[55] Qu S, Huang Y, Pharr G, Hwang K. The indentation size effect in the spherical indentation of iridium: a study via the conventional theory of mechanism-based strain gradient plasticity. Int J Plasticity 2006;22:1265-1286.

[56] Zhang F, Saha R, Huang Y, Nix WD, Hwang K, Qu S, Li M. Indentation of a hard film on a soft substrate: strain gradient hardening effects. Int J Plasticity 2007;23:25-43.

[57] Ruggieri C, Dodds RH. A transferability model for brittle fracture including constraint and ductile tearing effects: a probabilistic approach. Int J Fract 1996;79:309-340.

[58] Gao X, Dodds RH, Tregoning RL, Joyce JA. Effects of loading rate on the Weibull stress model for simulation of cleavage fracture in ferritic steels. American Society of Mechanical Engineers, Pressure Vessels and Piping Division (Publication) PVP. 2000;412:125-130.

[59] Bompas-Smith J. Mechanical survival: the use of reliability data. New York. 1973;McGraw-Hill.

[60] Tho KK, Swaddiwudhipong S, Hua J, Liu Z. Numerical simulation of indentation with size effect. Mater Sci Eng A. 2006;421:268-275.

[61] Taylor GI. The mechanism of plastic deformation of crystals. Part I. theoretical. Proc Roy Soc Lon A 1934;145:362-387.

[62] Bishop JFW, Hill R. A theory of plastic distortion of a polycrystalline aggregate under combined stresses. Phil. Mag. 1951;42:414-427.

[63] Nix WD, Gao H. Indentation size effect in crystalline materials: A law for strain gradient plasticity. J Mech Phys Solids 1998;46:411-425.

[64] Nye JF. Geometrical relations in dislocated crystals. Acta Metall et Mater 1953;1:153-162.

[65] Voyiadjis GZ, Almasri AH. Variable material length scale associated with nanoindentation experiments. J Eng Mech ASCE 2009;135:139-148.

[66] ABAQUS. ABAQUS "Standard User’s Manual Version 6.9". Pawtucket, RI: Hibbitt, Karlsson, & Sorensen, Inc. 2009.

[67] Dodds RH, Shi C, Anderson T. Continuum and micro-mechanics treatment of constraint in fracture. Int J Fract 1993;64:101-133.

[68] Qian XD, Zhang SF, Swaddiwudhipong S. Calibration of Weibull parameters using the conventional mechanism-based strain gradient plasticity. Eng Fract Mech 2011;78:1928-1944.

[69] Heerens J, Hellmann D. Development of the Euro fracture toughness dataset. Eng Fract Mech 2002;69:421-449.

[70] Fleck NA, Muller GM, Ashby MF, Hutchinson JW. Strain gradient plasticity: theory and experiment Acta Metall et Mater 1994;42:475-487.

[71] Williams M. On the stress distribution at the base of a stationary crack. J Appl Mech 1957;24:109-114.

[72] O'Dowd NP, Shih C. Family of crack-tip fields characterized by a triaxiality parameter-I. structure of fields. J Mech Phys Solids 1991;39:989-1015.

[73] GKSS ftp-server. ftp:// ftp. Gkss.de/pub/eurodataset 2001.

[74] Wallin K. Master curve analysis of the Euro fracture toughness dataset. Eng Fract Mech 2002;69:451-481.

[75] Stolken JS, Evans AG. A microbend test method for measuring the plasticity length scale. Acta Metall et Mater 1998;46:2855-2865.

[76] Shu JY, Fleck NA. The prediction of a size effect in micro-indentation. Int J Solids Struct 1998;35:1363-1383.

[77] Begley MR, Hutchinson JW. The mechanics of size-dependent indentation. J Mech Phys Solids 1998;46:2049-2068.

[78] Yuan H, Chen J. Identification of the intrinsic material length in gradient plasticity theory from micro-indentation tests. Int J Solids Struct 2001;38:8171-8187.

[79] Rashid K, Abu AR, Voyiadjis G. Determination of material intrinsic length scale of gradient plasticity theory. Int J Multiscale Comp Eng 2004;2:377-400.

[80] ASTM E 8. Standard test methods for tension testing of metallic materials. American Society for Testing and Materials Philadelphia. 2008.

[81] Hancock JW, Reuter WG, Parks DM. Constraint and Toughness Parameterized by T. Constraint Effect in Fracture. 1993;1171:21-40.

[82] Andersson H, Persson. In-situ SEM study of fatigue growth behavior in IN718. Int J fatigue 2004;26:211-219.

[83] Zhang JZ[a], Zhang JZ[b], Zhao XM. Direct high resolution in situ SEM observations of very small small fatigue crack growth in the ultra-fine grain aluminium alloy IN 9052. Scripta Materialia 2004;50:825-828.

[84] Zhang JZ, He XD, Tang H, Du SY. Direct high resolution in situ SEM observations of small fatigue crack opening profiles in the ultra-fine grain aluminium alloy. Mater Sci Eng A 2008;485:115-118.

[85] Zhang W, Liu Y. In situ SEM testing for crack closure investigation and virtual crack annealing model development. Int J fatigue 2012;43:188-196.

LIST OF PUBLICATIONS

The flowing is a list of publications based on the work reported in this thesis.

Journal Publications

[1] Qian XD, Zhang SF, Swaddiwudhipong S. Calibration of Weibull parameters using the conventional mechanism-based strain gradient plasticity. Eng Fract Mech 2011;78:1928-1944.

Conference Publications

[1] Zhang SF, Qian XD, Swaddiwudhipong S, Tho KK. Effect of strain gradient plasticity on the Weibull stress analysis of a small-scale yielding model. Proceeding of the 21st KKCNN Symposium on Civil Engineering, 2008, Singapore.

[2] Swaddiwudhipong S, Qian XD, Zhang SF, Tho KK. Conventional mechanism-based strain gradient plasticity and Weibull stress. International Symposium on Plasticity and Its Current Applications, Jan 2009, US.

[3] Swaddiwudhipong S, Qian XD, Zhang SF. Computing applications in offshore structures at NUS. The twelfth East Asia-Pacific Conference on Structural Engineering and Construction, Jan 2011, Hong Kong.